Hollow MoS_x nanomaterials for aqueous energy storage applications

D i s s e r t a t i o n

zur Erlangung des akademischen Grades

d o c t o r r e r u m n a t u r a l i u m

(Dr. rer. nat.)

im Fach Chemie

eingereicht an der

Mathematisch-Naturwissenschaftlichen Fakultät

der Humboldt-Universität zu Berlin

von

M. Sc. Ting Quan

Präsident der Humboldt-Universität zu Berlin
Prof. Dr.-Ing. Dr. Sabine Kunst

Dekan: der Mathematisch-Naturwissenschftlichen Fakultät
Prof. Dr. Elmar Kulke

Gutachter/in: 1. Prof. Matthias Ballauff

2. Prof. Nicola Pinna

3. Prof. Martin Oschatz

Tag der mündlichen Prüfung: 17.03.2021

All over the place was six pence, but he looked up at the moon.

The Moon and Sixpence

To My Family & Friends

Abstract

The present thesis focuses on the synthesis of novel hollow MoS_x nanomaterials with controllable size and shape through the colloidal template method. Their possible applications in aqueous energy storage systems, including supercapacitors and Li-ion batteries (LIBs), have been studied.

In the first part, hollow carbon-MoS_2-carbon nanoplates have been successfully synthesized through an L-cysteine-assisted hydrothermal method by using gibbsite as the template and polydopamine (PDA) as the carbon precursor. After calcination and etching of the gibbsite template, uniform hollow platelets, which are made of a sandwich-like assembly of partial graphitic carbon and two-dimensional layered MoS_2 flakes, have been obtained. The platelets have shown excellent dispersibility and stability in water, and good electrical conductivity due to carbon coating generated by the calcination of polydopamine. The material is then applied in a symmetric supercapacitor using 1 M Li_2SO_4 as the electrolyte, which exhibits a specific capacitance of 248 F/g (0.12 F/cm^2) at a constant current density of 0.1 A/g and an excellent electrochemical stability over 3000 cycles, suggesting that hollow carbon-MoS_2-carbon nanoplates are promising candidate materials for supercapacitors.

In the second part, 21 m LiTFSI, so-called "water-in-salt" (WIS) electrolyte, has been studied in supercapacitors with hollow carbon nanoplates as electrode materials. In comparison with 1 M Li_2SO_4 electrolyte used in the first part, significant improvements on a broader and stable potential window have been revealed in the present WISE, which is slightly influenced by the lower conductivity with the counterpart. The electrochemical impedance spectroscopy (EIS) has been extensively employed to provide an insight look on the formation of solid electrolyte interphase in the WIS-supercapacitors. Additionally, the effect of temperature on the electrochemical performance has also been investigated in the temperature range between 15 and 55 °C, yielding eminent specific capacitance of 128 F/g at the optimized condition of 55 °C. The EIS measurements disclosed the decrease of fitted resistances with the increase of temperature and vise versa, directly illuminating the relationship between electrochemical output and working temperature of supercapacitors for reliable practical applications.

In the third part, MoS_3, an amorphous chain-like structured transitional metal trichalcogenide, has been demonstrated as a promising anode in the "water-in-salt" Li-ion batteries (WIS-LIBs). Hollow MoS_3 nanospheres used in this part have been synthesized via a scalable room-temperature acid precipitation method using spherical polyelectrolyte brushes (SPB) as the

template. When applied in WIS-LIBs with $LiMn_2O_4$ as the cathode material, the prepared MoS_3 achieves a high specific capacity of 127 mAh/g at the current density of 0.1 A/g and good stability over 1000 cycles in both coin cells and pouch cells. The working mechanism of MoS_3 in WIS-LIBs has also been studied by ex-situ X-ray diffraction (XRD) measurements. During operation, MoS_3 undergoes irreversible conversion to Li_2MoO_4 during the initial Li ion uptake, and is then gradually converted to a more stable and reversible Li_xMoO_y ($2 \leq y \leq 4$)) phase along cycling. Amorphous Li-deficient $Li_{x-m}MoO_y/MoO_z$ is formed upon delithiation.

The results in the present thesis demonstrate facile approaches for synthesizing hollow MoS_x nanomaterials with controllable morphologies using a template-based method, which attribute to the promising performance of MoS_x for aqueous energy storage applications. The electrochemical studies of hollow MoS_x nanomaterials in aqueous electrolytes provide insight into the reaction mechanisms of aqueous energy storage systems and push forward the development of metal sulfides for aqueous energy storage applications.

Keyword: hollow nanostructure, MoS_2, MoS_3, aqueous electrolytes, supercapacitors, Li-ion batteries.

Zusammenfassung

Die vorliegende Arbeit konzentriert sich auf die Synthese von neuartigen hohlen MoS_x-Nanomaterialien mit kontrollierbarer Größe und Form durch die kolloidale Template Methode. Ihre möglichen Anwendungen in wässrigen Energiespeichersystemen, einschließlich Superkondensatoren und Li-Ionen-Batterien (LIBs), wurden untersucht.

Im ersten Teil wurde eine neue Nanostruktur aus hohlen Kohlenstoff-MoS_2-Kohlenstoff-nanoplättchen erfolgreich durch eine L-Cystein unterstützte hydrothermale Methode unter Verwendung von Gibbsit als Templat und Polydopamin (PDA) als Kohlenstoffvorläufer synthetisiert. Nach dem Kalzinieren und Ätzen des Gibbsit Templates wurden gleichförmige Hohlplättchen erhalten, die aus einer sandwichartigen Anordnung von teilweise graphitischem Kohlenstoff und zweidimensional geschichteten MoS_2 Flocken bestehen. Die Plättchen haben eine ausgezeichnete Dispergierbarkeit und Stabilität in Wasser sowie eine gute elektrische Leitfähigkeit aufgrund des durch die Kalzinierung von Polydopaminbeschichtungen erzeugten Kohlenstoffs gezeigt. Das Material wird dann in einem symmetrischen Superkondensator mit 1 M Li_2SO_4 als Elektrolyt aufgebracht, der eine spezifische Kapazität von 248 F/g (0.12 F/cm^2) bei einer konstanten Stromdichte von 0.1 A/g und eine ausgezeichnete elektrochemische Stabilität über 3000 Zyklen aufweist, was darauf hindeutet, dass hohle Kohlenstoff-MoS_2-Kohlenstoffnanoplättchen vielversprechende Materialien als Kandidaten für Superkondensatoren sind.

Im zweiten Teil wurde 21 molare LiTFSI, das sogenannte "Wasser-in-Salz" (WIS) Elektrolyt, in Superkondensatoren mit hohlen Kohlenstoffnanoplättchen als Elektrodenmaterial untersucht. Im Vergleich zu dem im ersten Teil verwendeten 1 molaren Li_2SO_4-Elektrolyten wurden bei dem vorliegenden WIS Elektrolyt signifikante Verbesserungen in einem breiteren und stabilen Potentialfenster festgestellt, das durch die geringere Leitfähigkeit mit dem Gegenstück leicht beeinflusst wird. Die elektrochemische Impedanzspektroskopie (EIS) wurde ausgiebig eingesetzt, um einen Einblick in die Reaktionsmechanismen der WIS-Superkondensatoren zu erhalten. Zusätzlich wurde auch der Einfluss der Temperatur auf die elektrochemische Leistung im Temperaturbereich zwischen 15 und 55 °C untersucht, was eine hervorragende spezifische Kapazität von 128 F/g bei dem optimierten Zustand von 55 °C ergab. Die EIS-Messungen deckten die Abnahme der angepassten Widerstände mit der Temperaturerhöhung und umgekehrt auf und beleuchteten direkt die Beziehung zwischen

elektrochemischer Leistung und Arbeitstemperatur von Superkondensatoren für zuverlässige praktische Anwendungen.

Im dritten Teil wurde MoS_3, ein amorphes, kettenförmig strukturiertes Übergangsmetall Trichalcogenid, als vielversprechende Anode in "Wasser-in-Salz" Li-Ionen-Batterien (WIS-LIBs) nachgewiesen. Die in diesem Teil verwendeten hohlen MoS_3-Nanosphären wurden mittels einer skalierbaren Säurefällungsmethode bei Raumtemperatur synthetisiert, wobei sphärische Polyelektrolytbürsten (SPB) als Schablonen verwendet wurden. Beim Einsatz in WIS-LIBs mit $LiMn_2O_4$ als Kathodenmaterial erreicht das präparierte MoS_3 eine hohe spezifische Kapazität von 127 mAh/g bei einer Stromdichte von 0.1 A/g und eine gute Stabilität über 1000 Zyklen sowohl in Knopf- als auch in Pouch-Zellen. Der Arbeitsmechanismus von MoS_3 in WIS-LIBs wurde auch durch Ex-situ-Röntgenbeugungsmessungen (XRD) untersucht. Während des Betriebs wird MoS_3 während der anfänglichen Li-Ionen-Aufnahme irreversibel in Li_2MoO_4 umgewandelt und dann allmählich in eine stabilere und reversible Li_xMoO_y-Phase ($2 \leq y \leq 4$)) entlang der Zyklen umgewandelt. Amorphes Li-defizientes $Li_{x-m}MoO_y/MoO_z$ wird bei der Delithiierung gebildet.

Die Ergebnisse der vorliegenden Studie zeigen einfache Ansätze zur Synthese hohler MoS_x-Nanomaterialien mit kontrollierbarer Morphologie unter Verwendung einer Template-basierten Methode, die auf die vielversprechende Leistung von MoS_x für wässrige Energiespeicheranwendungen zurückzuführen sind. Die elektrochemischen Untersuchungen von hohlen MoS_x-Nanomaterialien in wässrigen Elektrolyten geben Einblick in die Reaktionsmechanismen von wässrigen Energiespeichersystemen und treiben die Entwicklung von Metallsulfiden für wässrige Energiespeicheranwendungen voran.

Stichwörter: hohle Nanostrukturen, MoS_2, MoS_3, wässrige Elektrolyte, Superkondensatoren, Li-Ionen-Batterien.

Table of Contents

1 Introduction

With the increasing energy demand and rapid depletion of fossil fuels, the exploration of sustainable and renewable energy resources such as solar, wind and tide has moved to the center attention. Consequently, energy storage systems have become urgently needed to improve power reliability and quality as well as taking full advantage of high penetration of renewable energy sources.[1-3] The need to develop energy storage systems with low costs, low risks, high round-trip efficiency and long cycle life is recognized as an urgent priority. Based on this, batteries and supercapacitors are both regarded as the most promising electrochemical energy storage devices. Usually, both supercapacitors and batteries consist of four main components: cathode, anode, electrolyte, and separator.

1.1 Aqueous electrolytes for supercapacitors and Li-ion batteries

Electrolytes, as one of the key components of energy storage systems, provide ionic conductivity and thus facilitate charge compensation on each electrode. Electrolytes are prepared by dissolving salt, also called electrolyte solutes, into proper solvents, either water or organic molecules.[4] In supercapacitors and LIBs, electrolytes should cater to the needs of both electrodes because of their physical location. Usually, electrolyte components directly determine the operational voltage of the cells, through which both the energy and power densities are affected.

To date, although organic electrolytes can operate at high voltages and wide potential window, they usually suffer from low ionic conductivity and flammable and toxic properties.[5] Compared to organic solvents, water is an attractive alternative in electrolytes as it is not only intrinsically safe, but also an excellent solvent with both high acceptor and donor numbers. Therefore, aqueous electrolytes for both supercapacitors and LIBs usually have much higher ionic conductivity than organic electrolytes, making it promising in wide applications.

1.1.1 Aqueous supercapacitors

Supercapacitors, which are grouped into double-layer capacitors, pseudocapacitors and hybrid capacitors by the energy storage mechanism, have bridged the gap between electrolytic capacitors and high-energy-density Li-ion batteries.[6] In general, various types of electrolytes for supercapacitors have been developed up to now, *e.g.* aqueous electrolytes, organic electrolytes and ionic liquids. Among them, aqueous electrolytes have been applied intensively in research and development, which is mainly due to the fact that aqueous electrolytes can be easily handled and prepared without any special condition.

Normally, aqueous electrolytes for supercapacitors can be classified to acid, alkaline and neutral solutions, in which H_2SO_4, KOH and Na_2SO_4 are representatives. In aqueous supercapacitors, the cell voltages for acid and alkaline electrolytes are limited within 1.3 V due to the hydrogen evolution at a negative electrode potential and the oxygen evolution at a positive electrode potential.[7] Generally, the electrolyte properties, such as concentration, ion type and so on can influence the equivalent series resistance, specific capacitance and voltage stability window of supercapacitors.[8] Among them, the influence from electrolyte ion type is relatively complicated. This is because both the ionic radius and the diffusion rate of ions affect the performance, and the main factor is different for different electrode materials.

As mentioned above, among acid electrolytes, H_2SO_4 is the most common used one for aqueous supercapacitors mainly because of its high conductivity (0.8 S cm^{-1} for 1 M H_2SO_4 at 25 ºC).[5] Its ionic conductivity is dependent on the concentration of H_2SO_4, which can reach maximum when the concentration is 1 M at 25 ºC. In addition, when using pseudocapacitive electrode materials such as metal oxides and sulfides in acid electrolyte, the stability is poor due to the sensitivity of the materials to pH.[9-10] In order to further improve the chemical stability of pseudocapacitive electrode materials in acid electrolytes, to date, some alternative electrolytes have been explored. For example, Perret *et al.*[11] introduced a new acid electrolyte composed of methanesulfonic acid and lead methanesulfonate for carbon/PbO_2 asymmetric supercapacitors. In this case, the redox reactions of PbO_2 was changed from a solid/solid couple to a solid/ solvated ion one without any sulfation, which always takes place in sulfuric acid electrolyte. It is hypothesized that during charging process, Pb^{2+} was oxidized and PbO_2 was formed and electrodeposited on the electrode surface, thus improving the cycle life. It should be noted that beside H_2SO_4, there are other types of acid electrolytes, including perchloric acid, hexafluorosilic acid and so on. However, only limited research has been performed on these electrolytes because of a safety concern. Moreover, there is usually self-discharge of these electrolyte, especially in concentrated ones.[12]

Besides acid electrolytes, alkaline electrolytes are also one of the most widely used aqueous electrolytes for supercapacitors. Among various alkaline electrolytes, KOH is the most common used one because of its high ionic conductivity (a maximum value of 0.6 S cm^{-1} for 6 M at 25 ºC)[5], which can be applied in electric double layer capacitors (EDLCs), pseudocapacitors and hybrid capacitors. For carbon based EDLCs, the specific capacitance and energy densities in alkaline electrolytes are similar to those in acid electrolytes. When transition metal oxides and sulfides are used in alkaline electrolyte based supercapacitors, the working mechanism

normally involves the adsorption/desorption or insertion/desertion of electrolyte ions into/out of the electrode materials.[13] However, some metal sulfides such as CoS and NiS show poor supercapacitor performance in alkaline electrolytes due to their instability. After a few cycles, they electrochemically transform into new electroactive phases.

Additionally, neutral electrolytes have also been widely studied for supercapacitors attributed to their advantages such as larger working potential window, less corrosion and safety. Usually, the typical conducting salts in neutral electrolytes are Li, Na, K, Ca and Mg salts, among which Li_2SO_4 and Na_2SO_4 are the most common used ones. Compared to acid and alkaline electrolytes, neutral ones have higher operating voltages due to the increased electrolyte stable potential windows, which benefit from the lower H^+ and OH^- concentrations in neutral electrolytes.[14] To understand the effect of different ions, neutral electrolytes with different cation species have been carried out. It has been found that various cation species have different ionic sizes, viscosities, diffusion coefficients and ionic conductivities in supercapacitors, thus strongly influence the specific capacitance and equivalent series resistance (ESR).[8] Li *et al.*[15] prepared MnO_2 electrodes and studied the supercapacitor performance in Li_2SO_4, Na_2SO_4 and K_2SO_4. The resulted specific capacitance values as well as energy and power density rank in the order as follows: Li_2SO_4>Na_2SO_4>K_2SO_4. Based on the above results, neutral aqueous electrolytes for supercapacitors can not only suppress the corrosion of electrode materials, but also be more environmentally friendly and cost effective than acid and alkaline electrolyte. In addition, the operating voltage is increased, and the specific capacitance and energy density are thereby enhanced.

1.1.2 Aqueous Li-ion batteries

Since John Goodenough, Stanley Whittingham, Rachid Yazami and Akira Yoshino developed the technology of LIBs during the 1970s-1980s, rechargeable LIBs have been commonly used for portable electronics and electric vehicles, and are growing in popularity for military and aerospace applications. They show high energy density and energy efficiency.[16]

However, their adoption in more strategically important applications such as vehicle electrification and grid storage has been slower, mainly because of the safety, cost and environmental issues. Thus, new energy storage systems of high reliability and rapid charging are urgently needed. The use of aqueous electrolytes has been regarded as a promising approach to resolve these concerns. Firstly, it can replace highly toxic and flammable organic solvent. Secondly, the aqueous electrolytes are more easy-to-use and lower cost than organic

electrolytes. Finally, the ionic conductivity of the aqueous electrolyte is higher than those of organic electrolytes, resulting in high round-trip efficiency and energy density.[17-18] In aqueous Li-ion batteries (ALIBs), many side reactions from oxygen and water are involved, including the H_2/O_2 evolution reaction (HER/OER), and proton co-intercalation parallel to Li^+ intercalation, which make the design and selection of electrode materials complicated. In principle, the electrodes with an intercalation potential between 3 and 4 V before oxygen evolution can be used as cathode materials for ALIBs. Taking into account issues regarding the working voltage and the HER, electrodes with an intercalation potential between about 2–3 V *vs.* Li/Li^+ can be chosen for anode materials of ALIBs.[19]

Despite many efforts have been made on the study of acidic or basic environments, the best performance is usually achieved in a neutral pH. In general, 1 M Li_2SO_4 or $LiNO_3$ is considered as the most common electrolyte used for various electrode materials in neutral pH.[20] In addition, the concentration of electrolytes has an enormous impact on the electrochemical performance by affecting various controllable parameters such as the cell resistance, charge transfer resistance and transference number. Among all, LiTFSI offers good ionic conductivity, increased thermal and electrochemical stabilities and substantially lower sensitivity towards moisture than the conventional lithium salts.[21] The electrochemical stability window of electrolytes based on LiTFSI is exceeding 2 V, of which the highest value reaches 2.31 V.[22] As an emerging lithium salt, LiTFSI has been examined in various solvents due to its high solubility.[23-24]

1.1.3 “water-in-salt” electrolytes

As mentioned above, the electrochemical stability voltage of conventional ALIBs is limited due to the narrow thermodynamic stability window of water. In this regard, the concentrated electrolytes have been employed to expand the decomposition voltage of water. In 2005, Suo *et al.*[25] firstly reported “water-in-salt” electrolytes (WISE) by dissolving LiTFSI at extremely high concentration in water to form a dense interphase on the anode surface mainly arising from anion reduction. When the LiTFSI concentration is above 5 m (m: mol-salt in kg-solvent), the WIS definition applies, as the salt overnumbers the solvent in this binary system by both weight and volume. Particularly, at 21 m, there are only 2.6 water molecules per Li^+, which no longer forms solvation sheath. Consequently, the original cation solvation sheath structure is destructed and rearranged. In addition, the $TFSI^-$ in the electrolyte is reduced prior to HER and the solid-electrolyte interphase (SEI) is generated at the anode-electrolyte interphase, making the overpotential of HER enlarged. As a result, the highly concentrated aqueous electrolyte

provided an expanded voltage window of ~3 V. A full Li-ion battery (LIB) based on $LiMn_2O_4/Mo_6S_8$ achieved an open circuit potential of 2.3 V and was demonstrated to cycle up to 1000 times, with nearly 100% coulombic efficiency at both low (0.15 C) and high (4.5 C) discharge and charge rates. Subsequently, the WISE was also reported in other electrode materials, including TiS_2,[26] $LiNi_{0.5}Mn_{1.5}O_4$,[27] $LiMn_{0.8}Fe_{0.2}PO_4$,[28] and polytriphentl-amine,[29] which showed promising electrochemical performance.

Recently, Suo *et al.*[30] pointed out that the high concentration (21 m) of LiTFSI used in the WISE already approaches the saturation point of this lithium salt at room temperature, leaving barely any room for SEI improvement via further increase of salt concentration, thus limiting the full cell energy density. Based on it, they used a WISE as a parent hydrate salt to dissolve another lithium salt containing an anion of similar fluorinated structure, lithium trifluoromethane sulfonate (LiOTf). It is well known that a hydrated salt can dissolve another unhydrated salt of similar chemical properties and form mixed salt systems in the molten state with higher cation/water ratios.[31] The resulted electrolyte, called "water-in-bisalt", consists of 21 m LiTFSI and 7 m LiOTf, providing a molten electrolyte with 28 m Li^+ and the cation/water ratio of approximately 1:2. The higher cation/water ratio contributes to a more compact and protective SEI. The full cell delivers an unprecedented energy density of 100 Wh/kg, along with excellent cycling stability and high coulombic efficiency.

Besides the aqueous LIBs, WISE has also been widely applied in other energy storage devices, such as supercapacitors.[32-34] Zang *et al.*[35] reported 21 m LiTFSI as the electrolyte in supercapacitors with TiS_2 coated vertically aligned carbon nanotubes (TiS_2-VACNT) as electrode materials. Three-electrode results demonstrated that the system showed a capacitance of 195 F/g within a potential range of 3 V, corresponding to an energy density of 60.9 Wh/kg for a symmetric cell. The WISE was found to extend the electrochemical potential window of TiS_2/CNT electrodes from 1.9 V (1 m) to 3 V (21 m). However, due to the restriction of low conductivity and high viscosity, the rate capability is limited under high scan rate. Based on it, a co-solvent-in-salt system was reported by mixing acetonitrile with the 21 m LiTFSI electrolyte to construct a novel "acetonitrile/water-in-salt" (AWIS) electrolyte.[36] The hybrid electrolyte provided significantly improved conductivity, reduced viscosity and an expanded applicable temperature range while maintaining the important physicochemical properties of the WISE. The density functional theory-based molecular dynamics (DFT-MD) simulations revealed that acetonitrile molecules could easily coordinate to Li^+ ions for the remaining space of the Li^+ solvation sheath because of their smaller size and thus less steric interaction than

$TFSI^-$ anions. With this AWIS electrolyte, the supercapacitors based on activated carbon electrodes present a specific capacitance of 21.9 F/g at the current density of 10 A/g, which is 2.4 times higher with respect to the original WISE.

As mentioned above, in WIS-LIBs, a SEI forms by manipulating electrolyte decomposition products during the very first charging depth, generating a Li^+-solvation protective sheath. However, the inadequate observation of this protective layer evolution in supercapacitors during repeated charge/discharge cycles inquiries more research effort for thorough understanding of the advantage of WIS electrolytes. Therefore, Chapter 4 in this thesis will present the intensive study of electrochemical impedance spectroscopy (EIS), providing a fundamental technique for revealing the formation of SEI layer in WIS supercapacitors. Moreover, the thermal dependence of the electrochemical performance of the symmetric supercapacitor has been also included in this study, optimizing the best performance for various specific applications.

1.2 Transition metal sulfides for supercapacitors and Li-ion batteries

With regard to the various types of energy storage devices, their performance is strongly dominated by electrode materials. Up to now, for both supercapacitors and LIB, numerous electrode materials have been studied, including carbon materials,[37] conducting polymers,[38] transition metal oxides[39] and so on. However, their respective shortcomings limit them from further applications. For example, during the operation of supercapacitors, carbon materials tend to restack and then decrease the specific surface area, which is an important index for energy storage. Conducting polymers show the same phenomenon that the original structure will collapse during the long-term charge/discharge of energy storage devices. The poor electron conductivity of metal oxides compared to carbon materials influences their electrochemical performance, such as a resulted low specific capacity in batteries.[40] Based on it, transition metal sulfides (TMSs) have emerged as one of the most prominent candidates for LIBs and supercapacitors due to its tunable stoichiometric compositions, unique crystal structures, rich redox sites, and relatively higher electrical conductivity in comparison to their TMD counterparts.[41]

1.2.1 Transition metal sulfides

TMSs, designated as MS_x (M=Fe, Co, Ni, Mo, etc.), have received attention over the past decades due to their unique properties. Briefly, the metal and sulfur atomic arrangements in TMSs are combined by a close-packed system, engaged by ionic size and charge.[42-43]

It was reported that sulfides and oxides of transition metal contain either localized or itinerant *3d* electrons or both simultaneously. However, *d* electrons in TMSs participate in covalent bonding, which reduces the formal charge on transition metals and favours formation of metal-metal bonds. As a result, the properties of TMSs are quite different from those of oxides, such as better electrical conductivity, lower melting points, better mechanical and thermal stability and so on.[44] In addition, structures of TMSs are quite different from those of the corresponding oxides, which can be attributed to the following factors:[44] (a) hybridization of anion *3s* and *3p* orbitals with the anion *3d* orbitals can stabilize 6 nearest-neighbour cations in a trigonal-pyramid configuration; (b) sulfur-sulfur bonding gives rise to molecular anions and the assimilation of S_2 pairs in some metal sulfides is allowed; (c) layer covalency reduces the effective charges on the anions, and (d) the large polarizability of the anions favours formation of layer structures with van der Waals forces between layers. Furthermore, due to the high theoretical volume expansion calculated from the traditional conversion reaction formula,[43] some TMSs, such as MoS_2, have a layered structure, which can help alleviate the strain induced by a volume expansion. Therefore, the study on TMSs provides a route to select suitable materials for energy storage applications.

Among them, MoS_x (x=2 or 3) have been intensively investigated as electrode materials owing to their preferential exposure of active edge sites and unique atomic arrangements.[45] Different synthesis methods have been developed to generate MoS_x materials with varied properties and applications. To date, the study on the synthesis of MoS_2 nanomaterials is numerous while that of MoS_3 is limited.

Until now, two typical methods have been applied to prepare MoS_2, including top-down and bottom-up approach. In a top-down method, bulk MoS_2 crystals are used as the raw material, which can be easily exfoliated to thin layers through high-energy sonication, liquid exfoliation, mechanical cleavage and chemical intercalation-exfoliation methods. The top-down methods are realized based on the special feature of MoS_2 that the interlayers are contacted by weak van der Waals forces.[46] Compared to it, the bottom-up method is simpler with the reaction of Mo and S precursors, and then the subsequent annealing. Generally for the synthesis of MoS_2, the bottom-up method can be divided into two approaches: (1) chemical vapour deposition (CVD) method with the features of high quality, controllable thickness and compatible substrates. By this technique, MoS_2 with controllable layers can be synthesized by adjusting the annealing period.[47] (2) hydrothermal method or solvothermal method in which abundant active sites and controllable morphologies can be obtained. [48-49] In the hydrothermal system, precursors of Mo

salts are used to allow a reaction with sulfide source materials or simply sulfur in an autoclave, where a sequence of physicochemical reactions take place under high temperature and pressure conditions. Different substrates such as carbon nanospheres, carbon nanotubes, graphene films and so on can be used as the templates. As a result, the final products are MoS_2 of different shapes and sizes. In a typical example, Sun *et al.*[50] reported the facile one-step hydrothermal synthesis of MoS_2 on three-dimensional graphene skeleton by mixing $NaMoO_4$ and NH_2CSNH_2 in deionized water in an autoclave at 200 ºC for 24 h. During hydrothermal process, NH_2CSNH_2 will decompose and release S^{2-} ions, which act as the sulfur source and reducing agent for the formation of MoS_2.

Unlike MoS_2, the traditional synthesis of MoS_3 requires more sophisticated and expensive equipment such as sonochemical synthesis[51], laser ablation[52], and so on. To overcome the limitation, two simple and inexpensive methods have been exploited in recent years to synthesize MoS_3 materials, which are thermal decomposition method and acid precipitation method. Zhang *et al.*[53] found that when heated at 150-200 ºC in an inert atmosphere, $(NH_4)_2MoS_4$ can decompose to MoS_3. Then a conversion from MoS_3 to MoS_2 happened when the temperature was increased to 360 ºC. However, the morphology of MoS_3 materials during the thermal decomposition process is uncontrollable. Compared to it, the acid precipitation method is easy to form MoS_3 with different shapes using various templates at room temperature. The tetrathiomolybdate anion in an acid medium is known to form a MoS_3 precipitate. The overall chemistry pertaining is $(NH_4)_2MoS_4 + 2HCl \rightarrow MoS_3 \downarrow + H_2S \uparrow + 2NH_4Cl$.[54]

Despite the efforts, the practical application of MoS_x materials is largely restricted by their intrinsic limitations such as pronounced volume change and insufficient electrochemically active sites for energy storage devices. Designing the MoS_x nanomaterials to hollow structure is an effective route. The hollow structure can deliver high surface area, which ensures large electrode-electrolyte contact area and plenty of electrochemical active sites. In addition, the internal void spaces of hollow materials effectively alleviate the stress-induced structural variation during long cycling of energy storage systems.[45] However, current works on synthesis of hollow MoS_x nanomaterials mainly apply the removable metal oxides as templates, which are difficult to be large-scaly prepared. Based on it, in Chapter 5 of my study, spherical polyelectrolyte brushes (SPB) have been used as template to directly grow MoS_3, followed by the removing of template. The SPB nanospheres are suspended in water and soluble in tetrahydrofuran (THF), making the preparation simple and scalable. In addition, although various morphologies have been well developed, two-dimensional plate-like hollow MoS_x

materials have not been reported.[55] The plate-like structure obtained from template-methods can shorten the ion transport distance in their nanoscaled dimension. Therefore, in Chapter 3 of my thesis, hollow MoS_2 nanoplates have been prepared using gibbsite as template. Colloidal gibbsite nanoplates can be large-scaly synthesized in the presence of aluminum sec-butoxide (ASB) and aluminum isopropoxide (AIP) in water solutions, and can be easily removed by acid.

1.2.2 Molybdenum disulfide for supercapacitors

MoS_2, a kind of TMSs having van der Waals crystal structures, have showed great promise as the supercapacitor electrode material owing to the remarkably wide range of oxidation states. It has graphene-like nanosheet structures with ideal super short electron transport length and small ion transport distance for fast electrochemical processes.[56]

Research results have suggested that MoS_2 sheets have comparable supercapacitor performance to that of carbon nanotube arrays and a theoretical capacity (~1000 F/g) higher than that of graphite.[57] In 2007, Soon *et al.*[58] first reported the preparation of edge-oriented MoS_2 films by single source precursor chemical vapor deposition, which exhibited excellent electrochemical charge storage properties in supercapacitors. The assembled supercapacitor achieved a very high capacitance of 70 mF/cm^2 at a scan rate of 1 mV/s with 0.5 M H_2SO_4 as the electrolyte. It was found that the edge-oriented MoS_2 films showed not only double-layer capacitive behavior, but also faradaic capacitive behavior from the diffusion of the ions into the films. In the following, various attempts have been made to study the properties of MoS_2 with different morphologies as electrode materials for supercapacitors.[59-60] However, these electrodes showed poor cycle stability due to the volume change during the Faradaic process of supercapacitors. Based on it, Wang *et al.*[61] presented the synthesis of hollow MoS_2 nanospheres via a hydrothermal approach with template-assisted method. The MoS_2 electrode showed a high specific capacitance of 142 F/g at 0.59 A/g in 1 M KCl solution. In addition, the MoS_2 electrode showed excellent cyclic stability with remaining 92.9% of the initial capacitance after 1000 cycles. The results indicated that the hollow sphere, which possessed highly exposed active edge sites, large specific surface area and low density, demonstrated excellent supercapacitive performance.

MoS_2 with a 2H phase crystal structure (the coordination of its metal atoms is trigonal prismatic) has a monolayer bandgap of ~1.9 eV,[62] which limits its conductivity and therefore influences its performance in supercapacitors. By contrast, metallic 1T MoS_2 is theoretically metastable and has the basal plane with more chemical activity over that of the 2H phase. It has very high

electrical conductivity (10−100 S/cm of monolayered 1T MoS_2 sheet at room temperature), which is close to that of the best-performing reduced graphene oxide sheets (~100 S/cm).[57] The promising application of metallic 1T MoS_2 in supercapacitors was demonstrated by Acerce *et al.*[63] in 2015. The 1T MoS_2 was obtained from bulk MoS_2 powders through well-established chemical exfoliation method. Owing to the high conductivity, thin flexible supercapacitors were fabricated purely from these 1T MoS_2 sheets (thickness up to 5 μm) without any binding agent. The assembled supercapacitor showed volumetric capacitances ranging from 400 to 700 F/cm^3, along with very high energy density, power density and excellent stability.

Besides the synthesis of metallic 1T MoS_2, other methods have also been developed to improve the electrochemical performance of MoS_2, such as addition of secondary electrode-active materials to synthesize hybrid electrode materials. Combining MoS_2 with the electrochemically active organic or inorganic materials is one of the prudent approaches to mitigate the intrinsically low electrical conductivity of MoS_2. Among all, nanostructured carbonaceous materials are the most promising candidates for supercapacitors due to their unique features such as high electrical conductivity, large surface area, good chemical and electrochemical stability, and environmental-friendliness. Hence, they have been widely used as conductive additives for the preparation of MoS_2-based hybrid materials.[64-66] The semiconducting MoS_2 could then benefit from the excellent electrical conductivity of carbon materials such as graphene and carbon nanotubes.

Compared with the reported morphology of MoS_2 nanomaterials, two-dimensional hollow structures with high aspect ratio and finite lateral size have rarely been investigated. Hollow carbon nanoplates, generated by using gibbsite as the template and PDA as the carbon precursor, have recently been synthesized and implied in supercapacitors, which could shorten the ion transport distance in their nano scaled dimension.[67] Therefore, the exploration of two-dimensional hollow and nanostructured MoS_2 materials with regular morphologies and hybridized with mesoporous carbon will provide great opportunities to find attractive properties in supercapacitors, which will be demonstrated in Chapter 3.

1.2.3 Molybdenum trisulfide for Li-ion batteries

Currently, LIBs have attracted wide attention due to their high energy density, high capacity, and long cycle life.[68-69] Electrode materials especially anode materials are the key factors to affect the electrochemical performance of LIBs. Thus, it is necessary to find anode materials with high performance to storage Li^+ ions to satisfy the future energy requirements. Among

anode materials, TMSs are one kind of promising candidates due to the high specific capacities.[70-71] Particularly, transition metal polysulfides, such as FeS_2, TiS_3, and so on, exhibit anionic redox driven chemistry for energy storage. In these transition metal polysulfides, the S_2^{2-} anions undergo a reversible transformation as follows: $S_2^{2-} + 2e^- \leftrightarrow 2S^{2-}$, which enables higher reversible capacities of LIBs.[72] As a representative member of the transition metal polysulfides family, amorphous MoS_3 has also aroused great attention because of its special structure.[73-74] Compared to crystalline MoS_2, the structure of amorphous MoS_3 naturally contains more active sulfide groups with unsaturated coordination bonds due to the random arrangement of Mo-S clusters in the long range.[75] In addition, amorphous MoS_3 features the one-dimensional chain-like structure,[74] which provides more open sites to storage Li^+ ions during the electrochemical reaction, thus resulting in higher specific capacity. With the amorphous structure, it also decreases the activation energy barriers of the structural rearrangement and facilitates the ion diffusion. Moreover, MoS_3 has a higher electrical conductivity than MoS_2, which is regarded as a fundamental prerequisite to govern a superior electrochemical performance.[53] All these advantages make MoS_3 a promising anode material for LIBs.

However, as a bulk material, amorphous MoS_3 suffers from the low specific surface area (4.4–6.5 m^2/g).[53] Encouraged by it, Wang *et al.*[76] were the first one to study nanosized MoS_3 as a battery material in 2007. The nanosized amorphous MoS_3 was synthesized by acidification of an $(NH_4)_2MoS_4$ aqueous solution in conjunction with a microemulsion-based method and the bulk amorphous MoS_3 was obtained by using the thermal decomposition of $(NH_4)_2MoS_4$. After charge/discharge in LIBs with 1 M LiTFSI in a solvent of poly(ethylene glycol) dimethyl ether 500 (PEGDME 500) as the electrolyte, the nanosized MoS_3 showed higher capacity than the bulk sample. They also pointed out that the MoS_3 molecules were not a mixture of MoS_2 and elemental S, but existed as Mo_3S_9 clusters, which are linked by bridging S-S bonds. However, for the pure nanosized MoS_3 electrode materials, the big volume changes upon cycling led to material pulverization and capacity decay after long cycles. To further improve the electrochemical performance of MoS_3 in LIBs, nanocomposites of ultrasmall amorphous MoS_3 nanoparticles loaded with graphene oxide (GO/MoS_3) were prepared through a facile acid precipitation method.[54] Using GO as the buffer layer in the electrode materials for LIBs, the volume change was effectively suppressed and the resulted electrochemical performance was better than that of pure MoS_3. The reversible capacity of the GO/MoS_3 electrode material reached as high as 685 mAh/g after 1000 cycles at a high current density of 2 A/g, showing an

excellent cycling stability. The above electrochemical performance indicates that the amorphous MoS_3 nanomaterials are promising candidates for LIBs applications.

Despite these research efforts, the working mechanism of MoS_3 for Li-ion storage in organic electrolytes remains unclear and controversial, largely hindering its development. Chang *et al.*[73] presented that, during the initial cycles, amorphous MoS_3 is converted to crystalline MoS_2 and Li_2S. Li *et al.*[77] reported that the lithiation of MoS_3 involves in the generation of amorphous Li_xMoS_3 in Li-ion batteries. In addition, to the best of our knowledge, amorphous MoS_3 remains unexplored in aqueous electrolytes based LIBs, which may be limited by the low potential of Li ion uptake in MoS_3, about 2.0 V *vs.* Li/Li^+,[76] at which HER happens in conventional aqueous electrolytes. Moreover, MoS_3 suffers from severe volume change upon Li-ion adsorption, which, upon repetitive dis-/charge, will lead to material pulverization and capacity decay.[78] Therefore, the exploration of MoS_3 with unique structures to release the volume change during cycling and the mechanism study of MoS_3 in LIBs become urgent. Based on it, in my study, hollow MoS_3 nanospheres have been synthesized and applied in the WIS-LIBs. The hollow structure accommodates the volume change effectively upon Li ion uptake/release and thus enhances the cycle life of the cell. This thesis will also investigate the working mechanism of amorphous MoS_3 in WIS-LIBs through XRD measurements, providing great opportunities for the development of MoS_3 materials for aqueous LIBs.

1.3 Objectives

The main objective of this thesis is to prepare hollow structured MoS_x particles with controllable size and shape, and to investigate their corresponding properties and applications in aqueous energy storage devices. The hollow nanostructure could act as ion-buffering reservoirs to prevent the volume expansion of the materials caused from the charge/discharge cycles in the devices.

Firstly, hollow carbon-MoS_2-carbon nanoplates with high surface area and improved conductivity have been synthesized and applied in aqueous supercapacitors. The investigation is carried out as follows:

- Gibbsite nanoplates with disk-like shape and large aspect ratio have been applied as the template to synthesize hollow MoS_2-based nanomaterial. Dopamine as carbon precursor is self-polymerized on the surface of the template, which assists the further nucleation of MoS_2 nanosheets onto the gibbsite-PDA template. MoS_2 nanosheets is then synthesized through the L-cysteine-assisted hydrothermal method in the presence of sodium molybdate. In order to further improve the conductivity and prevent the particles from aggregation, another layer of PDA has been coated onto the nanoplates. Each single particle is then immobilized and insulated in silica gel via a silica nanocasting method. After calcination and etching of the gibbsite template and silica, uniform and discrete hollow carbon-MoS_2-carbon nanoplates can be obtained.
- To follow the morphology and phase transformation of the target particles from the beginning, transmission electron microscopy (TEM) and XRD measurement have been applied at different steps of the synthesis procedure. In addition, thermogravimetric analysis (TGA), N_2 adsorption/desorption, and Raman measurements have also been conducted to study the features of the hybrid material.
- The obtained nanomaterials can show immediate applications in symmetric supercapacitors with aqueous electrolytes. The electrochemical performance of hollow carbon-MoS_2-carbon nanoplates based supercapacitors have been investigated by using 1 M Li_2SO_4 as electrolyte.

The second work aims at studying the formation of SEI layer in WIS supercapacitors with hollow carbon nanoplates as the electrode material. The influence of temperature on the electrochemical performance has been studied. The investigation has been conducted as follows:

- To compare the electrochemical behaviours of 21 m LiTFSI and 1 m LiTFSI electrolytes in supercapacitors using mesoporous hollow carbon nanoplates electrodes, the cyclic voltammetry (CV) profiles and cycling performance have been investigated.
- To study the formation of SEI layer in WIS supercapacitors, the electrochemical impedance spectroscopy (EIS) technique has been used as a fundamental method and the corresponding equivalent circuit has been investigated.
- To evaluate the temperature dependence of the electrochemical performance, the WIS supercapacitors have been measured in a range from 15 °C to 55 °C.

The third part of work aims at synthesizing hollow MoS_3 nanospheres and studying their behaviours in the WIS-LIBs. The working mechanism of MoS_3 in WIS-LIBs has been also studied. The investigation has been performed as follows:

- Spherical polyelectrolyte brushes (SPB) have been applied as template to generate hollow MoS_3 particles. To immobilize the precursor of MoS_3 onto the template, cationic SPB particles with poly (amino-ethylmethacrylate hydrochloride) (PAEMH) chains have been used.
- To obtain the hollow structured MoS_3 nanospheres, removing of SPB templates with THF solutions has been carried out. A comprehensive characterization is performed to study *e.g.* the morphology of hollow MoS_3 nanospheres via TEM, high resolution transmission electron microscopy (HR-TEM), Cryo-TEM, and scanning transmission electron microscopy (STEM), the structure via XRD, Raman spectrum, and X-ray photoelectron spectroscopy (XPS) measurements, the elemental composition via energy dispersed X-ray spectroscopy (EDX) measurements, and the specific surface area via N_2 adsoprtion/desorption methods.
- The electrochemical performance of the obtained hollow MoS_3 nanospheres has been investigated in the WIS-LIB full cells with $LiMn_2O_4$ as the cathode material. 2032-type coin cells and pouch cells have both been fabricated. The CV profiles, and cycling performance have been compared with the bulk MoS_3 and bulk MoO_3 anode materials.
- In order to elucidate the working mechanism of MoS_3 in the WIS-LIBs, XRD measurement and scanning electron microscopy (SEM) imaging have been performed on cycled electrodes.

2 Theory

Electrochemical energy storage refers to a progress of converting electrical energy from a power network into a form that can be stored for converting back to electrical energy when needed.[79] Various types of energy storage can be divided into many categories, and over the past decade, steady progress has been made toward the development of high-power supercapacitors and high-energy rechargeable batteries. Characteristics of different systems are represented in a Ragone plot in Figure 2.1. Batteries are mature energy storage devices with high energy densities and high voltages, while supercapacitors provide high specific power and life cycle. Both devices contain two electrodes, an electrolyte, and a separator. Electrodes are active components of the energy storage system and are used for loading the active materials, which allow electrons to pass from one half-cell to the other through an external circuit. Electrolyte is a chemically stable liquid, gel or solid substance that provides conduction for the ions in the cell. Separator is a permeable membrane placed between the positive and negative terminals of the cell, which prevents instant self-discharge and electrical short circuits between the two electrodes while allowing the transport of ionic conductors that are essential for the flow of current in the cell.[80]

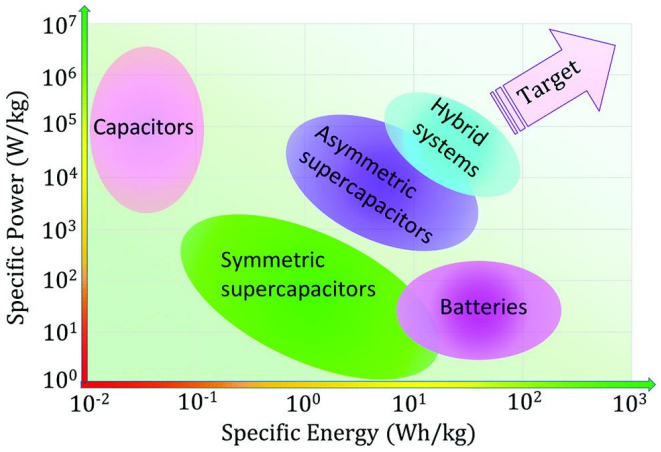

Figure 2.1 Ragone plot showing the specific power *vs.* specific energy of various energy storage devices.[80] Copyright 2019 with permission from *The Royal Society of Chemistry.*

2.1 Working mechanism of supercapacitors

Supercapacitors, also known as electrochemical capacitors or ultracapacitors, have attracted significant attention, due to their high power density, long cycle life and bridging function for the power and energy gap between traditional dielectric capacitors and batteries[81-82]. Despite the much lower energy density compared to batteries, supercapacitors can have much higher

power densities, which makes them promising for applications such as portable electronics, electric vehicles and smart grids. As mentioned in the beginning of this chapter, three key elements of a supercapacitor are the electrode, electrolyte and separator, and their properties directly determine the overall performance of supercapacitors. The dielectric strength, chemical inertness, porosity (ion permeable) and shallow thickness are the most important requirements for a separator for effective working of the supercapacitor.[83] The electrodes must be porous with high specific surface area, low electrical resistivity and high chemical stability. The main criteria for selection of an electrolyte are electrochemical stability and ionic conductivity.[84] Depending on the charge storage mechanism, supercapacitors can be briefly classified as electrochemical double-layer capacitors (EDLCs), pseudocapacitors (or capacitive supercapacitors), and hybrid capacitors (combination of the above two) as shown in Table 2.1.1.

Table 2.1.1 Characteristics of different types of supercapacitors.[6, 80] Copyright 2019 with permission from *The Royal Society of Chemistry* and copyright 2012 with permission from *American Society of Civil Engineers.*

	EDLC type	pseudocapacitor type	hybrid capacitor type
schematic diagram	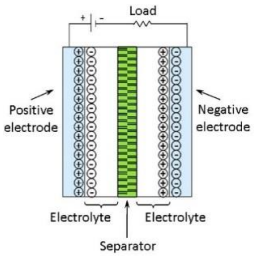	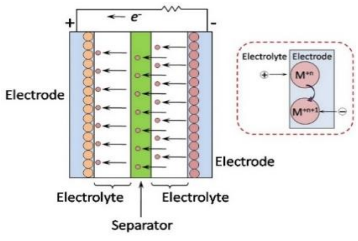	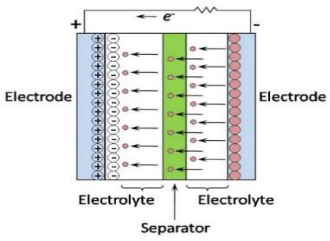
CV	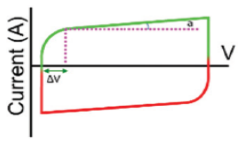	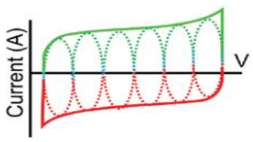	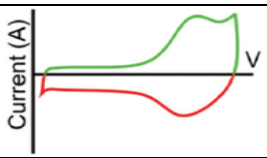

EDLCs are based on porous materials with high specific surface area as active electrode materials, where the capacitance is produced by the reversible adsorption of electrolyte ions onto the electroactive materials (Table 2.1.1). The surface electrode charge generation involves surface dissociation and ion adsorption from both the electrolyte and crystal lattice surface, so there is no charge transfer across the electrode/electrolyte interface and energy storage is a true capacitance effect.[85] The energy storage and release mechanism is based on nanoscale charge separation at the electrochemical interface formed between the electrode and electrolyte. During the charging process, the electrons travel from the negative electrode to the positive electrode through an external circuit, while the cations move from the positive electrode to the negative electrode inside the device through the electrolyte. During the discharging process, the reverse processes take place.[86] The mechanism is followed by the generation of two layers of polarized

ions at the electrode interface due to the applied voltage.[83] According to the working mechanism of EDLCs, high surface areas of electrode materials can contribute to more electrolyte ions accumulated at the electrode/electrolyte interface. Therefore, electrodes are usually made of carbon materials with high surface area and stable surface properties, for instance activated carbons, carbon aerogels, carbon nanotube, graphene, porous carbon spheres and so on.[87-89]

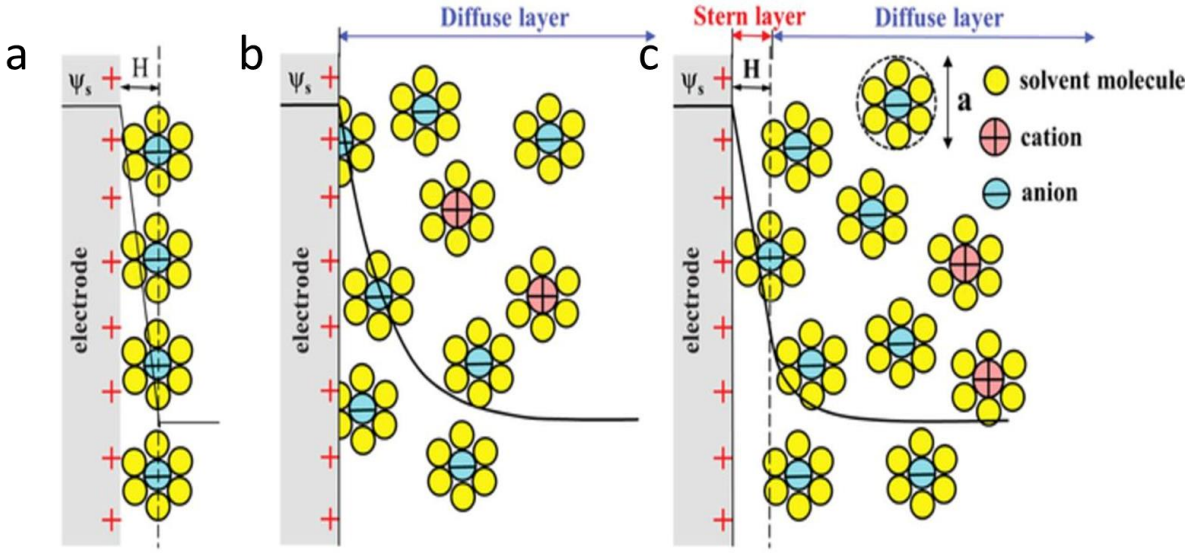

Figure 2.1.1 Schematic representation of electrical double layer structures according to (a) the Helmholtz model, (b) the Gouy-Chapman model, and (c) the Gouy-Chapman-Stern model. The double layer distance in the Helmholtz model and the Stern layer thickness are denoted by H while ψ_s is the potential at the electrode surface.[90]

Generally in EDLCs, an electric double layer appears when an electrode is immersed in the electrolyte which attracts counter-ions while repels co-ions.[80] The balancing counter charge for this charged surface will form in the liquid, concentrating near the surface. There are three theories or models for this interface between a solid and a liquid, including the Helmholtz model, the Gouy-Chapman model, and the Gouy-Chapman-Stern model, as illustrated in Figure 2.1.1.

The Helmholtz model[91] is the simplest approximation for modeling the spatial charge distribution at double layer interfaces, which suggests that a charged surface immersed in an electrolyte solution repels ions of the same charge (positive or negative) but attracts their counter ions.[90] The electrical double layer is formed by two layers: the layer of electronic charge at the electrode surface and the layer of counter ions in the electrolyte.[92-93] The Helmholtz model hypothesizes that counter ions form a monolayer near the electrode surface. This theory considers rigid layers counterbalancing the charges from the solid and is taken as the simplest one, which does not adequately explain what occurs in nature.

Due to the limitation of the Helmholtz model, Gouy[94] and Chapman[95] have modified it with the consideration that the ion distribution should be continuous in the electrolyte solution and given by the Boltzmann distribution. Gouy suggests that the same amount of opposite ionic charge appears in a liquid surrounding a charged solid, but the ions are not rigidly attached to the surface. The ions in the solution tend to diffuse into the liquid phase until the counter potential set up by their departure restricts this tendency. The Gouy-Chapman model presents that the ions are mobile in the electrolyte solution under the combined effects of ion diffusion driven by concentration gradients and electromigration driven by the electric potential gradient, which results the diffuse layer in the system.[90] This model makes a better approach to the reality than the Helmholtz model, but still has limited quantitative applications due to the overestimation of the electrical double layer capacitance.

Later, Stern[96] proposed a model combining the Helmholtz and Gouy-Chapman models by accounting for the accumulation of ions close to the electrode surface and the hydrodynamic motion of the ionic species in the diffuse layer. In the diffuse layer, the ions are mobile under the coupled influence of diffusion and electrostatic forces. Based on that, the differential, integral and equilibrium areal capacitance of one electrode can be computed by considering the Stern and diffuse layer capacitances by the following equation:[90]

$$\frac{1}{C_s} = \frac{1}{C_s^{St}} + \frac{1}{C_s^{D}} \tag{2.1.1}$$

where C_s^{St} and C_s^{D} are the Stern and diffuse layer areal capacitances on a differential, integral, or equilibrium basis, respectively.

Pseudocapacitors mainly rely on fast and reversible faradaic redox reactions to store charges (Table 2.1.1). In the faradaic charge process, electrons transfer across the electrode interface by the oxidation or reduction of a chemical species. When a potential is added, fast and reversible faradaic reactions take place on the electrode materials and involve the passage of charge across the double layer, similar to the charging and discharging processes occurring in batteries, resulting in faradaic current passing through supercapacitors. Normally during charging, the surface region of redox-active materials are reduced to lower oxidation states coupled with adsorption/insertion of cations from the electrolyte at/near the electrode surface. Upon discharge, the process can be fully reversed. However, the power density of pseudocapacitors is lower than that of EDLCs because the slower Faradaic mechanism exhibits shrinking and swelling during charging and discharging, which leads to poor mechanism stability.[97]

In electrochemistry, the term pseudocapacitance designates a capacitive material of electrochemical nature with the linear reliance of charge stored on the width of the potential window.[98] In pseudocapacitors, there involves charge passage across double layer with capacitance related to the amount of accepted charges and the operated potential. Electrode materials in pseudocapacitors are usually conducting polymers, metal oxides and metal sulfides, which can hold much higher specific capacitance values than EDLCs.[99-100] The pseudocapacitance (C) is given by the derivation of charge acceptance (Δq) and charging potential (ΔV) that is[101]:

$$C = \frac{d(\Delta q)}{d(\Delta V)} \tag{2.1.2}$$

Stemming from thermodynamic reasons, the faradaic charge transfer process across the electric double layer leads to a special potential-dependent charge accumulation or release phenomenon, so the derivation $d(\Delta q)/d(\Delta V)$ is equivalent to a capacitance.[102]

Based on it, pseudocapacitance can be described as follows[102]:

(i) two-dimensional depositions (so-called underpotential deposition) of adatom arrays on electrode surfaces, such as H or Cu on Pt, Pb on Au, Bi on Au, Bi on Ag, H on Rh or Pt.

(ii) redox processes in liquid or solid solutions, where the electrode potential E is a function of the log of ratio of reductant converted to oxidant (or vice-versa) in a redox system.

(iii) where, in some cases, chemisorption of anions at electrode interfaces and potential-dependent partial Faradaic transfer of an electronic charge[103-104] take place at the same time. In general, there can be coupling between non-Faradaic double-layer charging and Faradaic surface processes.[105]

Hybrid capacitors are composed of an EDLC electrode and a pseudocapacitive or battery type electrode, combining the properties of both systems and leading to an intermediate performance in some cases. With the latest development in this area, there are two types of hybrid supercapacitors. The first type is capacitor type electrode/capacitor type electrode and the second type is capacitor type electrode/battery type electrode (such as lithium ion capacitors).[106-107] Lithium ion batteries usually offer high energy density while suffering from a limited cycle life. Additionally, in lithium ion batteries, a fast charging rate would result in a high underpotential, leading to hazardous Li plating and subsequent deterioration of the cell

performance. Based on that, combination of the fast charging rate of supercapacitors with the high energy density of batteries is a good choice. The capacity of a battery-type electrode is usually many times larger than that of a capacity-type electrode. The lithium ion capacitors are regarded as hybrid capacitors as they have one EDLC or pseudocapacitive electrode combined with the other rechargeable battery-type electrode, which requires an electrode material with a large surface area to assist the mobility of the electrons and ions. It should be noted that the electrochemical performance of hybrid capacitors can be improved by optimal selection of synergistic electrode materials. Thus, the use of an appropriate Li intercalation compound as the electrode is crucial to the final operating voltage and electrochemical performance.

The capacitance (C) of supercapacitors is governed by some parameters, which is given by the equation[6, 82]:

$$C = (\varepsilon_r \cdot \varepsilon_0 \cdot A)/d \tag{2.1.3}$$

where ε_r is the dielectric constant of the electrolyte, ε_0 is the dielectric constant of vacuum, A is the geometric surface area of the electrode, and d is the distance between two oppositely biased electrodes. In EDLCs, a potential difference is created at the electrode-electrolyte interface upon application of an electric potential to the electrodes. The electrode-electrolyte interface incorporates a double layer formed between the electrolyte ions and electronic charges on the electrodes.[108] Based on it, d is the interplanar distance or the double layer thickness, which is very small.

To provide a basis for comparison between different electrode materials, it has become common practice to provide a specific (gravimetric) capacitance, which is related to the capacitance of one single electrode, C_{sp} (F/g). In case of a symmetric system, where both electrodes are equal in mass, thickness, size, and material, the following equation[84] can be used:

$$C_{sp} = 4 \cdot \frac{C}{M} \tag{2.1.4}$$

where M is the total mass of active material. The factor 4 is related to normalization to the mass of one electrode for the two identical capacitors in series.

The stored specific energy E (Wh/kg), also called energy density, in a supercapacitor is given by the following equation[84]:

$$E = \frac{CV^2}{2m \cdot 3600} \tag{2.1.5}$$

where m (kg) is the mass of the supercapacitor and V (V) is the maximum voltage window of electrochemical stability. The normalization to the supercapacitor mass provides a basis for comparison with other devices.

The maximum specific power P (W/kg) also depends on the voltage window and is given by the following equation[84]:

$$P = \frac{V^2}{4 \cdot ESR \cdot m} \tag{2.1.6}$$

where ESR (Ω) is the equivalent series resistance of the system. The ESR corresponds to the sum of the resistances related to the ionic resistance of the electrolyte impregnated in the separator, the electronic resistance of electrodes and interface resistances between electrodes and current collectors.

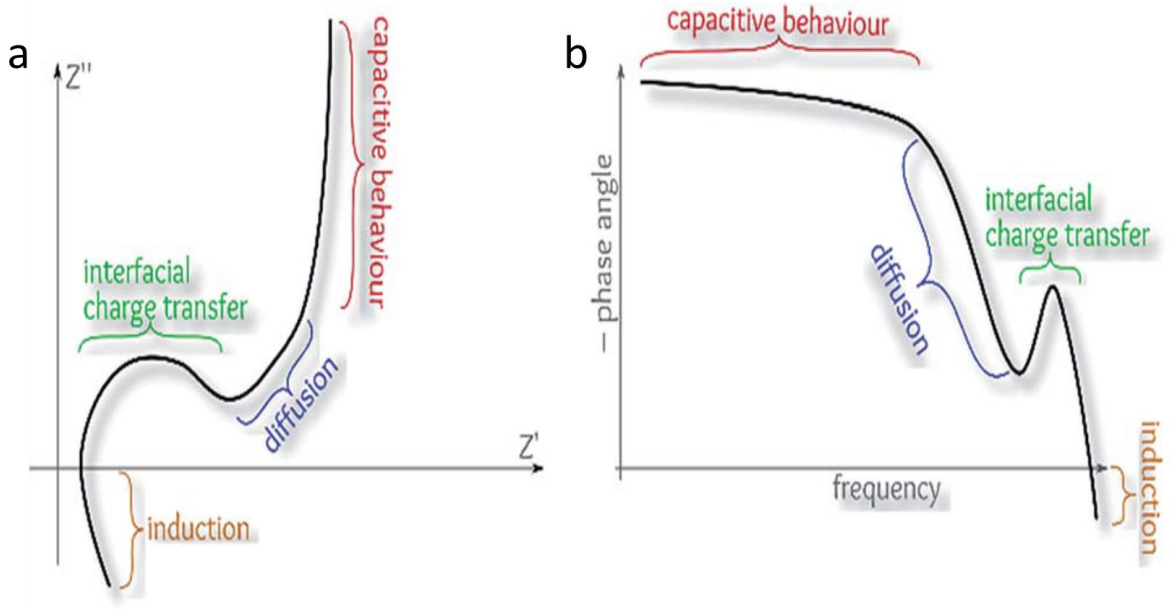

Figure 2.1.2 (a) Nyquist and (b) Bode plots for a schematic impedance model.[109] Copyright 2018 with permission from *The Royal Society of Chemistry.*

The electrical impedance of a supercapacitor can be determined by electrochemical impedance spectroscopy measurements at a specified potential. In the impedance measurements, the frequency can be directly correlated with the potential scan rate in cyclic voltammetry. Bode plots are simply utilized to detect the frequency in which the system reaches the phase

difference associated with the capacitive behavior. In general, the impedance can be represented as

$$Z(\omega) = Z_{Re} - jZ_{Im} \tag{2.1.7}$$

where Z_{Re} and Z_{Im} are the real and imaginary parts of the impedance, respectively. The magnitude of Z, written $|Z|$ or Z, is given by

$$|Z|^2 = (Z_{Re})^2 + (Z_{Im})^2 \tag{2.1.8}$$

and the phase angle, ϕ, is given by[110]

$$\tan\phi = \frac{Z_{Im}}{Z_{Re}} = \frac{1}{\omega RC} \tag{2.1.9}$$

where ω is the angular frequency, R is the electrical resistance, and C is the capacitance. The phase angle expresses the balance between capacitive and resistive components in the series circuit. For a pure resistance, $\phi = 0$; for a pure capacitive, $\phi = \pi/2$; for mixtures, intermediate phase angles are observed.

Figure 2.1.2 (a) displays a general impedance behavior of systems consisting of three main regions: high frequency semi-circle, mid-frequency Warburg impedance and low-frequency capacitive behavior.[87] The conventional capacitors have a very low equivalent series resistance and an almost entirely imaginary impedance, represented by a vertical line intercepting the real impedance axis at R_s. In supercapacitors, the role of solid-state diffusion is less significant. In most cases, there is a gradual transformation from the second to the third region as can be followed by a gradual change in the angle in Nyquist plots. In Bode plots, this can be seen as a gradual increase of the phase angle to reach a steady value close to 90°.[109]

2.2 Working mechanism of Li-ion batteries

Unlike supercapacitors, electrochemical batteries store energy in the form of chemical energy inside electrode active materials by chemical bonds, and convert the chemical energy into direct current electricity through redox reactions or intercalation.[111] Among them, the overwhelming appeal of Li-electrochemistry lies in its low molecular weight, small ionic radius which is beneficial for diffusion, and low redox potential [$E°(Li^+/Li)$ = -3.04 V *vs.* standard hydrogen electrode (SHE)][112]. The latter enables high-output voltages and therefore high power densities.

Such attractive properties, coupled with its long cycle life and rate capability, have enabled Li-ion technology to capture the portable electronics market.[113-114]

A rechargeable Li-ion battery generally consists of two electrodes, in which the active charge carrying elements have different chemical potentials, and in between there is an electrolyte as an ionic conducting medium. To obtain better electrochemical performance, Li-ion batteries are desired to meet the following requirements: high energy and power density, promising cyclic stability, low cost, environmental friendliness and safety. In a Li-ion battery, Li ions migrate across the electrolyte located between two electrodes, while electrons flow via the external circuit (Figure 2.2.1). The most common used commercial Li-ion battery system at present is graphite-$LiCoO_2$.[115] Industrially, both cathode and anode are produced from active materials mixed with 3-5 wt% of a polymer binder and 1-5 wt% of conductive carbon additive and casting on a metal current collector (aluminum foil for the cathode and copper foil for the anode).[116] Usually, in order to avoid short circuits, the electrodes are separated with a porous and electrically insulated membrane.

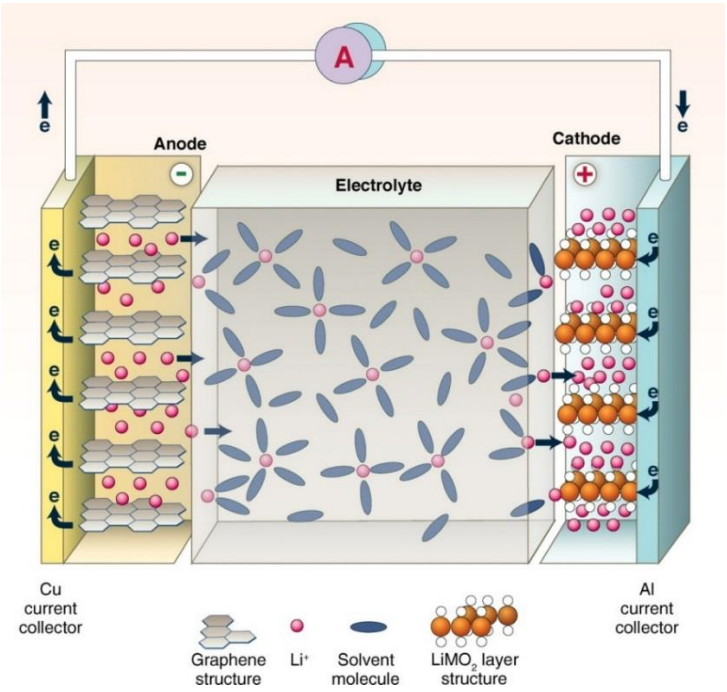

Figure 2.2.1 Schematic diagram of a Li-ion battery.[117] Copyright 2011 with permission from *American Association for the Advancement of Science.*

The working mechanism of Li-ion batteries can be decided by the ways of lithium ions interacting with the electrode active materials: insertion/extraction, alloy/de-alloy and conversion. For the first one, it is the most commercially successful one, mainly involving

transition metal oxide cathodes and graphite anodes. During the charging process, lithium ions transport from the positive electrode to the negative electrode by the oxidation of the anode. To maintain the charge balance, ionic migration occurs inside the battery through the electrolyte. The process is reversible while discharging.[118-119] This is also known as "shuttle chair" mechanism, where the Li ions shuttle between the anode and cathode during charge and discharge.

Electrochemical reactions at the two electrodes released the stored chemical energy.[120] The total Gibbs free energy change due to the electrochemical reactions on the two electrodes is determined by the electrode materials selected. Given the overall electrochemical reaction and charges transferred, the theoretical cell voltage can be estimated as follows[113]:

$$E^o = \frac{-\Delta G}{nF} \tag{2.2.1}$$

Here, *n* is the quantity of transferred electrons per mole electrode materials in the oxidation or reduction reactions. *F* is the Faraday constant (*F*= 96485 C/mol).

The practical voltage other than the standard state can be determined from the Nernst equation[121]:

$$E = E^0 - \frac{RT}{nF}\ln Q \tag{2.2.2}$$

where the reaction quotient *Q* contains the activities of all species in the reaction.

Usually two kinds of phase transitions can be observed during the Li^+ extraction/intercalation process. One is the first-order phase transition, which typically appears in the electrode materials such as $LiFePO_4$. Its charge-discharge curves can usually be presented as "L" shapes, indicating a clear potential plateau during Li^+ extraction/intercalation due to formation of a distinct new structural phase. The second behaves as a second-order phase transition. A typical charge-discharge "S" shape curve is usually observed, revealing a continuous change in electrochemical potential due to continuous formation of solid solution phases. It usually can be found in the Li^+ extraction/intercalation in $LiCoO_2$.[122] Phase transition is associated with the speed of the phase transition reaction. The speed of the electrochemical reaction during the process of Li^+ extraction/intercalation is not only related to the intrinsic ionic and electronic transfer of materials, but also to the interface between electrode and electrolyte.[122]

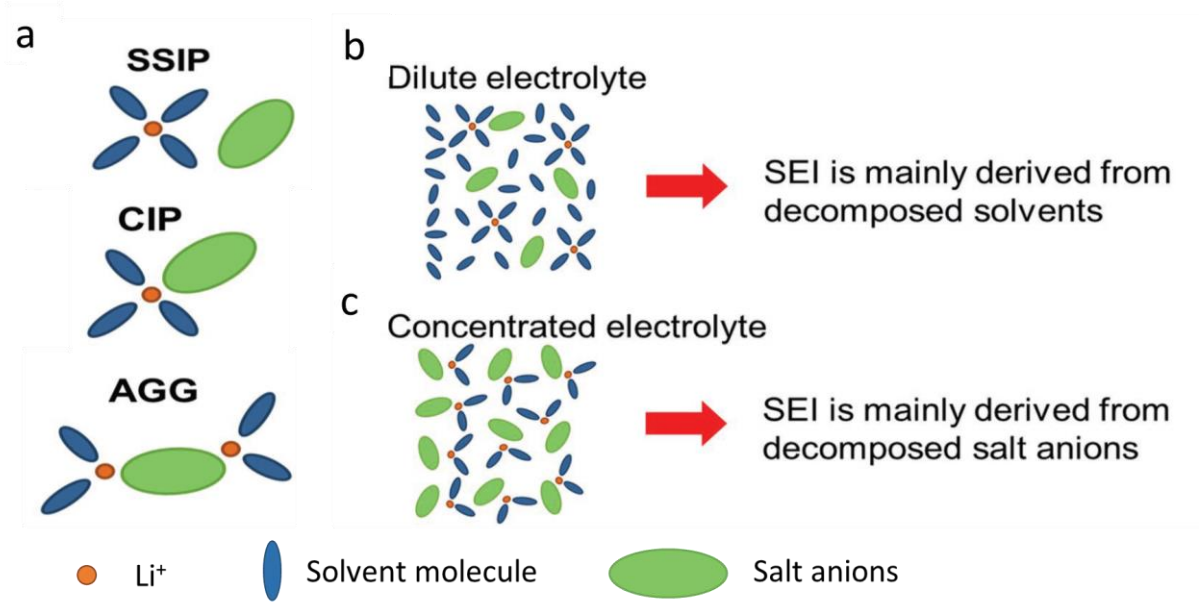

Figure 2.2.2 (a) Representative Li^+ cation solvate species (SSIP, CIP and AGGs) in dilute and concentrated electrolytes.Schematic illustration of the electrolyte reduction mechanism at the electrode/electrolyte interface in (b) dilute and (c) concentrated electrolytes.[123]

In an electrochemical device, interfaces between electrolyte and electrodes constitute the only legitimate sites for electron exchange. In lithium-based cells, because of the extreme potentials where anodes or cathodes operate, these interfaces are no longer the two-dimensional entities frequently encountered in low voltage electrochemical devices and well described in classical electrochemistry textbooks. Instead, they become three-dimensional independent interphases resulting from the sacrificial decomposition of electrolyte components, named solid electrolyte interphase (SEI) after their electrolyte nature.[124] SEI is important because they are essentially responsible for the reversibility of Li^+ intercalation chemistries while dictating the kinetics of overall cell reactions. However, they are difficult to characterize because of their sensitive chemical nature, elusive manner of formation. The synergistic effects of both salt and solvent molecules affect the quality of the SEI derived from the electrolytes. From a solvation structure point of view, a Li^+ is normally coordinated with 3 to 4 solvent molecules in the dilute electrolyte solution, which is dominated with solvent-separated ion pairs (SSIPs) and free solvent molecules (Figure 2.2.2 (a)).[125] Therefore, the SEI layer formed in regular electrolytes is mainly derived by the decomposition of electrolyte solvents (Figure 2.2.2 (b)). In the case of concentrated electrolyte (typically > 3.0 M being molarity (mol/L)), the coordination number is reduced to 1-2 due to the scarity of solvent molecules. Salt anions enter the solvation sheath to form contact ion pairs (CIPs) and cation-anion aggregates (AGGs). These salt anions thus participate in the SEI layer formation by shifting from a solvent decomposition to a salt anion

decomposition/reaction as a result of the increase of Li salt concentration (Figure 2.2.2 (c)). In concentrated electrolyte, the SEI layer is mainly derived from anions, which has improved qualities such as better adhesion to the electrode surface and enhanced mechanical property.[123]

The performance of Li-ion batteries can be evaluated by a number of parameters, such as specific energy, volumetric energy, specific capacity, cyclic stability and the dis/charge rate. Specific energy (Wh/kg) measures the amount of energy that can be stored and released per unit mass of the battery, which can be obtained by multiplying the specific capacity (Ah/kg) with operating battery voltage (V). Specific capacity determines the amount of charge that can be reversibly stored per unit mass. It is closely related to the number of electrons released from electrochemical reactions and the atomic weight of the host. Cyclic stability measures the reversibility of the Li-ion insertion and extraction process in terms of the number of charge and discharge cycles before the battery loses energy significantly, which is affected by depth of discharge and state of charge, as well as operating temperatures. The rate of charge or discharge measures how fast the battery can be charged and discharged, typically called as C rate. At n C, the battery is fully discharged releasing maximum capacity in $1/n$ h.[113] On discharge, an internal resistance R_b to the ionic current I_i reduces the output voltage V_{dis} of a cell by a polarization $\eta=I_iR_b$, relative to the open-circuit voltage V_{oc}. The voltage V_{ch} required to charge the cell is increased by η, which then represents an overvoltage. Therefore, the discharge and charge voltages of a cell are[126]

$$V_{dis} = V_{oc} - \eta(q, I_{dis}) \tag{2.2.3}$$

$$V_{ch} = V_{oc}(q, I_{ch}) + \eta(q, I_{ch}) \tag{2.2.4}$$

where q represents the state of charge and I_{dis}, I_{ch} are the discharge and charge currents, respectively. The total charge transferred by the current $i=dq/dt$ on discharge or charge is[126]

$$Q = \int_0^{\Delta t} I dt = \int_0^Q dq \tag{2.2.5}$$

Q is referred to as the cell capacity, which depends on I because the rate of transfer of ions across electrode-electrolyte interfaces becomes diffusion-limited at high currents. Moreover, on charge/discharge cycling, changes in electrode volume, electrode-electrolyte chemical reactions, and/or electrode decomposition can cause an irreversible loss of capacity, known as capacity fading.

The density of stored energy in a fully charged cell is obtained by measuring the time for its complete discharge at a constant current $I_{dis}=dq/dt$[126]:

$$\text{Energy density} = \int_0^{\Delta t} IV(t)dt/wt = \int_0^{Q} V(q)dq/wt \quad (2.2.6)$$

where *wt* is the weight of the cell. This gravimetric energy density (Wh/kg or mWh/g) is dependent on I_{dis} through $Q(I_{dis})$.

The theoretical capacity of active electrode materials in Li-ion batteries can be estimated based on electrochemical reactions involved. For example, electrochemical reaction for the anode of graphite that can intercalate reversibly with lithium ions to form LiC_6, the reaction is

$$Li^+ + e^- + 6C \leftrightarrow LiC_6$$

The intercalation of Li ions onto graphite occurs in stages such as LiC_{24}, LiC_{27} and LiC_{12} *via* first-order phase transition reactions between various stages.[127] The theoretical specific capacity (mAh/g) of graphite anode can be calculated as follows:

$$C_{specific} = \frac{xF}{nM} = \frac{1\times(96485C/mol)}{6\times(12g/mol)} = 372\ mAh/g \quad (2.2.7)$$

where *x* is number of electrons transferred in the reaction, *n* is number of moles of a chosen electroactive component that takes place in the reaction and *M* is the molecular weight of the same electroactive component.[113]

In practice, to evaluate specific capacity of a Li-ion battery cell, one not only has to take into consideration of the integration of cathode and anode materials but also other essential components, such as binders, conductive enhancers, separators, electrolyte, current collectors, case, tabs, as well as battery management systems. Therefore, the practical energy density is always less than that estimated from the battery chemistry.[113] For example, for $LiCoO_2$-graphite cells, the theoretical energy density is more than 250 Wh/kg, while in practice the value is only about 150 Wh/kg at cell level.

2.3 Principal of "water-in-salt" electrolytes for energy storage

Considering the cost, safety and environmental impacts, aqueous battery systems have regained interests in recent years for large-scale green energy storage. However, in a conventional aqueous electrolyte, the decomposition products (H_2, O_2 or OH^-) from water are incompetent

to deposit in a dense solid state to function as a protective interphase. Therefore, the aqueous based electrolytes suffer from a narrow electrochemical stability window (water splitting at > 1.23 V), intrinsically limiting the practical operating voltage and energy output. Based on it, the highly concentrated aqueous electrolyte for aqueous based Li-ion batteries has been proposed. One example of the highly concentrated electrolyte, which is usually called "water-in-salt" electrolyte, is >20 m (m: mol-salt in kg-solvent) LiTFSI in water. With a LiTFSI concentration of 21 m (cation: water molar ratio of 1:2.6), their molecular dynamics simulation predicted that on average two $TFSI^-$ anions would be involved in each Li^+ primary solvation sheath, leading to an interfacial chemistry dominated by the reduction of $TFSI^-$ anions. This reduction process generates sufficient LiF from $TFSI^-$ to form a robust anode SEI. The LiF-rich interphase serves as an electron barrier preventing the reduction of both $TFSI^-$ anions and water molecules while still allowing for prompt Li+ ion conduction. The formation of this unique electrode/electrolyte interface pushes both oxygen and hydrogen evolution potentials well beyond the stability limits of water. As a result, an extended electrochemical stability window is achieved for the concentrated solution containing 21 m LiTFSI.[123]

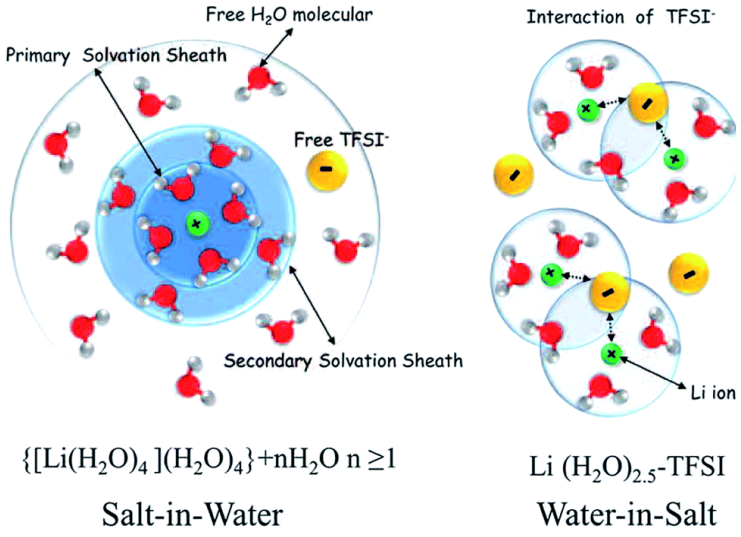

Figure 2.3.1 Illustration of the evolution of the Li^+ primary solvation sheath in diluted and "water-in-salt" solutions.[25] Copyright 2015 with permission from *American Association for the Advancement of Science.*

In "water-in-salt" electrolytes, LiTFSI is chosen as the salt because of its high solubility in water (21-22 m at 25 °C) and high stability against hydrolysis. When the LiTFSI concentration is above 5 m, the water-in-salt definition applies, as the salt outnumbers the solvent in the binary system by both weight and volume. In these solutions, the average number of water molecules available to solvate each ion is far below the "solvation numbers" that are well established in conventional electrolytes (~1.0 m). According to the thermal analysis of the highly concentrated

solutions in previous reports, solutions at both 20 and 21 m are “true” liquids at room temperature (25 °C) that can be supercooled down to -90 °C with negligible crystallinity. The room temperature conductivity of 21 m solution remains ~10 mS/cm, comparable to that of nonaqueous electrolytes (9.0 mS/cm).[25]

For dilute solutions (Figure 2.3.1), Li^+ remains well hydrated in its primary solvation sheath with sufficient free water available. In such electrolytes, attempts to lithiate an anode, whose lithiation potential is below that of water reduction, would lead to preferential reduction of water and sustained hydrogen evolution. Compared to it, with LiTFSI concentrations increased beyond 20 m, molecular dynamics simulation predicts that on average two TFSI anions are observed in each Li^+ primary solvation sheath, and such a high probability of $TFSI^-$ leads to an interphasial chemistry dominated by the reduction of $TFSI^-$. Such interphase serves as an electron barrier to prevent the reduction of water while allowing Li^+ migration, thus realizing the expanded electrochemical stability window of the system.[25]

Highly concentrated Li salt in the electrolyte alters the interfacial reaction pathways and the properties of the SEI layers. The fundamental reason is usually ascribed to the significant change in the electrolyte solution structures, reduction of free water molecules, and the corresponding modified highest occupied molecular orbital (HOMO) and lowest unoccupied molecular orbital (LUMO) energies.

Similar to that in Li-ion batteries, when applied in supercapacitors, the high LiTFSI concentration can increase the conductivity of ions and lower the electrolyte impedance to improve the power density performance. Contrary to the conventional aqueous electrolytes for supercapacitors, the water molecules in “water-in-salt” electrolytes do not play a direct role on the variation of the capacitance because most of them are strongly bound inside the first hydrogen shell of the Li^+ ions, so that the capacitive behavior overall displays similar features as in the case of pure ionic liquids.[128] The ions, instead of being completely solvated by the solvent, are mostly surrounded by their counter ions and only with a limited number of water molecules.[129]

2.4 Molybdenum sulfides for supercapacitors and Li-ion batteries

The phase diagram of molybdenum sulfide contains two common phases, MoS_2 and MoS_3, which are both chemically stable in ambient conditions.

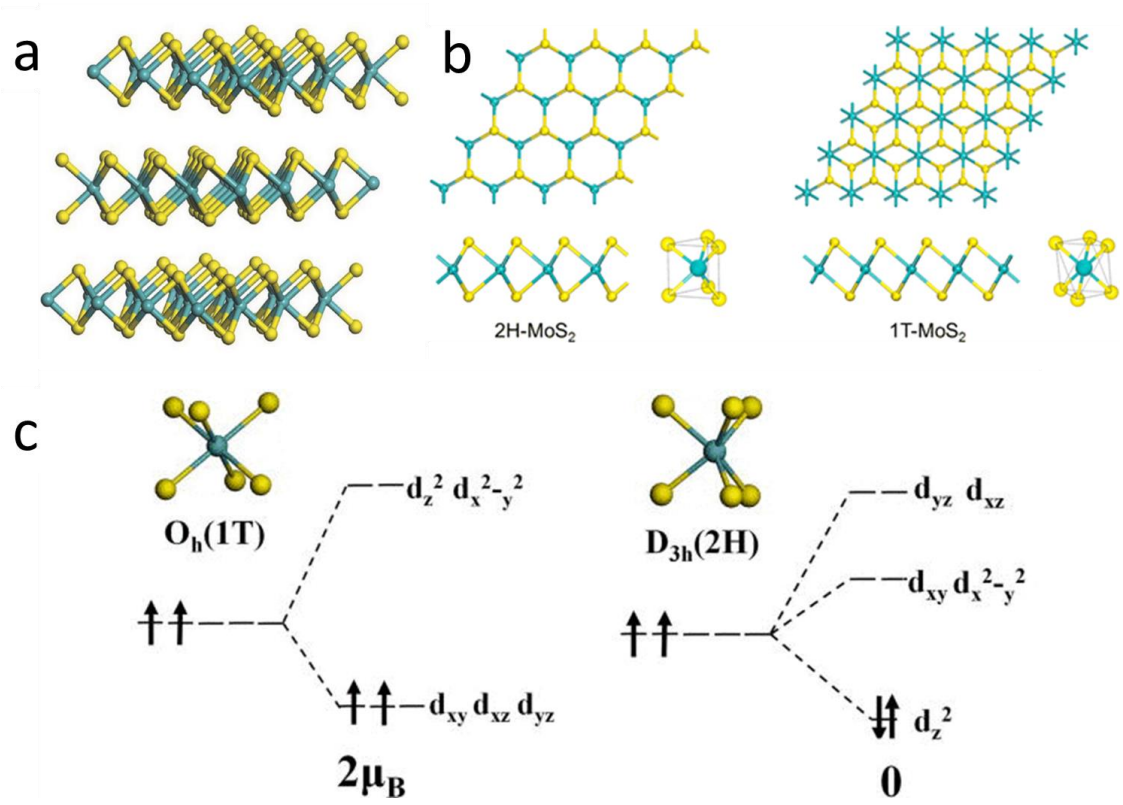

Figure 2.4.1 (a) Schematic structural illustrations of 2D layered MoS_2. The blue and yellow spheres represent Mo and S atoms, respectively,[78] (b) top and side views of the 2H (left) and 1T (right) structures for the MoS_2 monolayer, Mo, cyan; S, yellow,[130] (c) the occupation of electrons in Mo 4d orbits under the crystal fields of 1T phase and 2H phase.[131] Copyright 2017 with permission from *WILEY-VCH*, 2013 with permission from *Springer Nature* and 2015 with permission from *AIP Publishing*.

MoS_2 features the layered structure similar to graphene and each layer consists of one Mo layer and two S layers (S-Mo-S), which are bonded to adjacent MoS_2 layers by weak van der Waals force and the corresponding molecular structure scheme is shown in Figure 2.4.1 (a). The Mo atoms provide four electrons to fill the bonding states of MoS_2 such that the oxidation states of Mo and S atoms are +4 and -2, respectively. The lone-pair electrons of S atoms terminate the surfaces of the layers, and the absence of dangling bonds renders those layers stable against reactions with environmental species. Based on the crystal structure of MoS_2, three main types of atom arrangements (1T-MoS_2, 2H-MoS_2, and 3R-MoS_2) have been found. For the 1T phase, there is one layer per repeat unit; for the 2H phase, there are two layers per repeat unit; and for the 3R phase, there are three layers per repeat unit. As shown in Figure 2.4.1 (b), in 1T and 2H phases, each Mo center is surrounded by six S atoms. 2H phase is prismatically coordinated with S atoms in the upper and lower planes lying in a line, while in the 1T phase, the Mo atoms occupy the octahedral holes of the S layers, and the S atoms in the upper and lower planes are offset.[132] By sliding one S and/or one Mo atomic layer along the armchair direction, the 2H

phase can be transformed into the 1T phase. The atomic arrangements of the 2H and 1T structures strongly depend on the electronic structure of Mo and its 4d-electron count.[130, 133] As indicated in Figure 2.4.1 (c), the d orbitals of octahedrally coordinated 1T-phase MoS_2 form degenerate $d_{xy,xz,yz}$ (t_{2g}) and d_{z^2,x^2-y^2} (e_g) orbitals. Because of the incomplete occupation of the lower-lying t_{2g} orbital, 1T-phase MoS_2 has metallic electronic characteristics but is unstable. In trigonal prismatically coordinated 2H-phase MoS_2, a crystal field-induces splitting of the Mo 4d-orbitals leads to the formation of d_{z^2} (a_1'), $d_{x^2-y^2,xy}$ (e'), and $d_{xy,yz}$ (e'') bands separated by a sizeable energy gap ($\approx$1 eV) between the first two groups of orbitals. These two Mo d electrons fill the lower lying a_1' orbital, giving it semiconducting characteristics with high stability at room temperature.[134]

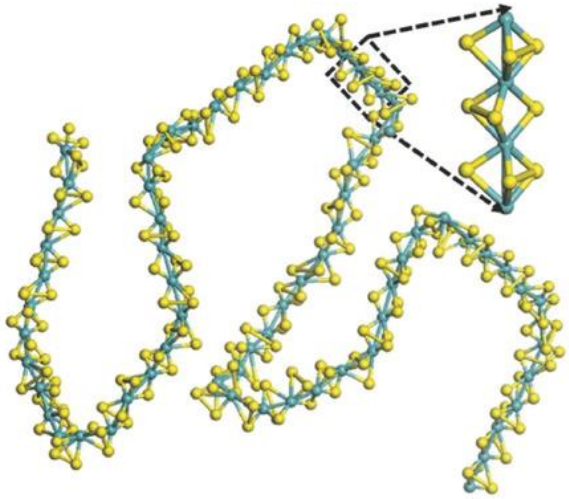

Figure 2.4.2 Schematic structural illustration of one-dimensional chain-like MoS_3, the blue and yellow spheres represent Mo and S atoms, respectively.[78] Copyright 2017 with permission from *WILEY-VCH.*

MoS_3 has a chain-like arrangement of molybdenum atoms, which have a trigonal prismatic coordination of six sulfur atoms. Adjacent Mo atoms are bridged by three sulfur atoms along the chain. Every two metal atoms in the chain are paired up with a shorter metal-metal distance and one S-S bond in every other triangle. The proposed arrangement of MoS_3 corresponds to a formal charge state of Mo^4 $(S_2^{2-})_{1/2}(S^{2-})_2$.[135] The Mo-Mo separation is 361.8 pm, and the terminal Mo-S bond length of 210.7 pm is largely shorter than those between molybdenum and bridging sulfurs (249.3 pm). The S-S distance in the $–S_2–$ bridge is 212.4 pm.[136]

2.4.1 Molybdenum disulfide for supercapacitors

As a typical two dimensional transition metal dichalcogenides, MoS_2, providing abundant active sites for charge accumulations and facile channels for the insertion/extraction of

electrolyte ions, has been widely explored as the electrode material for supercapacitors. MoS_2 is expected to exhibit good supercapacitive properties due to its sheet like morphology, which provides large surface area for double-layer charge storage, and a range of oxidation states from +2 to +6 of Mo for psudocapacitive storage. In addition, MoS_2 has the advantages of higher intrinsic fast ionic conductivity (than oxides) and higher theoretical capacity (than graphite). Supercapacitors based on MoS_2 as electrode undergo three main modes: (a) intersheet double-layer charge storage, (b) intra sheet double-layer charge storage on individual atomic MoS_2 layers through diffusion into the basal edges, (c) faradaic charge transfer process on the Mo transition metal center.[137] It is worth noting that for the faradaic charge transfer process, the high density of basal edges, consisting of charged S or Mo species, offers a large number of accessible "entry" sites, whereby intersheet diffusion of protons can occur. One possible mechanism is the intercalation of protons (H^+) or alkali metal (Li^+, Na^+) from electrolytes in the interlayers upon reduction, followed by deintercalation upon oxidation:[58]

$$MoS_2 + H^+ + e^- \leftrightarrow MoS\text{-}SH \qquad (2.4.1.1)$$

The intercalation reaction of Li proceeds by reduction of the MoS_2 layers and an insertion of Li^+ cations into the layers of MoS_2 (bonded by van der Waals intercalations) for charge compensation. This is accompanied by significant changes in the electronic and crystallographic structure of the host lattice. During the Li intercalation reaction, the semiconductor 2H-MoS_2 undergoes a phase transition to a metastable metallic 1T-MoS_2 polymorph.[138] Usually the favorable interaction is found along the van der Waals gap of the $(10\bar{1}0)$ surface. After charge process, both phases (1T and 2H) are present in the sample. In addition, the continual intercalation and deintercalation of the relatively large alkali ions in the electrolytes over repeated cycles can also lead to exfoliation of the MoS_2 layers that are restacked during the filtration process, leading to an increased surface area and subsequently a much larger specific capacitance.[139]

The nonfaradaic process involves the adsorption of protons or cations on the surface of MoS_2:[58]

$$(MoS_2)_{surface} + H^+ + e^- \leftrightarrow (MoS_2)_{surface}\text{-}H \qquad (2.4.1.2)$$

Larger-sized anions with lower electrophoretic mobility produce a more drastic reduction in the capacitance for thin films, which is due to the reason that thin films exemplified by the densely packed sheet-like structures do not allow close access of big anions to the surface because of electrostatic repulsion.

2.4.2 Molybdenum trisulfide for Li-ion batteries

As mentioned, all molybdenum in MoS_3 occurs in the 4+ oxidation state, while sulfur is present in two stages, including S^{2-} and S_2^{2-} ligands in different types of coordination. When applied as electrode material in Li-ion batteries there are multiple reaction mechanisms of sulfur with lithium. The first step is the transformation of sulfur to lithium polysulfide (Li_2S_n, $2<n<8$) at higher potential of about 2.5 V, and the second step is the change of lithium polysulfide to lithium sulfide (Li_2S) at lower potential of 1.8 V. Comparing the CV results on MoS_3 and S, a reduction peak at 2.5 V (*vs.* Li/Li^+) that represents the transformation of sulfur to lithium polysulfide is not observed, which means that elemental sulfur does not exist in the MoS_3 electrode.[76]

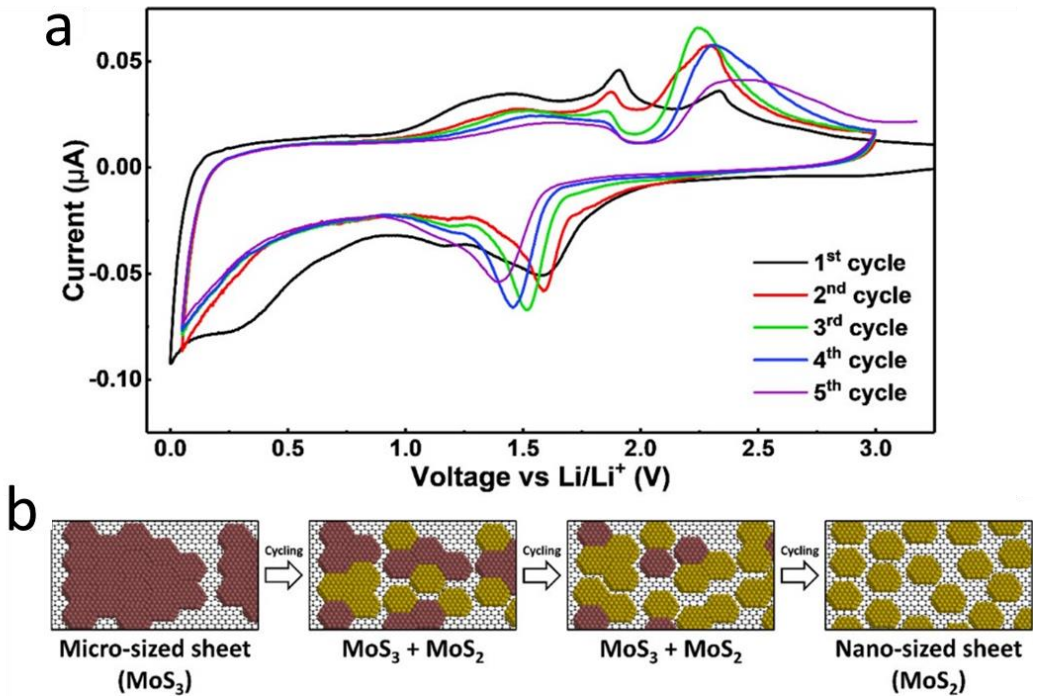

Figure 2.4.2.1 (a) Cyclic voltammetry for a MoS_3/r-GO half-cell with 1 M lithium hexafluorophosphate ($LiPF_6$) in ethylene carbonate (EC): diethyl carbonate (DEC) (1:1, v/v %) as electrolyte, (b) schematic showing the sequence of in situ electrochemical pulverizations in MoS_3/r-GO, which is caused by fully repetitive lithiation and delithiation during initial formation cycles.[73] Copyright 2019 with permission from *American Chemical Society.*

During the operation process, adsorption of Li^+ ions at the bridge sites between two adjacent S atoms is the most energetically stable. The chain-like molecular structure of MoS_3 has more open sites for Li^+ storage than the common studied MoS_2: it can uptake four alkali ions per MoS_3 with the 1D structure, while 2D MoS_2 can only uptake two Li^+ ions per MoS_2 unit, which gives rise to the larger capacity of MoS_3 than MoS_2. It also has been found that alkali ions can

easily diffuse along the MoS_3 chain and the optimal diffusion path is from one bridge site to the adjacent bridge site, passing through a metastable site. In addition, the diffusion energy barrier associated with the process is only 0.212 eV, much smaller than that of 2H-MoS_2 (0.68 eV). The small diffusion energy barrier facilitates fast charge and discharge processes in Li-ion batteries, and consequently enhances the battery rate capability.[78]

When using 1 M $LiPF_6$ in EC: DEC (1:1, v/v %) as electrolyte, MoS_3 undergoes the multiple phase transformation during cycling in Li-ion batteries, as shown in Figure 2.4.2.1. During the first formation cycling in the CV curve, lithiation peaks are observed at 1.59, 1.45 and 0.67 V, corresponding to the phase transformation of MoS_3 to metallic Mo and Li_2S by intercalation and conversion, respectively (Eq. 2.4.1-2.4.3).[73]

$$MoS_3 + 2Li^+ + 2e^- \rightarrow MoS_2 + Li_2S \qquad 1.59\ V_{Li+/Li} \qquad (2.4.1)$$

$$MoS_2 + xLi^+ + xe^- \rightarrow Li_xMoS_2 \qquad 1.45\ V_{Li+/Li} \qquad (2.4.2)$$

$$Li_xMoS_2 + (4-\text{-}x)Li^+ + (4-x)e^- \rightarrow Mo + 2Li_2S \qquad 0.67\ V_{Li+/Li} \qquad (2.4.3)$$

For the delithiation, two oxidation peaks appear at 1.44 and 1.89 V, corresponding to oxidation of Mo to Mo^{4+} and further to Mo^{6+}, respectively (Eq. 2.4.4 and 2.4.5). In addition, the oxidation peak for Li_2S is observed at 2.31 V (Eq.2.4.6).[73]

$$Mo \rightarrow Mo^{4+} + 4e^- \qquad 1.44\ V_{Li+/Li} \qquad (2.4.4)$$

$$Mo^{4+} \rightarrow Mo^{6+} + 2e^- \qquad 1.89\ V_{Li+/Li} \qquad (2.4.5)$$

$$3Li_2S \rightarrow 3S + 6Li^+ + 6e^- \qquad 2.31\ V_{Li+/Li} \qquad (2.4.6)$$

However, from the second cycle, the lithiation of MoS_3 to MoS_2 and Li_2S dramatically decreases and the intercalation of MoS_2 significantly increases, which indicates that during the initial formation cycles the lithiated MoS_3 starts to decompose into Li_xMoS_2 and Li_2S. Therefore, the reversible reaction is composed of both lithiation (Eq.2.4.7 and 2.4.8) and delithiation (Eq.2.4.9), and during this conversion, the amorphous MoS_3 is recombined to a relatively stable MoS_2 crystalline nanostructure with Li_2S.

$$MoS_2 + S + (2+x)e^- \rightarrow Li_xMoS_2 + Li_2S \qquad 1.58\ V_{Li+/Li} \qquad (2.4.7)$$

$$Li_xMoS_2 + (4-x)Li^+ + (4-x)e^- \rightarrow Mo + 2Li_2S \qquad 1.20\ V_{Li+/Li} \qquad (2.4.8)$$

$$Mo + 3Li_2S \rightarrow MoS_2 + S + 6Li^+ + 6e^- \qquad 2.31\ V_{Li+/Li} \qquad (2.4.9)$$

Based on the above analysis, fully repetitive lithiation and delithiation reactions in organic electrolyte-based Li-ion batteries lead to the conversion of amorphous MoS_3 to crystalline MoS_2 and the pulverization by repeatedly decomposing and recombining bonds between Mo and S.

The phase transformation of amorphous MoS_3 in aqueous Li-ion batteries is for the first time discussed in Chapter 5.

3 Highly dispersible hexagonal carbon-MoS_2-carbon nanoplates with hollow sandwich structures for supercapacitors

In recent years, mono- and multi-layered transition metal dichalcogenides (TMD) nanosheets have attracted intensive interest and have shown broad application on prospects such as catalysis,[140] electrochemistry,[57] and optics.[141] The TMD materials include the disulfides, diselenides, and ditellurides of Mo, Ti, Zr, Hf,V, Ta, Nb, Cr and W, yet only the Mo and W compounds (disulfides, diselenides, and ditellurides) form a hexagonal-type crystal structure.[46] Among all, MoS_2, a typical TMD material resembling graphene, has gained much attention.[142] MoS_2 has a layered structure and each layer is made of MoS_6 trigonal prisms which share edges with each other. The layers are stacked and held together by weak Van der Waals forces. The outstanding structures of mono- or few-layered MoS_2 can provide highly active sites, a high specific surface area and an extended contact with an electrolyte when it is applied in energy storage devices.[143-148] Thus, MoS_2 has been widely studied as promising anode material in lithium ion batteries (LIBs) and sodium ion batteries (SIBs) due to its low cost, high specific capacity, and layered structure with improved intercalation and de-intercalation dynamics of alkaline ions. Recently, metallic 1T-MoS_2 phase has been demonstrated as a highly efficient electrode material for supercapacitors, which in particular are an ideal technology to exploit the beneficial properties of 2D materials.[63, 149] Moreover, the energy storage performance of the devices strongly relies on the matching of the electrolyte interlayer spacing and the electrolyte ion diameter,[150] especially for supercapacitors. The average interlayer spacing of graphite materials is about 0.335 nm, which is quite smaller than that of electrolyte ion diameters (hydrated potassium ions is 0.66 nm and hydrated sodium ions is 0.72 nm).[151-154] This means there will be barrier for the electrolyte ions to diffuse into the electrode, which may cause limitations to the material applications in energy storage despite the excellent physical and chemical properties of graphite. With comparison, MoS_2 will present better performance with larger interlayer spacing about 0.615 nm, especially for aqueous electrolytes.

Up to now, MoS_2 can be synthesized through two methods,[155] including the top-down method (liquid phase exfoliation)[156] and the bottom-up method (wet chemical synthesis method)[157]. In order to control the size and shape of the particles, many researchers prefer to use the chemical synthesis, which shows advantages *e.g.* an easy control of size and shape of particles.[158] Recently, Lou *et al.*[159] synthesized hollow MoS_2 microboxes using L-cysteine as the S source by hydrothermal method and applied it in Li-ion batteries. Wu *et al.*[160] fabricated hollow

nanostructured MoS_2 using CTAB as an additive by hydrothermal method and measured the electrochemical performance in supercapacitors. In order to figure out the superior of hollow structure to other structures, they also produced two other morphologies, namely nanosheet and flower-like. They found that the hollow nanostructured MoS_2 has the best property with the specific capacitance of 160.1 F/g at a current density of 1 A/g and retention rate of 94.8% after 3000 cycles, while specific capacitances of the nanosheet structured and flower-like materials are only 141.4 F/g and 130.9 F/g with the retention rate of 84.1% and 73.2%, respectively.

However, there are still some challenges to apply MoS_2 in supercapacitors. Compared to typical carbon materials, the electronic conductivity of MoS_2 is limited, which can influence the electrochemical performance of devices. Therefore, combining MoS_2 with high conductive materials like carbon or graphite is a good solution. Hu *et al.*[161] used anodic aluminium oxide (AAO) as the template to synthesize carbon and MoS_2 on it. By removing the template, they finally got a porous tubular C/MoS_2 hybrid material, which has been further used as a novel electrode material. They found that the supercapacitor could deliver a high capacitance of 210 F/g at 1 A/g with excellent cycling stability over 1000 cycles. In addition, due to the interlayer van der Waals attraction and high surface energy, free-synthesized MoS_2 tends to aggregate not only during the synthesis but during charge-discharge cycling of supercapacitors, leading to undesirable energy storage behaviors. Assembling MoS_2 onto a support will provide this kind of 2D material with large specific surface area and highly exposed active sites. The existence of template will avoid the aggregation of the MoS_2 particles, thus improve the performance of energy storage. Moreover, the hollow structure obtained by removing the template further improves the contact of the interface electrolyte/active material and provides additional electrochemically active sites for energy storage.[159, 162-164]

In this chapter, hollow carbon-MoS_2-carbon nanoplates have been successfully synthesized by an L-cycteine assisted hydrothermal method using gibbsite as template and polydopamine as carbon precursor. After calcination and etching of gibbsite templates, uniform MoS_2 composite with the hollow hexagonal nanoplate structure exhibit high specific surface area and excellent dispersity and stability in water. A high electronic conductivity was also obtained by the introduction of carbon coatings. In addition, the hollow structure with well-defined interior voids can prevent the volume change during charge and discharge of supercapacitors, mainly caused by the intersheet and intrasheet double layer storage,[58] which always occurs in bulk MoS_2.

3.1 Synthesis of hollow carbon-MoS_2-carbon nanoplates

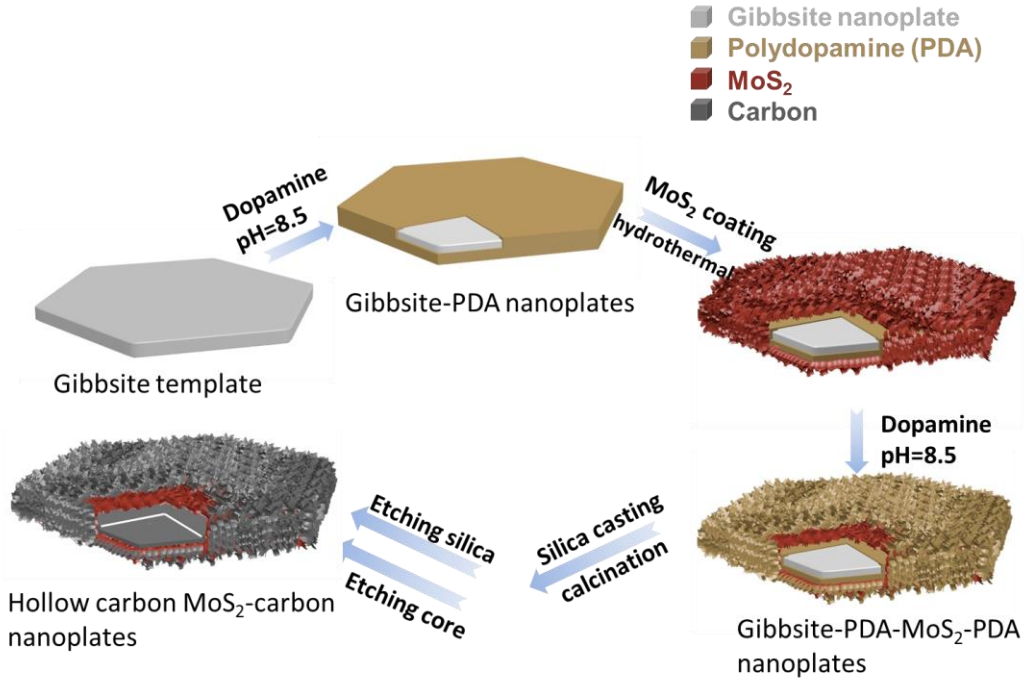

Figure 3.1.1 Synthesis procedure of the hollow carbon-MoS_2-carbon nanoplates.

In this work, a multistep strategy to synthesize hollow carbon-MoS_2-carbon nanoplates has been presented by the L-cysteine assisted hydrothermal method using gibbsite as template and polydopamine as the carbon precursor, as illustrated in Figure 3.1.1. L-cysteine is of particular interest in nanomaterial preparation due to its multifunctional groups (–SH, $–NH_2$ and $–COO^-$),[159, 165-166] which can be used for the conjugation of metallic ions or other functional groups. When heated, L-cysteines can release H_2S, which acts as sulfide source as well as a reducing agent, resulting in the formation of metal sulfide nanoparticles. In addition, under the solution-phase reaction, L-cysteines form a polymeric network structure, which facilitates the formation of a two-dimensional structure for the compounds. However, a drawback associated with hydrothermal method is the inevitable conglutination of the nanoparticles and the formation of non-dispersible bulk materials at high temperatures. The silica nanocasting technique introduced by Lu *et al.*[167] can help synthesize discrete and dispersible nanoparticles in an elegant way.

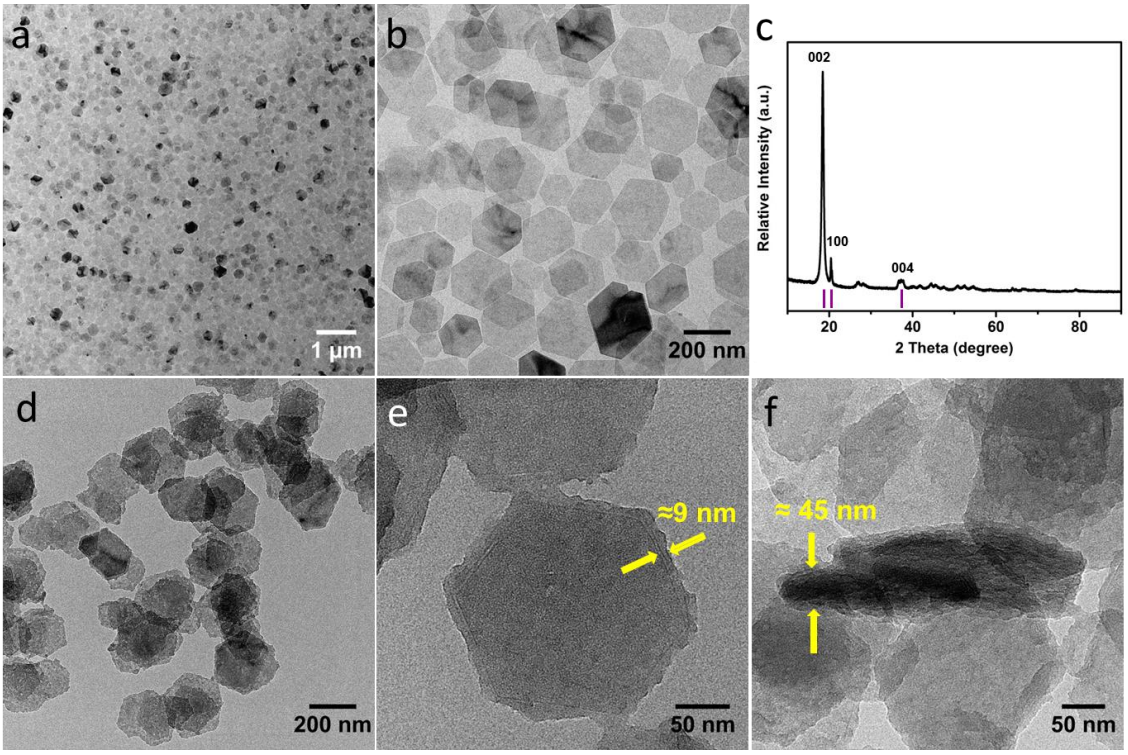

Figure 3.1.2 (a) (b) TEM images and (c) XRD pattern of the synthesized gibbsite nanoplates, (d) TEM image of the PDA-coated gibbsite nanoplates, (e) TEM image of the enlarged part of a gibbsite-PDA nanoplate, The yellow arrow points to the PDA layer (~9 nm), (f) TEM image of the standing nanoplates, which indicates the thickness and structures of the nanoplates.

Gibbsite nanoplates have been first synthesized according to the method developed by Wierenga *et al.*[168] The as-prepared gibbsite nanoplates can be dispersed easily in water and kept stable for a long time, which is beneficial for the further modification of the particles in aqueous solutions. TEM measurement is performed to investigate the morphology of the synthesized gibbsite nanoplates. TEM image in Figure 3.1.2 (a) shows the discrete state and homogeneous size distribution of the nanoplates The image in Figure 3.1.2 (b) shows the homogeneous hexagonal shape of the obtained nanoplates. In order to study the structure of the as-synthesized gibbsite nanoplates, XRD measurement was performed in Figure 3.1.2 (c). The reflections at 2θ = 18.3º, 20.4º and 30.2º can be assigned to (002), (110) and (004) planes of the gibbsite platelets, respectively.

To help the further growth of MoS_2 onto the template and enhance the electronic conductivity of the final product, a thin layer of PDA has been coated onto the gibbsite nanoplates. Firstly, dopamine monomer can be adsorbed onto the gibbsite surface via electrostatic interactions in the Tris buffer solution (pH=8.5). Polydopamine can be then formed through the self-polymerization of dopamine, involving oxidation of catechol to quinine, followed by

polymerization in a manner reminiscent of melanin formation. As shown in Figure 3.1.2 (d), no aggregation has been observed after PDA coating and the PDA shell onto the gibbsite nanoplates can be distinguished clearly from the TEM images according to the lower contrast of PDA. Moreover, the thickness of the PDA coating is about 9 nm and the rough surface is related to the fast polymerization speed. There is no change in shape of the nanoparticles after the coating of PDA shell, so a well-defined gibbsite-PDA core-shell structure has been obtained.

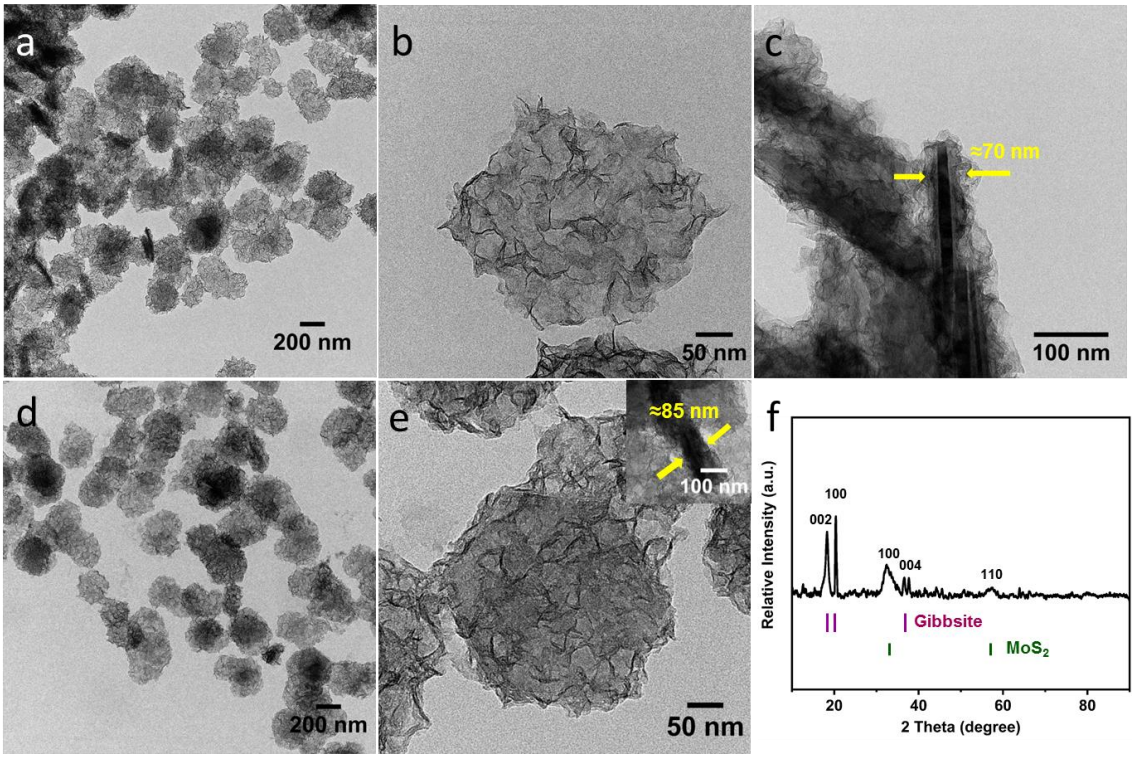

Figure 3.1.3 (a) (b) (c) TEM images of the gibbsite-PDA-MoS_2 nanoplates, (d) (e) TEM images and (f) XRD pattern of the gibbsite-PDA-MoS_2-PDA nanoplates.

In the next step, a MoS_2 layer is synthesized onto the gibbsite-PDA nanoplates via an L-cysteine assisted hydrothermal method. Here, Na_2MoO_4 and L-cysteine work as Mo and S sources, respectively. During the process, L-cysteine decomposes and releases S^{2-} ions, which act as the S source and the reducing agent for the formation of MoS_2 nanosheets. In addition, functional groups (–SH, $–NH_2$ and $–COO^-$) of L-cysteine conjugate with the Mo-containing ions and assist the growth of MoS_2 nanosheets onto the surface of gibbsite-PDA nanoplates.[159, 165-166] TEM images of the as-synthesized gibbsite-PDA-MoS_2 nanoplates show that the particles are highly uniform with the same hexagonal shape as the gibbsite template, and the thickness of the whole nanoplates is about 70 nm, indicating that the thickness of MoS_2 layer is only 13 nm. The results reveal that the MoS_2 shell is composed of randomly assembled ultrathin nanosheets and the

relatively large open space between MoS_2 nanosheets can be clearly observed. In order to further improve the electronic conductivity of the material, an additional layer of PDA is coated onto the nanoplates. The whole thickness of the gibbsite-PDA-MoS_2-PDA is about 85 nm, indicating the thickness of the PDA shell outside is about 7.5 nm. The structure of the material is then examined by XRD (Figure 3.1.3 (f)). Besides the reflections of gibbsite templates, the peaks centered at 2θ = 32.6º and 56.7º correspond to the 100 and 110 reflections of 2H-phase of MoS_2.

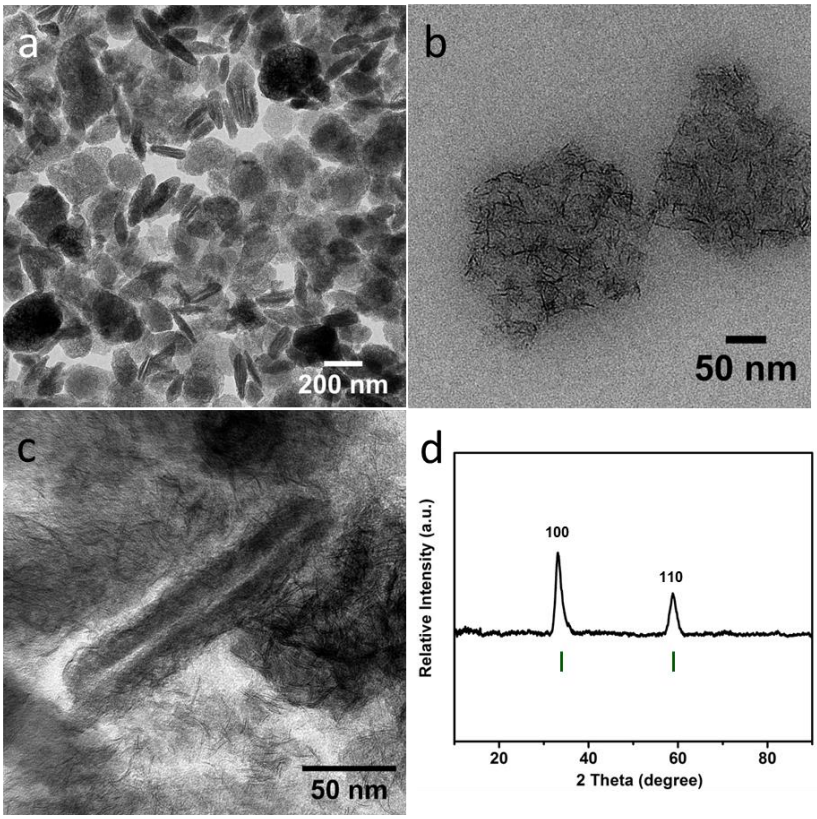

Figure 3.1.4 (a) (b) (c) TEM images and (d) XRD patterns of the hollow carbon-MoS_2-carbon nanoplates.

Normally, nanoparticles will inevitably conglutinate and non-dispersible bulk material forms during the high-temperature treatment. To overcome this limit, silica nanocasting technique is used before annealing of the nanoplates. After elimination of the silica portion by NH_4HF_2 and gibbsite templates by HCl, discrete and highly dispersed hollow carbon-MoS_2-carbon nanoplates are obtained. TEM images in Figure 3.1.4 (a) and (b) clearly show that the synthesized nanoparticles are highly dispersible and uniformly hexagonal, which is consistent with the particle shape of the gibbsite templates. Moreover, as can be seen in Figure 3.1.4 (c), the obtained nanoplate has a hollow core with a shell thickness of about 22 nm. For the XRD diffraction of the hollow carbon-MoS_2-carbon nanoplates, after the etching of the cores, the

diffraction peaks of gibbsite disappear totally, with only peaks centered at 2θ = 32.6º and 56.7º corresponding to the 100 and 110 reflections of MoS_2 observed. In addition, the asymmetric shape of the 100 reflection, with a rapid increase on the low angle side and a long tail on the high angle side, meets the feature of 2D crystals in XRD patterns.[169] The reflection peak at 2θ = 14º assigned to the 002 reflection of MoS_2 is extremely weak, suggesting that the stacking of MoS_2 layers along the c-axis is limited to only a few layers.[170] In addition, after the high-temperature treatment, the two peaks of MoS_2 become narrower and more obvious in the final product, indicating the better crystallinity of the MoS_2 after annealing. No peak of carbon was detected because of the small amount of carbon in the final product.[171]

3.2 Characterization of the hollow carbon-MoS_2-carbon nanoplates

The as-synthesized hollow carbon-MoS_2-carbon nanoplates are then characterized with high resolution TEM (HR-TEM), Raman spectroscopy, thermogravimetric analysis and nitrogen adsorption/desorption.

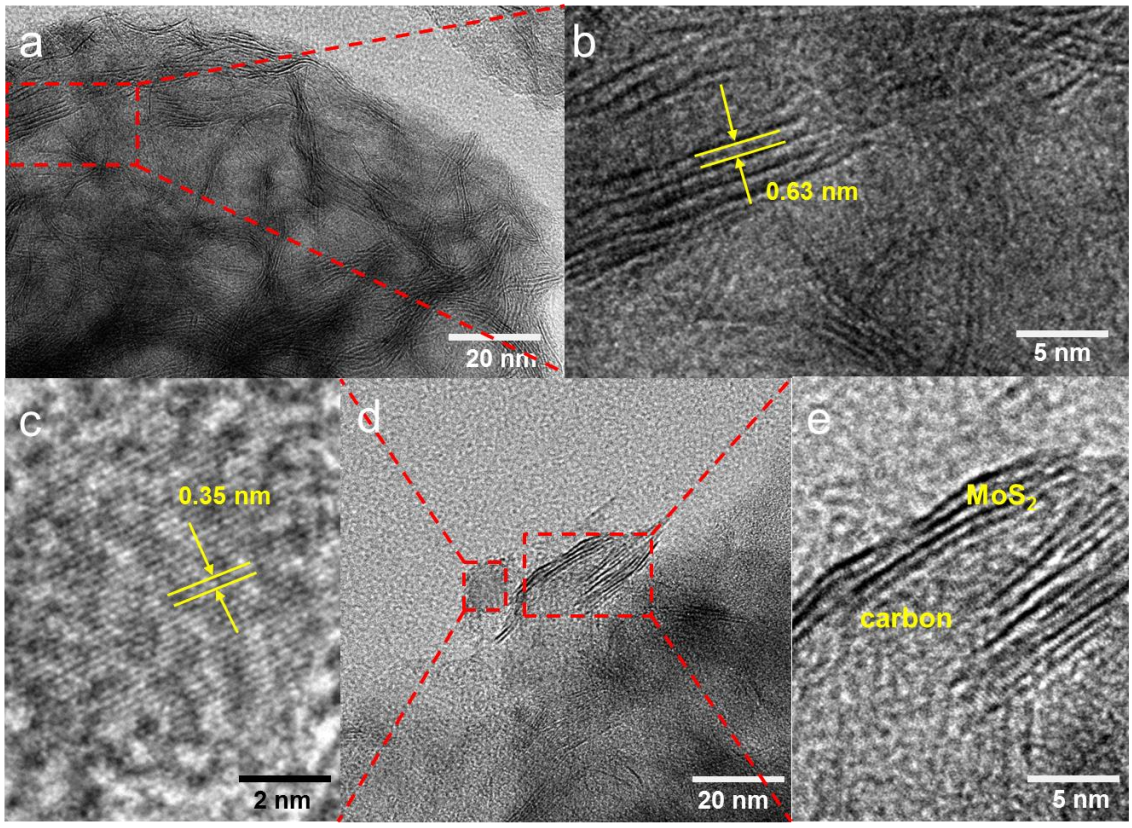

Figure 3.2.1 (a) and (d) HR-TEM images of the enlarged domain in the hollow carbon-MoS_2-carbon nanoplates, which indicate the layered structure of MoS_2 and graphite-like carbon. (b) (c) and (e) HR-TEM images of the parts indicated in (a) and (d). The interlayer distances of MoS_2 and carbon in the hybrid nanoplates are 0.63 nm and 0.35 nm, respectively.

To further investigate the details of the local structure, hollow carbon-MoS_2-carbon nanoplates have been measured by HR-TEM. As shown in Figure 3.2.1 (a) (d) and (e), layered stacking nanostructures of MoS_2 and graphite-like carbon with several layers can be clearly observed. The layered structures of MoS_2 and graphitized carbon co-exist at the same time and are embedded with each other in the hybrid material with the layer structure of MoS_2 uniformly distributed in the carbon sheet. Figure 3.2.1 (b) shows few layers of MoS_2 with the typical interlayer spacing of about 0.63 nm, indexed to the (002) plane of hexagonal phase of MoS_2, agreeing well with the XRD results. The images indicate that the hollow carbon-MoS_2-carbon nanoplates maintain the thin-layered structure of MoS_2, which will be essential for their electrochemical performance. In addition, the graphitic phase of carbon part has the interlayer spacing of about 0.35 nm, which agrees well with the previous reports.[172-175] The formation of graphitic nanostructure originates from the layered-stacking supramolecular structure of PDA, which converts to carbon during the high-temperature annealing.

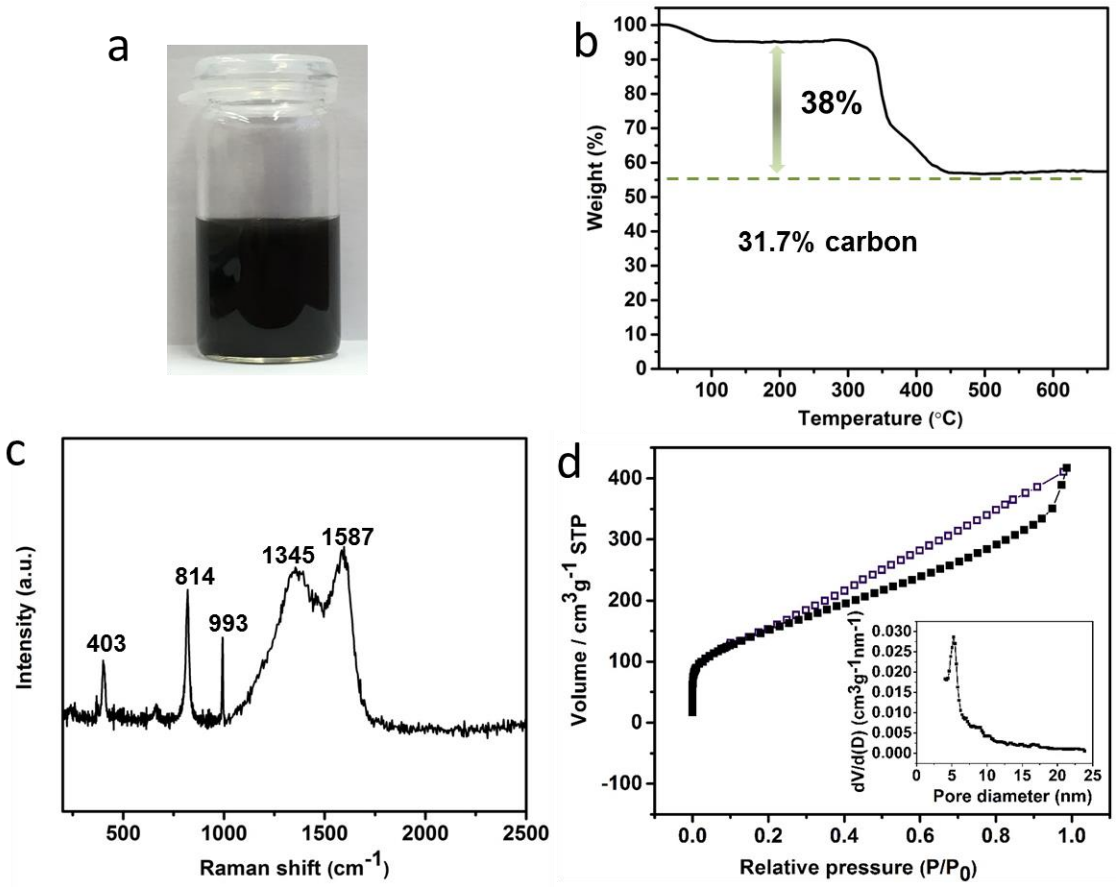

Figure 3.2.2 (a) Photograph of the hollow carbon-MoS_2-carbon nanoplates dispersed in water, (b) TGA profile, (c) Raman spectra, and (d) nitrogen adsorption/desorption isotherms of the hollow carbon-MoS_2-carbon nanoplates. The inset shows the pore size distributions obtained using the Barrett-Joyner-Halenda (BJH) method.

As the photograph shown in Figure 3.2.2 (a), the as-synthesized hollow carbon-MoS_2-carbon nanoplates are well dispersed in water, forming a stable colloidal suspension under neutral pH condition for more than 24 hours without any sign of precipitation. Despite no surfactant was used to stabilize the nanoplates, the electrostatic repulsion between the surface charged carbon coating provides the superior dispersity of nanoplates. The charged state of carbon materials from polydopamine can be proved by zeta-potential value in the literature.[67] The carbon wt. % in the hybrid material is determined by TGA analysis, as shown in Figure 3.2.2 (b). The unobvious mass difference up to 100 ºC is caused by the residual water in the product. During the measurement, MoS_2 is oxidized to MoO_3 under O_2 flow. The formation of MoO_3 from MoS_2 and CO_2 from carbon occurs in the same temperature range of 300- 400 ºC, leading to a mass loss of 38%. By assuming the final product after 600 ºC is MoO_3, the weight fraction of carbon in the initial sample is simply calculated to be 31.7%.[176]

Figure 3.2.2 (c) shows the typical Raman spectra of the hollow carbon-MoS_2-carbon nanoplates with a 633 nm laser at room temperature. The two characteristic vibrations of the S-Mo-S interaction and movement can be observed, in which the bands at 377 cm^{-1} and 403 cm^{-1} correspond to the in plane E^1_{2g} and out of plane A^1_g vibration modes of MoS_2, respectively. The in-plane E^1_{2g} mode can be assigned to an opposite vibration of the Mo atom with the respect to two S atoms, and the A^1_g mode is ascribed to the out-of-plane vibration of S atoms along the opposite directions.[170, 177] The stronger intensity of A^1_g peak compared to that of E^1_{2g} is due to the fact that the few-layer nature of MoS_2 leads to reduced interlayer van der Waals interactions which has an obvious increased out-of-plane atom vibration and limited impact on the in-plane vibration.[176] Moreover, the peaks at 814 cm^{-1} and 993 cm^{-1} should be the terminal stretching vibration of Mo=O, which results from the exposure to the air of MoS_2 during etching or stored process.[170] Additionally, there are two obvious bands appearing at 1345 cm^{-1} and 1587 cm^{-1}, which correspond to the D band and G band of sp^2 carbon, respectively. The D band is recognized as disordered band, and G band corresponds to the in plane stretching motion between sp^2 carbon atoms.[178-180] To further understand the porous texture of the hollow carbon-MoS_2-carbon nanoplates, nitrogen adsorption/desorption isotherms have been measured. As shown in Figure 3.2.2 (d), a distinct hysteresis loop can be observed with a quasi IV isotherm characteristic of mesoporous materials, indicating the existence of a mesoporous structure. The BET specific surface area is determined to be 543 m^2/g and the total pore volume is 0.677 cm^3/g. The inset pore size distribution curve shows a narrow peak and the pore size calculated using the BJH model shows to be 5.3 nm.

Based on the results above, we have successfully synthesized highly dispersible hollow sandwich-structured carbon-MoS_2-carbon nanoplates by the L-cysteine assisted hydrothermal method using gibbsite as the template and polydopamine as carbon precursor. After calcination and etching of the gibbsite template, uniform hollow platelets were obtained, which consist of a sandwich-like assembly of the partial graphitic carbon and the 2D layered MoS_2 flakes. HR-TEM and Raman measurements indicate that MoS_2 and graphitic carbon coexist at the same time. The product shows excellent colloidal stability and has a high specific surface area of 543 m^2/g with the pore size of 5.3 nm.

3.3 Electrochemical performance of the hollow carbon-MoS_2-carbon nanoplates in supercapacitors

As mentioned before, the hollow carbon-MoS_2-carbon with sandwich structures have unique advantages as the electrode material for supercapacitors. (1) The two dimensional hollow structure with high specific surface area delivers many active sites for energy storage. (2) The final material with the sandwich-like structure has high electronic conductivity to promote electrolyte ion diffusion. (3) Void space of the hollow structure can facilitate the mass transport and accommodate the volume change. With these merits in mind, the electrochemical performance of the hollow carbon-MoS_2-carbon nanoplates as electrode material for supercapacitors has been investigated.

3.3.1 Three-electrode performance

CV measurements in a three-electrode configuration with the hollow carbon-MoS_2-carbon nanoplates on a glassy carbon electrode as working electrode, a platinum wire as counter electrode and an Ag/AgCl in saturated KCl electrode as reference electrode have been carried out to assess the electrochemical stability of the as-synthesized hollow carbon-MoS_2-carbon nanoplates in 1 M Li_2SO_4. As following the potential opening approach, the stability window has been determined separately in both the negative potential and positive potential. Considering the hydrogen evolution at negative electrode and oxygen evolution at the positive electrode, the potential window for the system can be determined as -0.9 V to 0.5 V *vs.* Ag/AgCl. The electrochemical properties are further investigated by CV measurements at different scan rates with the potential window varied from -0.9 V to 0.5 V *vs.* Ag/AgCl. With the increasing of scan rates, CV curves exhibit rectangular and symmetric shapes, indicating ideal capacitive behaviour and desirable high-rate performance. The beginning of the redox

peaks can be observed from 0.3 V *vs.* Ag/AgCl in anodic scan and -0.7 V *vs.* Ag/AgCl in cathodic scan, which is attributed to the decomposition of the aqueous electrolytes.[181]

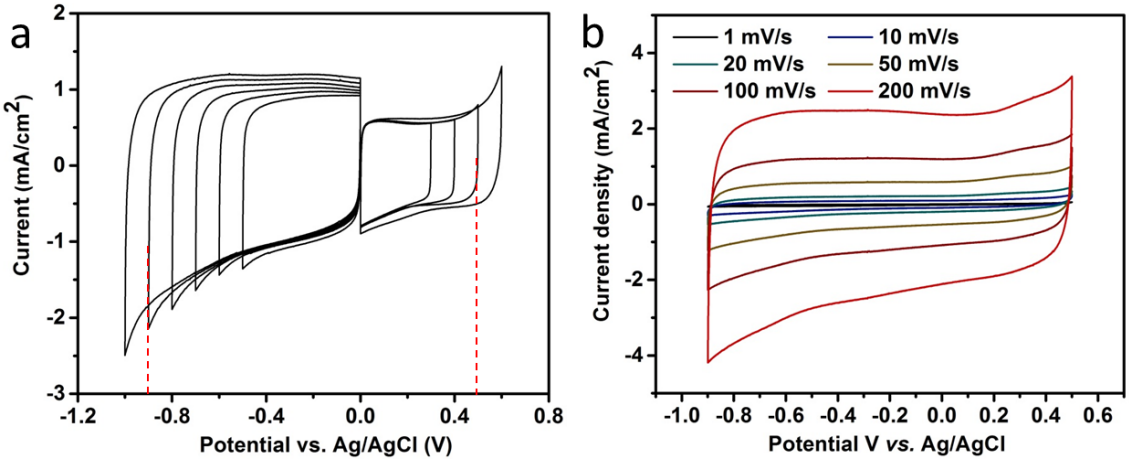

Figure 3.3.1.1 (a) Cyclic voltammetry (CV) graphs used to determine the stability window of the hollow carbon-MoS_2-carbon nanoplates in 1 M Li_2SO_4 at the scan rate of 100 mV/s, (b) CV curves of the hollow carbon-MoS_2-carbon nanoplates in a three-electrode cell in 1 M Li_2SO_4 aqueous electrolyte at different scan rates.

3.3.2 Two-electrode performance

In order to calculate the energy density as well as the power density of the as-synthesized hollow carbon-MoS_2-carbon nanoplates, a symmetric two-electrode supercapacitor has been fabricated.

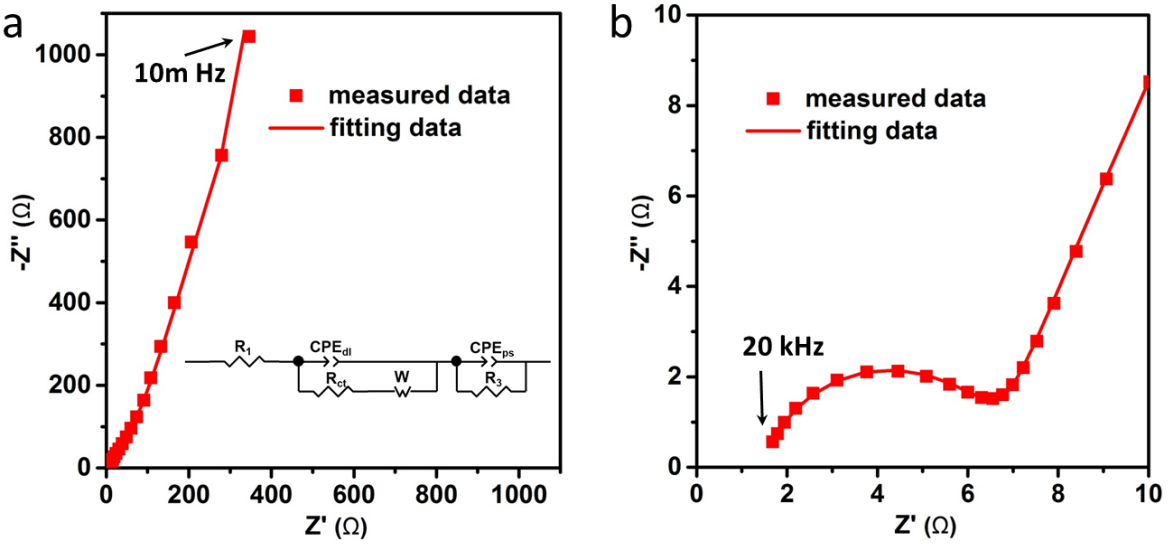

Figure 3.3.2.1 (a) Nyquist plots measured within frequency range from 20 kHz to 10 mHz, (the inset is the equivalent circuit which is employed to fit the impedance spectra, and the dots are measured data and solid line is fitting data), (b) the close-up view at the high frequency of the Nyquist plots.

Electrochemical impedance spectroscopy (EIS) measurements have been carried out on the two-electrode configuration within the frequency range from 20 kHz to 10 mHz to understand the ion diffusion of the electrodes (Figure 3.3.2.1). The EIS spectra exhibits two distinct parts including a semicircle in the high frequency region indicating the charge transfer process and a sloped straight line in the low frequency region corresponding to the diffusion-limited process. The equivalent circuit inset in Figure 3.3.2.1 (a) has been applied to fit the measured data. Here, R_1 represents the internal resistance of the electrolyte, CPE_{dl} and CPE_{ps} donate the constant phase element involving double layer and pseudo capacitance, while R_{ct} and W correspond to the charge-transfer resistance and associated Warburg impedance, respectively. The goodness of the fit χ^2 and other fitting parameters are given in Table 3.3.2.1. At low frequency, the nearly vertical slope shows the Warburg impedance, which represents electrolyte diffusion in the porous electrode and proton diffusion in the nanohybrid materials. In addition, the impedance data reveal nearly ideal capacitive behaviour influenced slightly by the ion diffusion process within the active electrode material. After fitted, R_1 and R_{ct} for the studied system is found to be 1.5 Ω and 4.7 Ω, respectively, indicating that the as-synthesized hollow carbon-MoS_2-carbon nanoplates not only exhibit good conductive capability due to the carbon coating, but also provide good diffusion of the electrolyte ions into the electrode material.[182-183]

Table 3.3.2.1 Fitting data of the Nyquist plots. In the electrical equivalent circuit (in Figure 3.3.2.1), R_1 is the resistance contributed by electrolyte solution, internal resistance of electrode and contact resistance. CPE_{dl}, R_{ct} and W_1 are electrical double layer capacitance, the charge transfer resistance and the Warburg resistance, respectively. R_3 and CPE_{ps} represent leak resistance and pseudocapacitance constant phase element, respectively. (Goodness of the fit χ^2 = 5.8E-5, Sum of square = 0.004)

Element	Value	Error	Error%
R_1	1.5	0.006	0.4
CPE_{dl}-T	5.7E-5	2.2E-6	3.8
CPE_{dl}-P	0.88	0.004	0.4
R_{ct}	4.7	0.04	0.8
W-R	1.6	0.1	8.5
W-T	0.006	0.0006	9.9
W-P	0.4	0.001	0.2
CPE_{ps}-T	0.01	9.2E-5	0.9
CPE_{ps}-P	0.7	0.003	0.4
R_3	55.13	1.4	2.6

To evaluate the electrochemical properties of the hollow carbon-MoS_2-carbon nanoplates, CV measurements at different scan rates from 0.5 mV/s to 300 mV/s have been performed. To moderate the electrolyte decomposition observed in the preliminary three-electrode results, the voltage range here is set to 1.2 V. From the CV curves (Figure 3.3.2.2 (a)), it demonstrates that all CV curves are close to symmetrical and quasi-rectangular shapes, indicating the electrical double-layer capacitance behaviour of the material. In addition, they also reveal the prominent reduction and oxidation peaks arising from the reversible faradaic reaction of MoS_2 at 0.6 V and 0.8 V. The oxidation/reduction peaks correspond to the valence state changing of Mo atoms in the MoS_2 layers, which ranges from +2 to +6.[150] Additionally, there is a broad hump at 0.8 V during charging and a hump at 0.6 V during discharging, attributed to the pseudocapacitive behaviour of MoS_2. It illustrates that the capacitance of the hollow carbon-MoS_2-carbon nanoplates is composed of electrical double-layer capacitance and pseudocapacitance. When the scan rate reaches 300 mV/s, the CV curves still maintain the symmetrical shape very well, suggesting that they possess excellent rate capability. The promising performance can be attributed to the fact that the hollow nanoplate morphology ensures the easy diffusion of the electrolyte and the conductivity of the nanocomposite is high. Based on the results above, the working mechanism based on MoS_2 as electrode materials includes three modes[58]: (i) intersheet double-layer charge storage, (ii) intrasheet double-layer charge storage on individual atomic MoS_2 layers through diffusion into the basal edges, and (iii) faradaic charge transfer process on the Mo center, which can exhibit oxidation states of Mo varying from +2 to +6.

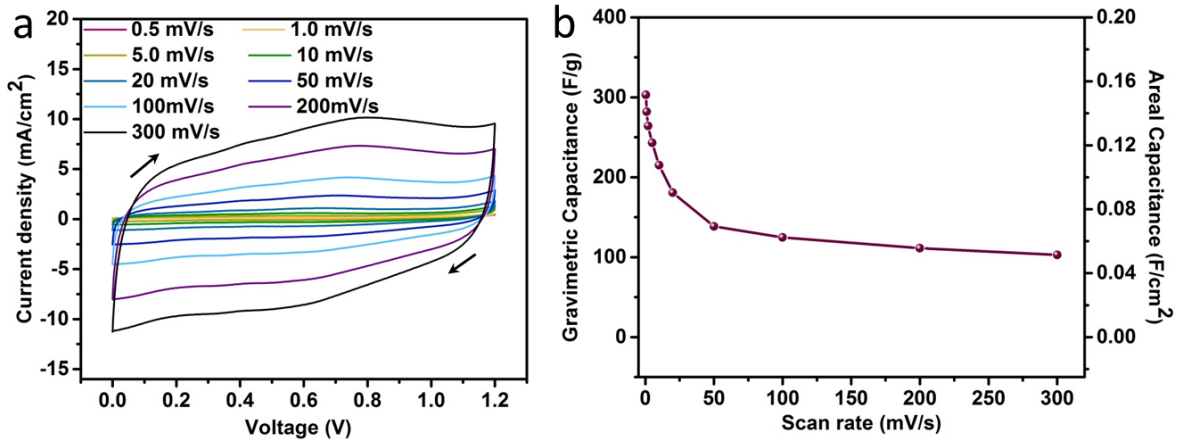

Figure 3.3.2.2 (a) CV profiles of the two-electrode system at different scan rates of 0.5-300 mV/s, (b) plot of specific capacitance of the material *vs.* the scan rate.

The specific capacitance is one important parameter that is widely used to determine the performance of supercapacitors. When calculated from CV curves (Figure 3.3.2.2 (b)), the

specific capacitance is a function of scan rate, where the values of specific capacitance decrease with increasing scan rate. This is due to the insufficient ion diffusion within a constant time that may take place at a high scan rate.[170, 184-185] The calculated value can reach 215 F/g (0.11 F/cm^2 in areal capacitance) at the scan rate of 10 mV/s in 1 M Li_2SO_4 electrolyte solution. The high specific capacitance is attributed to the hollow nanoplate structure of the hollow carbon-MoS_2-carbon nanoplates, which provides an easy intercalation mechanism of the electrolyte in/between the Van der Waals bonded MoS_2 layers. The presence of the carbon coating should prevent the agglomeration of the MoS_2 sheets and improve the conductivity.

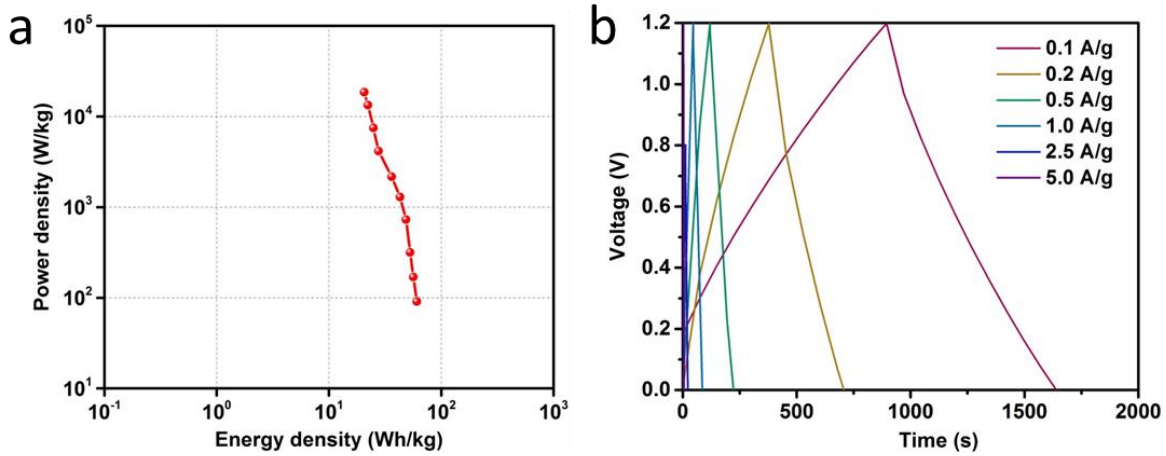

Figure 3.3.2.3 (a) Ragone plot of energy density *vs.* power density of the hollow carbon-MoS_2-carbon nanoplates, (b) galvanostatic charge/discharge curves of the symmetric supercapacitor at different current densities.

Table 3.3.2.2 Specific capacitance values of the carbon-MoS_2-carbon material in a symmetric supercapacitor at different current densities. All values are calculated from the galvanostatic charge/discharge curves.

Current density (A/g)	Specific capacitance
0.1	248 F/g (0.12 F/cm^2)
0.2	219 F/g (0.11 F/cm^2)
0.5	191 F/g (0.10 F/cm^2)
1.0	178 F/g (0.09 F/cm^2)

The energy density and power density of the system are then calculated from the CV curves. The maximum energy density and power density of the material in the symmetric supercapacitor are calculated to be 78 Wh/kg and 3806 W/kg, respectively. To further estimate the potential application of the material as electrode material for supercapacitors, galvanostatic charge/discharge measurements in symmetric two-electrode configurations have been carried

out. As shown in Figure 3.3.2.3 (b), the obtained curves display the characteristic triangle shape corresponding to the capacitive behaviour, and there is no obvious ohmic potential (IR) drop (the voltage drop due to the energy losses) during discharging. Accordingly, the specific capacitance values have been calculated and the relationships between the specific capacitance and current densities are illustrated in Table 3.3.2.2. It is noted that the maximum specific capacitance of the hollow carbon-MoS_2-carbon nanoplates can reach 248 F/g (0.12 F/cm^2) at 0.1 A/g. When the current density increases from 0.1 A/g to 1.0 A/g, the specific capacitance value decreases from 248 F/g (0.12 F/cm^2) to 178 F/g (0.09 F/cm^2), showing excellent high power capability of the material.

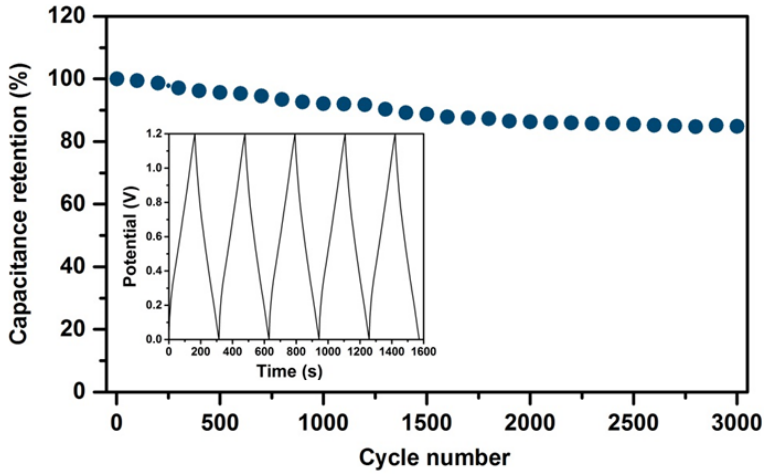

Figure 3.3.2.4 The cyclic performance of the symmetric two-electrode supercapacitor. (Inset is the charge/discharge profile of the last five cycles)

The long-term cycling test at current density of 1 A/g was tested to further investigate the cycling stability of the hollow carbon-MoS_2-carbon nanoplates. As shown in Figure 3.3.2.4, after 3000 charge/discharge cycles, the specific capacitance can keep 85% of the initial value, which is a little bit lower than that of hollow carbon nanoplates[67]. The inferior stability performance of the hollow carbon-MoS_2-carbon nanoplates can be attributed to the dissolution in the electrolyte of a small part of MoS_2 material, which can be triggered by dissolved oxygen and local pH variations that occur at both electrode and electrolyte interfaces during cycling.[186]

Table 3.3.2.3 lists the electrochemical performance of various nanostructured MoS_2 materials and related carbon materials in aqueous electrolytes from the literature. Significantly, the specific capacitance of the hollow carbon-MoS_2-carbon nanoplates is higher than that of pure hollow carbon nanoplates[67], MoS_2 nanospheres[170] and sponge MoS_2[187] and is comparable to the 2D layered MoS_2-rGO hybrids[170]. When the mass loading of the electrode increases from 0.5

mg/cm^2 to 1 mg/cm^2, the specific capacitance can still remain 163 F/g, which may benefit from the following facts. First, the highly conductive carbon layers on both sides of MoS_2 act as substrate with superb high ways for fast electron transportation and electrolyte ion diffusion towards MoS_2, which greatly increase the specific capacitance of the supercapacitor. Second, the hollow nanoplate structure not only contributes many active sites for energy storage, but serve as a reservoir to shorten the ionic diffusion distance to the interior surface, significantly contributing to the enhanced energy storage capacitance and long-term electrochemical stability.

Table 3.3.2.3 Summary of the present and reported data of MoS_2 or carbon related materials for symmetric supercapacitors. The capacitance values are presented per mass of active material, along with the mass loadings of the electrodes.

Sample	Binder	Electrolyte	Mass loading	Capacitance	Ref.
2D layered MoS_2-rGO hybrids	Nafion	1.0 M Na_2SO_4	2 mg/cm^2	190 F/g (1 A/g)	170
MoS_2 hollow spheres	Nafion	1.0 M Na_2SO_4	2 mg/cm^2	97.5 F/g (1 A/g)	170
MoS_2 sponge material	PVDF	0.5 M H_2SO_4	5 mg/cm^2	90.1 F/g (1 A/g)	187
2D exfoliated MoS_2/CNT hybrid ink	Binder free	PVA-H_2SO_4	1 mg/cm^2	18 F/g (1 A/g)	188
Hollow carbon nanoplates	PIL	1.0 M Li_2SO_4	1 mg/cm^2	84 F/g (1 A/g)	67
	PVDF			77 F/g (1 A/g)	
Hollow carbon-MoS_2-carbon nanoplates	PVDF	1.0 M Li_2SO_4	0.5 mg/cm^2	178 F/g (1 A/g)	This work
			1 mg/cm^2	163 F/g (1 A/g)	

In conclusion, the as-synthesized hollow carbon-MoS_2-carbon nanoplates have been used as electrode materials in symmetric supercapacitors with 1 M Li_2SO_4 as electrolytes. The results show that the prepared supercapacitor delivers a high specific capacitance and excellent electrochemical stability over 3000 cycles. This emphasizes the fact that such a hybrid nanostructure can benefit from the high electronic conductivity of the carbon and the high intrinsic electrochemical performance of MoS_2. Its well-defined hollow sandwich structure, hexagonal shape and colloidal stability make it promising for energy storage, especially in aqueous systems.

4 Solid electrolyte interphase in "water-in-salt" supercapacitors

As discussed in chapter 3, supercapacitors have attracted considerable interest due to their high power density, fast charge/discharge processes and long cycle life.[189-190] However, the major issue of poor energy density limits their further applications.[9, 191-192] According to the theoretical calculation formula $E = 0.5\ CV^2$,[9, 193-194] the important parameters for high energy density of a supercapacitor are the voltage window and the specific capacitance. Therefore, raising the voltage window should be an effective way to improve the energy density. As reported, electrochemical voltage window of supercapacitors is defined by the properties of the electrolyte solution, *i.e.*, solvent viscosity and bulk electrolyte resistivity, concentration.[128, 189, 195] Classical organic electrolytes for supercapacitors permit to design devices with a cell voltage more than 3 V, but they are flammable, thermally unstable and incurring high cost. Instead, aqueous electrolytes can solve these concerns, but the hydrogen evolution at the electrode surface presents the most severe challenge. In order to solve the problem, a highly concentrated electrolyte, 21 m (m: mol/kg) LiTFSI "water-in-salt" (WIS) electrolyte, has been recently reported[196-203] and been used in supercapacitors. For example, Hasegawa *et al.*[204] reported WIS based symmetric supercapacitor using porous carbon monoliths as the electrode, which allows charging up to 2.4 V without significant capacitance decay for 10000 cycles. The outstanding performance of WIS supercapacitors can be attributed to several reasons. On one hand, the water activity is reduced as a result of the super-concentrated salt solution as well as an inner Helmholtz layer in supercapacitors, which helps to inhibit water splitting reaction.[14, 25, 32, 202, 205-206] On the other hand, the formation of a passivation layer is proposed to be generated from reductive decomposition of electrolyte ions, which further reduces the kinetics of the hydrogen evolution reaction in WIS supercapacitors in a similar manner as a solid electrolyte interphase (SEI) in non-aqueous electrolyte does.[25]

In energy storage systems, solid electrolyte interphase (SEI) forms when an extreme potential is applied to maximize the energy output, which is far beyond the thermodynamic stability limits of electrolyte components.[207-208] This independent passivation phase on electrode surfaces transports electrolyte ions at the interface between the electrode and electrolyte but also prevents overvoltage.[124, 209] In recent years, much attention has been paid on the study of SEI in supercapacitors. For example, Choi *et al.*[210] confirmed the formation of a SEI layer in hybrid supercapacitors after the charge/discharge by using $LiPF_6$ in Acetonitrile as the electrolyte. The results indicated that the SEI was composed of $Li_4Ti_5O_{12}$ and LiF. On the

contrary, for supercapacitors with aqueous electrolytes such as 1 M Li_2SO_4 or KOH, SEI can not be spontaneously formed because none of the decomposition products from water can precipitate in solid state on electrode surfaces and form a protective interphase.[207] Instead, in WIS supercapacitors, high concentration of the electrolyte suppresses the activity of water molecules, which is proposed to enable the formation of a passivation layer from reductive decomposition of the electrolyte anions. However, the inadequate observation of this interphase layer in WIS supercapacitors requires much more intensive research efforts.

In addition, the dependence of the performance of supercapacitors on the effective temperature range is of substantial practical significance in specific applications. Over the past few years, the temperature-relative studies on supercapacitors mainly focus on the dilute aqueous electrolytes, such as 0.5 M Na_2SO_4, 1 M KOH or Li_2SO_4. For instance, Li *et al.*[211] have investigated the effect of temperature on the properties of supercapacitors based on the MnO_2 nanobelt electrode and 0.5 M Na_2SO_4 electrolyte. The specific capacitance has been observed to increase with increasing temperature. Despite these efforts, there is no report on the temperature-dependent studies on the electrochemical performance, such as resistance, specific capacitance and cycling stability, of supercapacitors based on WIS electrolytes.

In this chapter, various electrochemical techniques such as cyclic voltammetry (CV), electrochemical impedance spectroscopy (EIS) and constant current charge/discharge (CCCD) have been used to study the formation of a SEI layer by first in WIS supercapacitors and to investigate the effects of temperature on their overall capacitive performance. As reported,[67] hexagonal mesoporous nitrogen-doped hollow carbon nanoplates (HCPs) with a high specific surface area and accessible mesopores were introduced in aqueous supercapacitors based on 1 M Li_2SO_4 electrolyte and achieved a high double layer capacitance and good cycling stability. In this work, HCPs have been applied as the electrode material both in WIS and “salt-in-water” supercapacitors. Meanwhile, detailed fitting of impedance data with modified circuit shows that a SEI formation occurs during the initial charging process in WIS supercapacitors and keeps relatively stable afterwards, which is further evidenced by the X-ray photoelectron spectroscopy (XPS) measurement. Subsequently, the effect of temperature on the specific capacitance, cycling stability and the formation of SEI layer in WIS supercapacitors have been investigated. The fundamental understanding of SEI layer formation and electrochemical behavior at different temperatures for WIS supercapacitors provide insights towards the development of new generation supercapacitors.

4.1 Morphology of the hollow carbon nanoplates

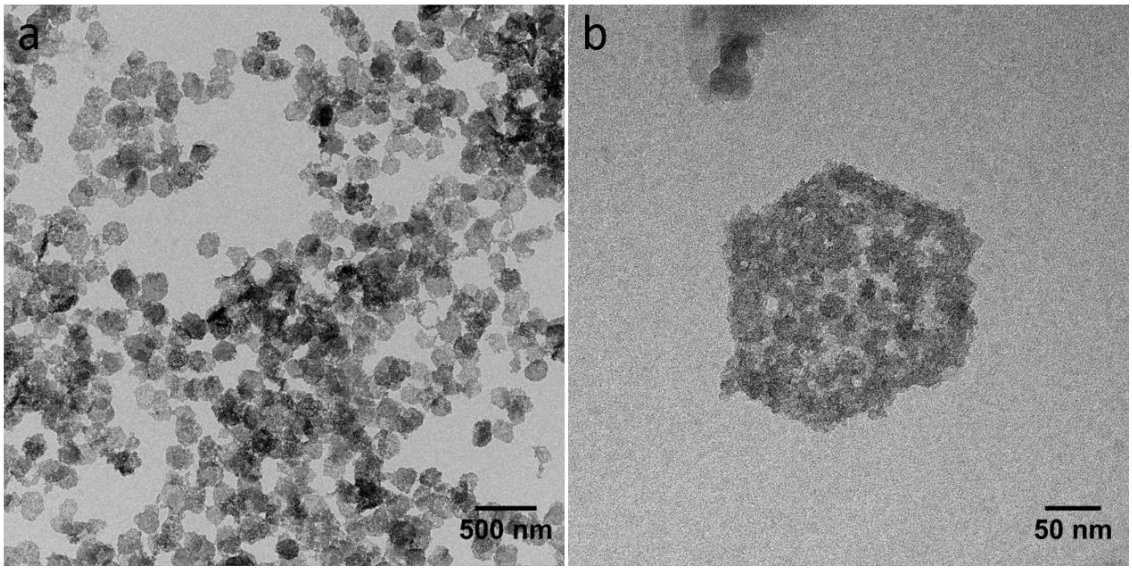

Figure 4.1.1 TEM image of the as-synthesized hollow carbon nanoplates (HCPs).

In this chapter, HCPs have been chosen as the electrode material for WIS and "salt-in-water" supercapacitors, which have high specific surface area of 460 m^2/g and fairly accessible mesopores (~3.8 nm).[67] They were synthesized using PDA as carbon precursor and hexagonal-shaped gibbsite as template through a silica nanocasting method. As mentioned in chapter 3, carbon nanostructures normally conglutinate during the high-temperature annealing and silica nanocasting technique is an effective technique to solve this problem. TEM images in Figure 4.1.1 show that the obtained hollow carbon nanoplates maintain the structural integrity and the hexagonal morphology as the template, with the size of approximately 200 nm. Moreover, no other amorphous clustered materials are observed.

4.2 Electrochemical performance of "water-in-salt" and "salt-in-water" supercapacitors

In order to compare the electrochemical performance of WIS (21 m LiTFSI) and "salt-in-water" (1 m LiTFSI) supercapacitors, several electroanalytical techniques have been performed. Firstly, the stability window of WIS supercapacitors based on HCPs is investigated by CV measurements at the scan rate of 50 mV/s. The reduction/oxidation profiles reveal a voltage window up to 1.8 V for WIS supercapacitors, above which profiles related to the hydrogen evolution are observed. Compared to the conventional "salt-in-water" supercapacitors, the WIS system shows an expanded voltage window, as shown in Figure 4.2.1 (b). This is due to the suppressed water-splitting issue in the WIS electrolytes. It can be explained by the interionic interactive nature of ion-rich WIS interface, leading to the agglomeration/diffusion of ions

through several surface layers, which is in good agreement with other concentrated electrolytes like ionic liquids.[13,19] To obtain the capacitance values of both systems, CCCD measurements have been conducted at different current densities of 0.5, 1.0, 2.5, 4.0, and 5.0 A/g in WIS and "salt-in-water" supercapacitors. As shown in Table 4.2.1, the gravimetric and volumetric capacitance of supercapacitors based on 21 m LiTFSI electrolyte is higher than that based on 1 m LiTFSI, no matter obtained from the CV curves or charge/discharge profiles. In order to avoid side effects during initial cycles, the charge/discharge profiles are recorded after 20 cycles' activation of supercapacitors. After calculation, the gravimetric capacitance of WIS supercapacitors can achieve 86.6 F/g at 0.5 A/g, while that of the"salt-in-water" supercapacitor is only 72 F/g.

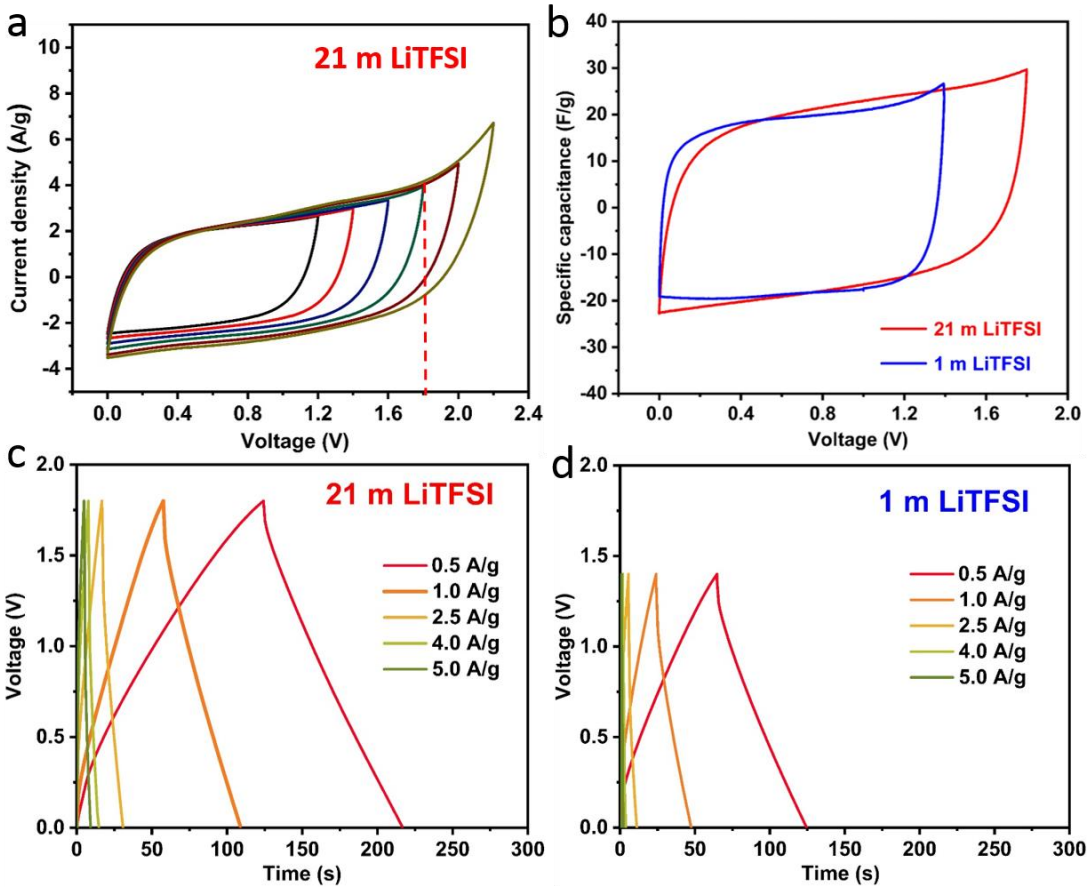

Figure 4.2.1 (a) CV curves at 50 mV/s with different potential windows of the supercapacitor using HCPs electrode and 21 m LiTFSI electrolyte, (b-d) comparison of supercapacitors using 1 m LiTFSI and 21 m LiTFSI electrolytes, (b) specific capacitance *vs.* voltage calculated from CV curves at 20 mV/s, (c, d) charge/discharge profiles after 20 cycles' activation of the supercapacitors.

Table 4.2.1 Specific capacitances of supercapacitors based on 21 m LiTFSI and 1 m LiTFSI electrolytes calculated from CV curves and charge/discharge curves, respectively. The volumetric capacitance is calculated based on the packing density of the active material.

	21 m LiTFSI ("water-in-salt")		1 m LiTFSI ("salt-in-water")
Voltage window (V)	1.8	1.4	1.4
Gravimetric capacitance calculated from CV (F/g) (20 mV/s)	90.44	71.58	71.12
Gravimetric capacitance calculated from charge/discharge (F/g) (0.5 A/g, 21st cycle)	86.6	70.36	72
Volumetric capacitance calculated from charge/discharge (F/cm^3) (0.5 A/g, 21st cycle)	133.4	108.35	110.88

In addition, the cyclic stability of WIS and "salt-in-water" supercapacitors have also been measured, as shown in Figure 4.2.2 (b). the WIS cell achieves excellent cycling stability at 1.0 A/g, delivering a stable gravimetric capacitance retention (92% of the 21st cycle) after 2000 cycles, similar to that of the "salt-in-water" cell (93.2% of the 21st cycle). It is clear that the iR drop of 21 m LiTFSI systems is higher than that of 1 m LiTFSI ones, indicating the higher internal resistance of the WIS supercapacitors. Interestingly, in WIS supercapacitors, the galvanostatic voltage profiles during the initial charge show the non-linear shape with extra capacitance beyond the conventional non-faradaic storage. However, the discharge curve is relatively linear, and the capacitance obtained during discharge is less than the charge capacitance, resulting in a limited Coulombic efficiency (63%). This clearly indicates that, next to the capacitive charge storage process, non-capacitive and irreversible process(es) occurs during the initial charge process of the WIS supercapacitors, which can probably be the SEI layer formation. Up to now, there are various reports that have predicted the formation of SEI layer in WIS based energy storage systems. For example, Suo *et al.*[25] demonstrated that in WIS electrolytes (21 m LiTFSI), there were two $TFSI^-$ anions on average in each Li^+ primary solvation sheath, and such a high concentration of $TFSI^-$ led to a SEI layer dominated by the reduction of $TFSI^-$. The SEI layer is rather stable without continuous growth, as indicated from the surge of the Coulombic efficiency in the next cycle (90%) and further improvement in the following cycles.

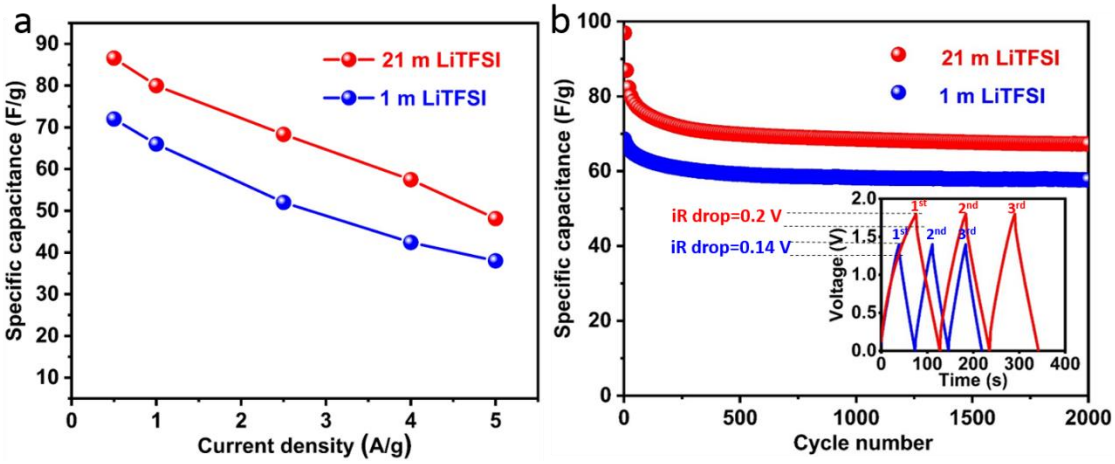

Figure 4.2.2 (a) The energy density *vs.* current density calculated from the charge/discharge profiles, (b) cycling ability at 1 A/g of supercapacitors using 1 m LiTFSI and 21 m LiTFSI electrolytes (inset is the charge/discharge profiles of the first three cycles).

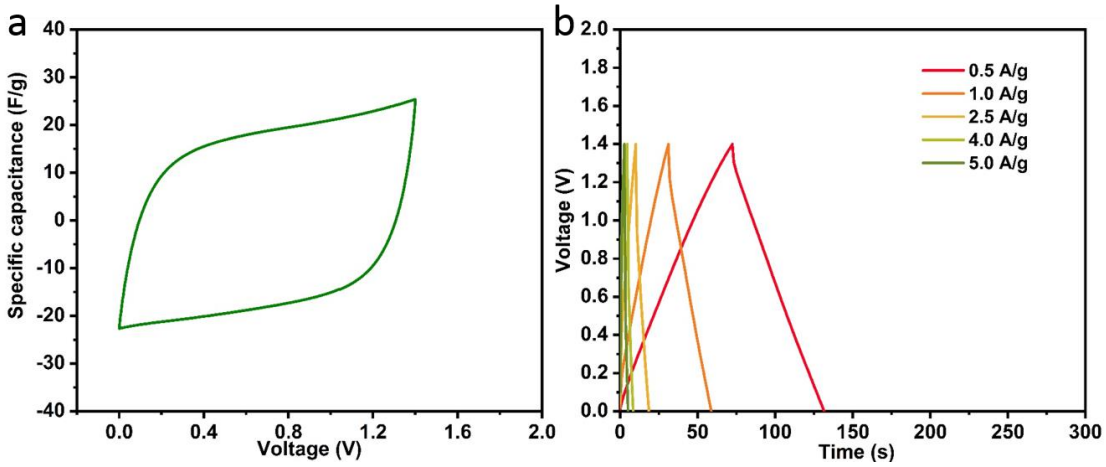

Figure 4.2.3 (a) CV curves at 20 mV/s and (b) charge/discharge profiles with the voltage range of 0-1.4 V of supercapacitors based on 21 m LiTFSI electrolyte.

To further investigate the influence of voltage window on the irreversible processes mentioned above, the voltage window is then set to 1.4 V to perform electrochemical measurements for WIS supercapacitors. It is worth to note that upon charging to 1.4 V (Figure 4.2.3), the WIS supercapacitor shows almost linear charge/discharge voltage curves, characteristic of the EDLC behavior of the HCPs electrodes. In addition, the specific capacitances calculated here, including gravimetric and volumetric capacitances, are much lower than the values from 1.8 V measurements. This clearly indicates that the SEI formation does not take place below the voltage of 1.4 V.

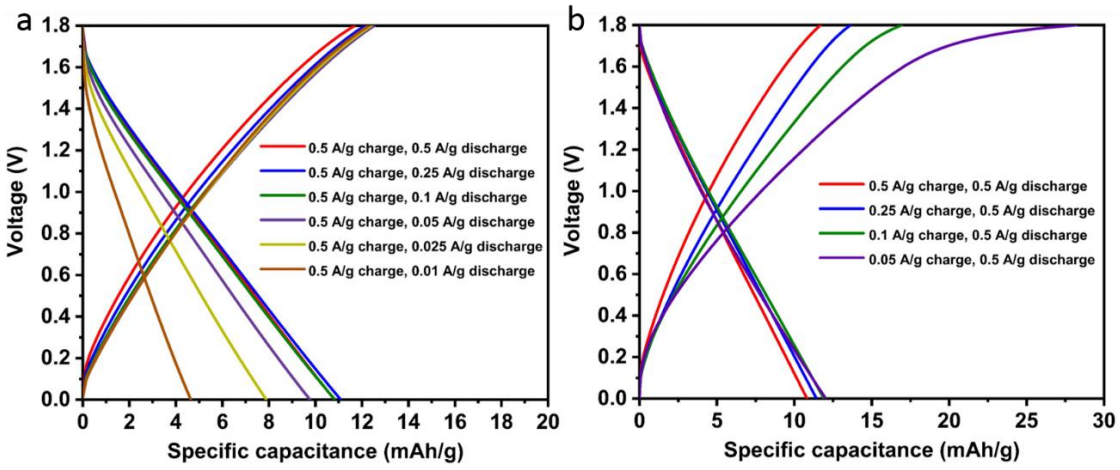

Figure 4.2.4 Charge/discharge profiles (a) at the same charging and different discharging current densities, (b) the same discharging and different charging current densities of supercapacitors based on 21 m LiTFSI electrolyte (both measurements were conducted after 20 cycles' activation).

Considering that the overpotential can also influence the output capacitance of supercapacitors, the current densities of charge/discharge have been changed for different conditions. When charging at the same current density but discharging at different ones, shown in Figure 4.2.4 (a), the gravimetric capacitance (calculated to mAh/g) decreases along the decrease of the current density. This is due to the fact that at a lower discharging current density (≤ 0.05 A/g), the overpotential for hydrogen evolution reaction tends to be lower.[212] For a specified voltage range, the hydrogen evolution becomes more significant with the decrease of the current density, resulting in a faster voltage collapse and lower gravimetric capacitance. When discharging at the same current density, while charging at different ones (Figure 4.2.4 (b)), the charging gravimetric capacitance increases along the decrease of the current density while the discharging gravimetric capacitance keeps nearly unchanged. During the charging process, the growth of SEI layer takes place, which is irreversible and indicated by the asymmetric shape of the charge/discharge curve. The lower current density leads to the lower overpotential, thus resulting in the higher charging gravimetric capacitance.

4.3 Study of the solid electrolyte interphase

4.3.1 X-ray photoelectron spectroscopy and scanning electron microscopy-energy dispersive X-ray spectroscopy elemental mapping

As discussed before, a SEI layer is proposed to grow in the initial cycles of WIS supercapacitors from the CCCD results, which consists of the products from the reduction of $TFSI^-$. The formation of a stable SEI layer is considered as being highly protective of the active material when a WIS electrolyte is used.[206, 213] XPS measurements have been further used to provide a

more comprehensive chemical analysis and confirm the existence of SEI on the surface of electrodes in WIS supercapacitors. To avoid the disturbance from PTFE binder or conductive additives, the samples were prepared by pressing pellets of pure HCPs. As shown in Figure 4.3.1.1, the XPS spectra of the pristine HCPs has been measured for comparison, where C 1s and N 1s serve as a reference, and F^- detected comes from the residual NH_4HF_2 used to remove silica.

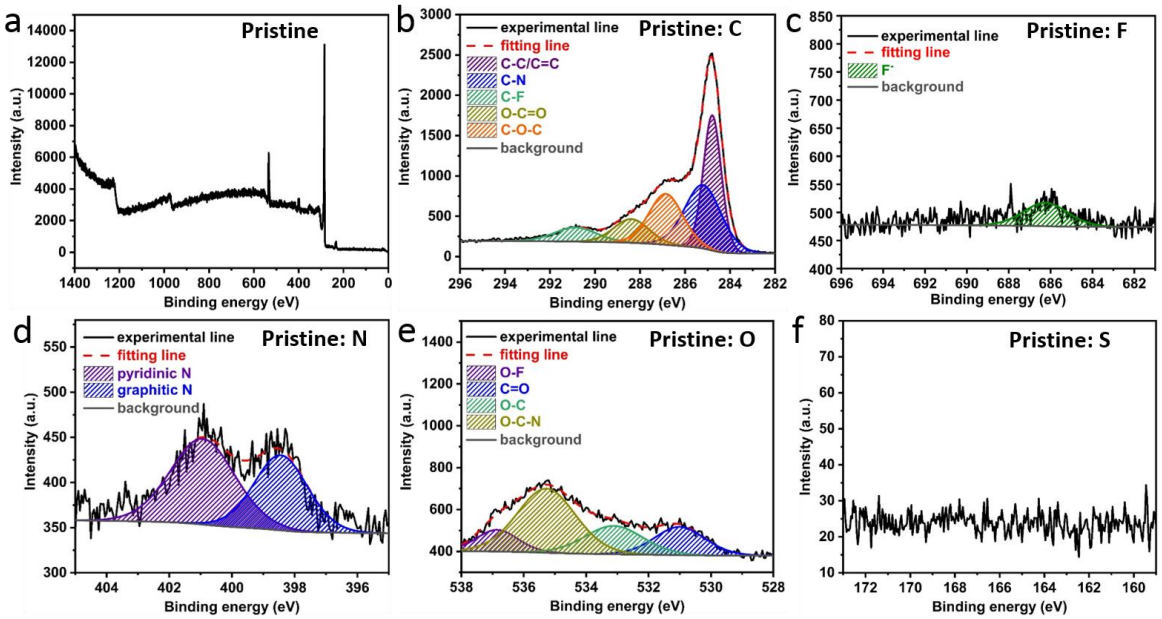

Figure 4.3.1.1 XPS conducted on pristine HCPs, (a) survey XPS spectrum, (b) C 1s spectra, (c) F 1s spectra and (d) N 1s spectra. (e) O 1s spectra and (f) S 1s spectra.

To detect the formation of SEI layer, the sample has been cycled in WIS supercapacitors at a current density of 0.5 A/g for 50 cycles. The symmetric WIS supercapacitor is cycled for 50 cycles at the fixed current density of 0.5 A/g. Then the electrodes are extracted from the cells, washed with ethanol for 2 times and dried under vacuum prior to the measurements. Here the negative electrode, which refers to the electrode on which the adsorption of Li^+ ions takes place when charging, is measured (Figure 4.3.1.2). The most conspicuous change after cycles is the decrease of C-C/C=C signals, companied with the increase of C-O-C signals on the cycled electrode, which are originated from the reduction of LiTFSI. The decrease of pyridinic N signal in the negative electrode also confirms this condition due to the fact that pyridinic N is easier to promote the reduction of $TFSI^-$ than graphitic N.[214] The presence of F detected in the cycled electrode comes from two different sources. The first is the residual lithium salt or its partially fragmented form, as evidenced by the C-F species. The other is from $TFSI^-$ reduction to form an SEI structure occurring at the electrode surface, such as simple inorganic salts LiF, which agrees well with earlier reports.[25] In addition, the appearance of S in the cycled electrode is also

from the $TFSI^-$ ions in electrolyte. From this on, post-mortem XPS analysis confirms the existence of an SEI layer on the surface of the negative electrode in WIS supercapacitors.

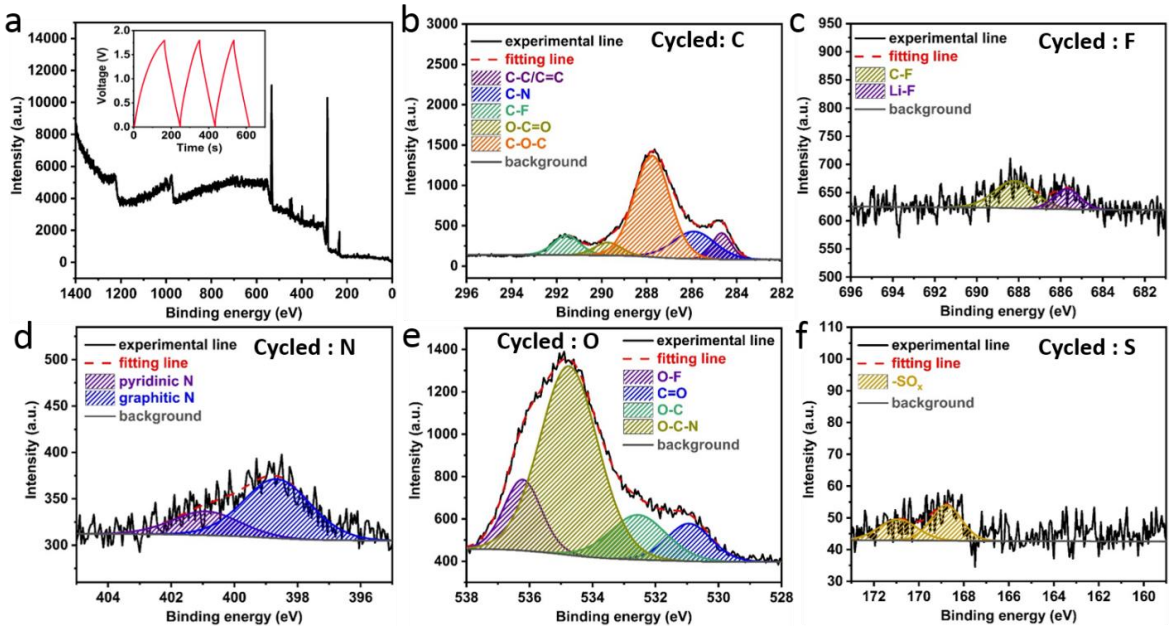

Figure 4.3.1.2 XPS conducted on the cycled HCPs after 50 cycles at 0.5 A/g, (a) survey XPS spectrum (inset is the charge/discharge profiles of the first three cycles), (b) C 1s spectra, (c) F 1s spectra and (d) N 1s spectra. (e) O 1s spectra and (f) S 1s spectra.

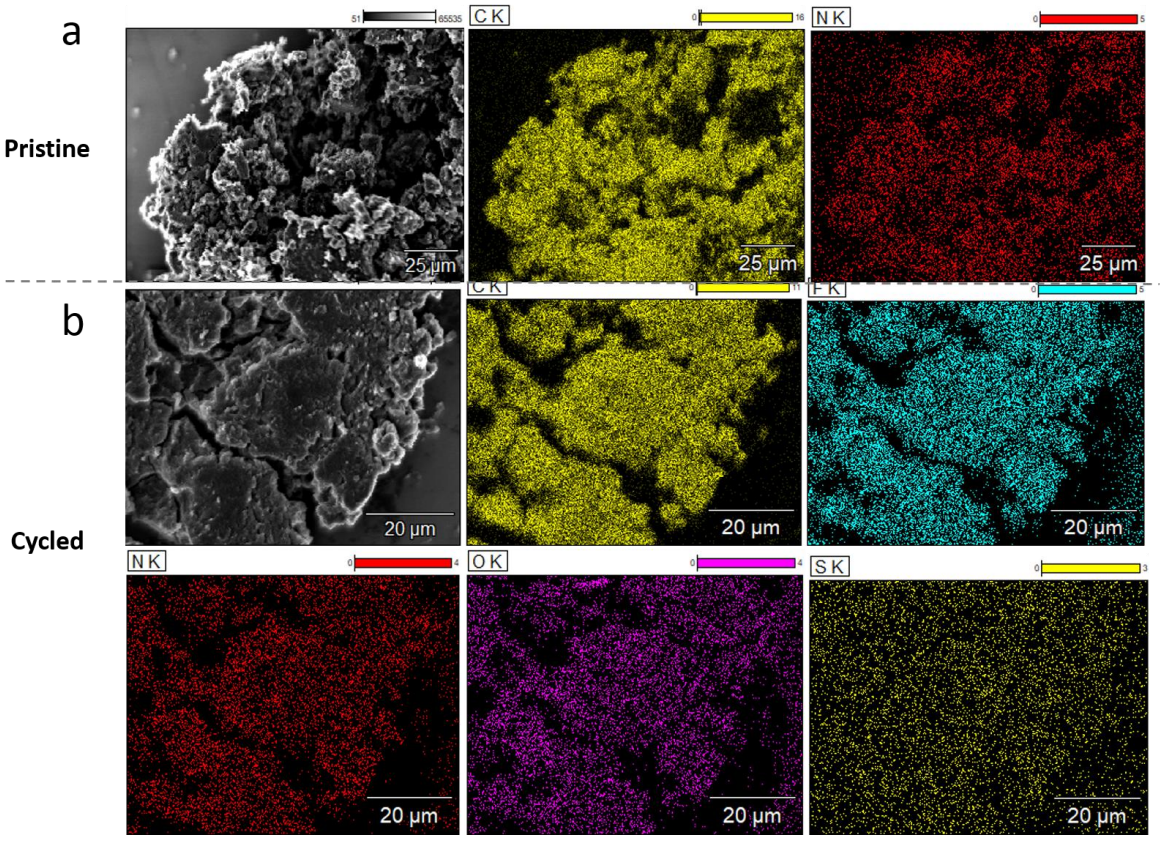

Figure 4.3.1.3 SEM-EDS mappings conducted on (a) pristine HCPs, (b) cycled HCPs after 50 cycles at 0.5 A/g.

The scanning electron microscopy-energy dispersive X-ray spectroscopy elemental mapping (SEM-EDS) (Figure 4.3.1.3) is used to further identify the formation of SEI on HCPs. Besides C, N elements same as the pristine material, additional F, O, S elements appear in the cycled electrodes, which are originated from the reduction of $TFSI^-$ in the electrolyte. The SEM-EDS mappings confirm the existence of SEI layer on the surface of the negative electrode in WIS supercapacitors.

4.3.2 Electrochemical impedance spectroscopy measurement

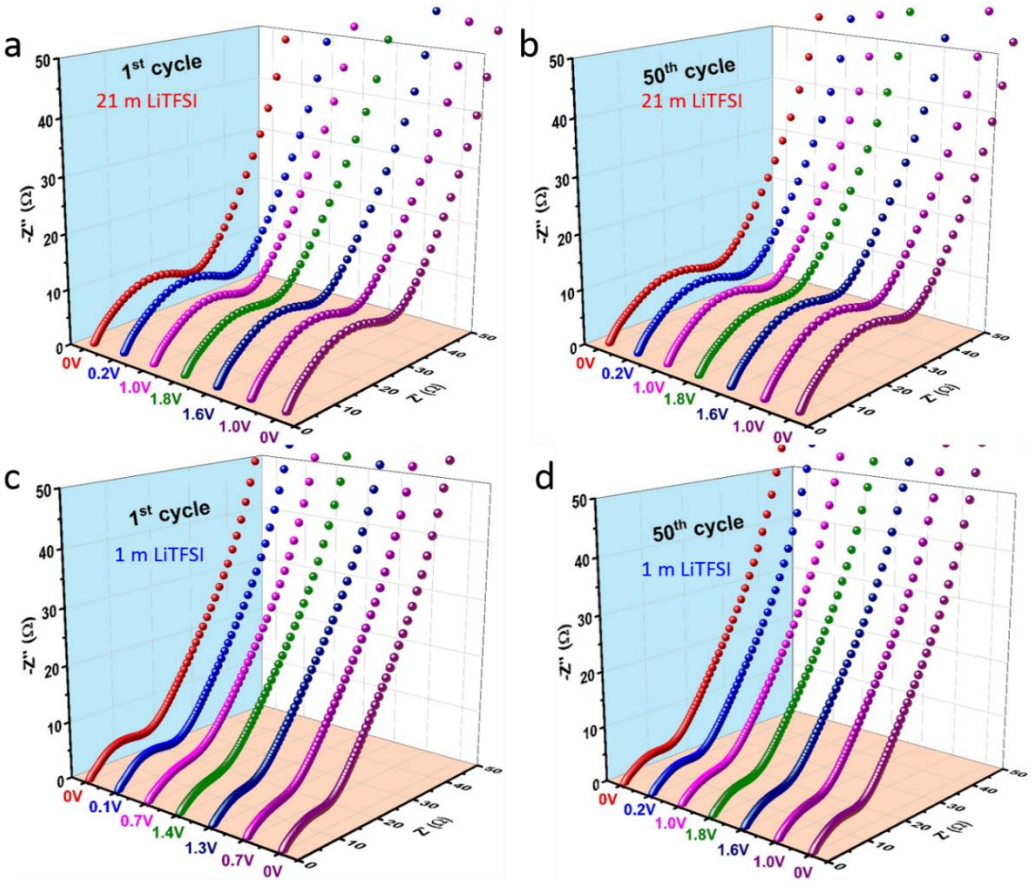

Figure 4.3.2.1 Nyquist plots at different voltages during the 1st and 50th CV scans of supercapacitors using (a, b) 21 m LiTFSI electrolytes and (c, d) 1 m LiTFSI electrolytes.

To deep study the formation of SEI layer on the HCPs electrode materials in WIS supercapacitors based on HCPs electrode materials, an *in-situ* EIS analysis was further conducted during the anodic/cathodic scans of the CV measurement at 20 mV/s. EIS presents the signal as a function of frequency at constant potential, which provides useful information about interfacial processes of supercapacitors.[215] The Nyquist plots at different cell potentials of both systems, namely, 0, 0.2, 1.0, and 1.8 V (anodic scan) and 1.6, 1.0, and 0 V (cathodic

scan) in the 1st and 50th cycles are presented in Figure 4.3.2.1. All Nyquist plots show a semicircle in the high-frequency region, along with a straight line in the low-frequency region. To study insight the change of impedance along cycling, several equivalent circuits have been tried to fit the data.

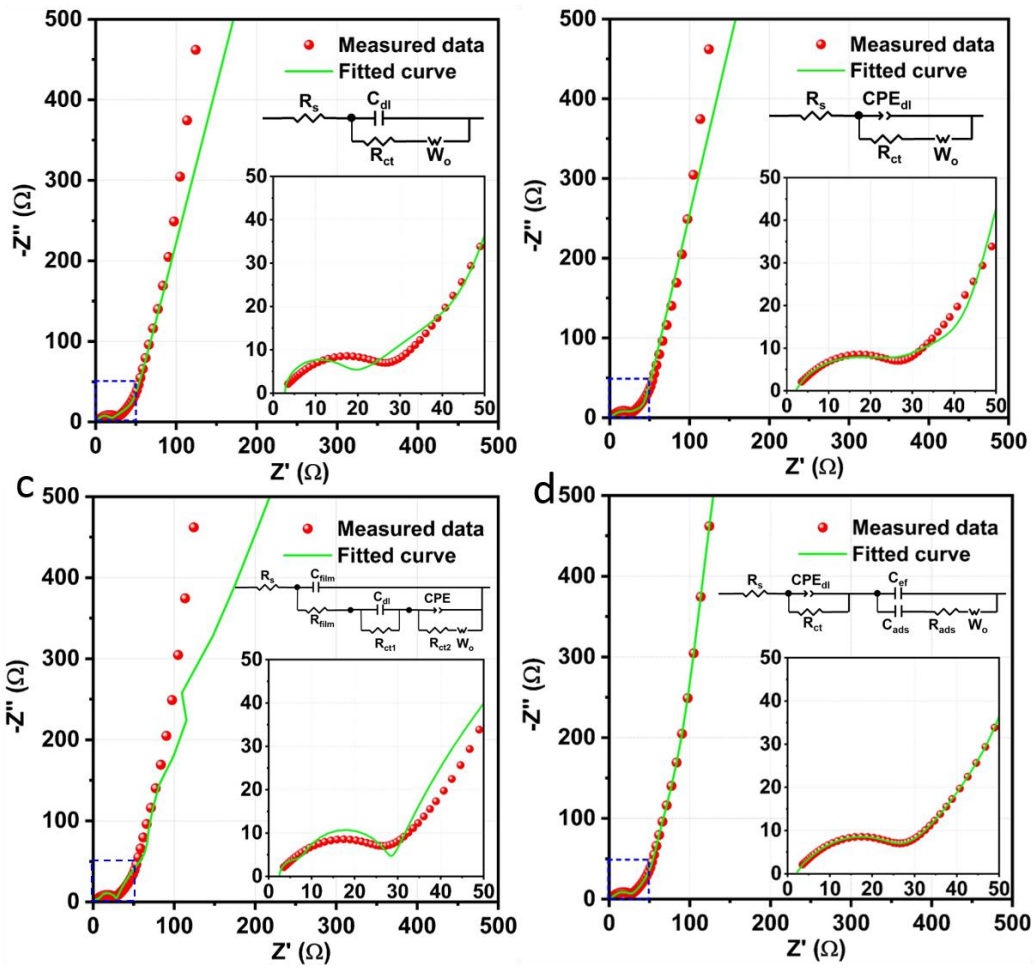

Figure 4.3.2.2 Nyquist plots and corresponding fitted curves at open circuit potential of supercapacitors using 21 m LiTFSI electrolytes (Inset is the enlarged part of the high frequency region and the equivalent circuit).

The fitting process starts with a simple Randle's circuit[216] consisting a set of resistors and capacitors in series and parallel (Figure 4.3.2.2 (a)). In this circuit, the first intersection point on the real axis in the high-frequency region provides the value of internal series resistance and is represented as R_s. The semicircle in the high-frequency region to mid-frequency is modeled by an interfacial charge transfer resistance R_{ct} and the double layer capacitance C_{dl}. After the semicircle, a long tail in the low-frequency region appears, pertaining to the diffusion of ions into the bulk of the electrode, represented by the Warburg element W_o.[215] Then the double layer capacitance is replaced by the constant phase element CPE_{dl}, which takes into account the low-frequency adsorption processes at/into the microporous electrode surface (Figure 4.3.2.2 (b)).

Considering the formation of SEI layer in WIS supercapacitors, a more general approximation is tried, in which the external interfacial impedance as well as a resistive film formation with C_{film} and R_{film} are added (Figure 4.3.2.2 (c)). In addition, the charge transfer resistance is divided into the internal and external parts with R_{ct1} and R_{ct2} to further study the internal and external charge transfer processes.[217] However, the fitting results with the above equivalent circuits are undesirable with high chi-squared function values (Table 4.3.2.1-4.3.2.3).

Table 4.3.2.1 Fitting data of the Nyquist plots at open circuit potential of the 21 m LiTFSI supercapacitor using the equivalent circuit in Figure 4.3.2.2 (a). (Goodness of the fit $\chi^2 = 0.03$, Sum of square = 4.97)

Element	Value	Error	Error%
R_s (Ω)	2.78	0.074	2.68
C_{dl} (F)	1.2E-5	5.5E-7	4.5
R_{ct} (Ω)	13.51	0.58	4.31
W-R (Ω)	81.75	9.12	11.15
W-T	1.02	0.01	17.09
W-P	0.42	5.47	4.52

Table 4.3.2.2 Fitting data of the Nyquist plots at open circuit potential of the 21 m LiTFSI supercapacitor using the equivalent circuit in Figure 4.3.2.2 (b). (Goodness of the fit $\chi^2 = 0.003$, Sum of square = 0.41)

Element	Value	Error	Error%
R_s (Ω)	2.12	0.03	1.48
CPE-T (F)	2.66E-4	2.2E-5	8.27
CPE-P (F)	0.67	0.0086	1.28
R_{ct} (Ω)	23.2	0.56	2.43
W-R (Ω)	51.97	2.8	5.4
W-T	0.58	0.04	7.37
W-P	0.67	0.0086	1.28

Table 4.3.2.3 Fitting data of the Nyquist plots at open circuit potential of the 21 m LiTFSI supercapacitor using the equivalent circuit in Figure 4.3.2.2 (c). (Goodness of the fit χ^2 = 0.019, Sum of square = 2.57)

Element	Value	Error	Error%
R_s (Ω)	2.5	0.056	2.23
C_{film} (F)	7.87E-6	3.91E-9	4.96
R_{film} (Ω)	7.37	0.38	5.18
C_{dl} (F)	4.55E-5	3.43E-6	7.55
R_{ct1} (Ω)	17.89	0.65	3.62
CPE-T (F)	0.01	2.54E-4	2.57
CPE-P (F)	0.77	0.01	1.31
R_{ct2} (Ω)	286.9	67.15	23.41
W-R (Ω)	17290	7393.1	42.75
W-T	4.55	0.21	4.51
W-P	2.91	0.09	3.1

Based on it, a modified equivalent circuit[218-219] has been used to fit the measured data and to provide a description of the electrochemical reaction, in which the interfacial components are taken into account (Figure 4.3.2.2 (d)). As shown in the case of the open circuit potential EIS spectra, the fitting results match well with the experimental plot as the chi-square function for fitting is $\chi^2 \approx 3E\text{-}4$ and $\Delta^2 \approx 0.05$. According to the modified equivalent circuit, the electrochemical resistance of the supercapacitors includes the following aspects: (i) ionic charge transfers through the electrolyte as well as protective separator, followed by penetration into the electrode surface (R_s); (ii) the impedance of infinite thin layer including: charge transfer resistance through the passivation layer (SEI) on particle interface (R_{ct}), along with double-layer capacitance (C_{dl}); (iii) the adsorption resistance (R_{ads}) depending on charges and associated with specific adsorption of charged species in the adsorption layer, accompanied with the "true" interfacial capacitance (without adsorption effects) (C_{ef}), adsorption capacitance (C_{ads}) and Warburg element (*W-R*).[218-219]

Table 4.3.2.4 Fitting data of the Nyquist plots at 0 V during the 1st cycle of the 21 m LiTFSI supercapacitor using the equivalent circuit in Figure 4.3.2.2 (d). (Goodness of the fit χ^2 = 3E-4, Sum of square = 0.05)

Element	Value	Error	Error%
R_s (Ω)	2.33	0.015	0.77
CPE-T (F)	4.4E-4	3.03E-5	6.87
CPE-P	0.63	0.0066	1.06
R_{ct} (Ω)	11.77	0.35	2.95
C_{ef} (F)	5.9E-5	2.2E-6	3.83
C_{ads} (F)	0.02	2.2E-4	1.03
R_{ads} (Ω)	5.54	0.1	1.81
W-R (Ω)	20.87	0.12	0.55
W-T	0.15	0.005	3.42
W-P	0.23	0.0041	1.81

Table 4.3.2.5 Fitting data of the Nyquist plots at 0 V during the 50th cycle of the 21 m LiTFSI supercapacitor using the equivalent circuit in Figure 4.3.2.2 (d). (Goodness of the fit χ^2 = 2.8E-4, Sum of square = 0.039)

Element	Value	Error	Error%
R_s (Ω)	2.33	0.011	0.46
CPE-T (F)	5.3E-4	1.04E-5	2.0
CPE-P	0.62	0.0022	0.36
R_{ct} (Ω)	34.09	0.21	0.62
C_{ef} (F)	0.0053	1.5E-4	2.86
C_{ads} (F)	0.032	8.3E-4	2.58
R_{ads} (Ω)	22.55	1.1	4.86
W-R (Ω)	10.18	0.15	1.43
W-T	0.07	0.0017	2.38
W-P	0.31	0.0035	1.14

Table 4.3.2.6 Fitting data of the Nyquist plots at 0 V during the 1st cycle of the 1 m LiTFSI supercapacitor using the equivalent circuit in Figure 4.3.2.2 (d). (Goodness of the fit χ^2 = 3.2E-4, Sum of square = 0.099)

Element	Value	Error	Error%
R_s (Ω)	0.83	0.003	0.37
CPE-T (F)	1.7E-4	1.19E-5	6.78
CPE-P	0.75	0.006	0.79
R_{ct} (Ω)	2.71	0.078	2.84
C_{ef} (F)	5.1E-5	1.2E-6	2.29
C_{ads} (F)	0.027	2.4E-4	0.9
R_{ads} (Ω)	3.8	0.11	2.97
W-R (Ω)	20.07	1.01	5.01
W-T	0.12	0.0014	1.18
W-P	0.25	0.0023	0.94

Table 4.3.2.7 Fitting data of the Nyquist plots at 0 V during the 50th cycle of the 1 m LiTFSI supercapacitor using the equivalent circuit in Figure 4.3.2.2 (d). (Goodness of the fit χ^2 = 5.4E-4, Sum of square = 0.17)

Element	Value	Error	Error%
R_s (Ω)	0.83	0.0043	0.5
CPE-T (F)	3.3E-4	2.9E-5	8.79
CPE-P	0.69	0.0075	1.1
R_{ct} (Ω)	3.25	0.15	4.66
C_{ef} (F)	7.24E-5	3.96E-6	5.47
C_{ads} (F)	0.04	5.48E-4	1.35
R_{ads} (Ω)	1.48	0.11	7.4
W-R (Ω)	19.3	1.14	5.93
W-T	0.19	0.0026	1.37
W-P	0.25	0.0032	1.28

The Nyquist plots of WIS and "salt-in-water" supercapacitors before and after 50 cycles are then fitted with the modified equivalent circuit discussed above (Figure 4.3.2.3). All the measured data can be fitted with the equivalent circuit well. The fitting results are listed in Table 4.3.2.4-4.3.2.7 and Figure 4.3.2.3. As compared, the WIS supercapacitors show higher series resistance R_s and charge transfer resistance R_{ct} than the "salt-in-water" systems, indicated by the larger intersection point and radius of the semicircle in Nyquist plots of WIS supercapacitors. In addition, there is obvious change after 50 cycles in Nyquist plots of WIS cells, revealing the side reactions beyond double layer capacitive behavior there, while the "salt-in-water" systems show good stability even after 50 cycles. Importantly, there is no shift in the transition frequency (24.93 and 62.92 Hz for 21 and 1 m LiTFSI, respectively) of semicircle in high–medium-frequency region to the low-frequency region of EIS profiles.

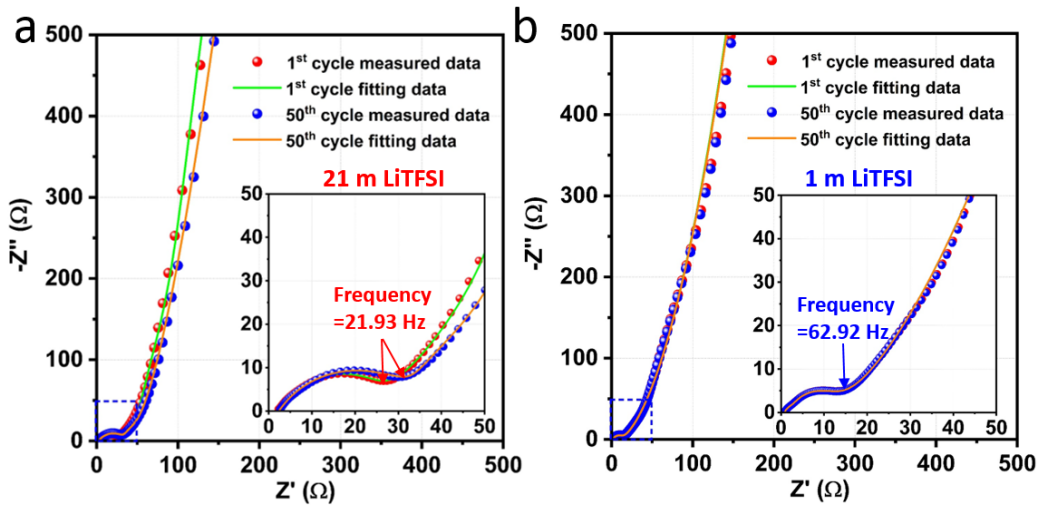

Figure 4.3.2.3 Nyquist plots at 0 V during CV scans of the 1st and 50th cycles of the supercapacitors using 21 m LiTFSI electrolyte and 1 m LiTFSI electrolytes, respectively (insets are the enlarged part of the high frequency region).

To obtain all the fitting parameters along cycling, the fitting of the impedance expression obtained from the modified equivalent circuit to the experimental Nyquist plots of both systems is further performed using EIS data fitting program Zview. Figure 4.3.2.4 indicates the variations of the components R_s, R_{ct}, R_{ads}, C_{ef} and *W-R* during charge/discharge using 21 m LiTFSI. The R_{ct}, R_{ads} and C_{ef} in the 21 m LiTFSI system increase gradually during the charging process in the first cycle, which can be attributed to the formation of SEI. The interfacial capacitance C_{ef} obtained from moderate and low frequencies presents close to the interfacial condition of the electrode. The increased value during initial charging reveals more accessible sites for charges due to the formation of SEI layer. Moreover, *W-R* describes the resistance of

diffusion-like processes in the low-frequency region. It is observed that the initial values of *W-R* in both systems are comparable due to the existence of surface water in both systems. As shown in Figure 4.3.2.4 (f), in WIS electrolytes, about 94% of water molecules are coordinated with Li-ions, and most of the water will follow the lithium electrosorption isotherm.[25, 220] At a high concentration (21 m LiTFSI), the reduced water activity leads to the suppressed water splitting reaction and an interphasial chemistry dominated by the reduction of $TFSI^-$.[221] Based on it, the surface water is limited in it. As a result, the surface polarization and diffusion of ions onto the surface are much easier, leading to the decrease of *W-R* values during charging. In addition, all values remain relatively unchanged in the following discharge process as well as in the 50th charge/discharge, revealing that the SEI formation occurs during the initial charging process and keeps relatively stable afterwards, which is consistent with the results of the cycling performance as discussed above.

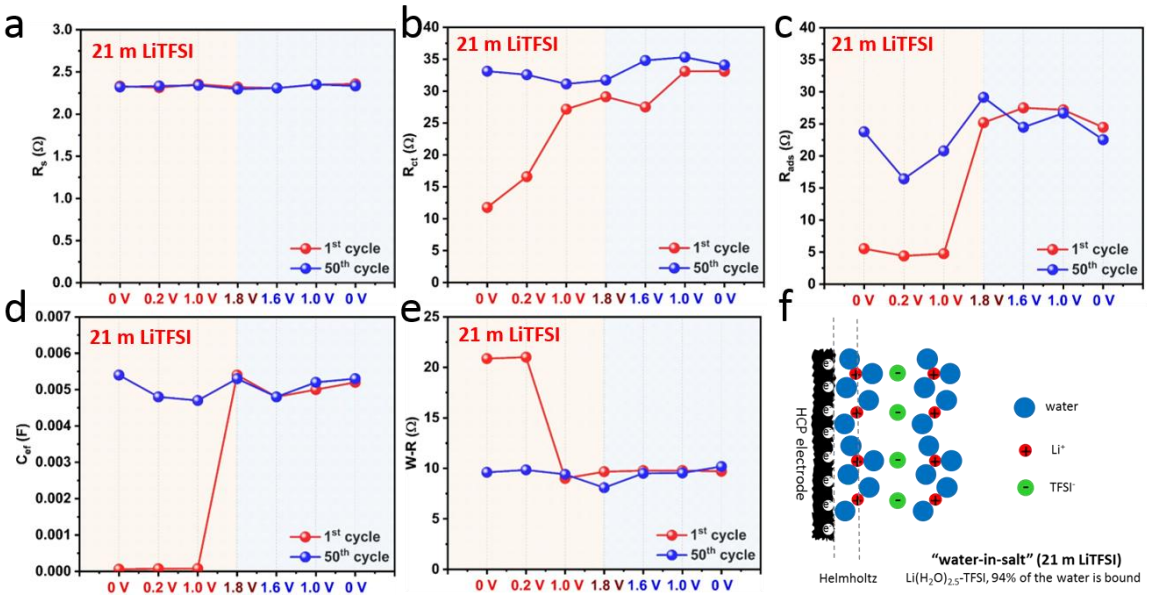

Figure 4.3.2.4 Fitting values with the modified equivalent circuit of (a) R_s, (b) R_{ct}, (c) R_{ads}, (d) C_{ef}, (e) *W-R* from EIS data during CV scans of the 1st and 50th cycles of the WIS supercapacitors and (f) schematic illustration of the HCPs electrode–electrolyte interface WIS supercapacitors (the solvation of $TFSI^-$ is ignored here).

The variations of the components R_s, R_{ct}, R_{ads}, C_{ef} and *W-R* during charge/discharge in "salt-in-water" supercapacitors have also been represented for a comparison, as shown in Figure 4.3.2.5. Overall, in the 1 m LiTFSI systems, the resistances show relatively low values and good stability along cycles. The lower resistance R_s than that in the 21 m LiTFSI system can be explained by the better ion mobility in the "salt-in-water" system. For the "salt-in-water" electrolytes, the charge in the electrolyte is assumed to be drifted by an electric field closer to the electrode/electrolyte interface, which produces a depletion region. In such electrolytes, Li^+

remains hydrated in its primary solvation sheath with sufficient free water available, which will lead to preferential reduction of water. The condition prevents any reduction of $TFSI^-$, thus inhibits the formation of SEI layer. As a result, the surface water is much more difficult to be removed clearly during the initial cycling, resulting in the nearly unchanged values of *W-R*. In addition, C_{ef} in the 1 m LiTFSI systems keep much lower and relatively stable values, indicating the unchanged interfacial phenomenon of the electrodes.

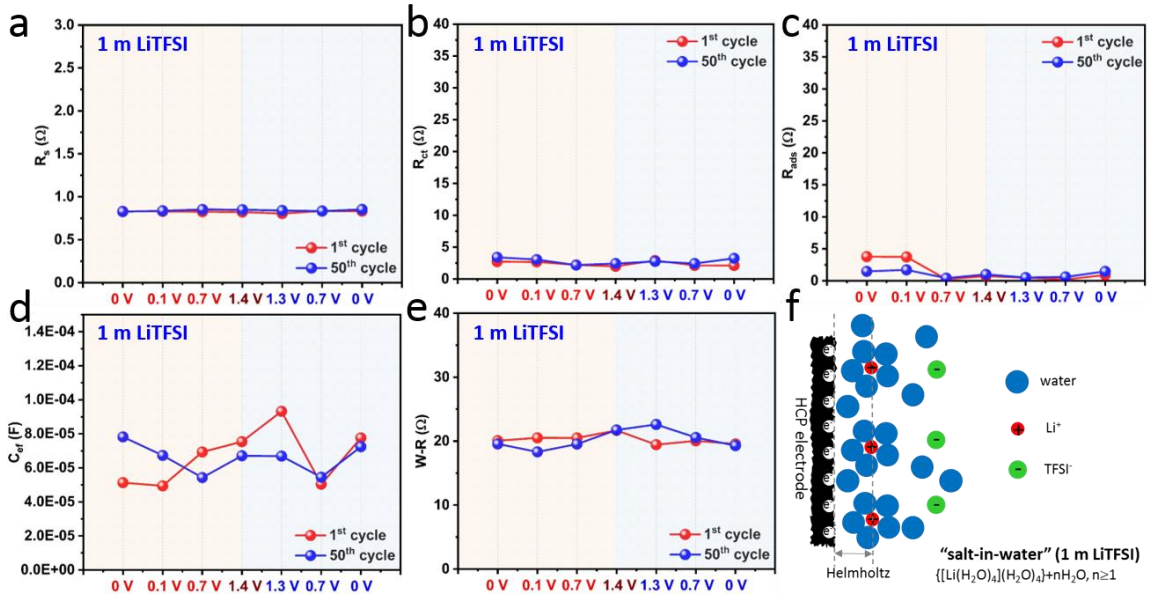

Figure 4.3.2.5 Fitting values with the modified equivalent circuit of (a) R_s, (b) R_{ct}, (c) R_{ads}, (d) C_{ef}, (e) *W-R* from EIS data during CV scans of the 1st and 50th cycles of the "salt-in-water" supercapacitors and (f) schematic illustration of the HCPs electrode–electrolyte interface "salt-in-water" supercapacitors (the solvation of $TFSI^-$ is ignored here).

4.4 Temperature-dependent electrochemical study

It is well known that temperature plays an important role in degradation and lifetime estimations of optimizing the performance of supercapacitors with respect to their applications, such as in the automotive industry. Therefore, it is important to study the influence of temperature on the electrochemical performance of supercapacitors. Based on it, an overall electrochemical characterization has been carried out to extensively study the properties of WIS supercapacitors based on HCPs electrode with respect to changes of temperatures from 15 ºC to 55 ºC. Figure 4.4.1 (a) shows the CV curves measured at 50 mV/s between 0 and 1.8 V at various temperatures from 15 ºC to 55 ºC. As the temperature increases, the CV curve shows less deviation from the rectangular shape, indicating its reduced resistance for ionic diffusion. Moreover, the WIS supercapacitor delivers a higher gravimetric capacitance with the increase

of temperature, which could be mainly contributed from the enhancement of ionic mobility and internal conductivity.[222-223] Then CV profiles at 20, 50, 100, 200, and 300 mV/s at 15 ºC and 45 ºC have been further measured to study the temperature dependence of the power and energy densities. At a lower temperature (15 ºC), the CV curve drastically deviates from the rectangular shape with the increase of the scan rate and results in a smaller enclosed area, *i.e.*, lower capacitance, which is caused by the high internal resistance. In comparison, the cell operated at 45 ºC shows less significant deviations from the rectangular shape and improved capacitances, demonstrating the reduction of the internal resistance at an increased temperature. The energy density and power density of the WIS supercapacitors are shown in Figure 4.4.1 (d). At 45 ºC, the WIS supercapacitor achieves the maximum power density of 3936 W/kg at 300 mV/s, while the highest energy density is about 15 Wh/kg at 10 mV/s. In comparison, at 15 ºC the highest power and energy density reaches merely 2005 W/kg and 12 Wh/kg, respectively. It is obvious that at higher temperature, the energy density and power density are increased.

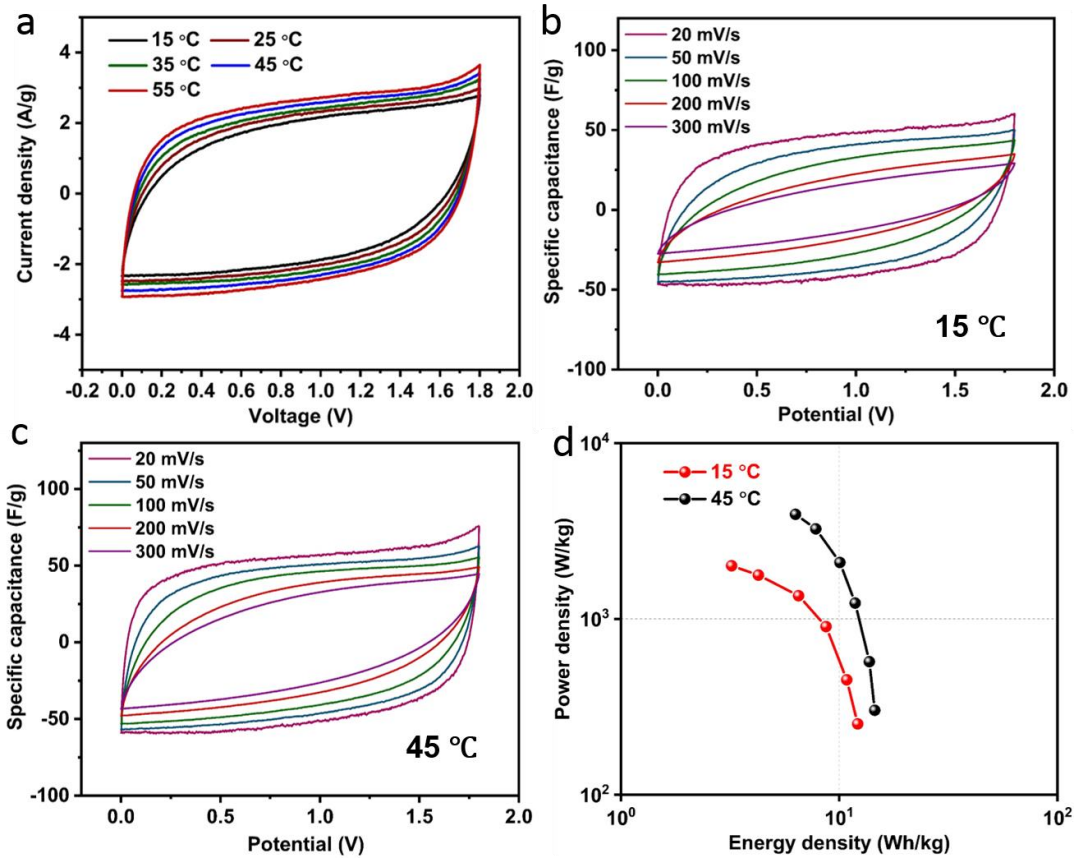

Figure 4.4.1 (a) CV curves measured as a function of temperature at the scan rate of 50 mV/s, (b, c) CV profiles at 15 ºC and 45 ºC with various scan rates from 10 mV/s to 300 mV/s, respectively, (d) Ragone plot of energy density *vs.* power density at 15 ºC and 45 ºC, respectively of supercapacitors using 21 m LiTFSI electrolytes.

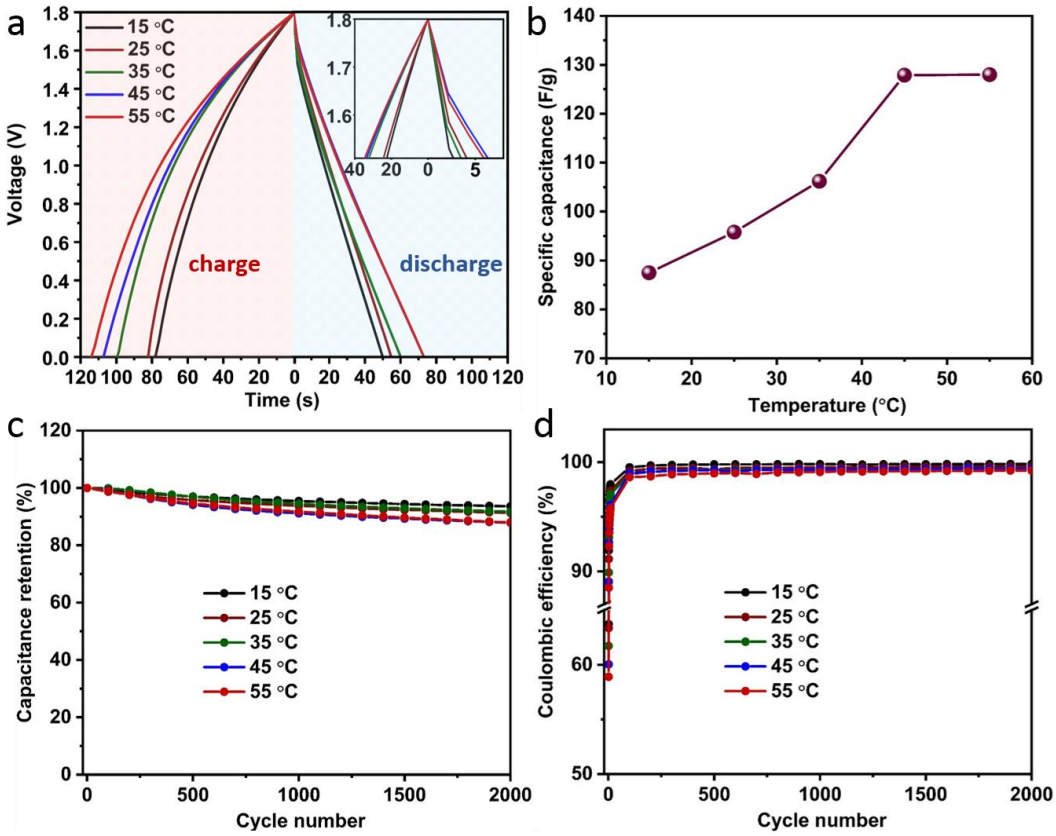

Figure 4.4.2 (a) Galvanostatic charge/discharge profiles at 1 A/g at various temperatures (insert is the enlarged part of the iR drop), (b) specific capacitance *vs.* temperature calculated from the charge/discharge profiles, (c) capacitance retention and (d) Coulombic efficiency along cycling of supercapacitors using 21 m LiTFSI electrolytes at different temperatures.

Table 4.4.1 Calculated results of the capacitance and capacitance retention after 2000 cycles at different temperatures.

Temperature (ºC)	Gravimetric capacitance (F/g)	Volumetric capacitance (F/cm^3)	Capacitance retention after 2000 cycles (%)
15	87.5	134.75	93.6
25	95.8	147.53	91.3
35	106.2	163.55	91
45	127.9	196.97	87.9
55	128	197.12	87.9

Figure 4.4.2 (a) shows the charge-discharge curves of the WIS supercapacitors at various temperatures from 15 ºC to 55 ºC at 1 A/g. A significant reduction of iR drop during discharge

was observed at an elevated temperature, which results from the reduction of the internal resistance at higher temperatures. Furthermore, calculated from galvanostatic charge/discharge data, the gravimetric capacitances at 15, 25, 35, 45, and 55 ºC are 87.5, 95.8, 106.2, 127.9, and 128 F/g, respectively, as shown in Figure 4.4.2 (b). The increased capacitance at higher temperatures may be caused by the improved charge transport properties of the electrode and better kinetics for ion adsorption. Besides, the capacity retentions of the supercapacitors based on WIS electrolytes at different temperatures are plotted in Figure 4.4.2 (c) and the detailed results were listed in Table 4.4.1. The gravimetric capacitance attenuation of 55 ºC cell is 12.1% after 2000 cycles, which is higher than that of the low-temperature cell (*e.g.*, 6.4% at 15 ºC). This may be due to the more severe side reactions at high temperatures. In addition, the Coulombic efficiency is lower at a higher temperature, especially during the initial cycles, revealing that the formation of SEI layer is more active at higher temperatures, as seen in Figure 4.4.2 (d).

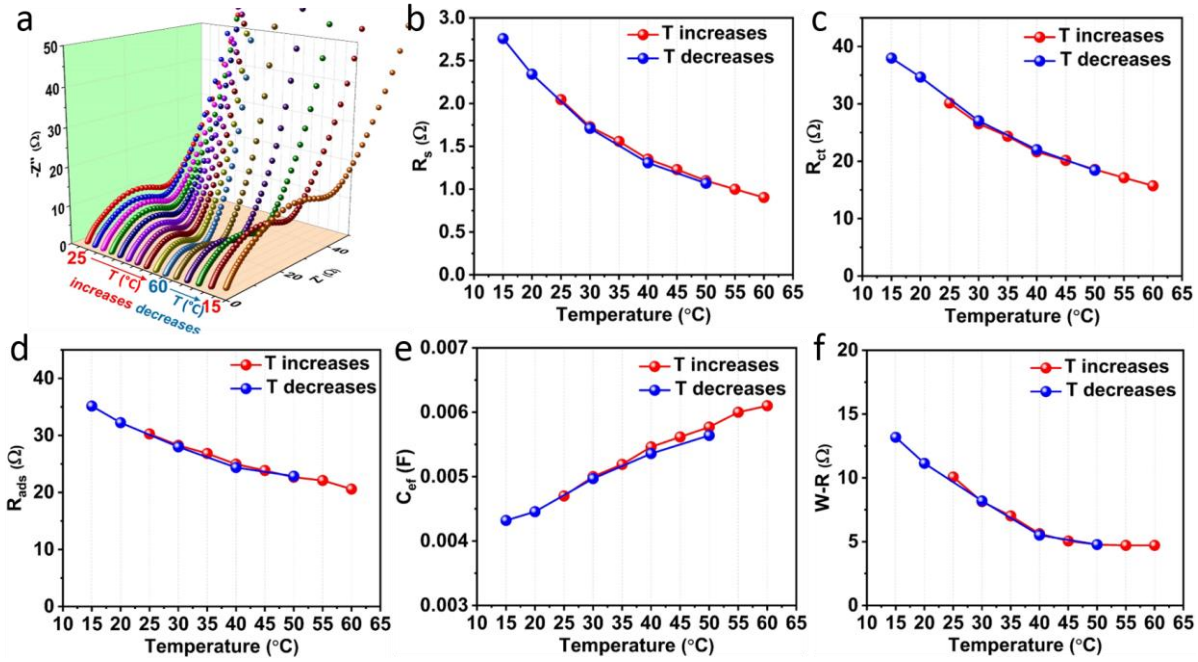

Figure 4.4.3 (a) Nyquist plots at different temperatures of the supercapacitor using 21 m LiTFSI electrolytes, (b-f) fitted results of R_s, R_{ct} R_{ads}, C_{ef}, and *W*-*R*, respectively.

To further gain insight into the temperature dependence of the performance of WIS supercapacitors, the *in-situ* EIS measurements at different temperatures in WIS supercapacitors have also been studied and all the measured data has been fitted by the modified equivalent circuit discussed above. Figure 4.4.3 (a) shows the Nyquist plots during heating from 25 ºC to 60 ºC and followed by cooling to 15 ºC. In the curve at 15 ºC, a semicircle with a large radius in a high–medium-frequency region illustrates a large charge transfer resistance, which

gradually shifts to a lower value (from ~31 Ω at 25 ºC to ~16 Ω at 60 ºC) during heating, and is reversed in the cooling process. The evolution of the parameters, R_s, R_{ct}, R_{ads}, C_{ef} and *W-R* with the change of operating temperature are demonstrated in Figure 4.4.3 (b)-(f). Overall, all the values of resistances significantly decrease and the value of C_{ef} increases along with the increase of temperature during heating from 25 ºC to 60 ºC, and return following the same routine during cooling, showing good thermal reversibility of this system. The R_s, R_{ct}, R_{ads} and *W-R* values at 60 ºC are approximately 33.8%, 40.7%, 59.7% and 35.7% of that at 15 ºC, exploring much better electronics and ionic conductivities in heated medium. As temperature increases, the decrease of R_s resulted from an increase in the conductivity of the electrolyte, which means the conductance of the electrolyte becomes much better with the increase of operating temperature.[224-225] As mentioned above, R_{ct} is composed of charge transfer resistance and SEI layer resistance on the electrode side. The overall R_{ct} decreases with increasing temperature, which is induced by a decrease in charge transfer resistance between electrode and electrolyte.[226-228] R_{ads} represents the adsorption of electrolyte ions onto the surface of electrodes, which also decreases along the increase of operating temperature. This behavior can be alternatively explained by the increase of ionic mobility and faster kinetics for the adsorption of ions.[229-230] In addition, the value of C_{ef} at 60 ºC is about 1.41 times higher than that at 15 ºC. The higher interfacial capacitance confirms the thicker SEI layer at higher temperatures. Note that the change of temperature does not lead to any shift in the transition frequency between high-medium-frequency region and the low-frequency region of EIS profiles, which always occurs at ~24.93 Hz. This phenomenon reveals the excellent thermal stability of the 21 m LiTFSI-based WIS electrolyte.

In conclusion, in this chapter the SEI layer formation and the temperature dependence of the overall capacitive performance in WIS supercapacitors have been investigated using hollow carbon nanoplates as electrodes. Compared to “salt-in-water” supercapacitors, the scarcity of free water molecules contributes to an enhanced voltage window up to 1.8 V and a higher specific capacitance 86.6 F/g at 0.5 A/g in the 21st cycle. More importantly, the formation of solid electrolyte interphase (SEI) layer in WIS supercapacitors is for the first time evidenced by the XPS measurement. In addition, investigated by the EIS technique and fitted by a modified circuit, the formation of the SEI layer during initial cycles has been further *in situ* quantitatively estimated in WIS supercapacitors, which is revealed by the increase of charge transfer resistance (R_{ct}), adsorption resistance(R_{ads}) and interfacial capacitance (C_{ef}). Furthermore, the influence of working temperature on the WIS supercapacitor performance has

been systematically investigated within the temperature range of 15 ºC to 55 ºC. With the increase of temperature, the specific capacitance increases from 87.5 F/g to 128 F/g, while the capacitance retention after 2000 cycles decreases from 93.6% to 87.9%. In addition, the EIS measurements have disclosed the increase of the interfacial capacitance (C_{ef}), indicating more favorable formation reaction of SEI layer at a higher temperature. In this chapter, we not only provide a fundamental study of the SEI layer formation, but also reveal the electrochemical performance of the WIS supercapacitors at different temperatures, which helps the efforts on the electrolyte selection, effective working temperature and the tailor-design of interphases in supercapacitors based on highly concentrated aqueous electrolytes.

5 Hollow MoS_3 nanospheres as electrode material for "water-in-salt" Li-ion batteries

Among the several types of electrochemical energy storage/conversion technologies for portable electronic devices and stationary power plants, rechargeable lithium-ion batteries (LIBs) are the most promising candidates due to their relatively high energy density, power density, long cycle life and high energy efficiency.[231-232] However, their safety issues due to the flammable organic electrolyte and the thermal runway caused by the reactivity of the electrode materials are still challenging to be solved.[4, 16, 233] In addition, the cost of LIBs is relatively high due to the special cell assembly technology and the requirement of a strictly dry environment during manufacturing process.

Aqueous rechargeable LIBs are promising alternatives to resolve the above challenges as the safety issues and rigorous manufacturing conditions can be avoided.[234-235] However, their narrow electrochemical stability window (1.23 V), imposed by hydrogen and oxygen evolution, severely deteriorates the electrode structure and present safety challenges.[19, 236-237] Thus, expanding the electrochemical stability window of aqueous electrolytes becomes a fundamental issue. Based on that, the develop of "water-in-salt" electrolyte (WISE, a kind of super-concentrated aqueous electrolyte) has made a significant breakthrough in doubling electrochemical stability window of aqueous electrolyte from 1.5 to 3 V, enabling more choices of electrode materials.[25] The WISE manages to form a solid-electrolyte-interface (SEI) for the first time in aqueous electrolytes by manipulating the structure of a Li^+-solvation sheath, which enables many Li-ion chemistries that are otherwise impossible.[238] Such a wide voltage window provides unprecedented flexibility in selecting the cathode-anode electrodes, making it possible to apply many electrode materials that are unsuitable in traditional aqueous electrolytes.

As reported, the electrode material is one of the key factors that influence the electrochemical performance of LIBs.[239-240] Transition metal sulfides (TMSs) have been widely applied due to their high specific capacity and structure merits,[159, 241-242] and the graphene-like structure and available oxidation valences of transition metal sulfides can provide space for efficient and reversible ion storage. As the best known TMSs material, MoS_2 has been widely explored for LIBs due to the facile Li ion intercalation in the layered structure.[243] However, the practical applications of MoS_2 in LIBs have been limited because of its poor cycle stability and severe volume change during charge/discharge. In addition, MoS_2 based nanomaterials are usually prepared through a hydrothermal method[244-245], which is costly and energy intensive.

Molybdenum trisulfide (MoS_3), which was introduced as an electrode material in LIBs in 1979,[246] has attracted reviving research interest but has rarely been used as electroactive materials for LIBs. Compared with MoS_2, MoS_3 has more inherent superiors as follows: Firstly, the molecular structure of MoS_3 consists of Mo ions bridged by two ligands, one sulfide and one disulfide, yielding the chemical formula of $Mo^{IV}(S^{2-})(S_2^{2-})$ or MoS_3.[247] The one dimensional chain structure has more open sites toward active Li^+ storage and thus provides a higher specific capacity. Secondly, its amorphous nature has low activation energy barriers toward the structural rearrangement during Li^+ uptake.[76] Thirdly, it has a higher electrical conductivity than MoS_2 (band gap of <1.5 eV for MoS_3 *vs.* 1.8 eV for MoS_2 [53]), which improves the electron transfer efficiency in LIBs as the electrical conductivity is regarded as a fundamental prerequisite to govern a superior electrochemical performance. All the above mentioned advantages make MoS_3 a promising candidate for battery applications. However, the synthesis of MoS_3 usually requires more sophisticates and expensive equipment such as sonochemical synthesis, laser ablation and magnetron sputtering,[51, 248] so it is necessary to exploit a simple and environmental friendly method to synthesize MoS_3. In addition, MoS_3 still remains unexplored in aqueous electrolytes based LIBs, which may be limited by the low potential of Li ion uptake in MoS_3, about 2.0 V *vs.* Li/Li^+,[76] at which HER happens in conventional aqueous electrolytes.

In this chapter, hollow MoS_3 nanospheres in WIS-LIBs will be investigated. Hollow MoS_3 nanospheres are facilely synthesized using spherical polyelectrolyte brushes (SPB) as carriers and templates through an acid precipitation method at room temperatures, as shown in Figure 5.1.1. The SPB templates are then removed by tetrahydrofuran (THF),[249] making the preparation simple and scalable. The obtained hollow MoS_3 nanospheres can work as the anode material in a bistrifluoromethanesulfonimide lithiums (LiTFSI) based WIS-LIB, which has a low potential limit of 1.9 V *vs.* Li/Li^+.[25] As the lithiation potential of MoS_3 is close to the lower potential limit of the WISE, it enables the full utilization of the offered electrochemical stability window of the WISE, and maximizes the working voltage and thus the energy and power density, when paired with an appropriate cathode material (*e.g.*, $LiMn_2O_4$ in this work). This work also studies the reaction mechanisms of MoS_3 in the WIS-LIBs using XRD measurement, providing insights in the direction towards its future improvement as well as the development of TMSs for aqueous LIBs.

5.1 Synthesis of hollow MoS_3 nanospheres

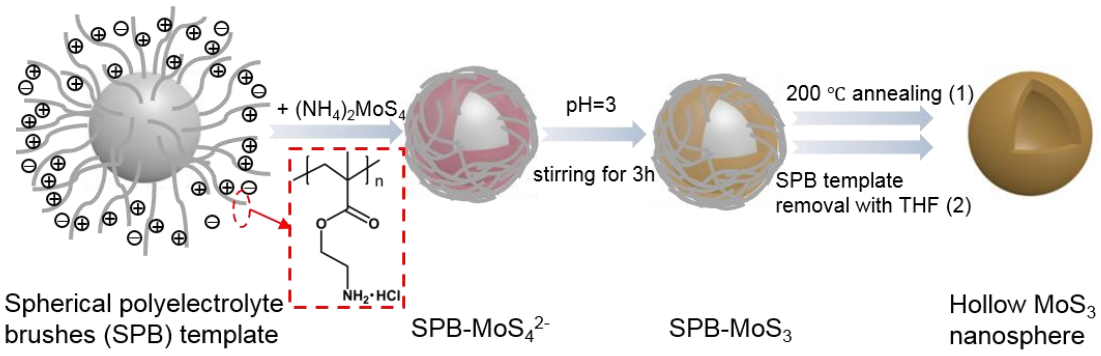

Figure 5.1.1 Synthesis procedure of hollow MoS_3 nanospheres.

Recently, SPB has been successfully used as the carrier system to immobilize different metallic nanoparticles due to the strong localization of their counterions on the surface.[250-251] The SPB nanoparticles consist of a polystyrene core (PS), onto which positively or negatively charged polyelectrolyte brushes are grafted. Inspired by it, the cationic SPB particles with chains of poly(aminoethyl methacrylate hydrochloride) (PAEMH) grafted on PS cores were used as template to synthesize hollow MoS_3 particles. The anionic MoS_4^{2-} are firmly immobilized in the brush layer by electrostatic interactions between the brushes and the ions. In this work, we choose the acid precipitation method to synthesize MoS_3 nanoparticles because it yields fine particles during the reaction. Upon acid being added dropwise, MoS_3 precipitated homogeneously onto the surface of SPB particles following the reaction: $MoS_4^{2-} + 2\ H^+ = MoS_3 \downarrow + H_2S \uparrow$.[247] The Mo^{VI} is reduced to Mo^{IV} and formed into the thermodynamically stable Mo(Ⅳ)-sulfur solid-state compound. Finally, the THF treatment is applied to remove the SPB templates, which results in the hollow nanosphere structure.

The SPB nanospheres used in this work have been prepared in a two-step polymerization. In the first step, the polystyrene core is synthesized through an emulsion polymerization with a thin layer of the photo initiator 2-[p-(2-Hydroxy-2-methylpropiophenone)]-ethyleneglycol methacrylate (HMEM) on the particle surface. The core particles exhibit a hydrodynamic radius of 51.3 nm as measured by DLS after cleaning by ultra-filtration. In the second step, a shell of polyelectrolyte brushes is grown onto the surface of the nanoparticles by photo-emulsion polymerization. From TEM images in Figure 5.1.2 (a) and (b), the SPB nanoparticles show the homogeneous nanosphere morphology. Size distribution measurements confirmed the growth of the polyelectrolyte shell with the thickness of 218 nm.

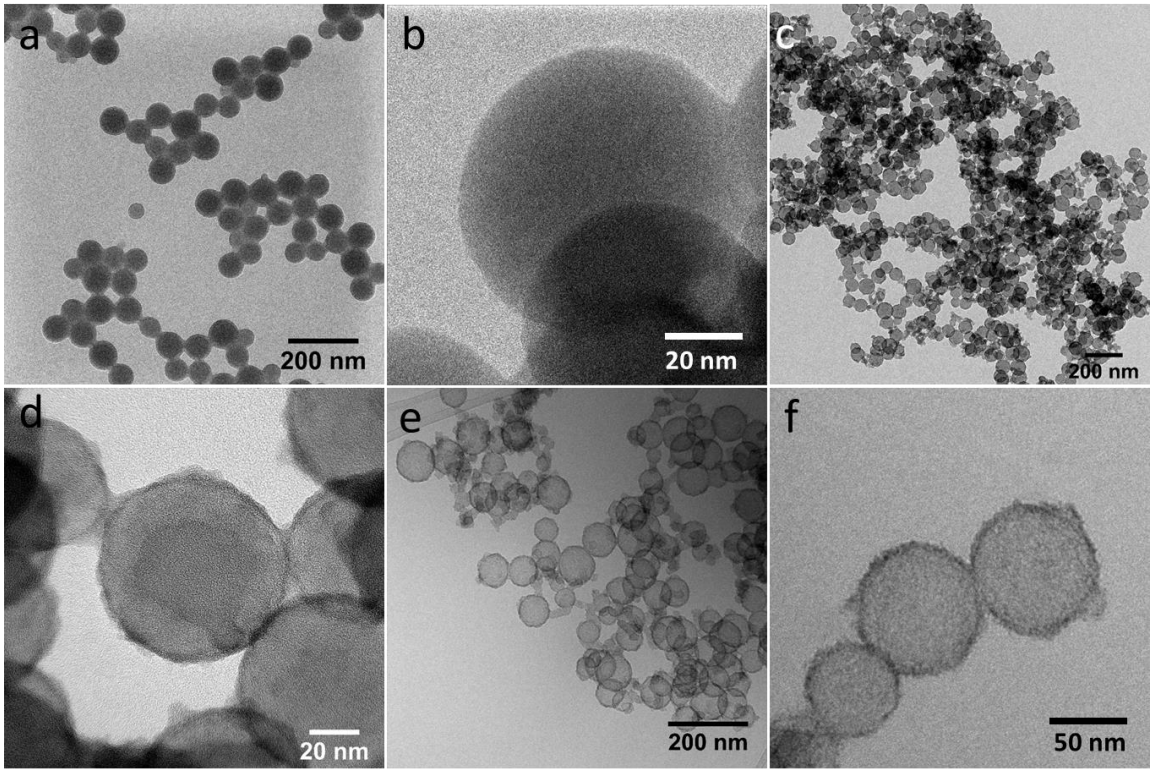

Figure 5.1.2 (a) (b) TEM images of the SPB nanospheres, (c) (d) TEM images of the SPB-MoS_3 nanospheres before annealing, (e) (f) cryo-TEM images of the SPB-MoS_3 before annealing.

The coating of MoS_3 onto the SPB nanospheres is based on the electrostatic interactions between the brushes and the MoS_4^{2-} ions. After the addition of acid, MoS_3 precipitates homogeneously onto the surface of SPB particles following the reaction: $MoS_4^{2-} + 2\ H^+ = MoS_3 \downarrow + H_2S \uparrow$.[247] After cleaning with water for several times, the obtained products can be well dispersed without any aggregation, as shown in Figure 5.1.2 (c). Figure 5.1.2 (d) shows that a thin MoS_3 layer with the thickness around 5 nm has been coated on the surface of SPB nanoparticles and the spherical structures are well maintained. In order to further study the morphology of SPB-MoS_3 nanoparticles *in situ*, cryo-TEM measurements have been carried out by verifying the suspension of the particles. Figure 5.1.2 (e) and (f) show that the MoS_3 nanoparticles are immobilized within the brushes and no free MoS_3 particles are observed, demonstrating that MoS_4^{2-} precursors are successfully immobilized into the SPB templates and no aggregation is observed.

To prepare the hollow nanospheres, SPB templates are removed via the THF treatment, which is a good solvent for PS. The TEM micrographs in Figure 5.1.3 demonstrate that the hollow MoS_3 nanospheres maintained the spherical morphology after the removal of the SPB templates. The hollow structure is evidenced judging from the signification contrast between

the shell and the inner part. Additionally, no free residual materials can be found in the medium, indicating the high effectiveness of the removal of SPB by THF.

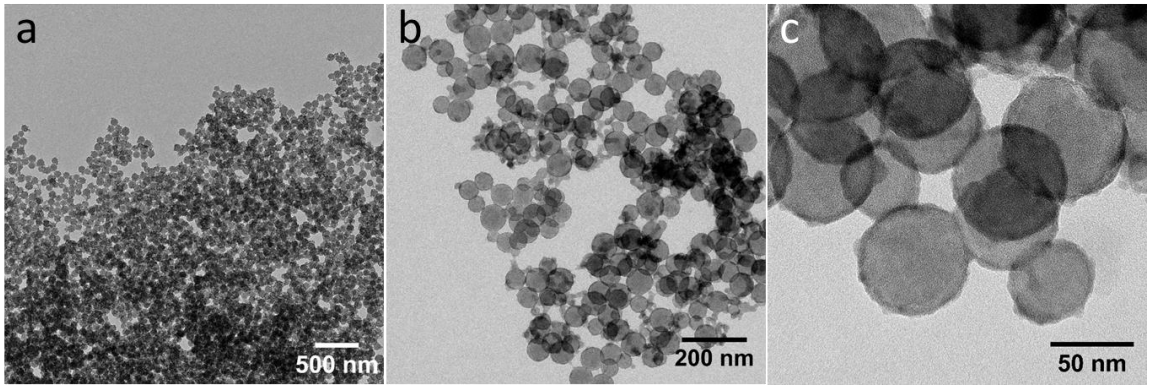

Figure 5.1.3 TEM images of the hollow MoS_3 nanospheres.

5.2 Characterization of the hollow MoS_3 nanospheres

The synthesized hollow MoS_3 nanospheres are firstly examined under SEM and TEM. From the STEM-based high angle annular dark field (HAADF) imaging and the corresponding energy-dispersed X-ray spectroscopy (EDS) elemental mapping, the relative distribution of Mo and S within a particle has been mapped out, as shown in Figure 5.2.1 (a)-(c). Both elements show very high special correlation with each other and are located within the shell of the particle, suggesting the homogeneous chemical composition of MoS_3 as well as its uniform distribution as a shell in the hollow structure. The amorphous nature of the prepared MoS_3 is manifested in the diffusion halo rings in its selected area electron diffraction (SAED) pattern. No obvious lattice fringes can be observed under the HR-TEM. The SEM image in Figure 5.2.1 (f) reveals the homogeneous nanosphere structure of the MoS_3 particles and no aggregation is observed. Moreover, using wavelength dispersive spectroscopy (WDS), it further reveals the correct atom percent ratio of S to Mo in MoS_3. No carbon is observed. As listed, the S/Mo ratio is nearly 3, which also represents its chemical content in the form of MoS_3. All these characterizations confirmed the formation of amorphous MoS_3 and the successful removing of the SPB core.

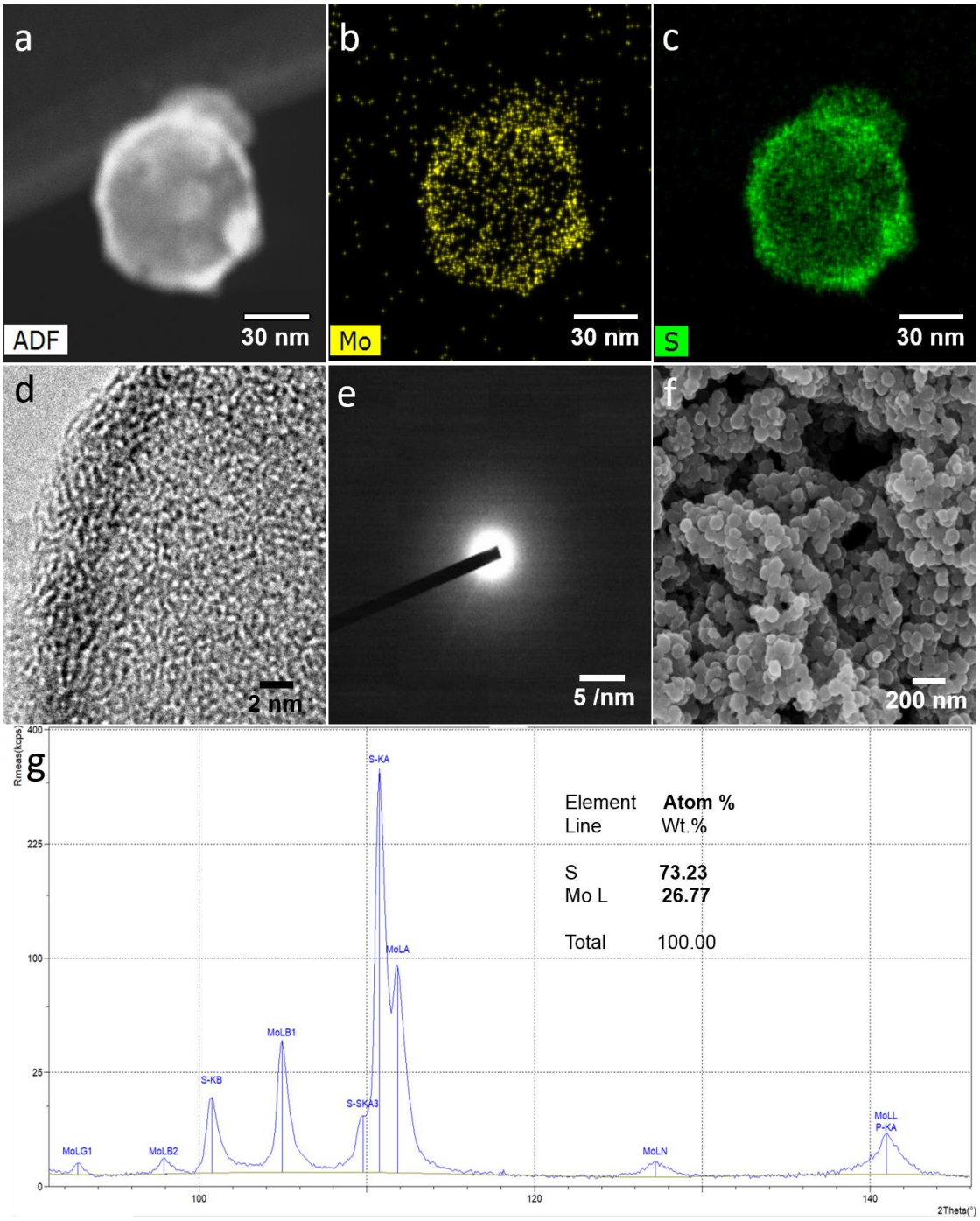

Figure 5.2.1 Electron microscopic characterization of the hollow MoS_3 nanospheres. (a) STEM-HAADF image of a hollow MoS_3 nanosphere, (b) (c) its corresponding EDS elemental mappings, (d) HR-TEM image, (e) the SAED pattern over a large area, (f) SEM image and (g) the WDS spectra of the synthesized hollow MoS_3 nanospheres.

Multiple spectroscopic characterizations have been carried out to study the structure and composition of the synthesized product. The structure of the hollow MoS_3 nanospheres appears to be amorphous which is attested by the featureless XRD pattern except for a broad and diffuse peak at 14 ° as illustrated in Figure 5.2.2 (a), consistent with the SAED results. Figure 5.2.2 (b)

displays the Raman spectrum of the final product. The distinctive peaks at 242, 280, 338, 378, 465 cm^{-1} are corresponding to the various Mo-S stretches in MoS_3, in good agreement with literature.[252] The oxidation state of Mo and S in MoS_3 are investigated by XPS analysis and the results are shown in Figure 5.2.2 (c) and (d). The $Mo3d_{3/2}$ and $Mo3d_{5/2}$ doublet binding energies are located at 232.5 eV and 229.3 eV, which can be assigned to the Mo^{4+} in MoS_3.[253] The XPS result indicates that the reduction of Mo^{6+} to Mo^{4+} is effective by the acid precipitation method. The S2p XPS spectrum shows a broad envelop which can be fit to two doublets with $S2p_{3/2}$ energies, assigned to the bridging S_2^{2-} and/or apical S^{2-} ligands and terminal S_2^{2-} and/or S^{2-}. The doublet at lower binding energy is assignable to terminal disulfide and/or sulfide ligands, while the doublet at higher binding energy is assignable to bridging disulfide and/or apical sulfide ligands.[78] These results demonstrate that MoS_3 is successfully obtained.

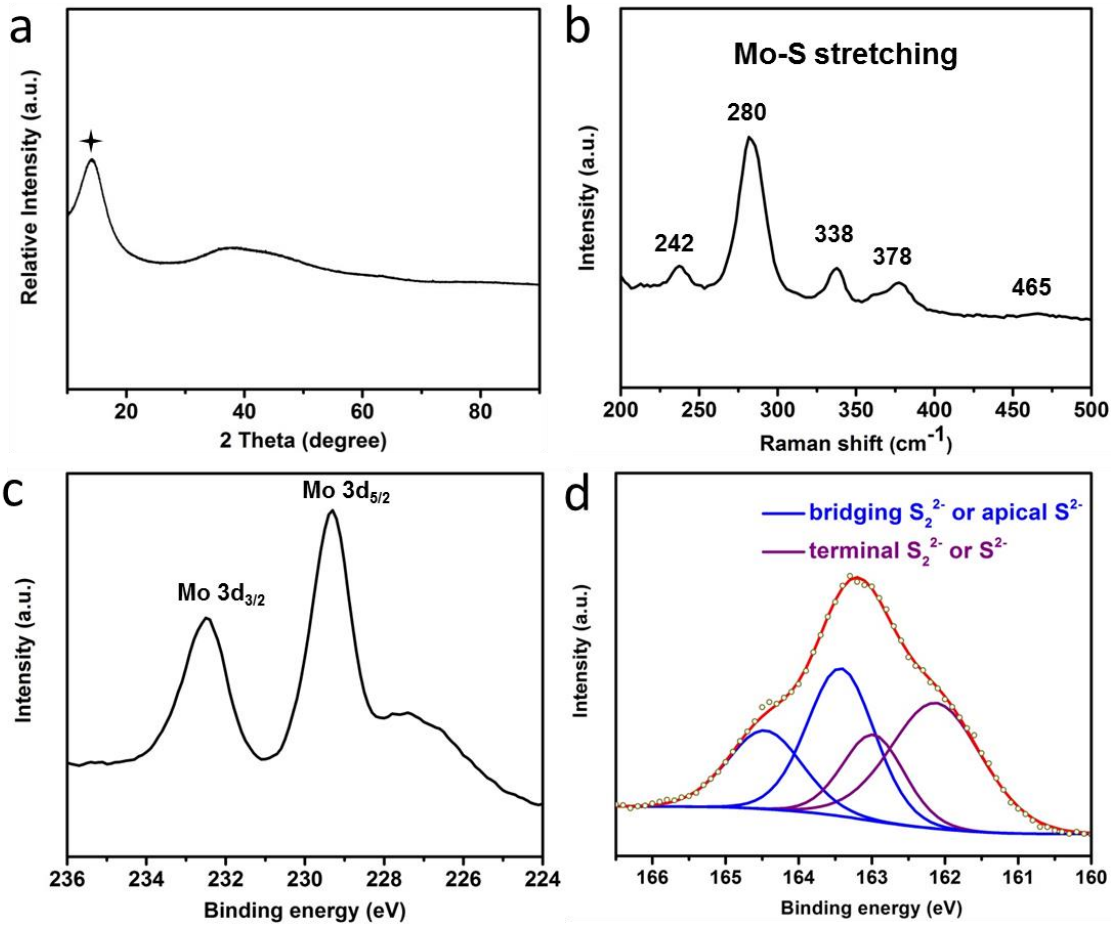

Figure 5.2.2 Spectroscopic characterization of the hollow MoS_3 nanospheres. (a) XRD pattern, (b) Raman spectrum, (c) Mo 3d XPS spectrum and (d) S 2p spectrum.

As shown in Figure 5.2.3 (a), the as-synthesized hollow MoS_3 nanospheres present a colloidally stable system, with no sign of precipitation at the bottom. The suspension of hollow MoS_3

nanospheres in water keeps stable after standing over 24 hours at room temperature. To further understand the porous texture of the final product, N_2 adsorption-desorption isotherms have been carried out, as shown in Figure 5.2.3 (b) and (c). The N_2 adsorption-desorption isotherms clearly demonstrate the mesoporosity of the hollow MoS_3 nanospheres. The BET specific surface area of 87 m^2/g has been determined, which is higher than the reported MoS_3 nanomaterials.[254] The pore size distribution curve shows a narrow peak of mesopore size of about 5 nm, calculated from the desorption data in terms of the Barrett-Joyner-Halenda (BJH) model.

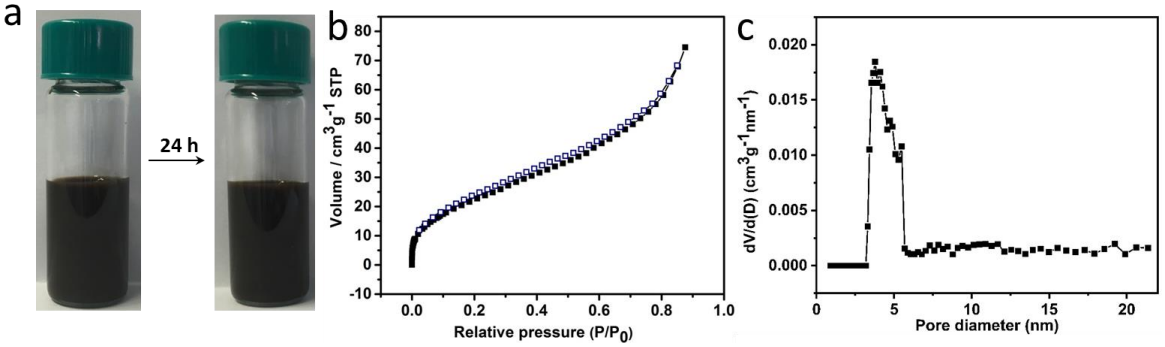

Figure 5.2.3 (a) Photographs of the hollow MoS_3 nanospheres dispersion in water, (b) Nitrogen adsorption/desorption isotherms and (c) the pore size distribution obtained using the BJH method.

The above microscopic and spectroscopic characterizations corroborate the formation of amorphous hollow MoS_3 nanospheres from the simple and scalable acid precipitation method with SPB as template. The unique one dimensional chain-like structure of MoS_3 is found to be distinct from the layered MoS_2 and holds special promise for Li^+ ion storage. The high specific surface area from the hollow nanosphere structure not only delivers more active sites for Li^+ ions uptake, but also releases the volume change upon repetitive dis-/charge.

5.3 Electrochemical performance of hollow MoS_3 nanospheres in "water-in-salt" Li-ion batteries

The obtained hollow MoS_3 nanospheres are assembled into "water-in-salt" LIBs to investigate their lithium storage performances. Note that the MoS_3 hollow spheres demonstrate a high specific surface area facilitating ion diffusion, and exhibit a high dispersity and colloidal stability in water as indicated above, making it particularly suitable for aqueous battery systems. In addition, the lithiation potential of MoS_3 is close to the lower potential limit of WISE, which enables the maximum working voltage when paired with an appropriate cathode material. Considering the following applications, in the first step, hollow MoS_3 nanospheres are

measured in a three-electrode configuration to determine the working voltage in WISE. Then $LiMn_2O_4$ is chosen as the cathode material to pair with hollow MoS_3 nanospheres to make the full cell. In addition, both coin cell type and pouch cell type have been studied for the full cell.

5.3.1 Three-electrode measurements

The electrochemical stability window of hollow MoS_3 nanospheres in the 21 m (m: mol-salt in kg-solvent) LiTFSI electrolyte was measured by CV using MoS_3 nanospheres as a working electrode, Pt wire as a counter electrode and Ag/AgCl as a reference electrode, respectively. The working electrode was prepared by mixing 1 mg hollow MoS_3 nanospheres, 190 µL H_2O, 50 µL ethanol and 10 µL 5 wt% Nafion under ultrasonication for 20 minutes to form a homogeneous dispersion. Afterwards, 10 µL of the mixture was drop casted on the surface of a glassy carbon electrode and was subsequently dried in air. As Figure 5.3.1.1 shows, a stability window of ≈3.1 V was achieved, with cathodic limit at -1.2 V (vs. Ag/AgCl) and anodic limit at 1.9 V (vs. Ag/AgCl), revealing the high reversibility of the working electrode material. In particular, during the scanning, hollow MoS_3 nanospheres shows excellent stability and compatibility in the concentrated electrolyte, which is attributed to the protective effect of the formed SEI.

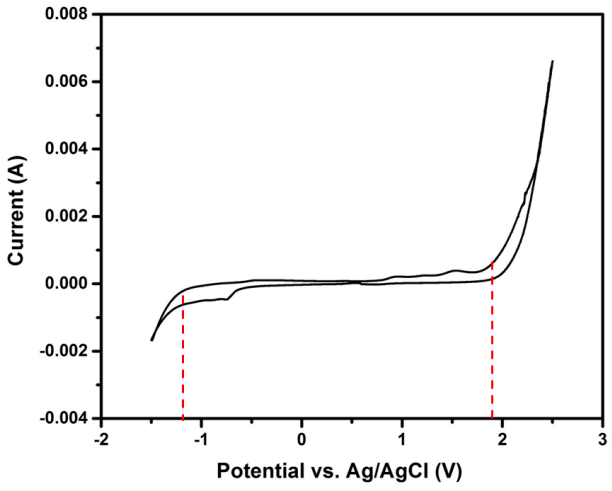

Figure 5.3.1.1 Cyclic voltammetry curves of the hollow MoS_3 nanospheres in a three-electrode configuration in 21 m LiTFSI aqueous solution at 1 mV/s.

5.3.2 Two-electrode measurements

The use of $LiMn_2O_4$ as the cathode material is due to that the lithiation/delithiation plateaus of it is well inside of the stability window of 21 m LiTFSI electrolyte and can stably cycle in "water-in-salt" electrolyte over 1000 times.[25] The $LiMn_2O_4/MoS_3$ mass ratio was set to 2:1 in

order to compensate the irreversible capacity at the anode due to formation of SEI during initial cycles.[28]

5.3.2.1 Electrochemical performance in the coin cell

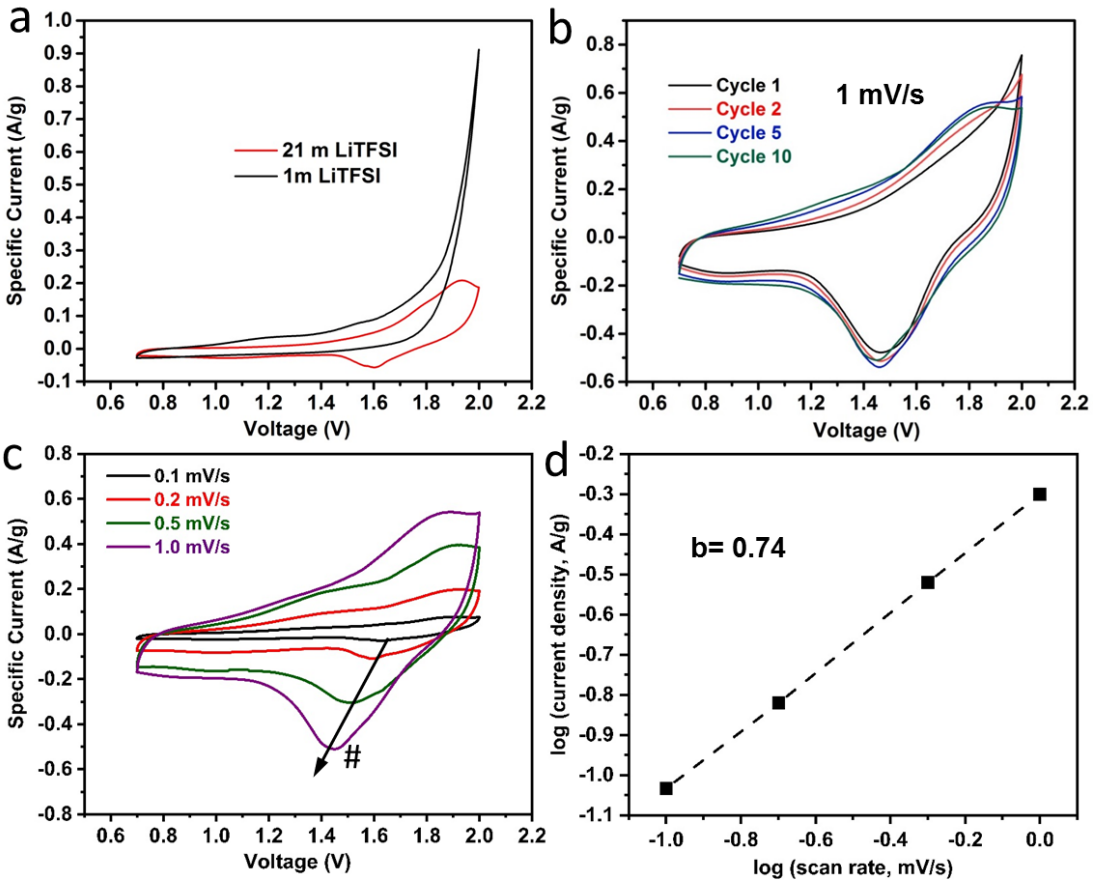

Figure 5.3.2.1.1 (a) Cyclic voltammetry curve comparison of the $LiMn_2O_4$/hollow MoS_3 nanospheres cells in 1 m and 21 m LiTFSI aqueous electrolytes at 0.1 mV/s, (b) cyclic voltammetry curves at initial cycles at 1 mV/s, (c) at different scan rates and (d) the kinetic fitting of the peak current by equation $i=av^b$, where i is the peak current density, and v is the scan rate of the $LiMn_2O_4$/hollow MoS_3 nanospheres cells in 21 m LiTFSI aqueous electrolytes.

The electrochemical performance of the hollow MoS_3 nanospheres in full cell setup is first assessed by pairing it with $LiMn_2O_4$ in standard 2032-type coin cells. The areal loading of hollow MoS_3 nanospheres is intentionally kept at $\approx$1 mg/cm^2 for this part of evaluation so as to expose its full potential and to allow a relevant comparison with literature results which are usually achieved at similarly loadings.

To compare the working potentials of 1 M LiTFSI and 21 m LiTFSI aqueous electrolytes with hollow MoS_3 nanospheres as anode materials, cyclic voltammetry (CV) measurements have been carried out. Figure 5.3.2.1.1 (a) demonstrates that a significant HER process occurs when

the voltage is higher than 1.8 V in 1 m LiTFSI, while no obvious HER peaks can be observed up to 2 V when using the 21 m LiTFSI, indicating the suppressed oxygen evolution and higher electrochemical stability of aqueous Li-ion batteries when a WISE electrolyte is used. This can be attributed to the low fraction of free water molecules[32] and the formation of a solid electrolyte interphase (SEI).[25] In addition, based on the result, the voltage window for the WIS-LIBs based on $LiMn_2O_4$/hollow MoS_3 nanospheres cells in 21 m LiTFSI aqueous electrolytes is set to 0.7 V to 2 V in the following measurements. Figure 5.3.2.1.1 (b) shows the CV curves at 1 mV/s in the initial cycles. There is one broad but distinct redox peak couple of lithiation/delithiation after the initial two cycles. In the initial cycles, the cathodic scan (*i.e.* battery charging) profile transforms from a relatively featureless curve at the first cycle to a broad peak at about 1.8 V from the fifth cycle, implying an irreversible phase transformation of MoS_3 during its lithiation at the initial cycles. The cathodic scan profile remains rather stable after 5 cycles, indicating the stabilization and reversibility of electrode materials after the initial transformation. Meanwhile, an anodic peak can be observed around 1.5 V during battery discharging, corresponding to the release of Li-ions from the lithiated product of MoS_3 and their insertion into the cathode material. Figure 5.3.2.1.1 (c) unveils the CV behavior of the hollow MoS_3 nanospheres in WIS-LIBs at various scan rates from 0.1 mV/s to 1 mV/s in the voltage range between 0.7 V and 2 V after the electrode activation process. At different scan rates, the CV curves keep their typical shape while the peaks shift gradually to a higher voltage during charge and a lower one during discharge when increasing the scan rate, indicating a diffusion-controlled battery-type energy storage. After log-log calculation of the anodic peak (marked as #), a linear relationship can be observed between the scan rate and peak current density (Figure 5.3.2.1.1 (d)). The kinetic factor that dominates the reaction can be identified on the basis of b value by fitting the data to equation $i=av^b$ (i is the peak current density, and v is the scan rate), where b=1 represents a surface-controlled reaction, corresponding to capacitive behavior, and b=0.5 represents a diffusion-controlled reaction, corresponding to battery-type behavior.[255] The b value for the anodic peak in the CV curves is 0.74, indicating the contribution from both capacitive and battery-type charge storage, where the high specific surface area arising from hollow nanostructure facilitates a surface-controlled Li-ion adsorption, while Li-ion storage in the bulk part of the active material behaves following a diffusion-controlled reaction.

Consistent results have also been obtained from galvanostatic charge-discharge experiments at the current density of 0.1 A/g. The hollow MoS_3 nanospheres in WIS-LIBs have a one-stage sloping profile with the plateau ~1.7 V (mid-voltage) during charge and ~1.5 V during

discharge, despite that it appears to be more sloped in the initial cycle. The specific capacity of the as-synthesized hollow MoS_3 nanospheres amounts to 127 mAh/g at 0.1 A/g. These observations, together with the differential capacity (dQ/dV) profile (Figure 5.3.2.1.2 (b)) recalculated from the voltage profile, are in good agreement with the results of CV (Figure 5.3.2.1.1 (b)). It supports that MoS_3 first undergoes irreversible conversion and then remains stable. The detailed reactions during cycling are elucidated and described in the latter part of this work.

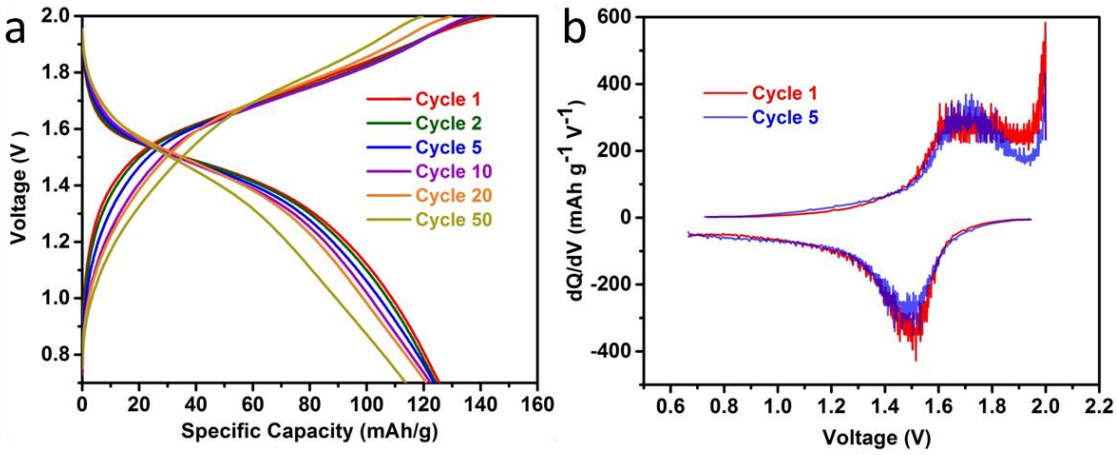

Figure 5.3.2.1.2 (a) Galvanostatic charge-discharge profiles at different cycles at 0.1 A/g, (b) differential capacity (dQ/dV) profile calculated from the cycle 1 and 5 charge/discharge curve of the $LiMn_2O_4$/hollow MoS_3 nanospheres cells in 21 m LiTFSI aqueous electrolytes.

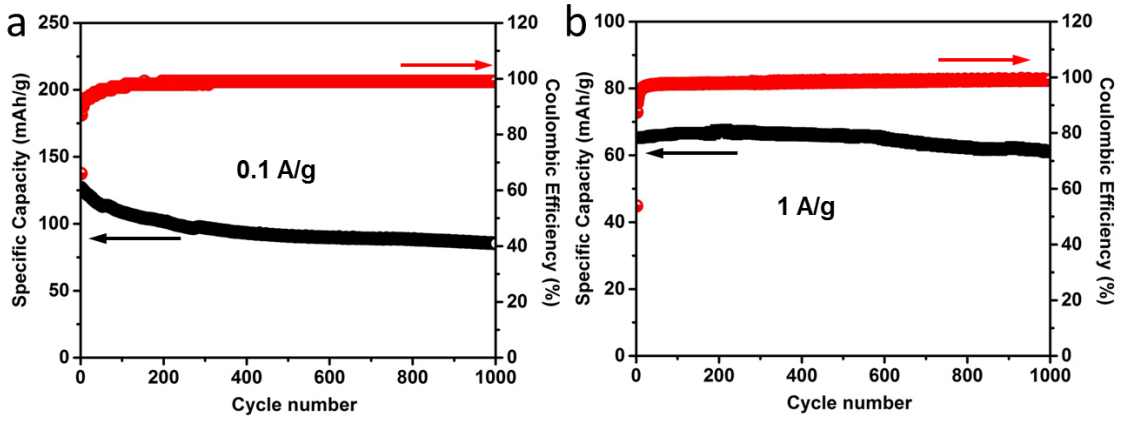

Figure 5.3.2.1.3 (a) The cycle life and Coulombic efficiency at 0.1 A/g and (b) at 1 A/g of the $LiMn_2O_4$/hollow MoS_3 nanospheres cells in 21 m LiTFSI aqueous electrolytes.

Galvanostatic cycling is another means to measure the performance of the material in WIS-LIBs. As reported, the most rigorous proof of stability does not come from the number of cycles, but rather from the time spent by a system at fully charged state as well as from high Coulombic

efficiency at low current densities.[256] In previous studies, the cycling stability of aqueous LIBs was often tactically evaluated at high rates instead of low rates, so that the effect of residual hydrogen and oxygen evolution on cycling stability would be less apparent. Based on that, the cycling stability of the full cell was evaluated at both low (0.1 A/g, Figure 5.3.2.1.3 (a)) and high (1 A/g, Figure 5.3.2.1.3 (b)) current densities for 1000 cycles. The specific capacity of MoS_3 amounts to 127 mAh/g at 0.1 A/g and 65.1 mAh/g at 1 A/g, respectively, for the first cycle. Excellent cycling stability is achieved with a capacity retention of 89 mAh/g and 61.2 mAh/g in 1000 cycles, corresponding to a capacity decay rate of 0.03 % per cycle and 0.006 % per cycle, at 0.1 A/g and at 1 A/g, respectively. Moreover, the initial Coulombic efficiency of the cell is merely 70 % and 50 % at 0.1 and 1 A/g, respectively, due to the irreversible phase transformation of MoS_3 and the formation of solid electrolyte interphase (SEI).[30, 206] The Coulombic efficiency increases to 90 % after 2 cycles and approaches to ≥99 % afterwards at both current densities, revealing that the completion of phase transformation and formation of a stable and protective SEI has been achieved within the first two cycles. This is also consistent with the CV and cycling voltage profiles.

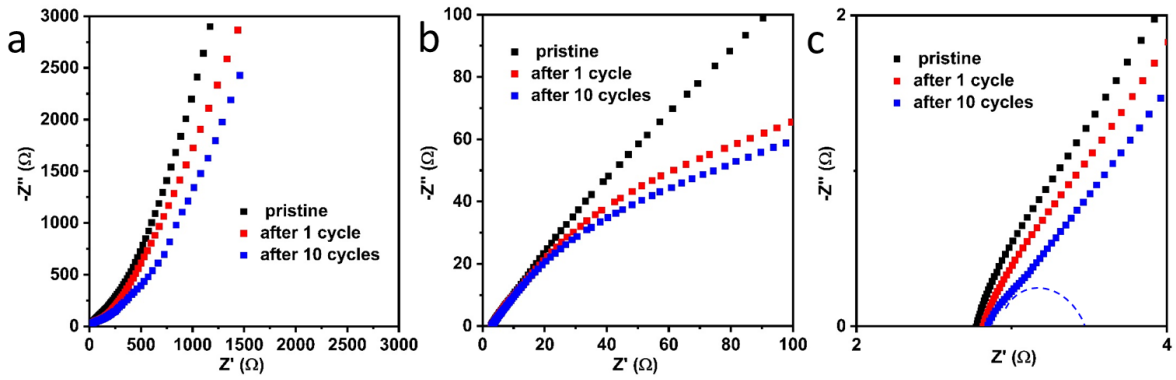

Figure 5.3.2.1.4 (a) Nyquist plots (measured with frequency range from 20 kHz to 10 mHz) after galvanostatic charging/discharging and (b, c) the magnified view at the high frequency range of the Nyquist plots in panel (a).

The Nyquist plots displayed in Figure 5.3.2.1.4 compare the electrochemical impedance of the full cell after different cycles. It can be seen that the material generates a depressed semicircle in the high frequency region and a slope in the low frequency region. Firstly, the Nyquist plots have an intercept smaller than 15 Ω at the high frequency region related to the electronic resistance (R_b) of the electrode, which combines the particle-particle contact resistance, electrolyte resistance and the electrode-current collector resistance. Secondly, in the following there is a depressed semicircle corresponding to the charge transfer resistance (R_{ct}) associated with the Li ion transport at the electrode-electrolyte interface, and a slope line in the low

frequency range related to the Warburg resistance which reveals the solid diffusion rate of Li ions in the electrode material.[257] In this work, after different cycles there is no obvious change in R_b, indicating the stable electronic conductivity and structure of the electrode over cycling. With the increasing cycles, R_{ct} gradually decreases, revealing the aforementioned electrode activation processes and the increasingly facilitated Li ion diffusion into the active material during the initial 50 cycles. Based on it, the ionic and electronic transport along the electrode-electrolyte interface is excellent and the particle-particle contact is still strong even after 50 cycles, so a kinetic improvement upon cycling is observed. In addition, after 10 cycles, the EIS spectra see an emerging depressed semicircle at the high frequency region, which represents the presence of an SEI film.[258] The SEI film protects the electrode material from further parasitic reactions along cycling. The chemical content of the SEI layer may be a LiF-based composite, originating from LiTFSI reduction.[25]

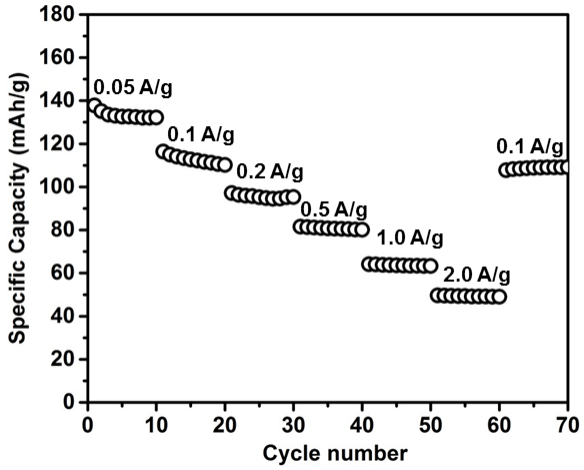

Figure 5.3.2.1.5 Rate capability from 0.05 A/g to 2 A/g of the $LiMn_2O_4$/hollow MoS_3 nanospheres cells in 21 m LiTFSI aqueous electrolytes.

The promising performance of the hollow MoS_3 nanospheres is also reflected by its excellent rate capability at various current densities ranging from 0.05 A/g to 2 A/g (Figure 5.3.2.1.5). At 2 A/g, MoS_3 demonstrates a capacity of 49.7 mAh/g, corresponding to 37 % of the capacity at 0.05 A/g. Important to note is that at the highest specific current under study here, the charging and discharging process is completed in minutes. Remarkably, a high capacity of 109 mAh/g can be recovered when the current density is reset to 0.1 A/g, implying that the relative lower capacity at a higher current rate is mainly limited by the poor kinetics of Li ion diffusion, not the degradation of electrode materials.

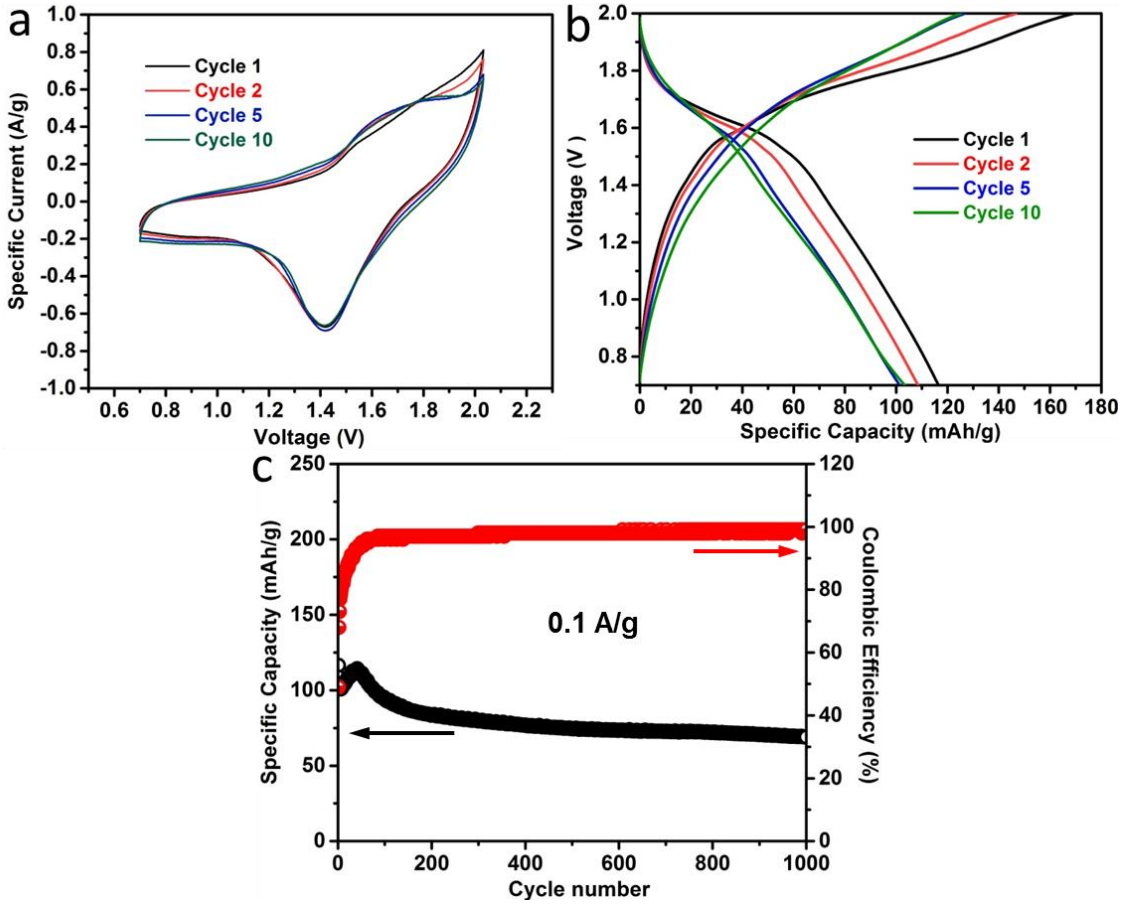

Figure 5.3.2.1.6 (a) Cyclic voltammetry curves at 1 mV/s, (b) galvanostatic charge-discharge profiles at 0.1 A/g and (c) cyclic performance at 0.1 A/g of the $LiMn_2O_4$/bulk MoS_3 cells in 21 m LiTFSI aqueous electrolytes.

For comparison, bulk MoS_3 nanoparticles are also prepared by the same method without the addition of SPB templates. Under the identical test conditions, the bulk MoS_3 nanoparticles exhibit same redox peaks as hollow MoS_3 nanospheres, indicating the change in structures will not influence the working mechanism of MoS_3 in concentrated LiTFSI electrolyte. However, the galvanostatic charge-discharge profiles of the bulk MoS_3 in Figure 5.3.2.1.6 (b) appear to be more sloped with a much shorter voltage plateau. As a result, a lower specific capacity retention over long-term cycling is obtained compared to the hollow structured MoS_3, specifically, 89 mAh/g for the hollow MoS_3 *vs.* 69 mAh/g for the bulk MoS_3 in 1000 cycles at 0.1 A g^{-1}, though their initial capacities are rather comparable (127.3 and 116 mAh/g, respectively, for the hollow and bulk MoS_3). Moreover, the Coulombic efficiency of the battery with bulk MoS_3 increases tardily and reaches 90 % after 30 cycles, which is also limited by the kinetics of Li ion diffusion. Such inferior performance originates from the sluggish Li ion diffusion in the bulk solid of MoS_3 and thus demonstrates the advantages of the hollow nanostructure in facilitating ion transport, especially at higher current rates. The results further

confirm that the hollow MoS_3 nanospheres have better electronic and ionic conductivity than bulk MoS_3 nanoparticles, which will contribute to the greatly enhanced electrochemical performance.

Table 5.3.2.1 Summary of the present work and recently reported materials in WIS-LIBs. The capacity values are presented in per mass of active material.

Cathode	Anode	Electrolyte	Specific capacity of anode materials (mAh/g)	Stability	Ref.
$LiMn_2O_4$	Mo_6S_8	LiTFSI (21 m)	≈147 (at 0.019 A/g*)	68 % after 1000 cycles	25
$LiFePO_4$	Mo_6S_8	LiTFSI (21 m)	110 (at 0.13 A/g*)	60 % after 1000 cycles	238
$LiMn_2O_4$	C/TiO_2	LiTFSI (21 m) +LiOTf (7 m)	144 (at 0.075 A/g)	78 % after 1000 cycles	30
$LiNi_{1/3}Co_{1/3}Mn_{1/3}O_2$	graphite	LiTFSI (5 M) +TMP	118 (at 0.18 A/g*)	99 % after 100 cycles	259
$LiMn_2O_4$	Hollow MoS_3 nanospheres	LiTFSI (21 m)	127 (at 0.1 A/g)	70 % after 1000 cycles	This work
			65.1 (at 1 A/g)	94 % after 1000 cycles	

*: recalculated data based on the reference papers.

LiOTf：lithium trifluoromethane sulfonate.

TMP: trimethyl phosphate.

Table 5.3.2.1 lists the electrochemical performance of other reported WIS-LIBs in comparison with this work. The hollow MoS_3 nanospheres show a high specific capacity with the common used WIS electrolyte, which is comparable or superior to the reported electrode materials for WIS-LIBs, such as Mo_6S_8[25], TiO_2[30, 238] and graphite[259]. After long cycling, no matter at a low current density or a high current density, the cycling stability of hollow MoS_3 nanospheres is better than that of the reported materials even with improved electrolytes.

5.3.2.2 Performance in the pouch cell

In order to evaluate the actual performance of the hollow MoS_3 nanospheres in WIS-LIBs, soft packed full $LiMn_2O_4$/hollow MoS_3 nanospheres LIBs have been assembled using 21 m LiTFSI aqueous solutions as electrolytes (Figure 5.3.2.2.1). Rather than using the metal electrical feed-

through, conductive foil-tabs are welded to the electrodes and brought to the outside in a fully sealed way in the pouch cell. They offer a simple, flexible and lightweight solution to battery design, in which the stack pressure is recommended. Compared to coin cells, the pouch cells can deliver high load currents and can make most efficient use of space and achieve 90-95% packaging efficiency. Pouch cells are used in consumer, military and automotive applications.[260] The galvanostatic charge-discharge profiles of the pouch cell in Figure 5.3.2.2.1 (a) are similar to that of coin cells, but the achieved capacity, 75 mAh/g at the initial cycle (Figure 5.3.2.2.1 (b)), is lower, due to the lower compressive stack pressure in the pouch cell. Sufficient compressive stack pressure in LIBs is necessary to maintain intimate contact between battery components as well as to prevent layer delamination and deformation during operation.[261] Except the first 20 cycles, good cycling stability is achieved for the pouch cell, similar to that of coin cells.

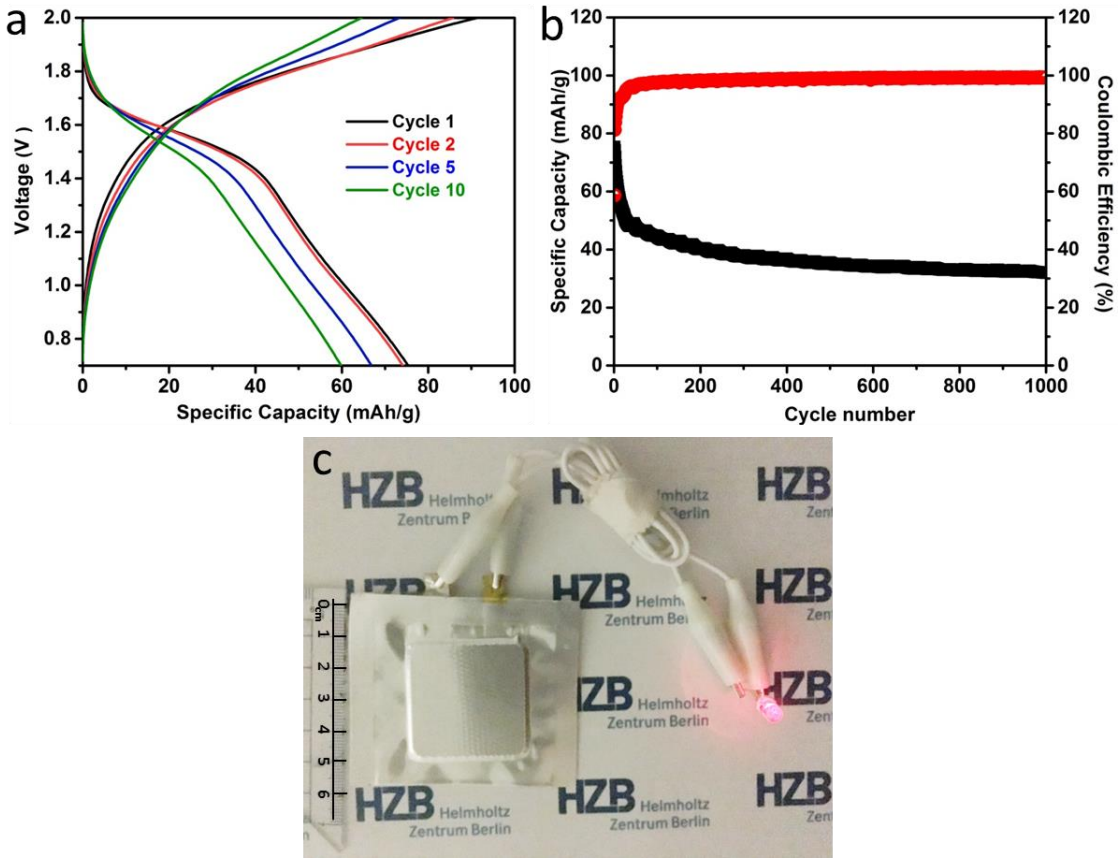

Figure 5.3.2.2.1 Electrochemical performance of the WISE-based $LiMn_2O_4/MoS_3$ pouch cell. (a) Galvanostatic charge-discharge profiles, (b) the cycle life and Coulombic efficiency at 0.1 A/g of the pouch cell and (c) photograph of the pouch cell.

5.4 Working mechanism of MoS_3 in "water-in-salt" Li-ion batteries

From the above measurements, hollow MoS_3 nanospheres have been confirmed to have enhanced specific capacity, rate capability and cycling stability. However, its working mechanism in aqueous LIBs has not been studied. In this part, we will discuss the transformation of MoS_3 during Li^+ ions uptake/release in WIS-LIBs using XRD measurements and its structural stability by SEM imaging.

5.4.1 XRD study on the working mechanism

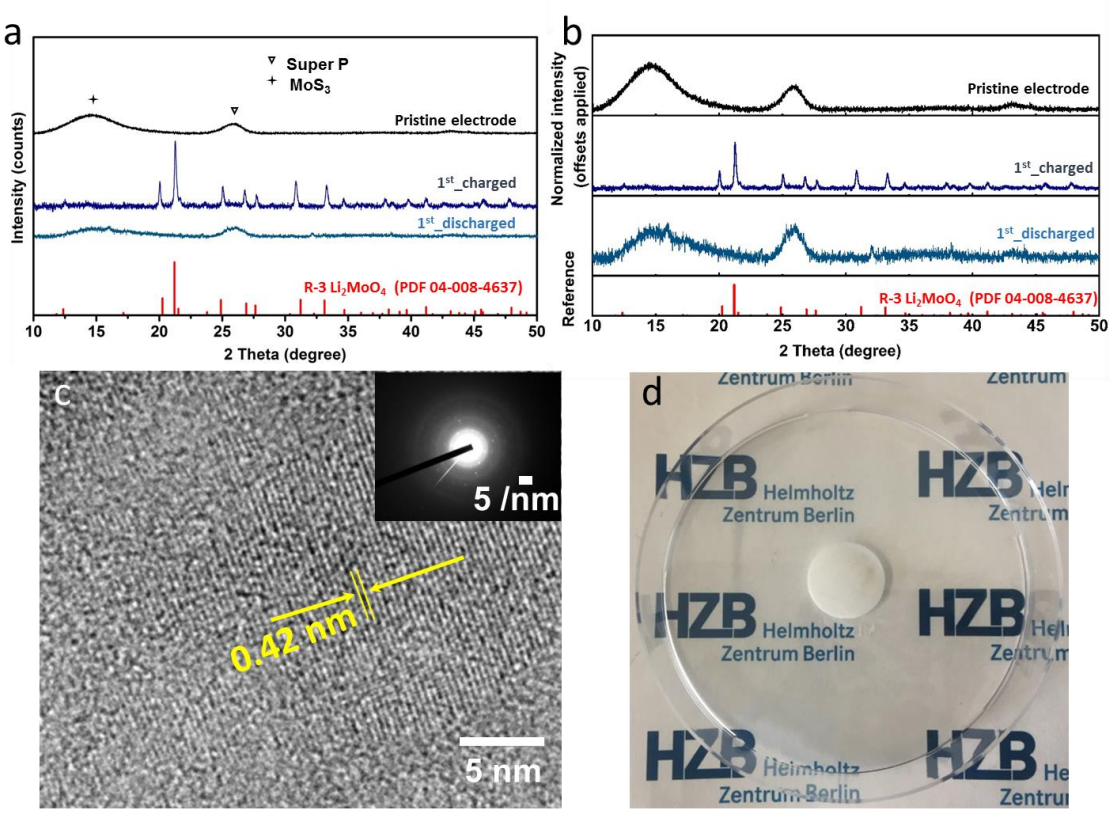

Figure 5.4.1.1 (a) XRD patterns of the pristine, 1st_charged and 1st_discharged electrode of MoS_3 & carbon black, (b) normalized XRD patterns of the pristine, 1st_charged and 1st_discharged electrodes of MoS_3 & carbon black, (c) HR-TEM image (inset: SAED pattern) of MoS_3 after initial charging, (d) photograph of a separator extracted from the charged cell of $LiMn_2O_4/MoS_3$ in 21m LiTFSI.

In order to elucidate the working mechanism of MoS_3 in the WIS-LIBs, ex situ XRD measurement has been performed on cycled electrodes. In the XRD patterns of the pristine MoS_3 & carbon black (without a binder) pellet electrode (Figure 5.4.1.1 (a)), a broad hump at 14° can be observed, arising from the amorphous MoS_3. The weak and broad bump at 26° is assigned to the carbon black conducting additive in the electrode.[258] After initial charging at the current density of 20 mA/g, several new and sharp peaks appear in the XRD pattern (Figure

5.4.1.1 (a)) while the hump of MoS_3 vanishes, indicating the reaction of MoS_3 with the formation of new phase(s), which is identified as R-3 structure rhombohedral Li_2MoO_4 (PDF #04-008-4637). This is also consistent with high-resolution TEM and SAED in Figure 5.4.1.1 (c). The crystalline lattice with a d-space of 0.42 nm in the TEM image can be assigned to the (211) plane of Li_2MoO_4.[262] Moreover, it is noted that elemental sulfur is absent in the charged electrode, as seen from the separator extracted from the charged battery, which remains white and clean (Figure 5.4.1.1 (d)). After discharging, the sharp crystalline peaks disappear and the hump at 14° and 26° appears again.

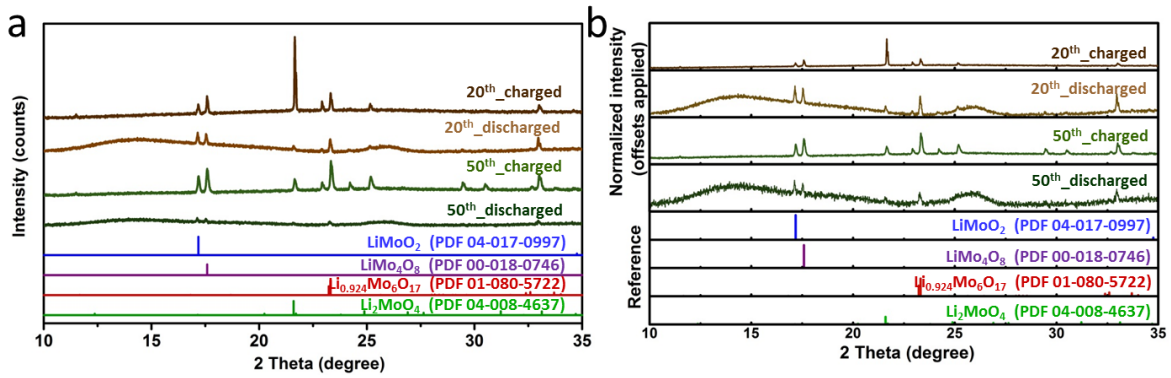

Figure 5.4.1.2 (a) XRD pattern of the 20th_charged, 20th_discharged, 50th_charged and 50th_discharged electrode of MoS_3& carbon black, all data are absolute, (b) normalized XRD patterns of the 20th_charged, 20th_discharged, 50th_charged and 50th_discharged electrodes of MoS_3 & carbon black.

Further investigations on structural changes of the electrode materials have been carried out after 20 and 50 cycles of the WIS-LIBs. After 20 and 50 cycles, Li_2MoO_4 remains visible in the XRD peaks (Figure 5.4.1.2) of the charged electrodes but its relative intensity gets weaker and weaker along cycling. Meanwhile, new crystalline peaks emerge in the XRD patterns of charged electrodes, which can be allocated to $LiMoO_2$ (PDF #04-017-0997), $LiMo_4O_8$ (PDF #00-018-0746) and $Li_{0.924}Mo_6O_{17}$ (PDF #01-080-5722), as shown in Figure 5.4.1.2. The XRD peaks at 23° (in all XRD patterns after 20 and 50 cycles), 29.45° and 30.5° (in the charged electrode after 50 cycles) are yet identified. Moreover, similar to the first cycle, the crystalline peaks of the discharged electrodes after 20 and 50 cycles are greatly reduced in intensity while the broad humps at 14° and 26° reappear. The results indicate the appearance of new phases during cycling accompanied with the consumption of the Li_2MoO_4 composition.

After cycling in the potential window from 0.7 V to 2 V, the ex situ XRD analysis on hollow MoS_3 nanospheres electrodes reveals phase transformation of the anode materials compared to the pristine state. The overall electrochemical process is illustrated in Figure 5.4.1.3. During

the initial charging process of the WIS-LIB, amorphous MoS_3 is converted to Li_2MoO_4 together with the evolution of H_2S (a-$MoS_3 + 2Li^+ + 2OH^- + 2H_2O \rightarrow Li_2MoO_4 + 3H_2S\uparrow$). For charge balance, this reaction is accompanied with HER ($2H^+ + 2e^- \rightarrow H_2\uparrow$). On subsequence discharge from 2 V to 0.7 V, considering that the conversion from MoS_3 to Li_2MoO_4 (with H_2S evolution) is apparently irreversible, the delithiated phase(s) upon discharge is identified as amorphous Li-deficient $Li_{2-x}MoO_4$ or MoO_z, but the exact chemical composition is yet known. Along cycling, the repetitive de-/lithiation reaction results in the formation of crystalline Li_xMoO_y phase at charged state and amorphous $Li_{x-m}MoO_y/MoO_z$ upon discharge. Moreover, degradation happens to Li_xMoO_y along cycling, and the ratio of O to Mo in Li_xMoO_y gradually reduces from 4:1 to 3:1 and 2:1. The oxygen-less phases appear to be more stable and reversible during dis-/charge judging from the increasingly improved Coulombic efficiency over cycling. Despite the irreversible transformation of MoS_3 in WIS-LIBs and the gas evolution of the electrolyte, the MoS_3 based WIS-LIBs still exhibit enhanced cycling stability and rate capability compared with the performance of MoS_3 in organic electrolytes based LIBs[73, 77, 263]. The outstanding performance is due to the high ionic conductivity of the aqueous electrolyte.

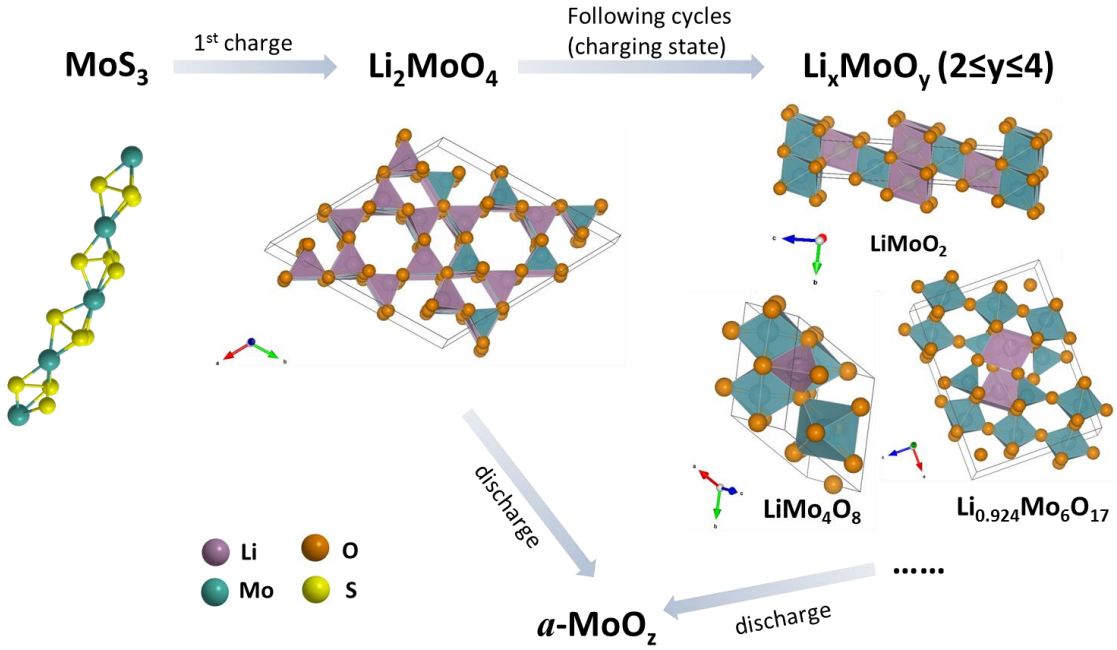

Figure 5.4.1.3 Schematic illustration of the working mechanism of MoS_3 in the WIS-LIBs.

It is noted that during cycling in WIS-LIBs, MoS_3 tends to irreversibly convert to Li_xMoO_y. It stimulates us to study the behaviors of Li ion insertion in MoO_z. In this work, we compared the performance of MoS_3 and MoO_3 (both in bulk), among which MoO_3 was synthesized by annealing MoS_3 in air, as anode material in the WIS-LIBs. In the CV curves of MoO_3 based

WIS-LIBs (Figure 5.4.1.4 (a)), there appears a pair of humps in the initial cycle, which are assigned to the insertion/desertion of Li ions in the material. With continuous scanning, the two humps become weaker and weaker, indicating the poor reversibility. The initial specific capacity of bulk MoO_3 is merely 62.1 mAh/g (Figure 5.4.1.4 (b)), which is much lower than that of bulk MoS_3 (116 mAh/g, Figure 5.3.2.1.6 (b)). Moreover, MoO_3 presents a rapid capacity fading in the following cycles, showing a worse cycling stability compared to that of MoS_3. The superior performance of MoS_3 can be attributed to its one dimensional chained structure facilitating active Li^+ ion storage during the electrochemical reaction. Moreover, MoO_3 suffers from the dissolution of Mo ions in aqueous electrolytes, which leads to the loss of active materials and thus low capacity retention over cycling.[264]

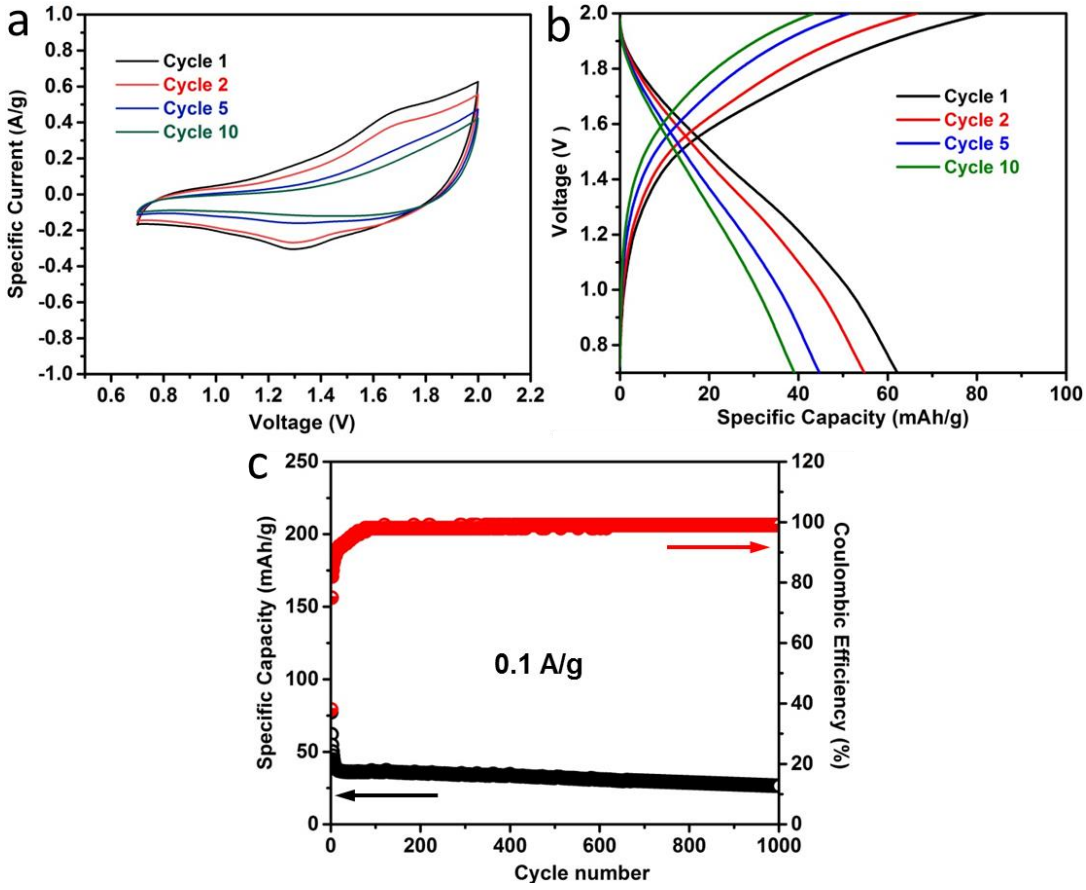

Figure 5.4.1.4 (a) Cyclic voltammetry curves at 1 mV/s, (b) galvanostatic charge-discharge profiles at 0.1 A/g and (c) cyclic performance at 0.1 A/g of the $LiMn_2O_4$/bulk MoO_3 cells in 21 m LiTFSI aqueous electrolytes.

It is worth to note that the ex situ XRD results of the MoS_3 based WIS-LIBs, HER, which is supposed to be absent considering the wide electrochemical stability window of the WISE, still occurs. This fact may be attributed to the catalytic behavior of MoS_3 in promoting HER in water splitting systems.[253, 265] The detailed catalytic mechanism of MoS_3 in HER in the WIS-LIBs is

out of the scope of this chapter. The HER process is undesired and increases the safety concerns during battery charging. Therefore, it is of significant relevance to suppress the HER process, *e.g.*, by reducing the charging cutoff-voltage. Based on it, CVs of the MoS_3 based WIS-LIBs with decreasing upper voltage limit stepwise from 2.0 V to 1.6 V have been measured (Figure 5.4.1.5). It shows that the characteristic HER-associated cathodic profile and the corresponding anodic peak at ~1.5 V remain distinct in the CV plots when the upper voltage limit is set to 1.9 V and 1.8 V. Such characteristics vanish when the voltage is limited to ≤ 1.7 V. However, it shows a typical capacitive storage curve and the current response is considerably lower when compared to the performance from 0.7 V to 2 V.

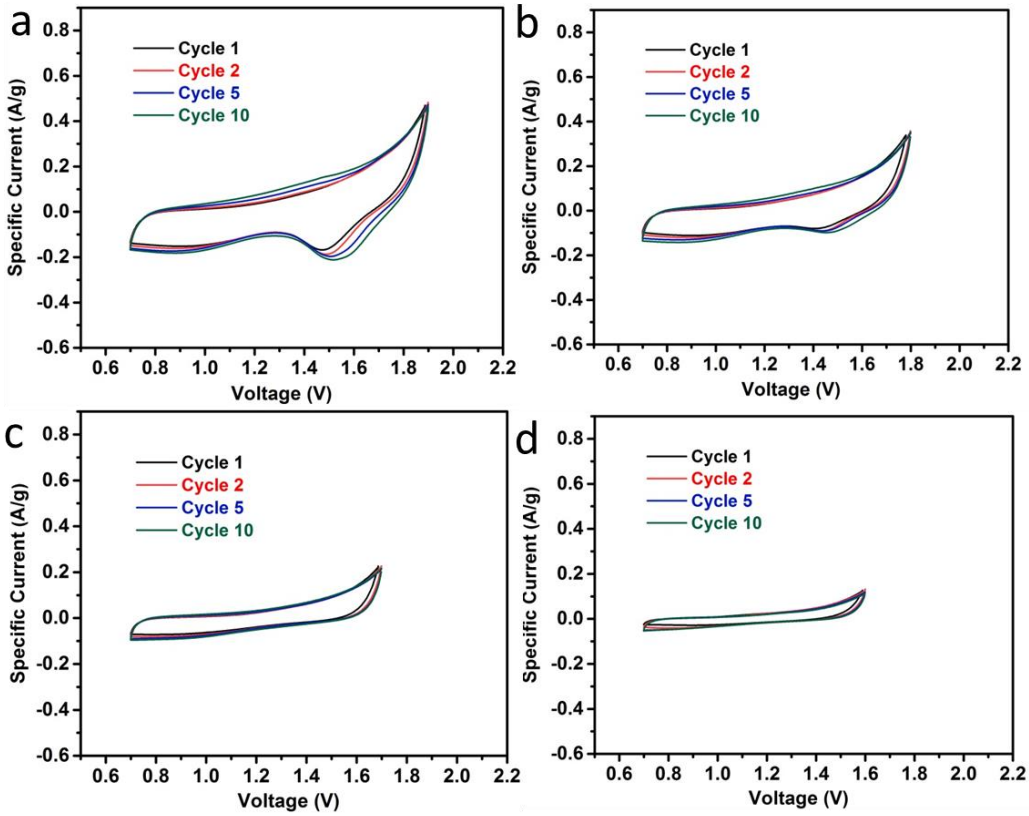

Figure 5.4.1.5 Cyclic voltammograms at 1 mV/s with the voltage ranges from 0.7 V to 2 V, 1.9 V, 1.8 V, 1.7 V and 1.6 V, respectively.

In order to confirm the capacitive behavior of the MoS_3 based WIS-LIBs with the voltage range of 0.7 – 1.6 V, XRD measurement has been performed on the MoS_3 electrode when the battery is charged to 1.6 V. It is clear that there is no obvious peaks on the XRD pattern of the charged electrode, indicating absence of phase transformation at the voltage of 1.6 V. In addition, as shown in Figure 5.4.1.6 (b), the achieved capacity charge to 1.6 V is extremely low (8.4 mAh g^{-1} at the first cycle), which is far below that of 2 V (127 mAh g^{-1}), which is due to the simple

capacitive working mechanism here. Thus, the HER process can be suppressed by lowering the charging cutoff voltage, but the battery type working mechanism of MoS_3 materials will not be fully applied, which results in the greatly sacrificed achieved capacity. To avoid gas evolution in practical applications, pre-lithiation of MoS_3 (with the conversion to Li_xMoO_y) may be considered.

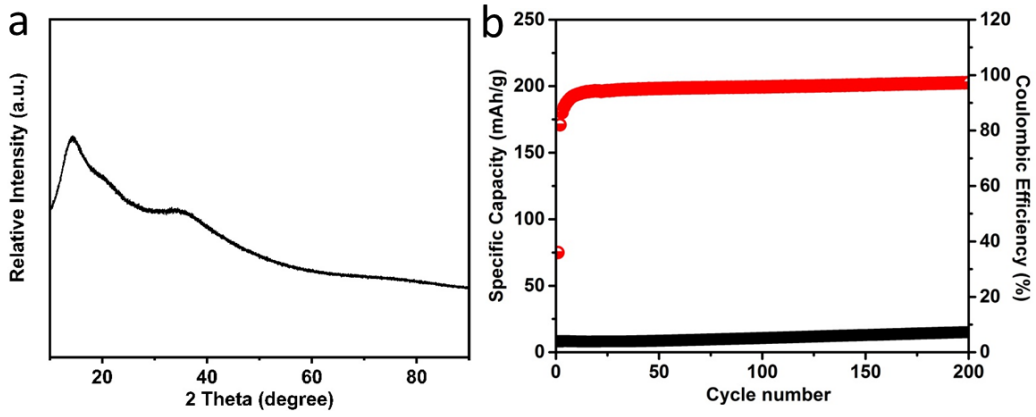

Figure 5.4.1.6 (a) The XRD pattern of the electrode of the hollow MoS_3 nanospheres after charging to 1.6 V, (b) cycling performance at 0.1 A/g between 0.7 V and 1.6 V.

5.4.2 Morphology study on the electrodes

The structural stability of the hollow MoS_3 nanospheres after cycling in WIS-LIBs has also been examined by post-mortem SEM characterization as shown in Figure 5.4.2.1. The hollow MoS_3 nanospheres keep well-integrated with the conductive agent after 400 cycles, without any evident structural deformation and crack observed in the cycled electrode. Meanwhile, the MoS_3 nanoparticles still remain their typical morphology and no structure collapse or aggregation can be found. Such structural integrity results in a low and stable electrical resistance, leading to the battery cycling stability. The excellent performance of the hollow MoS_3 nanospheres in the WIS-LIBs can be ascribed to the following features. (a) The hollow nanosphere structure and the one dimensional chained molecular structure of MoS_3 deliver many open sites toward Li^+ ion storage during the electrochemical reaction. (b) The hollow nanostructure is effective to relieve the structural strain from the repeated uptake/release of Li ions and thereby to prolong its cycle life.

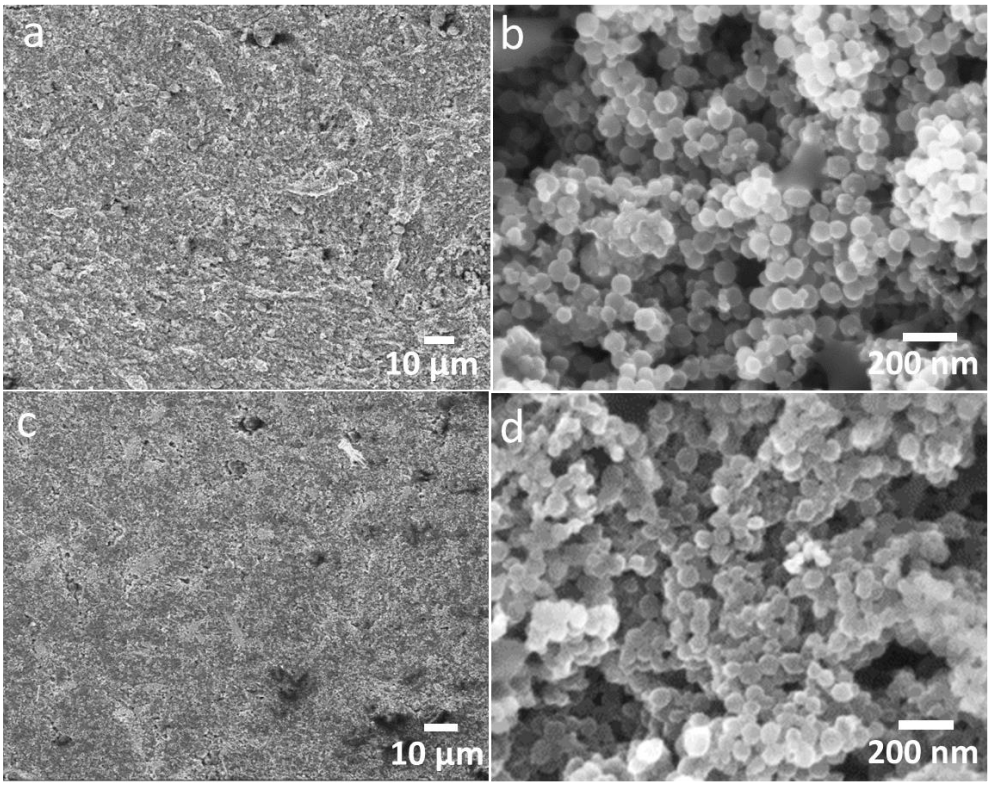

Figure 5.4.2.1 Post-mortem characterization on cycled MoS_3 electrodes. (a) and (b) SEM images of the pristine electrode, (c) and (d) SEM images of the electrode after 400 cycles.

In this chapter, we demonstrate that MoS_3, an amorphous chain-like structured transitional metal trichalcogenide, is promising as anode in the WIS-LIBs. The hollow MoS_3 nanospheres are synthesized via an acid-induced precipitation method using spherical polyelectrolyte brushes as the template. When applied in WIS-LIBs, the hollow MoS_3 nanospheres achieve a high specific capacity of 127 mAh/g at the current density of 0.1 A/g and excellent stability over 1000 cycles. During battery operation, MoS_3 is converted to Li_2MoO_4 in the initial Li^+ ion uptake, and then gradually to a more stable and reversible Li_xMoO_y phase along cycling. The discharge product appears to be amorphous Li-deficient $Li_{x-m}MoO_y/MoO_z$. Nevertheless, MoS_3 outperforms MoO_3 in WIS-LIBs, which could be accredited to its initial one-dimensional molecular structure and the amorphous nature of the delithiated product. The results break new ground for the preparation of metal sulfides/oxides with controlled nanostructures using template based methods and will push forward the development of metal sulfides in aqueous energy storage as well as conversion systems.

6 Summary

This thesis focuses on the study of high-performance hollow MoS_x based electrode materials for aqueous energy storage systems, including supercapacitors and Li-ion batteries. Novel hollow MoS_x nanoparticles have been synthesized using sacrificial templates through colloidal methods. High specific capacitance/capacity and stable cycling performance have been achieved for energy storage, and electrochemical analysis has been performed to provide insight into the reaction mechanisms.

MoS_2, a typical layered TMD, is promising as an electrode material for supercapacitors. However, its low electrical conductivity leads to limited capacitance if applied in aqueous electrochemical devices. To overcome this problem, in the first part of this thesis, highly dispersible hollow sandwich-structured carbon-MoS_2-carbon nanoplates have been synthesized through an L-cysteine-assisted hydrothermal method by using gibbsite nanoplates as template and PDA as the carbon precursor. After calcination and etching of the gibbsite template, uniform hollow MoS_2 platelets have been obtained, which are coated by partial graphitic carbon. The presence of a partial graphitic carbon coated on both sides of the MoS_2 nanoplate has improved the electrical conductivity and dispersibility of the hybrid material. When applied in 1 M Li_2SO_4 based symmetric supercapacitors, the active electrode material exhibits nearly ideal capacitive behaviour. The hollow structure not only provides more active sites for energy storage, but prevents volume change during the charge/discharge process, which contributes to a high specific capacitance of 248 F/g at a constant current density of 0.1 A/g and good electrochemical stability over 3000 cycles. The maximum energy density is calculated to be 78 Wh/kg, which is comparable to other MoS_2-based electrode materials in supercapacitors.

In the second part of the thesis, “water-in-salt” (WIS) electrolyte (a highly concentrated aqueous solution) has been applied for supercapacitors using hollow carbon nanoplates (HCPs) as the electrode material. The high compatible system with 21 m LiTFSI as the electrolyte shows an enhanced working potential from 0 to 1.8 V with superior performance when compared with that of 1 m LiTFSI design. In addition, the formation of solid electrolyte interphase (SEI) during the initial cycles in WIS supercapacitors has been investigated by the EIS technique as a fundamental and trustworthy approach. According to the fitting results, the growth of SEI layer on the surface of electrode materials have been observed and studied. The SEI formation is further supported by the XPS measurement. Furthermore, the influence of working temperature on the performance of supercapacitors using 21 m LiTFSI electrolyte has been systematically

reviewed in a temperature range from 15 ºC to 55 ºC. All resistance parameters are decreased along with the increase of temperature and reverse following the same routine during cooling, showing good thermal reversibility of the system. In addition, the EIS measurements have disclosed the increase of the interfacial capacitance (C_{ef}) at a higher temperature, indicating more favorable formation of SEI layer.

Inspired by it, WISE has been further used in Li-ion batteries with hollow MoS_3 nanospheres as the anode material. The hollow MoS_3 nanospheres are synthesized via an acid-induced precipitation method using spherical polyelectrolyte brushes as the template. We have also, for the first time, assessed the capability of MoS_3 as electrode material in WIS-LIBs, which have achieved promising electrochemical performance with a considerable specific capacity (127 mAh/g) and excellent stability over 1000 cycles. During the operation in WIS-LIBs with $LiMn_2O_4$ as the cathode material, MoS_3 is converted to Li_2MoO_4 in the initial Li^+ ion uptake, and then gradually to a more stable and reversible Li_xMoO_y phase along cycling. The discharge product appears to be amorphous Li-deficient $Li_{x-m}MoO_y/MoO_z$. This part demonstrates the working mechanism of MoS_3 in the WIS-LIBs and will push forward the development of MoS_x for aqueous energy storage applications.

In summary, this thesis studies novel hollow MoS_x nanomaterials with excellent performance for aqueous energy storage applications, and looks insight into the working mechanisms of WIS systems, which show great potential towards the development of MoS_x materials in high energy-density aqueous supercapacitors and LIBs.

7 Experimental

7.1 Chemicals and materials

Aluminum isopropoxide (AIP), tetraethyl orthosilicate (TEOS), 3-hydroxytyramine hydrochloride (dopamine), aluminum sec-butoxide (ASB), ammonia, polyvinylpyrrolidone (PVP, 40,000 g/mol), tris(hydroxymethyl) aminomethane (Tris), ammonium hydrogen difluoride (NH_4HF_2), lithium sulfate monohydrate ($Li_2SO_4•H_2O$), polyvinylidene fluoride (PVDF), Nafion (117), sodium molybdate (Na_2MoO_4,), L-cysteine, HCl (37%), 2,2'-azobis(2-amidinopropane)dihydrochloride (V50, 98 %), ammonium tetrathiomolybdate ($(NH_4)_2MoS_4$), cetyltrimethylammonium bromide (CTAB), tetrahydrofuran (THF), poly(tetrafluoroethylene) (PTFE, 60 wt% dispersion in H_2O), bistrifluoromethanesulfonimide lithium (LiTFSI), water (HPLC grade), and 1-methyl-2-pyrrolidinone (NMP) were obtained from Sigma-Aldrich and used as received. 2-Amino-ethylmethacrylate hydrochloride (AEMH, 90%) was purchased from Polyscience. Lithium manganese oxide ($LiMn_2O_4$) was received from MTI Corporation. Carbon black (Super P) was obtained from Alfa Aesar. Ethanol (absolute) was purchased from VWR. Styrene (BASF, 99 %) was destabilized by Al_2O_3 column and stored in a refrigerator before use. 2-[p-(2-Hydroxy-2-methylpropiophenone)]-ethyleneglycol methacrylate (HMEM) was used as the photo-initiator to graft the brushes on the polystyrene (PS) cores. Milli-Q water with a resistivity 18.2 MΩ•cm at 25 ºC and a TOC<5 ppb was used in all preparations except electrolytes. Aqueous electrolytes were prepared by dissolving electrolyte salts in water with HPLC grade and stirring for 24 hours.

7.2 Synthesis procedure

7.2.1 Hollow carbon-MoS_2-carbon nanoplates

7.2.1.1 Synthesis of gibbsite nanoplates

The synthesis of gibbsite nanoplates was referred to the literatures.[168, 266] In a typical run, 0.12 mol ASB and 0.12 mol AIP were dissolved in 1.5 L water and then 11 ml HCl (37%) was added to acidify the solution. After mechanically stirring for 10 days (150 rpm), the turbid solution was transferred into a polypropylene bottle and heated in a water bath at 85 ºC for 3 days.

After cooling down, the suspension of the gibbsite nanoplates was cleaned by dialysis as schematically shown in Figure 7.2.1.1.1. Firstly the regenerated cellulose tube (MWCO 14 000) was placed in Milli-Q water to soak for 15 min prior to use in order to soften it for handling. The water was changed every day. The stirring of the cellulose tube was monitored by the electric rotator. Dialysis was stopped until the conductivity of the serum was below 20 μS/cm.

In the last step, the gibbsite particles in the colloidal dispersion were precipitated by centrifugation (1200 g, 20 h) and the sediment was dispersed in water. The final gibbsite dispersion with the concentration of 4.0 wt% was stored in a polypropylene bottle for further characterization and use.

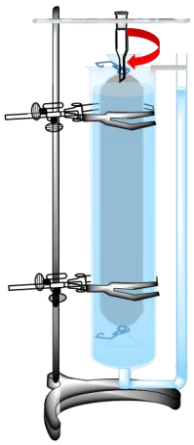

Figure 7.2.1.1.1 Schematic dialysis setup for the purification of nanoparticles.

7.2.1.2 Synthesis of PDA coated gibbsite nanoplates

The coating of PDA onto the gibbsite nanoplates was conducted by a self-oxidation polymerization method. Briefly, 1.25 ml gibbsite dispersion (4.0 wt%) was dispersed in 100 ml Tris buffer solution (10mM, pH 8.5). Under constant ultrasonication at 37 kHz (Elmasonic P120H, Elma Schmidbauer GmbH, Germany), 50 mg dopamine was added into the solution and the ultrasonication was continued for 2 h to avoid the aggregation of particles. During this process, the temperature of water in the sonicating bath was kept below 35 ºC. The white suspension gradually turned to black during the self-oxidation polymerization process. After stirring overnight, the final product was washed several times with water by centrifugation at 8000 rpm for 30 minutes until the supernatant remained colourless.

7.2.1.3 Synthesis of gibbsite-PDA-MoS_2 nanoplates

The synthesis of MoS_2 was realized by an L-cysteine-assisted hydrothermal method in the presence of the nanoplates.[159, 165] In a typical synthesis, the synthesized gibbsite-PDA nanoplates were dispersed into 100 ml water and Na_2MoO_4 was added into the solution under stirring. After two minutes' stirring at room temperature, L-cysteine was added and sonicated for 30 minutes. After that, a certain amount HCl (37%) was added drop by drop under stirring until the pH of the solution was adjusted to the desired value. The above solution was transferred to a 120 ml Teflon-lined autoclave which was sealed. A hydrothermal process was induced by

heating the autoclave in the oven at 200 ºC for 24 hours and naturally cooled down to room temperature. The resulted suspension was centrifuged at 8000 rpm for 30 minutes to collect the nanoplates and washed several times with water. In order to obtain nanoparticles with desirable morphologies, the experiments were performed under various conditions (Table 7.2.1.3.1). After comparison, resulted nanoparticles in Condition 1-4 are aggregated in water solutions. Most of the MoS_2 nanoparticles synthesized in Condition 6 and 7 are not successfully coated onto the templates. Based on this, for the further synthesis, following conditions were used: the amount of Na_2MoO_4 and L-cysteine were 0.121 g and 0.303 g, respectively, and the pH was adjusted to 2.3 by adding a certain amount of HCl (37%) into the 100 ml water solution.

Table 7.2.1.3.1 Amount variation of Na_2MoO_4 and L-cysteine and the pH value for the synthesis of MoS_2.

No.	Na_2MoO_4 (g)	L-cysteine (g)	pH	H_2O (ml)
1	0.121	0.303	1	100
2	0.121	0.303	1.5	100
3	0.121	0.303	2	100
4	0.0605	0.1515	1	100
5	0.121	0.303	2.3	100
6	0.242	0.606	2.3	100
7	0.1815	0.4545	2.3	100

7.2.1.4 Synthesis of gibbsite-PDA-MoS_2-PDA nanoplates

A thin layer of PDA was coated onto the gibbsite-PDA -MoS_2 nanoplates with the same PDA deposition step as described above.

7.2.1.5 Synthesis of gibbsite-PDA-MoS_2-PDA-silica gel

A silica nanocasting process was applied to avoid the aggregation of nanoplates during high temperature calcination. 1.14 ml HCl (37%) was added into 100 ml of gibbsite-PDA-MoS_2-PDA nanoplates dispersion (4.5 g/L) under vigorous stirring. After 10 minutes' stirring followed by 10 minutes' ultrasonication, 8.56 ml TEOS was added in portions under the liquid surface

of the vigorously stirred solution during 30 minutes. The reaction was run overnight at room temperature and then the mixture was freeze-dried afterwards.

7.2.1.6 Synthesis of hollow carbon-MoS_2-carbon nanoplates

Calcination was performed at 700 ºC for 3 hours (heating rate: 2 ºC/min) under argon to convert PDA to carbon. After cooling down to room temperature, the products were firstly treated by an aqueous solution of 4 M NH_4HF_2 for two weeks to remove silica. After that, the dispersion was carefully cleaned with water for several times and the collected nanoparticles were then dispersed in HCl (37%) for another two weeks to remove the gibbsite templates. During the process, the centrifugation, decantation and re-dispersion process were carried out every day to change the NH_4HF_2 solution and HCl. The desired products were obtained by washing with water for several times and were freeze-dried before further use.

7.2.2 Hollow carbon nanoplates

Hollow carbon nanoplates were synthesized through the silica-nanocasting method according to the literature.[67] The detailed synthesis process is described as follows.

7.2.2.1 Synthesis of hollow silica nanoplates

Gibbsite nanoplates with silica coating were prepared according to the modified Stöber method. In a typical run, PVP water solution was prepared by adding 50 g PVP into 500 ml water and stirring for 3 hours to obtain the transparent solution. Then 25 ml gibbsite dispersion (4 wt%) was added into the PVP water solution to prepare the PVP-stabilized gibbsite nanoplates. The mixture was kept under stirring at 500 rpm for 24 hours and the particles were collected by centrifugation at 500 g for 20 hours. The sediment was then redispersed in 794 ml ethanol via ultrasonication (37 kHz) and mechanical stirring (150 rpm). Under constant ultrasonication and stirring, 46 ml ammonia (30%) (300 ml/h) and 1.4 ml TEOS (9 ml/h) were injected slowly into the mixture at the same time. Afterwards, ultrasonication was kept for another one hour. The reaction lasted for 6 hours under mechanical stirring. The suspension was centrifuged at 8000 rpm for 30 minutes to collect the products and cleaned with ethanol twice and followed with water for three times. Gibbsite templates were then etched away by keeping the nanoparticles in concentrated HCl (37%, 300 ml) for one month. HCl was changed once a week by centrifugation at 8000 rpm. After eventual removal of the gibbsite cores, hollow silica nanoplates were washed several times with water by centrifugation at 8000 rpm for 30 minutes until the pH reached neutral.

7.2.2.2 Synthesis of hollow silica-PDA nanoplates

The coating of PDA onto hollow silica nanoplates was conducted by self-oxidation polymerization of dopamine as described before. 10 mM pH 8.5 Tris buffer was firstly prepared by adding 2.42 g Tris in 1.8 L water and a certain amount of HCl (37%) to adjust the pH to 8.5. After vigorous stirring, the solution was transferred to a 2 L volumetric flask and the volume was set to 2 L by adding water for further use. In a typical run, the hollow silica nanoplates collected in the last step were dispersed in 280 ml 10 mM Tris buffer (pH 8.5) under stirring. Then under constant ultrasonication, 0.14 g dopamine was added into the solution and ultrasonication was applied for another 2 hours to avoid aggregation of the particles. After stirring at 300 rpm overnight, the nanoparticles were collected by centrifugation at 8000 rpm for 30 minutes and cleaned with water for three times until the secondary PDA particles were totally removed. The synthesis process was repeated once more to make the coating of PDA to a certain thickness.

7.2.2.3 Synthesis of hollow carbon nanoplates

To avoid aggregation of nanoplates during high temperature treatment, silica nanocasting technique was applied here. 80 mg hollow silica-PDA nanoplates were dispersed in 20 ml water and 2 ml of HCl (0.1 M) was added under stirring (300 rpm). After 10 minutes' stirring followed by 10 minutes' ultrasonication (37 kHz), 15 ml TEOS was added in portions with pump under liquid surface for one hour under mechanical stirring (150 rpm). After stirring overnight at room temperature, the mixture was rotary evaporated to remove ethanol and freeze dried to remove water. The product was then carbonized under argon at 800 ºC for 2 hours (heating rate of 2 ºC/min). After cooling down to room temperature, the pyrolyzed product was treated with NH_4HF_2 aqueous solution (4 M) for two weeks to remove the silica. NH_4HF_2 was changed twice every week by centrifugation. The desired hollow carbon nanoplates were obtained by centrifugation (8000 rpm, 30 minutes) and washed with water for three times.

7.2.3 Hollow MoS_3 nanospheres

7.2.3.1 Synthesis of spherical polyelectrolyte brushes (SPB)

Firstly, the polystyrene (PS) cores were synthesized by emulsion polymerization of styrene. In a typical experiment, 1.998 g CTAB was dissolved into 300 g water. Oxygen in the solution was removed with the nitrogen flow for half an hour, followed by addition of 78 g inhibitor-free styrene into the solution under mechanical stirring. After that, 0.3 g V50 dissolved in 15 ml degassed water was added and the mixture was heated in a water bath at 60 ºC to initiate the

reaction. After two hours' reaction, 8.73 g photo initiator HMEM dissolved in 10 ml acetone was added in portions with pump within 3 hours and the reaction was allowed to continue for another 2 hours at 65 ºC in a water bath and then cooled down to room temperature. The procedure required to avoid irradiation of light. The PS cores coated with HMEM were cleaned through ultrafiltration until the conductivity of the serum was reached 20~30 μScm^{-1}. Here for PS cores purification, membranes with pores of 50 nm were used. The radius of the poly(styrene)-core-HMEM particles is 39.5 nm and the concentration is 2.0 wt% in water.

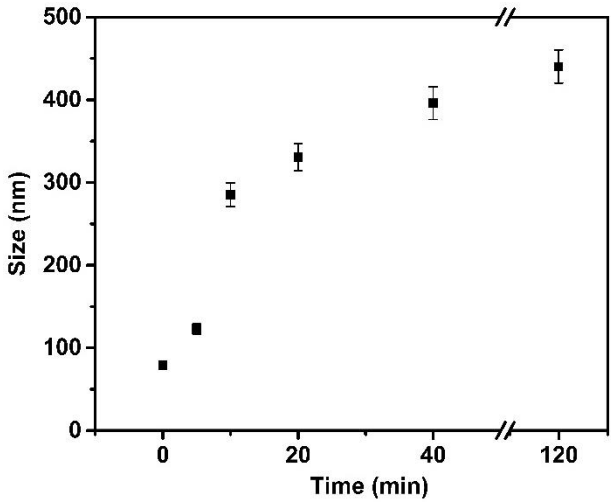

Figure 7.2.3.1.1 Size of the nanoparticles after photo-polymerization.

Afterwards, AEMH was chosen as the monomer and the polyelectrolyte chains were grafted onto the PS cores by photo-emulsion polymerization, which was carried out by UV-vis irradiation. In a typical run, 6.3 g AEMH was firstly dispersed into 20 ml water and then slowly added under stirring into 650 ml PS-HMEM water solution (2.0 wt%) in the photo reactor, followed by the removal of O_2 through purging with N_2 several times. After that, the mixture was irradiated for 60 minutes at room temperature by a mercury lamp of UV-reactor (Heraeus TQ150 Z3, Haraeus Noblelight, range of wavelength 200~600 nm). The suspension was then cleaned by ultrafiltration until the conductivity of the filtrate was between 3 μScm^{-1} to 5 μScm^{-1}. The resulted product was store in a polypropylene bottle for further characterization and use. The membranes with pores of 100 nm were applied.

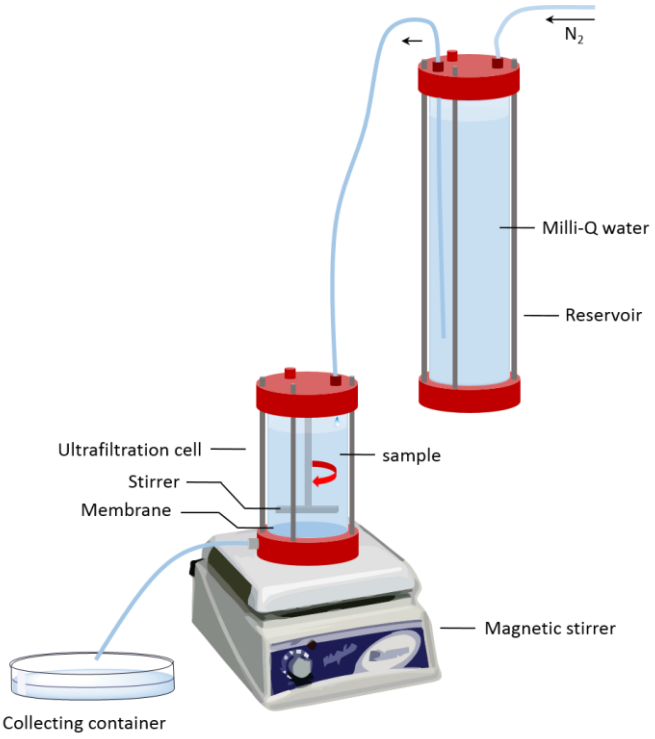

Figure 7.2.3.1.2 Schematic ultrafiltration cell for the purification of SPB nanoparticles.

As mentioned, the suspension of PS core as well as the SPB particles were cleaned by ultrafiltration Figure 7.2.3.1.1). The ultrafiltration cell contains a membrane of cellulose nitrate (Schleicher & Schuell and Millipore) with pore size of 50 or 100 nm. The polymer latex dispersion was filled into the ultrafiltration cell. Millipore water was pushed in from a reservoir cell by an overpressure of N_2. Generally, about 15 to 40 L water was consumed in the purification process. Unreacted monomers, dissolved polymers and surfactant molecules can pass through the membrane and be removed from the latex dispersion. The progress of the purification was monitored by measuring the conductivity of the serum in the collecting container. The polymer dispersion was stirred by magnetic stirring with the speed of about 300 rpm.

7.2.3.2 Coating of MoS_3 onto SPB nanospheres

The synthesis of hollow MoS_3 nanospheres was realized with an acid precipitation of MoS_3 on SPB nanospheres followed by the removal of SPB using THF. 0.2 g SPB was firstly dispersed in 200 ml water followed by addition of $(NH_4)_2MoS_4$ under vigorously stirring (about 300 rpm). The stirring was continued for another 3 hours in order to allow the complete adsorption of MoS_4^{2-} ions onto the surface of the brushes. The pH of the obtained suspension was adjusted to be ≤ 3 with HCl (1 mol/L) drop by drop under stirring. The addition of HCl initiated the

precipitation of dark red colloidal solids. The solution was further stirred for another 2 hours. At the end, solid products were collected by centrifugation for 30 minutes at 8000 rpm and washed with water for several times. In order to obtain the uniform coating of MoS_3 onto SPB templates, two different strategies have been tried (Table 7.2.3.2.1). For Recipe I, MoS_3 was coated onto SPB nanospheres with one step, while for Recipe II, the coating was divided into two steps. The MoS_3 growths in both methods were all based on the method described above. It was found the resulted coating of MoS_3 in Recipe II is more homogeneous, so it was used for the further synthesis. After freeze-drying, the solid products were finally annealed under argon at 200 ºC for 2 hours (heating rate: 2 ºC/min).

Table 7.2.3.2.1 Two recipes for the coating of MoS_3 onto SPB nanospheres.

		$(NH_4)_2MoS_4$ (g)
Recipe I	One step coating	0.2
Recipe II	Step I: first layer of MoS_3 coating	0.1
	Step II: second layer of MoS_3 coating	0.1

7.2.3.3 Preparation of the hollow MoS_3 nanospheres

The preparation procedure for the hollow MoS_3 nanospheres was mainly divided into three steps. Firstly, the SPB-MoS_3 solid products were diluted with 30 ml THF in a 50 ml glass bottle with a cap. The nanoparticles dispersed in THF were stirred for 12 h. Secondly, the dispersions were purified by centrifugation (4000 rpm) to remove the dissolved PS. During the centrifugation process (Figure 7.2.3.2.1 (b)), the residual nanoparticles were precipitated at the bottom, while the dissolved SPB stayed in THF as the supernatant. The nanoparticles were re-dispersed in THF after the centrifugation and were kept under stirring for 12 h. The centrifugation, decantation and re-dispersion process were carried out every 12 h every day for about two weeks until the nanoparticles were free of SPB. After that, the solution was centrifuged for 30 minutes at 4000 rpm and re-dispersed in THF for three times. Then the collected nanoparticles were dispersed in Milli-Q water and another three cycles of centrifugation, decantation and re-dispersion process were performed to replace THF from the cleaning procedure. In the end, the hollow MoS_3 nanospheres powder was obtained by freeze-drying overnight.

7.3 Electrochemical measurements

7.3.1 Hollow carbon-MoS_2-carbon nanoplates for supercapacitors

A three-electrode system was firstly applied to explore the working mechanism of hollow carbon-MoS_2-carbon nanoplates in symmetric supercapacitors. For the configuration, 1 M Li_2SO_4 was used as electrolyte, and an Ag/AgCl in saturated KCl electrode and a platinum wire were used as reference and counter electrode, respectively. The working electrode was prepared by mixing 1 mg active material, 190 μL H_2O, 50 μL ethanol and 10 μL 5 wt% Nafion under ultrasonication for 20 minutes to form a homogeneous dispersion. Afterwards, 10 μL of the mixture was drop casted on the surface of a glassy carbon electrode and was subsequently dried in air. Before measurements, the working electrode was kept in electrolytes for 12 hours. Typically, the surface area of the glassy carbon electrode was 0.077 cm^2.

A two-electrode symmetric cell was then fabricated for further measurements. The electrodes were prepared by mixing 80 wt% of the active materials with 10 wt% of carbon black as conductive additive and 10 wt% of PVDF as binder in NMP to form a homogeneous slurry. Then the slurry was spread with a doctor-blade apparatus on an aluminium foil used as a current collector and dried overnight in a vacuum oven at 60 ºC to remove the solvent. Then the electrode disks of 12 mm in diameter were cut. The mass loading was typically 0.5 mg/cm^2. The cut out electrodes were subsequently dried at 120 ºC under vacuum for 48 hours before measurements. The two-electrode symmetric supercapacitors were assembled by sandwiching a porous glassy microfiber membrane GF/A (thickness: 0.26 mm) between two electrodes which have the same mass loading, employing 100 μL 1.0 M Li_2SO_4 aqueous solution as an electrolyte. All two-electrode configurations were assembled with CR 2032 coin cells and the assembled cells were left for stabilization and wetting overnight before characterizations.

All three-electrode electrochemical measurements were carried out with GAMRY instruments (GAMRY interface 1000) and all two-electrode test cells were measured with a Biologic electrochemical workstation (MPG2 galvanostat/ potentiostat). All electrochemical characterizations were performed at room temperature. For three-electrode measurements, cyclic voltammetry (CV) was performed between different potential windows with a scan rate of 100 mV/s to determine the stability window and then at various scan rates in the potential window of -0.9 V to 0.5 V *vs* Ag/AgCl. In two-electrode measurements, CV was also performed at various scan rates from 0.5 to 300 mV/s. Three cycles were recorded for each measurement

to reduce the influence of wetting phenomena. The specific capacitance ($C_{sp\text{-}cv}$) is firstly calculated from CV curves using the following equation (1)[170, 267]:

$$C_{sp-CV} = 2 \times \frac{\int I(V)dV}{\nu m \Delta V} \qquad (1)$$

Where $\int I(V)dV$ is the area of the CV closed curve, ν is the scan rate (V/s), m is the mass loading of the active material on one electrode (g), ΔV is the potential window (V).

The specific energy density (*ED*) and power density (*PD*) can be calculated based on the following equations (2) and (3)[268]:

$$ED = \frac{1}{2} \times C_{sp}(\Delta V)^2 \qquad (2)$$

$$PD = \frac{1}{2} \times C_{sp}(\Delta V)\nu \qquad (3)$$

The capacitance of the two-electrode symmetric supercapacitor was also determined by galvanostatic charge/discharge (GCD) test at fixed currents from 0.1 to 5.0 A/g within the voltage range from 0 to 1.2 V. From the GCD cycling, the capacitance (C_{Gc}) can be calculated using the equation (4) as follows:

$$C_{GC} = \frac{I \times \Delta t}{\Delta V \times m} \qquad (4)$$

Where I is the applied current in ampere (A), Δt is the discharging time (s), ΔV is the potential range (V) and m corresponds to the total mass of active material of both electrodes (g). C_{GC} is the gravimetric capacitance of the symmetric supercapacitor (F/g). To obtain the gravimetric capacitance value of the hollow carbon-MoS_2-carbon nanoplates in symmetric supercapacitors, the above value was multiplied per 4 as shown in equation (5):

$$C_{sp-GC} = 4 \times C_{GC} \qquad (5)$$

The same procedure was applied to obtain the areal capacitance of the supercapacitor and material by replacing the mass values with the area of the electrodes.

The electrochemical impedance spectroscopy of the two-electrode systems was conducted at open circuit voltage with the frequency range from 20 kHz to 10 mHz. The recorded values were fitted with ZView software Version: 2.1C.

7.3.2 Hollow carbon nanoplates for "water-in-salt" supercapacitors

1 m and 21 m (m: mol-salt in kg-solvent) LiTFSI electrolytes were prepared by dissolving respective amounts of LiTFSI in water (HPLC grade) and stirring for 24 hours before use.

Symmetric two-electrode measurements were performed in 2032 coin cells with the "water-in-salt" solution as electrolyte and glass fiber as separator. Electrodes were fabricated by mixing the active material, carbon black and PTFE with the mass ratio of 8:1:1. The mixtures were dried naturally to partially evaporate solvents. The resulting black pastes were then cold rolled into films with a certain thickness depending on the case, subsequently dried at 60 ºC to remove all traces of ethanol. Afterwards, the films were cut into small pieces with the mass loading of hollow carbon nanoplates about 2 mg/cm^2. To determine the packing density of the electrode, the thickness and geometric area of the compressed electrode were measured. The calculated packing density is about 1.54±0.15 g cm^{-3}. Each electrode was obtained by sandwiching the film between two pieces of stainless steel (SS, type 316, 40 mesh, 1 cm^2) grids and pressing to 10 ton force to facilitate electrical connection. CV was conducted between different potential windows to determine the stability window of the system and the impedance spectroscopy was performed with the frequency range from 1 MHz to 10 mHz at different voltages to find the resistance change during CV scanning. The temperature based measurements, including electrochemical impedance, CV and galvanostatic charge/discharge was performed in a GAMRY instrument (GAMRY interface 1000) connected to a MTC-Multi Temperature Chamber (Arbin, USA). The assembled cells were put into the chamber and left for one hour at the set temperature before each measurement. The impedance spectroscopy was performed with the frequency range from 1 MHz to 10 mHz, CV was measured at 50 mV/s and cells were charged and discharged at the current density of 1 A/g at different temperatures.

All electrochemical measurements were carried out with GAMRY instruments (GAMRY interface 1000). The recorded values of impedance were fitted with ZView software Version: 2.1C.

7.3.3 Hollow MoS_3 nanospheres for "water-in-salt" Li-ion batteries

The electrochemical properties of the hollow MoS_3 nanospheres were evaluated in both CR 2032 and pouch cells testing against $LiMn_2O_4$ as counter electrode. The electrodes were fabricated by uniformly mixing active material, carbon black and PTFE (60 wt% dispersion in H_2O) with the weight ratio of 8:1:1 for $LiMn_2O_4$ and 7:2:1 for hollow MoS_3 nanospheres

suspended in ethanol under agitation, respectively. Carbon black was required to enhance the electronic conductivity of the electrodes and PTFE was chosen to provide a good mechanical integrity to the electrodes, especially when preparing the thick films. The mixtures were dried naturally to partially evaporate solvents. The resulting black pastes were then cold rolled into films with a certain thickness depending on the case, subsequently dried at 60 ºC to remove all traces of ethanol. Afterwards, the films were cut into small pieces with the mass ratio of $LiMn_2O_4$/hollow MoS_3 nanospheres set to 2:1 and the loading of MoS_3 about 2 mg/cm^2. Each electrode was obtained by sandwiching the film between two pieces of stainless steel (SS, type 316, 40 mesh) grids and pressing to 10 ton force to facilitate electrical connection. The SS grids were thoroughly cleaned with ethanol under ultrasonication at 37 kHz for half an hour, followed by washing with water for several times and drying before use. The comparative electrodes composed of bulk MoS_3 and MoO_3 were prepared as the same way. Aqueous electrolytes were prepared by molarity (mol-salt in kg-solvent) with certain concentrations and all electrolytes were stirred at 300 rpm for 24 hours before use.

The full Li-ion batteries in both CR 2032-type coin cells and pouch cells were using $LiMn_2O_4$ as cathode, hollow MoS_3 nanospheres as anode and porous glassy microfiber membranes GF/A (thickness: 0.26 mm) as separator. The pouch cell was fabricated with the cathode and anode spaced by the separator, and sealed with the pouch film. Copper tabs were used to connect the electrode to the outside cycler. In total, 100 μL and 500 μL electrolytes were added to the coin cell and the pouch cell, respectively. Cyclic voltammetry and galvanostatic electrochemical cycling curves were recorded with a Biologic electrochemical workstation (MPG2 galvanostatic/potentiostat) in the voltage range of 0.7 to 2.0 V at room temperature. The capacitance in this work was calculated based on the mass of active materials.

The electrochemical impedance spectroscopy of coin cells was performed at open circuit voltage, by sweeping the frequencies from 20 kHz to 10 mHz with an amplitude of 10 mV.

7.4 Characterization

7.4.1 Transmission electron microscopy (TEM)

TEM was performed to characterize the morphology and size of as-synthesized nanoparticles. The conventional TEM is a wide-beam technique, in which a close-to parallel electron beam floods the whole area of interest and the image, formed by an imaging lens after the thin specimen. During the formation of images, the beam of electrons from the electron gun is focused into a small, thin, coherent beam by the use of the condenser lens. This beam is

restricted by the condenser aperture, which excludes high angle electrons. The beam then strikes the specimen and parts of it are transmitted depending upon the thickness and electron transparency of the specimen. This transmitted portion is focused by the objective lens into an image on phosphor screen or charge coupled device camera. Optional objective apertures can be used to enhance the contrast by blocking out high-angle diffracted electrons.[269] The TEM images are formed in two stages, as shown in Figure 7.4.1.1. Stage A is the scattering of an incident electron beam by the specimen. This scattered radiation passes through an objective lens, which focuses it to form the primary image. Stage B uses the primary image obtained in stage A and magnifies this image using additional lenses to form a highly magnified final image. In the process of forming the primary image, the objective lens produces a diffraction pattern at its back focal plane. The diffraction pattern is a Fourier transform of the scattered electron wave. The primary image is the Fourier transform of the diffraction pattern and is an interference pattern of the beams formed at the back focal plane of the objective lens.[270]

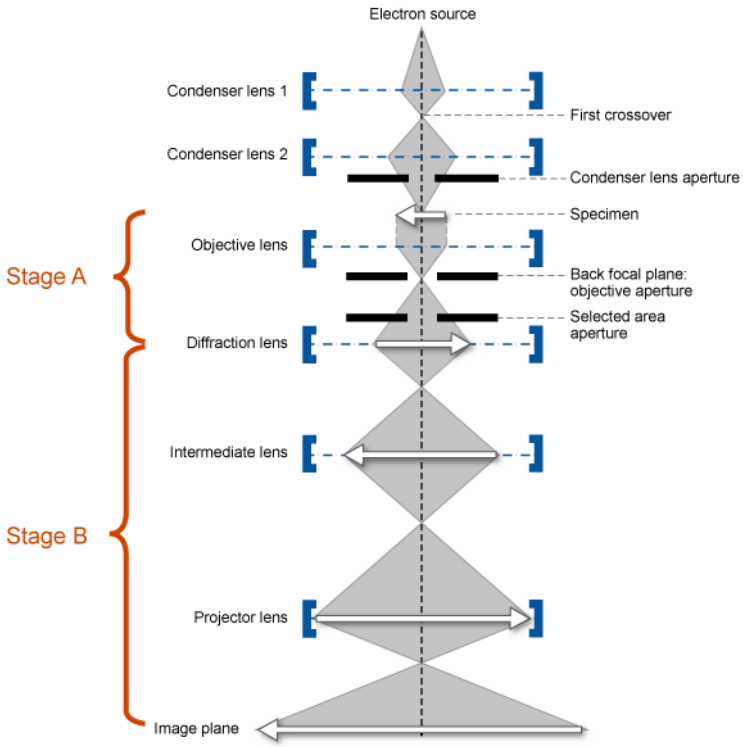

Figure 7.4.1.1 Schematic representation of TEM.[270]

Prior to sample preparation for TEM, carbon-coated copper TEM grids (200 mesh, Science Services, Munich, Germany) were pre-treated with glow discharge for 20 s. 5 µl of dispersion (0.05-0.1 wt%) was dropped onto the grids to prepare the TEM specimens. After naturally drying in fume hood for at least 1 hour, the specimen was inserted into the sample holder

(EM21010, JEOL GmbH, Eching, Germany) and then transferred to a JEOL JEM-2100 with a LaB_6 cathode (JEOL GmbH, Eching, Germany) at a 200 kV acceleration voltage. All images were recorded by a bottom-mounted 4k CMOS camera system (TemCam-F416, TVIPS, Gauting, Germany) and proceeded with a digital imaging processing system (EM-Menu 4.0, TVIPS, Gauting, Germany).

The morphology of SPB-MoS_3 particles was visualized by cryo-TEM. Samples were prepared by dropping 5 µl of the sample dispersion (0.05-0.1 wt%) on a lacey carbon-coated TEM grid (200 mesh, Science Services, Munich, Germany) and most of the liquid were removed with blotting paper, leaving a thin film of particles stretched over the grid holes. The specimen then were vitrified by rapidly immersing the samples into liquid ethane at its freezing point and cooled to 90 K using an automated plunge freezer (Zeiss Cryobox, Zeiss NTS GmbH, Oberkochen, Germany). The temperature was kept constant during all preparation procedures. After freezing, the sample was inserted into a pre-cooled Gatan CT3500 cryo-transfer holder and transferred into a JEOL JEM-2100, operating at 200 kV equipped with a bottom mounted 4k CMOS camera (TemCam-F416, TVIPS).

Scanning transmission electron microscopy (STEM) was used to investigate the elemental mapping of the as-synthesized nanoparticles and sample preparing procedure is the same as TEM. Typically, a drop of dispersion was dried on a standard lacey carbon-coated TEM grid. STEM data was collected on a JEOL HEM-2200FS transmission electron microscope operated at 200 kV and equipped with a high angle annular dark field (HAADF) STEM detector and a Brucker silicon detector for energy dispersed X-ray spectroscopy (EDX).

All images were processed by the free software package ImageJ.

7.4.2 Scanning electron microscopy (SEM) and wavelength-dispersive spectroscopy (WDS)

SEM imaging was operated with a LEO GEMINI 1530 field emission SEM and WDS was measured by an Axios max X-ray fluorescence spectrometer (XRF) at 2 kV. The samples were prepared by dropping 100 µL of dispersions (0.05 wt%) on the silicon wafer surface and drying at room temperature.

SEM produces images by recording various signals resulting from interactions of an electron beam with the sample as it is scanned in a raster pattern across the sample surface. A fine electron probe, with a spot size from a few angstroms to several hundred nanometers, is

generated by focusing electrons emanating from an electron source onto the surface of the specimen using a series of electro-optical lens elements. The combination of the source and the lens elements is called the electron column. Electrons are emitted from a very fine heated filament with a high electrostatic extraction potential. The electrons are then immediately accelerated to a desired kinetic energy and propagate down the electron column. Next, some of the electrons are cut off by an aperture. The focusing strength of the condenser lens and the size of the aperture determine the beam current in the final spot. A final objective lens assembly then focuses the beam down to the desirable spot size. An image is built up simply by scanning the electron beam across the specimen in exact synchrony with the scan of the electron beam in the cathode ray tube.[271]

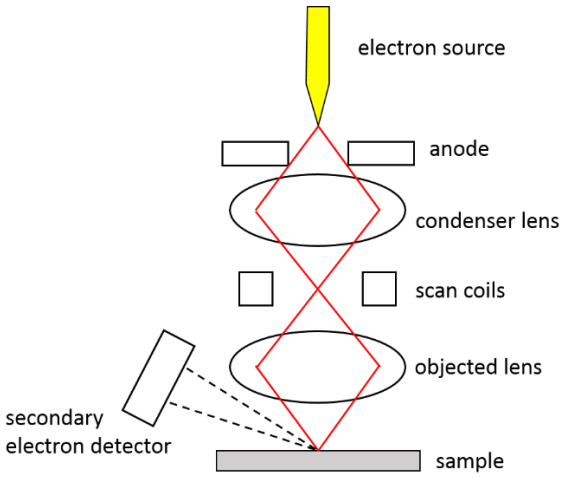

Figure 7.4.2.1 Schematic representation of basic components in SEM.

WDS uses the characteristic X-rays generated from a sample bombarded with electrons to identify the elemental constituents comprising the sample. The technique generates a spectrum in which the peaks correspond to specific X-ray lines and the element can be easily identified. The electron beam is generated by the electron gun encased within the column of the XRF. When the electron beam interacts with the sample surface, secondary and backscattered electrons are emitted from the excited surface. The topography revealed by the collected electrons is used to develop an image of the sample surface. In addition, the wavelength and intensities of these collected electrons are analyzed and used to identify the elements contained within the near sample surface.[272]

7.4.2.1 SEM measurements of MoS_3 electrodes in "water-in-salt" Li-ion batteries

Pristine and cycled electrodes for SEM measurements were taken from Swagelok-type batteries assembled same as the coin cells described above. The electrodes here are composed of hollow MoS_3 nanospheres, carbon black and PTFE (7:2:1) in mass. The cycled electrode was cleaned thoroughly with water and dried naturally before measurement.

7.4.3 X-ray diffraction (XRD)

XRD measurements were performed in a Bruker D8 diffractometer in the locked coupled mode (2θ ranging from 10 º to 90 º) with Cu Kα radiation working at 40 kV with 0.05 º/min scan rate, the incident wavelength is 1.5406 Å. For the accomplished measurements the acceleration voltage is set to 40 kV and the filament current to 40 mA.

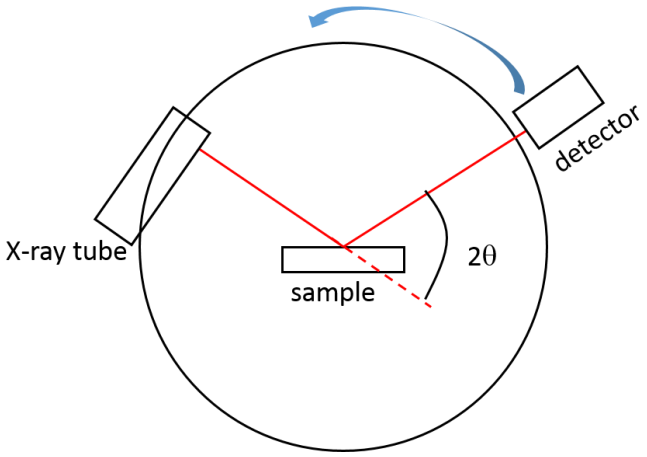

Figure 7.4.3.1 Schematic representation of the XRD measurement.

X-rays are produced by bombarding a metal with high-energy electrons. They can be diffracted when passed through a crystal. X-ray diffraction depends on the range of the incident beam, which can be described in the Bragg equation, in the form

$$n\lambda = 2d \sin \theta$$

where λ is the wavelength of the incident X-ray (in the range between 0.001 and 50 Å), d is the interplanar spacing of the crystal and n (=1, 2, …) is an integer and is associated with the a given interference pattern.[273]

X-ray diffractometers consist of three basic elements: an X-ray tube, a sample holder, and an X-ray detector (Figure 7.4.3.1). X-rays are generated in a cathode ray tube by heating a filament to produce electrons, accelerating the electrons toward a target by applying a voltage, and bombarding the target material with electrons. When electrons have sufficient energy to dislodge inner shell electrons of the target material, characteristic X-ray spectra are produced.

Analysis of XRD gives numerical values of two important parameters: the interplanar spacing and the intensity of diffraction. Interplanar spacing is characteristic of the pattern of the crystal from which one learns the packing of the repeating units, while the intensities of a certain number of diffractions can provide information on the structure of a crystal.[273]

7.4.3.1 Ex-situ XRD measurements of MoS_3 electrodes in "water-in-salt" Li-ion batteries

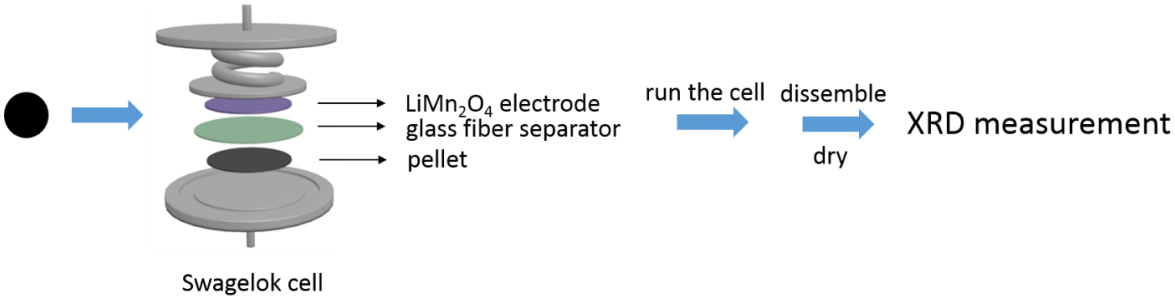

Figure 7.4.3.1.1 Schematic sample preparation routine for ex-situ XRD measurement.

For the XRD measurements on cycled electrodes, pellet-like electrodes composed of hollow MoS_3 nanospheres and carbon black (8:2) in mass excluding binder were utilized (Figure 7.4.3.1.1). Firstly, MoS_3 powder and carbon black were thoroughly mixed in the crucible. Then the mixture was pressed into a hard pellet by a manual hydraulic press (Tmax, Xiamen) with the pressure of 1 ton, followed by being cut into a circular pellet suitable for the Swagelok cell. Swagelok-type batteries were assembled with electrodes composed of $LiMn_2O_4$ as cathode and pellet-like electrodes of hollow MoS_3 nanospheres as anode, using 21 m LiTFSI as electrolytes. After charging/discharging treatments, the electrodes were extracted from the batteries and dried at natural conditions prior to the measurement.

7.4.4 Raman spectroscopy

Raman spectroscopy on nanomaterials was carried out by using a LabRAM HR Evolution Raman spectrometer. The wavelength of the HeNe laser applied is 633 nm. Samples were prepared by loading dried powders of nanoparticles (5-10 mg) on a clean glass sheet.

Raman spectroscopy is the study of inelastic scattering of light. The inelasticity stems from a transfer of energy between the incident radiation field and the material under investigation. The technique provides important information about the vibrational state of matter. When light is irradiated on molecules, it is scattered by molecules. Most of scattered light have the same frequency with incident light but some fraction of light have different frequency due to interaction between oscillation of light and molecular vibration. The phenomenon that the light is scattered with frequency change is called Raman scattering. Because this frequency modulation is specific to molecular vibration and phonon in crystal, it is possible to analyze composition of material or crystal lattice information by anayzing spectrum of Raman scattered light.[274]

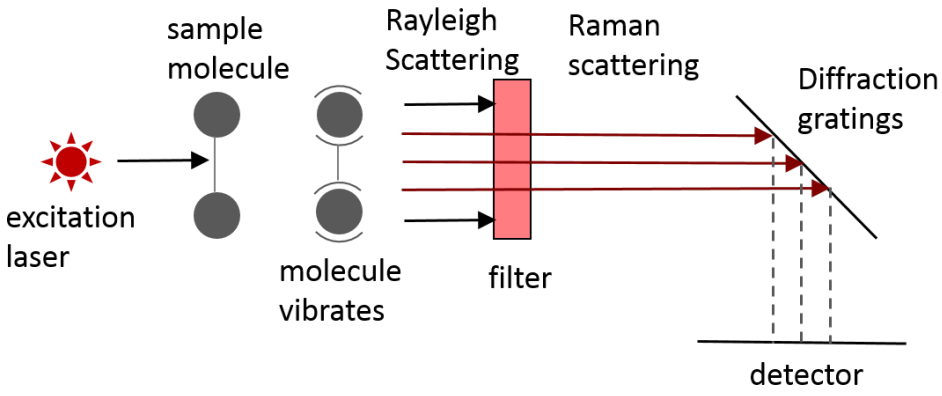

Figure 7.4.4.1 Schematic presentation of Raman spectroscopy.

7.4.5 Thermogravimetric analysis (TGA)

TGA measurements were conducted to analyze physical and chemical properties of as-synthesized nanomaterials with constant heating. It provides physical and chemical information about the nanomaterials such as phase transitions, chemisorptions, solid-gas reactions and so on. These processes can be measured by the change in mass in respect to the temperature. The experiments were performed on a Perkin-Elmer Pyris 1 under a continuous air stream. 10 mg of dried samples were filled in the crucible and heated from 25 ºC to 680 ºC at a heating rate of 10 ºC/min. In case of the hollow carbon-MoS_2-carbon nanoplates, the weight loss was attributed to carbon and the oxidation of MoS_2 to MoO_2.

7.4.6 Nitrogen adsorption/desorption measurement

Specific surface area and pore size of nanomaterials were determined by nitrogen adsorption/desorption measurements, which were conducted by using a Quantachrome

Autosorb-1 systems at 77 K. Before all measurements, samples were outgassed at 100 ºC for 12 hours under vacuum. Specific surface areas of samples were calculated using the Brunauer-Emmett-Teller (BET) method based on a multipoint analysis and the pore size distributions were obtained from the Barrett-Joyner-Halenda (BJH) method.

7.4.7 X-ray photoelectron spectroscopy (XPS)

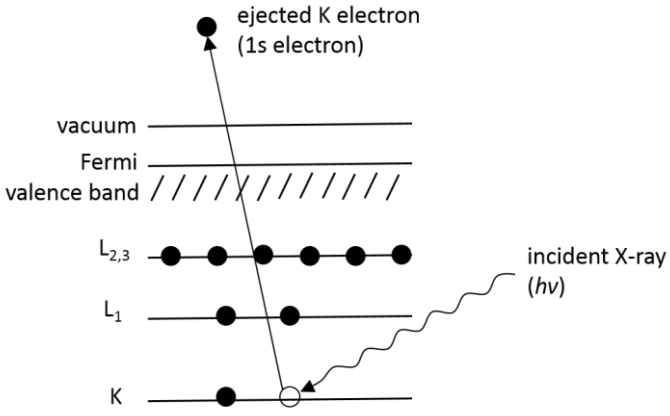

Figure 7.4.7.1 Schematic diagram of the XPS process, showing photoionization of an atom by the ejection of a 1s electron.[275]

XPS measurements were performed using a ThermoFisher Scientific ESCALAB 250Xi instrument, with an Al Kα source, in constant analyzer energy mode with a pass energy of 50 eV and a spot size of 400 μm.

XPS is used to measure the energy of electrons emitted from the surface of a material. In the simplest terms, an electron spectrometer consists of the sample under investigation, a source of primary radiation and an electron energy analyzer contained within a vacuum chamber operating in the ultra-high vacuum regime. The process of photoemission is shown in Figure 7.4.7.1, where an electron from the K shell is ejected from the atom (a 1s photoelectron). In XPS, the ejection of an electron forms a core level by a X-ray photon of energy *hv*. The energy of the emitted photoelectrons is then analyzed by the electron spectrometer and the data presented as a graph of intensity *vs.* electron energy. The photoelectron spectrum will reproduce the electronic structure of an element quite accurately since all electrons with a binding energy less than the photon energy will feature in the spectrum. The kinetic energy (E_k) of the electron is experimental quantity measured by the spectrometer, which depends on the photon energy of the X-rays employed. The binding energy of the electron (E_B) is the parameter which identifies

the electron specifically, both in terms of its parent element and atomic energy level. The relationship between the parameters involved in the XPS experiment is:

$$E_B = h\nu - E_k - W$$

where $h\nu$ is the photon energy, E_k is the kinetic energy of the electron, and W is the spectrometer work function.[275]

Bibliography

(1) Mizushima, K.; Jones, P. C.; Wiseman, P. J.; Goodenough, J. B., LixCoO$_2$ "(0 less-than x less-than-or-equal-to 1) - A New Cathode Material for Batteries of High-Energy Density. *Mater. Res. Bull.* **1980,** *15* (6), 783-789.

(2) Wang, G. J.; Fu, L. J.; Zhao, N. H.; Yang, L. C.; Wu, Y. P.; Wu, H. Q., An Aqueous Rechargeable Lithium Battery with Good Cycling Performance. *Angew. Chem.-Int. Edit.* **2007,** *46* (1-2), 295-297.

(3) Yang, Z. G.; Zhang, J. L.; Kintner-Meyer, M. C. W.; Lu, X. C.; Choi, D. W.; Lemmon, J. P.; Liu, J., Electrochemical Energy Storage for Green Grid. *Chem. Rev.* **2011,** *111* (5), 3577-3613.

(4) Xu, K., Nonaqueous Liquid Electrolytes for Lithium-Based Rechargeable Batteries. *Chem. Rev.* **2004,** *104* (10), 4303-4417.

(5) Zhong, C.; Deng, Y. D.; Hu, W. B.; Qiao, J. L.; Zhang, L.; Zhang, J. J., A Review of Electrolyte Materials and Compositions for Electrochemical Supercapacitors. *Chem. Soc. Rev.* **2015,** *44* (21), 7484-7539.

(6) Vangari, M.; Pryor, T.; Jiang, L., Supercapacitors: Review of Materials and Fabrication Methods. *J. Energy Eng.-ASCE* **2013,** *139* (2), 72-79.

(7) Chabot, V.; Higgins, D.; Yu, A. P.; Xiao, X. C.; Chen, Z. W.; Zhang, J. J., A Review of Graphene and Graphene Oxide Sponge: Material Synthesis and Applications to Energy and the Environment. *Energy Environ. Sci.* **2014,** *7* (5), 1564-1596.

(8) Tian, Y.; Yan, J. W.; Xue, R.; Yi, B. L., Influence of Electrolyte Concentration and Temperature on the Capacitance of Activated Carbon. *Acta Phys.-Chim. Sin.* **2011,** *27* (2), 479-485.

(9) Conway, B. E., *Electrochemical Supercapacitors: Scientific Fundamentals and Technological Applications*. Springer Science & Business Media: 2013.

(10) Yan, X. D.; Yu, Y. H.; Yang, X. P., Effects of Electrolytes on the Capacitive Behavior of Nitrogen/Phosphorus Co-Doped Nonporous Carbon Nanofibers: An Insight into the Role of Phosphorus Groups. *Rsc Adv.* **2014,** *4* (48), 24986-24990.

(11) Perret, P.; Khani, Z.; Brousse, T.; Belanger, D.; Guay, D., Carbon/PbO$_2$ Asymmetric Electrochemical Capacitor Based on Methanesulfonic Acid Electrolyte. *Electrochim. Acta* **2011,** *56* (24), 8122-8128.

(12) Andreas, H. A.; Lussier, K.; Oickle, A. M., Effect of Fe-Contamination on Rate of Self-Discharge in Carbon-Based Aqueous Electrochemical Capacitors. *J. Power Sources* **2009,** *187* (1), 275-283.

(13) Nam, K. W.; Kim, K. B., A study of the Preparation of NiO_x Electrode via Electrochemical Route for Supercapacitor Applications and Their Charge Storage Mechanism. *J. Electrochem. Soc.* **2002,** *149* (3), A346-A354.

(14) Demarconnay, L.; Raymundo-Pinero, E.; Beguin, F., A Symmetric Carbon/Carbon Supercapacitor Operating at 1.6 V by Using a Neutral Aqueous Solution. *Electrochem. Commun.* **2010,** *12* (10), 1275-1278.

(15) Li, S. H.; Qi, L.; Lu, L. H.; Wang, H. Y., Facile Preparation and Performance of Mesoporous Manganese Oxide for Supercapacitors Utilizing Neutral Aqueous Electrolytes. *Rsc Adv.* **2012,** *2* (8), 3298-3308.

(16) Armand, M.; Tarascon, J. M., Building Better Batteries. *Nature* **2008,** *451* (7179), 652-657.

(17) Bin, D.; Wen, Y.; Wang, Y.; Xia, Y., The Development in Aqueous Lithium-Ion Batteries. *J. Energy Chem.* **2018,** *27* (2095-4956), 1521.

(18) Tang, W.; Zhu, Y. S.; Hou, Y. Y.; Liu, L. L.; Wu, Y. P.; Loh, K. P.; Zhang, H. P.; Zhu, K., Aqueous Rechargeable Lithium Batteries as an Energy Storage System of Superfast Charging. *Energy Environ. Sci.* **2013,** *6* (7), 2093-2104.

(19) Wang, Y. G.; Yi, J.; Xia, Y. Y., Recent Progress in Aqueous Lithium-Ion Batteries. *Adv. Energy Mater.* **2012,** *2* (7), 830-840.

(20) Wen, Y. P.; Chen, L.; Pang, Y.; Guo, Z. W.; Bin, D.; Wang, Y. G.; Wang, C. X.; Xia, Y. Y., TiP_2O_7 and Expanded Graphite Nanocomposite as Anode Material for Aqueous Lithium-Ion Batteries. *ACS Appl. Mater. Interfaces* **2017,** *9* (9), 8075-8082.

(21) Kalhoff, J.; Bresser, D.; Bolloli, M.; Alloin, F.; Sanchez, J. Y.; Passerini, S., Enabling LiTFSI-based Electrolytes for Safer Lithium-Ion Batteries by Using Linear Fluorinated Carbonates as (Co) Solvent. *ChemSusChem* **2014,** *7* (10), 2939-2946.

(22) Lux, S. F.; Terborg, L.; Hachmoller, O.; Placke, T.; Meyer, H. W.; Passerini, S.; Winter, M.; Nowak, S., LiTFSI Stability in Water and Its Possible Use in Aqueous Lithium-Ion Batteries: pH Dependency, Electrochemical Window and Temperature Stability. *J. Electrochem. Soc.* **2013,** *160* (10), A1694-A1700.

(23) Han, H. B.; Zhou, S. S.; Zhang, D. J.; Feng, S. W.; Li, L. F.; Liu, K.; Feng, W. F.; Nie, J.; Li, H.; Huang, X. J.; Armand, M.; Zhou, Z. B., Lithium Bis(fluorosulfonyl)imide (LiFSI) as

Conducting Salt for Nonaqueous Liquid Electrolytes for Lithium-Ion Batteries: Physicochemical and Electrochemical Properties. *J. Power Sources* **2011,** *196* (7), 3623-3632.

(24) Pohl, B.; Grunebaum, M.; Drews, M.; Passerini, S.; Winter, M.; Wiemhofer, H. D., Nitrile Functionalized Silyl Ether with Dissolved LiTFSI as New Electrolyte Solvent for Lithium-Ion Batteries. *Electrochim. Acta* **2015,** *180*, 795-800.

(25) Suo, L. M.; Borodin, O.; Gao, T.; Olguin, M.; Ho, J.; Fan, X. L.; Luo, C.; Wang, C. S.; Xu, K., "Water-in-Salt" Electrolyte Enables High-Voltage Aqueous Lithium-Ion Chemistries. *Science* **2015,** *350* (6263), 938-943.

(26) Sun, W.; Suo, L. M.; Wang, F.; Eidson, N.; Yang, C. Y.; Han, F. D.; Ma, Z. H.; Gao, T.; Zhu, M.; Wang, C. S., "Water-in-Salt" Electrolyte Enabled $LiMn_2O_4/TiS_2$ Lithium-Ion Batteries. *Electrochem. Commun.* **2017,** *82*, 71-74.

(27) Zhao, J. W.; Li, Y. Q.; Peng, X.; Dong, S. M.; Ma, J.; Cui, G. L.; Chen, L. Q., High-Voltage $Zn/LiMn_{0.8}Fe_{0.2}PO_4$ Aqueous Rechargeable Battery by Virtue of "Water-in-Salt" Electrolyte. *Electrochem. Commun.* **2016,** *69*, 6-10.

(28) Wang, F.; Suo, L. M.; Liang, Y. J.; Yang, C. Y.; Han, F. D.; Gao, T.; Sun, W.; Wang, C. S., Spinel $LiNi_{0.5}Mn_{1.5}O_4$ Cathode for High-Energy Aqueous Lithium-Ion Batteries. *Adv. Energy Mater.* **2017,** *7* (8), 6.

(29) Dong, X. L.; Yu, H. C.; Ma, Y. Y.; Bao, J. L.; Truhlar, D. G.; Wang, Y. G.; Xia, Y. Y., All-Organic Rechargeable Battery with Reversibility Supported by "Water-in-Salt" Electrolyte. *Chem.-Eur. J.* **2017,** *23* (11), 2560-2565.

(30) Suo, L. M.; Borodin, O.; Sun, W.; Fan, X. L.; Yang, C. Y.; Wang, F.; Gao, T.; Ma, Z. H.; Schroeder, M.; von Cresce, A.; Russell, S. M.; Armand, M.; Angell, A.; Xu, K.; Wang, C. S., Advanced High-Voltage Aqueous Lithium-Ion Battery Enabled by "Water-in-Bisalt" Electrolyte. *Angew. Chem.-Int. Edit.* **2016,** *55* (25), 7136-7141.

(31) Angell, C. A.; Byrne, N.; Belieres, J. P., Parallel Developments in Aprotic and Protic Ionic Liquids: Physical Chemistry and Applications. *Accounts Chem. Res.* **2007,** *40* (11), 1228-1236.

(32) Reber, D.; Kuhnel, R. S.; Battaglia, C., High-Voltage Aqueous Supercapacitors Based on NaTFSI. *Sustain. Energ. Fuels* **2017,** *1* (10), 2155-2161.

(33) Mahankali, K.; Thangavel, N. K.; Ding, Y.; Putatunda, S. K.; Arava, L. M. R., Interfacial Behavior of Water-in-Salt Electrolytes at Porous Electrodes and its Effect on Supercapacitor Performance. *Electrochim. Acta* **2019,** *326*, 8.

(34) Lannelongue, P.; Bouchal, R.; Mourad, E.; Bodin, C.; Olarte, M.; le Vot, S.; Favier, F.; Fontaine, O., "Water-in-Salt" for Supercapacitors: A Compromise between Voltage, Power Density, Energy Density and Stability. *J. Electrochem. Soc.* **2018,** *165* (3), A657-A663.

(35) Zang, X. N.; Shen, C. W.; Kao, E.; Warren, R.; Zhang, R. P.; Teh, K. S.; Zhong, J. W.; Wei, M. S.; Li, B. X.; Chu, Y.; Sanghadasa, M.; Schwartzberg, A.; Lin, L. W., Titanium Disulfide Coated Carbon Nanotube Hybrid Electrodes Enable High Energy Density Symmetric Pseudocapacitors. *Adv. Mater.* **2018,** *30* (5), 8.

(36) Dou, Q. Y.; Lei, S. L.; Wang, D. W.; Zhang, Q. N.; Xiao, D. W.; Guo, H. W.; Wang, A. P.; Yang, H.; Li, Y. L.; Shi, S. Q.; Yan, X. B., Safe and High-Rate Supercapacitors Based on an "Acetonitrile/Water in Salt" Hybrid Electrolyte. *Energy Environ. Sci.* **2018,** *11* (11), 3212-3219.

(37) Zhu, Y. W.; Murali, S.; Stoller, M. D.; Ganesh, K. J.; Cai, W. W.; Ferreira, P. J.; Pirkle, A.; Wallace, R. M.; Cychosz, K. A.; Thommes, M.; Su, D.; Stach, E. A.; Ruoff, R. S., Carbon-Based Supercapacitors Produced by Activation of Graphene. *Science* **2011,** *332* (6037), 1537-1541.

(38) Xia, C.; Chen, W.; Wang, X. B.; Hedhili, M. N.; Wei, N. N.; Alshareef, H. N., Highly Stable Supercapacitors with Conducting Polymer Core-Shell Electrodes for Energy Storage Applications. *Adv. Energy Mater.* **2015,** *5* (8), 9.

(39) Brown, C. R.; McCalla, E.; Watson, C.; Dahn, J. R., Combinatorial Study of the Li-Ni-Mn-Co Oxide Pseudoquaternary System for Use in Li-Ion Battery Materials Research. *ACS Comb. Sci.* **2015,** *17* (6), 381-391.

(40) Geng, P. B.; Zheng, S. S.; Tang, H.; Zhu, R. M.; Zhang, L.; Cao, S.; Xue, H. G.; Pang, H., Transition Metal Sulfides Based on Graphene for Electrochemical Energy Storage. *Adv. Energy Mater.* **2018,** *8* (15), 26.

(41) Yuan, H.; Kong, L.; Li, T.; Zhang, Q., A Review of Transition Metal Chalcogenide/Graphene Nanocomposites for Energy Storage and Conversion. *Chin. Chem. Lett.* **2017,** *28* (12), 2180-2194.

(42) Hauck, J.; Mika, K., Ordering of Metal Atoms in Wurtzite and Sphalerite Structures. *J. Solid State Chem.* **1998,** *138* (2), 334-341.

(43) Chandrasekaran, S.; Yao, L.; Deng, L. B.; Bowen, C.; Zhang, Y.; Chen, S. M.; Lin, Z. Q.; Peng, F.; Zhang, P. X., Recent Advances in Metal Sulfides: From Controlled Fabrication to Electrocatalytic, Photocatalytic and Photoelectrochemical Water Splitting and Beyond. *Chem. Soc. Rev.* **2019,** *48* (15), 4178-4280.

(44) Rao, C. N. R.; Pisharody, K. P. R., Transition Metal Sulfides. *Prog. Solid State Ch.* **1976,** *10*, 207-270.

(45) Yu, X. Y.; Yu, L.; Lou, X. W., Hollow Nanostructures of Molybdenum Sulfides for Electrochemical Energy Storage and Conversion. *Small Methods* **2017,** *1* (1-2), 8.

(46) Wang, T.; Chen, S.; Pang, H.; Xue, H.; Yu, Y., MoS2-Based Nanocomposites for Electrochemical Energy Storage. *Adv. Sci. (Weinh)* **2017,** *4* (2), 1600289.

(47) Zhang, W. S.; Zhang, P. P.; Su, Z. Q.; Wei, G., Synthesis and Sensor Applications of MoS_2-Based Nanocomposites. *Nanoscale* **2015,** *7* (44), 18364-18378.

(48) Hart, P. B.; Brown, C. S., The Synthesis of New Calcium Borate Compounds by Hydrothermal Methods. *J. Inorg. Nucl. Chem.* **1962,** *24* (DEC), 1057-1065.

(49) Lei, Z. B.; You, W. S.; Liu, M. Y.; Zhou, G. H.; Takata, T.; Hara, M.; Domen, K.; Li, C., Photocatalytic Water Reduction under Visible Light on a Novel $ZnIn_2S_4$ Catalyst Synthesized by Hydrothermal Method. *Chem. Commun.* **2003,** (17), 2142-2143.

(50) Sun, T. H.; Li, Z. P.; Liu, X. H.; Ma, L. M.; Wang, J. Q.; Yang, S. R., Facile Construction of 3D Graphene/MoS_2 Composites as Advanced Electrode Materials for Supercapacitors. *J. Power Sources* **2016,** *331*, 180-188.

(51) Mdleleni, M. M.; Hyeon, T.; Suslick, K. S., Sonochemical Synthesis of Nanostructured Molybdenum Sulfide. *J. Am. Chem. Soc.* **1998,** *120* (24), 6189-6190.

(52) Hu, J. J.; Zabinski, J. S.; Sanders, J. H.; Bultman, J. E.; Voevodin, A. A., Pulsed Laser Syntheses of Layer-Structured WS_2 Nanomaterials in Water. *J. Phys. Chem. B* **2006,** *110* (18), 8914-8916.

(53) Zhang, T.; Kong, L. B.; Dai, Y. H.; Yan, K.; Shi, M.; Liu, M. C.; Luo, Y. C.; Kang, L., A Facile Strategy for the Preparation of MoS_3 and its Application as a Negative Electrode for Supercapacitors. *Chem.-Asian J.* **2016,** *11* (17), 2392-2398.

(54) Zhou, Y. L.; Li, Y. Y.; Wang, Q. Q.; Wang, Q.; Du, R.; Zhang, M.; Sun, X. Q.; Zhang, X. Y.; Kang, L. T.; Jiang, F. Y., Ultrasmall MoS_3 Loaded GO Nanocomposites as High-Rate and Long-Cycle-Life Anode Materials for Lithium- and Sodium-Ion Batteries. *ChemElectroChem* **2019,** *6* (12), 3113-3119.

(55) Wu, P. R.; Cheng, Z. L.; Kong, Y. C.; Ma, Z. S.; Liu, Z., Templated Synthesis of Plate-like MoS2 Nanosheets Assisted with HNTs and their Tribological Performance in Oil. *J. Nanopart. Res.* **2018,** *20* (5), 12.

(56) Cherusseri, J.; Choudhary, N.; Kumar, K. S.; Jung, Y.; Thomas, J., Recent Trends in Transition Metal Dichalcogenide Based Supercapacitor Electrodes. *Nanoscale Horiz.* **2019,** *4* (4), 840-858.

(57) Lin, L. X.; Lei, W.; Zhang, S. W.; Liu, Y. Q.; Wallace, G. G.; Chen, J., Two-Dimensional Transition Metal Dichalcogenides in Supercapacitors and Secondary Batteries. *Energy Storage Mater.* **2019,** *19*, 408-423.

(58) Soon, J. M.; Loh, K. P., Electrochemical Double-Layer Capacitance of MoS_2 Nanowall Films. *Electrochem. Solid State Lett.* **2007,** *10* (11), A250-A254.

(59) Huang, K. J.; Zhang, J. Z.; Shi, G. W.; Liu, Y. M., Hydrothermal Synthesis of Molybdenum Disulfide Nanosheets as Supercapacitors Electrode Material. *Electrochim. Acta* **2014,** *132*, 397-403.

(60) Ren, L.; Zhang, G.; Yan, Z.; Kang, L.; Xu, H.; Shi, F.; Lei, Z.; Liu, Z. H., Three-Dimensional Tubular MoS_2/PANI Hybrid Electrode for High Rate Performance Supercapacitor. *ACS Appl. Mater. Interfaces* **2015,** *7* (51), 28294-302.

(61) Wang, L. N.; Ma, Y.; Yang, M.; Qi, Y. X., Hierarchical Hollow MoS_2 Nanospheres with Enhanced Electrochemical Properties Used as an Electrode in Supercapacitor. *Electrochim. Acta* **2015,** *186*, 391-396.

(62) Splendiani, A.; Sun, L.; Zhang, Y. B.; Li, T. S.; Kim, J.; Chim, C. Y.; Galli, G.; Wang, F., Emerging Photoluminescence in Monolayer MoS_2. *Nano Lett.* **2010,** *10* (4), 1271-1275.

(63) Acerce, M.; Voiry, D.; Chhowalla, M., Metallic 1T Phase MoS_2 Nanosheets as Supercapacitor Electrode Materials. *Nat. Nanotechnol.* **2015,** *10* (4), 313-318.

(64) Yang, M.; Hwang, S. K.; Jeong, J. M.; Huh, Y. S.; Choi, B. G., Nitrogen-Doped Carbon-Coated Molybdenum Disulfide Nanosheets for High-Performance Supercapacitor. *Synth. Met.* **2015,** *209*, 528-533.

(65) Masikhwa, T. M.; Madito, M. J.; Bello, A.; Dangbegnon, J. K.; Manyala, N., High Performance Asymmetric Supercapacitor Based on Molybdenum Disulphide/Graphene Foam and Activated Carbon from Expanded Graphite. *J. Colloid Interface Sci.* **2017,** *488*, 155-165.

(66) Huang, K. J.; Wang, L.; Zhang, J. Z.; Wang, L. L.; Mo, Y. P., One-Step Preparation of Layered Molybdenum Disulfide/Multi-Walled Carbon Nanotube Composites for Enhanced Performance Supercapacitor. *Energy* **2014,** *67*, 234-240.

(67) Cao, J.; Jafta, C. J.; Gong, J.; Rang, Q. D.; Lin, X. Z.; Felix, R.; Wilks, R. G.; Bar, M.; Yuan, J. Y.; Ballauff, M.; Lu, Y., Synthesis of Dispersible Mesoporous Nitrogen-Doped Hollow Carbon Nanoplates with Uniform Hexagonal Morphologies for Supercapacitors. *ACS Appl. Mater. Interfaces* **2016,** *8* (43), 29628-29636.

(68) Tang, Y. X.; Zhang, Y. Y.; Li, W. L.; Ma, B.; Chen, X. D., Rational Material Design for Ultrafast Rechargeable Lithium-Ion Batteries. *Chem. Soc. Rev.* **2015,** *44* (17), 5926-5940.

(69) Zhou, Y. L.; Yan, D.; Xu, H. Y.; Feng, J. K.; Jiang, X. L.; Yue, J.; Yang, J.; Qian, Y. T., Hollow Nanospheres of Mesoporous Co_9S_8 as a High-Capacity and Long-Life Anode for Advanced Lithium Ion Batteries. *Nano Energy* **2015,** *12*, 528-537.

(70) Shao, J.; Qu, Q. T.; Wan, Z. M.; Gao, T.; Zuo, Z. C.; Zheng, H. H., From Dispersed Microspheres to Interconnected Nanospheres: Carbon-Sandwiched Mono layered MoS_2 as High-Performance Anode of Li-Ion Batteries. *ACS Appl. Mater. Interfaces* **2015,** *7* (41), 22927-22934.

(71) Sharma, N.; Phase, D.; Thotiyl, M. O.; Ogale, S., Single-Phase Cu_3SnS_4 Nanoparticles for Robust High Capacity Lithium-Ion Battery Anodes. *ChemElectroChem* **2019,** *6* (5), 1371-1375.

(72) Zhang, Q.; Ding, Z. G.; Liu, G. Z.; Wan, H. L.; Mwizerwa, J. P.; Wu, J. H.; Yao, X. Y., Molybdenum Trisulfide Based Anionic Redox Driven Chemistry Enabling High-Performance All-Solid-State Lithium Metal Batteries. *Energy Storage Mater.* **2019,** *23*, 168-180.

(73) Chang, U.; Lee, J. T.; Yun, J. M.; Lee, B.; Lee, S. W.; Joh, H. I.; Eom, K.; Fuller, T. F., In Situ Self-Formed Nanosheet MoS_3/Reduced Graphene Oxide Material Showing Superior Performance as a Lithium-Ion Battery Cathode. *ACS Nano* **2019,** *13* (2), 1490-1498.

(74) Chang, C. H.; Chan, S. S., Infrared and Raman Studies of Amorphous MoS_3 and Poorly Crystalline MoS_2. *J. Catal.* **1981,** *72* (1), 139-148.

(75) Fu, W.; Yang, S. Y.; Yang, H.; Guo, B.; Huang, Z. Q., 2D Amorphous MoS_3 Nanosheets with Porous Network Structures for Scavenging Toxic Metal Ions from Synthetic Acid Mine Drainage. *J. Mater. Chem. A* **2019,** *7* (32), 18799-18806.

(76) Wang, J.; Ng, S. H.; Chew, S. Y.; Wexler, D.; Wang, G. X.; Liu, H. K., Characterization of Nanosize Molybdenum Trisulfide for Lithium Batteries and MoS_3 Structure Confirmation via Electrochemistry. *Electrochem. Solid State Lett.* **2007,** *10* (9), A204-A207.

(77) Li, X. D.; Wu, G. X.; Chen, J. W.; Li, M. C.; Li, W.; Wang, T. Y.; Jiang, B.; He, Y.; Mai, L. Q., Low-Crystallinity Molybdenum Sulfide Nanosheets Assembled on Carbon Nanotubes for Long-Life Lithium Storage: Unusual Electrochemical Behaviors and Ascending Capacities. *Appl. Surf. Sci.* **2017,** *392*, 297-304.

(78) Ye, H. L.; Wang, L.; Deng, S.; Zeng, X. Q.; Nie, K. Q.; Duchesne, P. N.; Wang, B.; Liu, S.; Zhou, J. H.; Zhao, F. P.; Han, N.; Zhang, P.; Zhong, J.; Sun, X. H.; Li, Y. Y.; Li, Y. G.; Lu, J., Amorphous MoS_3 Infiltrated with Carbon Nanotubes as an Advanced Anode Material of Sodium-Ion Batteries with Large Gravimetric, Areal, and Volumetric Capacities. *Adv. Energy Mater.* **2017,** *7* (5), 9.

(79) Chen, H. S.; Cong, T. N.; Yang, W.; Tan, C. Q.; Li, Y. L.; Ding, Y. L., Progress in Electrical Energy Storage System: A Critical Review. *Prog. Nat. Sci.* **2009,** *19* (3), 291-312.

(80) Noori, A.; El-Kady, M. F.; Rahmanifar, M. S.; Kaner, R. B.; Mousavi, M. F., Towards Establishing Standard Performance Metrics for Batteries, Supercapacitors and Beyond. *Chem. Soc. Rev.* **2019,** *48* (5), 1272-1341.

(81) Moussa, M.; El-Kady, M. F.; Zhao, Z. H.; Majewski, P.; Ma, J., Recent Progress and Performance Evaluation for Polyaniline/Graphene Nanocomposites as Supercapacitor Electrodes. *Nanotechnology* **2016,** *27* (44), 21.

(82) Gonzalez, A.; Goikolea, E.; Barrena, J. A.; Mysyk, R., Review on Supercapacitors: Technologies and Materials. *Renew. Sust. Energ. Rev.* **2016,** *58*, 1189-1206.

(83) Panda, P. K.; Grigoriev, A.; Mishra, Y. K.; Ahuja, R., Progress in Supercapacitors: Roles of Two Dimensional Nanotubular Materials. *Nanoscale Adv.* **2020,** *2* (1), 70-108.

(84) Beguin, F.; Presser, V.; Balducci, A.; Frackowiak, E., Carbons and Electrolytes for Advanced Supercapacitors. *Adv. Mater.* **2014,** *26* (14), 2219-2251.

(85) Zhang, Y.; Feng, H.; Wu, X. B.; Wang, L. Z.; Zhang, A. Q.; Xia, T. C.; Dong, H. C.; Li, X. F.; Zhang, L. S., Progress of Electrochemical Capacitor Electrode Materials: A Review. *Int. J. Hydrog. Energy* **2009,** *34* (11), 4889-4899.

(86) Wang, G. P.; Zhang, L.; Zhang, J. J., A Review of Electrode Materials for Electrochemical Supercapacitors. *Chem. Soc. Rev.* **2012,** *41* (2), 797-828.

(87) Rangom, Y.; Tang, X.; Nazar, L. F., Carbon Nanotube-Based Supercapacitors with Excellent ac Line Filtering and Rate Capability via Improved Interfacial Impedance. *ACS Nano* **2015,** *9* (7), 7248-7255.

(88) Pan, H.; Li, J. Y.; Feng, Y. P., Carbon Nanotubes for Supercapacitor. *Nanoscale Res. Lett.* **2010,** *5* (3), 654-668.

(89) Li, Y. M.; van Zijll, M.; Chiang, S.; Pan, N., KOH Modified Graphene Nanosheets for Supercapacitor Electrodes. *J. Power Sources* **2011,** *196* (14), 6003-6006.

(90) Pilon, L.; Wang, H.; d'Entremont, A., Recent Advances in Continuum Modeling of Interfacial and Transport Phenomena in Electric Double Layer Capacitors. *J. Electrochem. Soc.* **2015,** *162* (5), A5158-A5178.

(91) Helmholtz, H., Studien über electrische Grenzschichten. *Annalen der Physik* **1879,** *243* (7), 337-382.

(92) Jacob H. Masliyah; Bhattacharjee, S., *Electrokinetic and Colloid Transport Phenomena*. John Wiley & Sons, Hoboken, NJ: 2006.

(93) Bagotsky, V. S., *Fundamentals of Electrochemistry*. John Wiley & Sons, Hoboken, NJ: 2005.

(94) Gouy, M., Sur la Constitution de la Charge Electrique à la Surface d'un Electrolyte. *J. Phys. Theor. Appl.* **1910,** *9* (1), 457-468.

(95) Chapman, D. L., LI. A Contribution to the Theory of Electrocapillarity. *The London, Edinburgh, and Dublin Philosophical Magazine and Journal of Science* **1913,** *25* (148), 475-481.

(96) Stern, O., Zur Theorie der Elektrolytischen Doppelschicht. *Zeitschrift für Elektrochemie und angewandte physikalische Chemie* **1924,** *30* (21-22), 508-516.

(97) Zhu, Z. Z.; Wang, G. C.; Sun, M. Q.; Li, X. W.; Li, C. Z., Fabrication and Electrochemical Characterization of Polyaniline Nanorods Modified with Sulfonated Carbon Nanotubes for Supercapacitor Applications. *Electrochim. Acta* **2011,** *56* (3), 1366-1372.

(98) Balducci, A.; Bardi, U.; Caporali, S.; Mastragostino, M.; Soavi, F., Ionic Liquids for Hybrid Supercapacitors. *Electrochem. Commun.* **2004,** *6* (6), 566-570.

(99) Miller, J. R.; Simon, P., Materials Science - Electrochemical Capacitors for Energy Management. *Science* **2008,** *321* (5889), 651-652.

(100) Chae, J. H.; Ng, K. C.; Chen, G. Z., Nanostructured Materials for the Construction of Asymmetrical Supercapacitors. *Proc. Inst. Mech. Eng. Part A-J. Power Energy* **2010,** *224* (A4), 479-503.

(101) Park, S. K.; Nakhanivej, P.; Park, H. S., Two-Dimensional Nanomaterials as Emerging Pseudocapacitive Materials. *Korean J. Chem. Eng.* **2019,** *36* (10), 1557-1564.

(102) Conway, B. E.; Birss, V.; Wojtowicz, J., The Role and Utilization of Pseudocapacitance for Energy Storage by Supercapacitors. *J. Power Sources* **1997,** *66* (1-2), 1-14.

(103) Koppitz, F. D.; Schultze, J. W., Bond Formation in Electrosorbates-II Electrosorption and Double-Layer Properties in Non-Aqueous Solvents. *Electrochim. Acta* **1976,** *21* (5), 337-343.

(104) Delahay, P.; Holub, K., Coupling of Charging and Faradaic Processes Electrode Admittance for Reversible Processes. *J. Electroanal. Chem.* **1968,** *16* (2), 131-&.

(105) Salie, G.; Lorenz, W., Partielle Ladungsuberganskoeffizienten Elektrochemischer Reaktionen aus Stromimpulsmessungen. *Berichte Der Bunsen-Gesellschaft Fur Physikalische Chemie* **1964,** *68* (2), 197-208.

(106) Wu, S. L.; Zhu, Y. W., Highly Densified Carbon Electrode Materials Towards Practical Supercapacitor Devices. *Sci. China-Mater.* **2017,** *60* (1), 25-38.

(107) Zhang, J. T.; Zhao, X. S., On the Configuration of Supercapacitors for Maximizing Electrochemical Performance. *ChemSusChem* **2012,** *5* (5), 818-841.

(108) Arepalli, S.; Fireman, H.; Huffman, C.; Moloney, P.; Nikolaev, P.; Yowell, L.; Higgins, C. D.; Kim, K.; Kohl, P. A.; Turano, S. P.; Ready, W. J., Carbon-Nanotube-Based Electrochemical Double-Layer Capacitor Technologies for Spaceflight Applications. *Jom* **2005,** *57* (12), 26-31.

(109) Eftekhari, A., The Mechanism of Ultrafast Supercapacitors. *J. Mater. Chem. A* **2018,** *6* (7), 2866-2876.

(110) Roe, D. K., Alternating Current Polarography and Tensammetry. *Science* **1963,** *142* (3598), 1450-1450.

(111) Liu, C. F.; Neale, Z. G.; Cao, G. Z., Understanding Electrochemical Potentials of Cathode Materials in Rechargeable Batteries. *Mater. Today* **2016,** *19* (2), 109-123.

(112) Etacheri, V.; Marom, R.; Elazari, R.; Salitra, G.; Aurbach, D., Challenges in the Development of Advanced Li-Ion Batteries: A Review. *Energy Environ. Sci.* **2011,** *4* (9), 3243-3262.

(113) Deng, D., Li-Ion Batteries: Basics, Progress, and Challenges. *Energy Sci. Eng.* **2015,** *3* (5), 385-418.

(114) Eftekhari, A., High-Energy Aqueous Lithium Batteries. *Adv. Energy Mater.* **2018,** *8* (24), 14.

(115) Tarascon, J. M.; Armand, M., Issues and Challenges Facing Rechargeable Lithium Batteries. *Nature* **2001,** *414* (6861), 359-367.

(116) Nitta, N.; Yushin, G., High-Capacity Anode Materials for Lithium- Ion Batteries: Choice of Elements and Structures for Active Particles. *Part. Part. Syst. Charact.* **2014,** *31* (3), 317-336.

(117) Dunn, B.; Kamath, H.; Tarascon, J. M., Electrical Energy Storage for the Grid: A Battery of Choices. *Science* **2011,** *334* (6058), 928-935.

(118) Gulzar, U.; Goriparti, S.; Miele, E.; Li, T.; Maidecchi, G.; Toma, A.; De Angelis, F.; Capiglia, C.; Zaccaria, R. P., Next-Generation Textiles: From Embedded Supercapacitors to Lithium Ion Batteries. *J. Mater. Chem. A* **2016,** *4* (43), 16771-16800.

(119) Cabana, J.; Monconduit, L.; Larcher, D.; Palacin, M. R., Beyond Intercalation-Based Li-Ion Batteries: The State of the Art and Challenges of Electrode Materials Reacting Through Conversion Reactions. *Adv. Mater.* **2010,** *22* (35), E170-E192.

(120) Deng, D.; Kim, M. G.; Lee, J. Y.; Cho, J., Green Energy Storage Materials: Nanostructured TiO_2 and Sn-Based Anodes for Lithium-Ion Batteries. *Energy Environ. Sci.* **2009,** *2* (8), 818-837.

(121) Treptow, R. S., The Lead-Acid Battery: Its Voltage in Theory and in Practice. *J. Chem. Educ.* **2002,** *79* (3), 334-338.

(122) Hou, P. Y.; Chu, G.; Gao, J.; Zhang, Y. T.; Zhang, L. Q., Li-ion batteries: Phase transition. *Chin. Phys. B* **2016,** *25* (1), 11.

(123) Zheng, J. M.; Lochala, J. A.; Kwok, A.; Deng, Z. Q. D.; Xiao, J., Research Progress towards Understanding the Unique Interfaces between Concentrated Electrolytes and Electrodes for Energy Storage Applications. *Adv. Sci.* **2017,** *4* (8), 19.

(124) Xu, K., Electrolytes and Interphases in Li-Ion Batteries and Beyond. *Chem. Rev.* **2014,** *114* (23), 11503-11618.

(125) Cresce, A. V.; Borodin, O.; Xu, K., Correlating Li^+ Solvation Sheath Structure with Interphasial Chemistry on Graphite. *J. Phys. Chem. C* **2012,** *116* (50), 26111-26117.

(126) Goodenough, J. B., Evolution of Strategies for Modern Rechargeable Batteries. *Acc. Chem. Res.* **2013,** *46* (5), 1053-1061.

(127) Kamali, A. R.; Fray, D. J., Review on Carbon and Silicon Based Materials as Anode Materials for Lithium Ion Batteries. *J. New Mat.Electrochem. Syst.* **2010,** *13* (2), 147-160.

(128) Li, Z. J.; Jeanmairet, G.; Mendez-Morales, T.; Rotenberg, B.; Salanne, M., Capacitive Performance of Water-in-Salt Electrolytes in Supercapacitors: A Simulation Study. *J. Phys. Chem. C* **2018,** *122* (42), 23917-23924.

(129) Baptista, J. M.; Sagu, J. S.; Wijayantha, K. G. U.; Lobato, K., State-of-the-Art Materials for High Power and High Energy Supercapacitors: Performance Metrics and Obstacles for the Transition from Lab to Industrial Scale - A Critical Approach. *Chem. Eng. J.* **2019,** *374*, 1153-1179.

(130) Chhowalla, M.; Shin, H. S.; Eda, G.; Li, L. J.; Loh, K. P.; Zhang, H., The Chemistry of Two-Dimensional Layered Transition Metal Dichalcogenide Nanosheets. *Nat. Chem.* **2013,** *5* (4), 263-275.

(131) Yan, S. M.; Qiao, W.; He, X. M.; Guo, X. B.; Xi, L.; Zhong, W.; Du, Y. W., Enhancement of Magnetism by Structural Phase Transition in MoS_2. *Appl. Phys. Lett.* **2015,** *106* (1), 5.

(132) Tang, Q.; Jiang, D. E., Stabilization and Band-Gap Tuning of the 1T-MoS_2 Monolayer by Covalent Functionalization. *Chem. Mat.* **2015,** *27* (10), 3743-3748.

(133) Enyashin, A. N.; Yadgarov, L.; Houben, L.; Popov, I.; Weidenbach, M.; Tenne, R.; Bar-Sadan, M.; Seifert, G., New Route for Stabilization of 1T-WS_2 and MoS_2 Phases. *J. Phys. Chem. C* **2011,** *115* (50), 24586-24591.

(134) Lei, Z. D.; Zhan, J.; Tang, L.; Zhang, Y.; Wang, Y., Recent Development of Metallic (1T) Phase of Molybdenum Disulfide for Energy Conversion and Storage. *Adv. Energy Mater.* **2018,** *8* (19), 29.

(135) Weber, T.; Muijsers, J. C.; Niemantsverdriet, J. W., Structure of Amorphous MoS_3. *J. Phys. Chem.* **1995,** *99* (22), 9194-9200.

(136) Jiao, H. J.; Li, Y. W.; Delmon, B.; Halet, J. F., The Structure and Possible Catalytic Sites of Mo_3S_9 as a Model of Amorphous Molybdenum Trisulfide: A Computational Study. *J. Am. Chem. Soc.* **2001,** *123* (30), 7334-7339.

(137) Theerthagiri, J.; Senthil, R. A.; Senthilkumar, B.; Polu, A. R.; Madhavan, J.; Ashokkumar, M., Recent Advances in MoS_2 Nanostructured Materials for Energy and Environmental Applications - A Review. *J. Solid State Chem.* **2017,** *252*, 43-71.

(138) Firmiano, E. G. D.; Rabelo, A. C.; Dalmaschio, C. J.; Pinheiro, A. N.; Pereira, E. C.; Schreiner, W. H.; Leite, E. R., Supercapacitor Electrodes Obtained by Directly Bonding 2D MoS_2 on Reduced Graphene Oxide. *Adv. Energy Mater.* **2014,** *4* (6), 8.

(139) Bissett, M. A.; Kinloch, I. A.; Dryfe, R. A. W., Characterization of MoS_2-Graphene Composites for High-Performance Coin Cell Supercapacitors. *ACS Appl. Mater. Interfaces* **2015,** *7* (31), 17388-17398.

(140) Woods, J. M.; Jung, Y.; Xie, Y. J.; Liu, W.; Liu, Y. H.; Wang, H. H.; Cha, J. J., One-Step Synthesis of MoS_2/WS_2 Layered Heterostructures and Catalytic Activity of Defective Transition Metal Dichalcogenide Films. *ACS Nano* **2016,** *10* (2), 2004-2009.

(141) Li, B. W.; Zu, S.; Zhou, J. D.; Jiang, Q.; Du, B. W.; Shan, H. Y.; Luo, Y.; Liu, Z.; Zhu, X.; Fang, Z. Y., Single-Nanoparticle Plasmonic Electro-optic Modulator Based on MoS_2 Monolayers. *ACS Nano* **2017,** *11* (10), 9720-9727.

(142) Huang, Y. X.; Guo, J. H.; Kang, Y. J.; Ai, Y.; Li, C. M., Two Dimensional Atomically Thin MoS_2 Nanosheets and Their Sensing Applications. *Nanoscale* **2015,** *7* (46), 19358-19376.

(143) Liu, Y. C.; Jiao, L. F.; Wu, Q.; Zhao, Y. P.; Cao, K. Z.; Liu, H. Q.; Wang, Y. J.; Yuan, H. T., Synthesis of rGO-Supported Layered MoS_2 for High-Performance Rechargeable Mg Batteries. *Nanoscale* **2013,** *5* (20), 9562-9567.

(144) Ma, D. W.; Ju, W. W.; Li, T. X.; Zhang, X. W.; He, C. Z.; Ma, B. Y.; Tang, Y. A.; Lu, Z. S.; Yang, Z. X., Modulating Electronic, Magnetic and Chemical Properties of MoS_2

Monolayer Sheets by Substitutional Doping with Transition Metals. *Appl. Surf. Sci.* **2016,** *364*, 181-189.

(145) Liu, J.; Lu, P. J.; Liang, S.; Liu, J.; Wang, W.; Lei, M.; Tang, S.; Yang, Q., Ultrathin Li_3VO_4 Nanoribbon/Graphene Sandwich-like Nanostructures with Ultrahigh Lithium Ion Storage Properties. *Nano Energy* **2015,** *12*, 709-724.

(146) Lu, Y. T.; Chu, D. M.; Zhu, M. S.; Du, Y. K.; Yang, P., Exfoliated Carbon Nitride Nanosheets Decorated with NiS as an Efficient Noble-Metal-Free Visible-Light-Driven Photocatalyst for Hydrogen Evolution. *Phys. Chem. Chem. Phys.* **2015,** *17* (26), 17355-17361.

(147) Ma, L.; Xu, L. M.; Zhou, X. P.; Xu, X. Y., Biopolymer-Assisted Hydrothermal Synthesis of Flower-Like MoS_2 Microspheres and Their Supercapacitive Properties. *Mater. Lett.* **2014,** *132*, 291-294.

(148) David, L.; Bhandavat, R.; Singh, G., MoS_2/Graphene Composite Paper for Sodium-Ion Battery Electrodes. *ACS Nano* **2014,** *8* (2), 1759-1770.

(149) Savjani, N.; Lewis, E. A.; Bissett, M. A.; Brent, J. R.; Dryfe, R. A. W.; Haigh, S. J.; O'Brien, P., Synthesis of Lateral Size-Controlled Monolayer 1H-MoS_2@Oleylamine as Supercapacitor Electrodes. *Chem. Mat.* **2016,** *28* (2), 657-664.

(150) Zhou, R.; Han, C. J.; Wang, X. M., Hierarchical MoS_2-Coated Three-Dimensional Graphene Network for Enhanced Supercapacitor Performances. *J. Power Sources* **2017,** *352*, 99-110.

(151) Yang, X. W.; Cheng, C.; Wang, Y. F.; Qiu, L.; Li, D., Liquid-Mediated Dense Integration of Graphene Materials for Compact Capacitive Energy Storage. *Science* **2013,** *341* (6145), 534-537.

(152) Nightingale, E. R., Phenomenological Theory of Ion Solvation - Effective Radii of Hhydrated Ions. *J. Phys. Chem.* **1959,** *63* (9), 1381-1387.

(153) Andalib, P.; Wood, M. J.; Korn, S. J., Control of Outer Vestibule Dynamics and Current Magnitude in the Kv2.1 Potassium Channel. *J. Gen. Physiol.* **2002,** *120* (5), 739-755.

(154) Zhou, J. W.; Qin, J.; Zhang, X.; Shi, C. S.; Liu, E. Z.; Li, J. J.; Zhao, N. Q.; He, C. N., 2D Space-Confined Synthesis of Few-Layer MoS_2 Anchored on Carbon Nanosheet for Lithium-Ion Battery Anode. *ACS Nano* **2015,** *9* (4), 3837-3848.

(155) Zhang, X.; Lai, Z. C.; Tan, C. L.; Zhang, H., Solution-Processed Two-Dimensional MoS_2 Nanosheets: Preparation, Hybridization, and Applications. *Angew. Chem. Int. Edit.* **2016,** *55* (31), 8816-8838.

(156) Coleman, J. N.; Lotya, M.; O'Neill, A.; Bergin, S. D.; King, P. J.; Khan, U.; Young, K.; Gaucher, A.; De, S.; Smith, R. J.; Shvets, I. V.; Arora, S. K.; Stanton, G.; Kim, H. Y.; Lee, K.;

Kim, G. T.; Duesberg, G. S.; Hallam, T.; Boland, J. J.; Wang, J. J.; Donegan, J. F.; Grunlan, J. C.; Moriarty, G.; Shmeliov, A.; Nicholls, R. J.; Perkins, J. M.; Grieveson, E. M.; Theuwissen, K.; McComb, D. W.; Nellist, P. D.; Nicolosi, V., Two-Dimensional Nanosheets Produced by Liquid Exfoliation of Layered Materials. *Science* **2011,** *331* (6017), 568-571.

(157) Matte, H.; Gomathi, A.; Manna, A. K.; Late, D. J.; Datta, R.; Pati, S. K.; Rao, C. N. R., MoS_2 and WS_2 Analogues of Graphene. *Angew. Chem.-Int. Edit.* **2010,** *49* (24), 4059-4062.

(158) Xie, J. F.; Zhang, H.; Li, S.; Wang, R. X.; Sun, X.; Zhou, M.; Zhou, J. F.; Lou, X. W.; Xie, Y., Defect-Rich MoS_2 Ultrathin Nanosheets with Additional Active Edge Sites for Enhanced Electrocatalytic Hydrogen Evolution. *Adv. Mater.* **2013,** *25* (40), 5807-+.

(159) Zhang, L.; Wu, H. B.; Yan, Y.; Wang, X.; Lou, X. W., Hierarchical MoS_2 Microboxes Constructed by Nanosheets with Enhanced Electrochemical Properties for Lithium Storage and Water Splitting. *Energy Environ. Sci.* **2014,** *7* (10), 3302-3306.

(160) Wu, D.; Zhang, C.; Xu, S.; Zhu, Y.; Xiong, D.; Wang, L.; Chu, P. K., Fabrication and Enhanced Supercapacitance of Hollow Nanostructured MoS_2 Prepared by a CATB-Assisted Hydrothermal Process. *Mater. Lett.* **2016,** *184*, 96-99.

(161) Hu, B. L.; Qin, X. Y.; Asiri, A. M.; Alamry, K. A.; Al-Youbi, A. O.; Sun, X. P., Synthesis of Porous Tubular C/MoS_2 Nanocomposites and Their Application as a Novel Electrode Material for Supercapacitors with Excellent Cycling Stability. *Electrochim. Acta* **2013,** *100*, 24-28.

(162) Ishimoto, S.; Asakawa, Y.; Shinya, M.; Naoi, K., Degradation Responses of Activated-Carbon-Based EDLCs for Higher Voltage Operation and Their Factors. *J. Electrochem. Soc.* **2009,** *156* (7), A563-A571.

(163) Wang, P. P.; Sun, H. Y.; Ji, Y. J.; Li, W. H.; Wang, X., Three-Dimensional Assembly of Single-Layered MoS_2. *Adv. Mater.* **2014,** *26* (6), 964-969.

(164) Ye, L.; Guo, W.; Yang, Y.; Du, Y. F.; Xie, Y., Directing the Architecture of Various MoS_2 Hierarchical Hollow Cages through the Controllable Synthesis of Surfactant/Molybdate Composite Precursors. *Chem. Mat.* **2007,** *19* (25), 6331-6337.

(165) Park, S. K.; Yu, S. H.; Woo, S.; Quan, B.; Lee, D. C.; Kim, M. K.; Sung, Y. E.; Piao, Y., A Simple $_L$-Cysteine-Assisted Method for the Growth of MoS_2 Nanosheets on Carbon Nanotubes for High-Performance Lithium Ion Batteries. *Dalton Trans* **2013,** *42* (7), 2399-405.

(166) Chang, K.; Chen, W. X., L-Cysteine-Assisted Synthesis of Layered MoS_2/Graphene Composites with Excellent Electrochemical Performances for Lithium Ion Batteries. *ACS Nano* **2011,** *5* (6), 4720-4728.

(167) Lu, A. H.; Sun, T.; Li, W. C.; Sun, Q.; Han, F.; Liu, D. H.; Guo, Y., Synthesis of Discrete and Dispersible Hollow Carbon Nanospheres with High Uniformity by Using Confined Nanospace Pyrolysis. *Angew. Chem.-Int. Edit.* **2011,** *50* (49), 11765-11768.

(168) Wierenga, A. M.; Lenstra, T. A. J.; Philipse, A. P., Aqueous Dispersions of Colloidal Gibbsite Platelets: Synthesis, Characterisation and Intrinsic Viscosity Measurements. *Colloid Surf. A-Physicochem. Eng. Asp.* **1998,** *134* (3), 359-371.

(169) Yang, D.; Frindt, R. F., Powder X-Ray Diffraction of Two-Dimensional Materials. *J. Appl. Phys.* **1996,** *79* (5), 2376-2385.

(170) Kamila, S.; Mohanty, B.; Samantara, A. K.; Guha, P.; Ghosh, A.; Jena, B.; Satyam, P. V.; Mishra, B. K.; Jena, B. K., Highly Active 2D Layered MoS_2-rGO Hybrids for Energy Conversion and Storage Applications. *Sci. Rep.* **2017,** *7*, 13.

(171) Sari, F. N. I.; Ting, J. M., Direct Growth of MoS_2 Nanowalls on Carbon Nanofibers for Use in Supercapacitor. *Sci. Rep.* **2017,** *7*, 13.

(172) Liu, R.; Mahurin, S. M.; Li, C.; Unocic, R. R.; Idrobo, J. C.; Gao, H. J.; Pennycook, S. J.; Dai, S., Dopamine as a Carbon Source: The Controlled Synthesis of Hollow Carbon Spheres and Yolk-Structured Carbon Nanocomposites. *Angew. Chem.-Int. Edit.* **2011,** *50* (30), 6799-6802.

(173) Song, Y. Z.; Song, Y.; Zhong, H., Gold Nanoparticle/Double-Walled Carbon Nanotube-Modified Glassy Carbon Electrode and Its Application. *Gold Bull.* **2011,** *44* (2), 107-111.

(174) Seok, S.; Choi, I.; Lee, K. G.; Choi, B. G.; Park, K. J.; Park, J. Y.; Kwon, O. J.; Lee, S. J.; Kim, D. H., Dopamine-Induced Pt and N-Doped Carbon@Silica Hybrids as High-Performance Anode Catalysts for Polymer Electrolyte Membrane Fuel Cells. *Rsc Adv.* **2014,** *4* (80), 42582-42584.

(175) Qiao, M.; Meysami, S. S.; Ferrero, G. A.; Xie, F.; Meng, H.; Grobert, N.; Titirici, M. M., Low-Cost Chitosan-Derived N-Doped Carbons Boost Electrocatalytic Activity of Multiwall Carbon Nanotubes. *Adv. Funct. Mater.* **2018,** *28* (16), 7.

(176) Chen, G.; Wang, S. P.; Yi, R.; Tan, L. F.; Li, H. B.; Zhou, M.; Yan, L. T.; Jiang, Y. B.; Tan, S.; Wang, D. H.; Deng, S. G.; Meng, X. W.; Luo, H. M., Facile Synthesis of Hierarchical MoS_2-Carbon Microspheres as a Robust Anode for Lithium Ion Batteries. *J. Mater. Chem. A* **2016,** *4* (24), 9653-9660.

(177) Zheng, X. L.; Xu, J. B.; Yan, K. Y.; Wang, H.; Wang, Z. L.; Yang, S. H., Space-Confined Growth of MoS_2 Nanosheets within Graphite: The Layered Hybrid of MoS_2 and Graphene as an Active Catalyst for Hydrogen Evolution Reaction. *Chem. Mat.* **2014,** *26* (7), 2344-2353.

(178) Ferrari, A. C., Raman Spectroscopy of Graphene and Graphite: Disorder, Electron-Phonon Coupling, Doping and Nonadiabatic Effects. *Solid State Commun.* **2007,** *143* (1-2), 47-57.

(179) Jin, X. B.; He, R.; Dai, S., Electrochemical Graphitization: An Efficient Conversion of Amorphous Carbons to Nanostructured Graphites. *Chem.-Eur. J.* **2017,** *23* (48), 11455-11459.

(180) Juhl, A. C.; Schneider, A.; Ufer, B.; Brezesinski, T.; Janek, J.; Froba, M., Mesoporous Hollow Carbon Spheres for Lithium-Sulfur Batteries: Distribution of Sulfur and Electrochemical Performance. *Beilstein J. Nanotechnol.* **2016,** *7*, 1229-1240.

(181) da Silveira Firmiano, E. G.; Rabelo, A. C.; Dalmaschio, C. J.; Pinheiro, A. N.; Pereira, E. C.; Schreiner, W. H.; Leite, E. R., Supercapacitor Electrodes Obtained by Directly Bonding 2D MoS_2 on Reduced Graphene Oxide. *Adv. Energy Mater.* **2014,** *4* (6), 1301380.

(182) Pham, K. C.; McPhail, D. S.; Wee, A. T. S.; Chua, D. H. C., Amorphous Molybdenum Sulfide on Graphene-Carbon Nanotube Hybrids as Supercapacitor Electrode Materials. *Rsc Adv.* **2017,** *7* (12), 6856-6864.

(183) Wu, X. Z.; Xing, W.; Zhang, L.; Zhuo, S. P.; Zhou, J.; Wang, G. Q.; Qiao, S. Z., Nickel Nanoparticles Prepared by Hydrazine Hydrate Reduction and their Application in Supercapacitor. *Powder Technol.* **2012,** *224*, 162-167.

(184) Krishnamoorthy, K.; Kim, S. J., Growth, Characterization and Electrochemical Properties of Hierarchical CuO Nanostructures for Supercapacitor Applications. *Mater. Res. Bull.* **2013,** *48* (9), 3136-3139.

(185) Ratha, S.; Rout, C. S., Supercapacitor Electrodes Based on Layered Tungsten Disulfide-Reduced Graphene Oxide Hybrids Synthesized by a Facile Hydrothermal Method. *ACS Appl. Mater. Interfaces* **2013,** *5* (21), 11427-11433.

(186) Wang, Z. Y.; von dem Bussche, A.; Qiu, Y.; Valentin, T. M.; Gion, K.; Kane, A. B.; Hurt, R. H., Chemical Dissolution Pathways of MoS_2 Nanosheets in Biological and Environmental Media. *Environ. Sci. Technol.* **2016,** *50* (13), 7208-7217.

(187) Balasingam, S. K.; Lee, M.; Kim, B. H.; Lee, J. S.; Jun, Y., Freeze-Dried MoS_2 Sponge Electrodes for Enhanced Electrochemical Energy Storage. *Dalton Trans.* **2017,** *46* (7), 2122-2128.

(188) Liu, A. M.; Lv, H.; Liu, H.; Li, Q. G.; Zhao, H., Two Dimensional MoS_2/CNT Hybrid Ink for Paper-Based Capacitive Energy Storage. *J. Mater. Sci.-Mater. Electron.* **2017,** *28* (12), 8452-8459.

(189) Fic, K.; Platek, A.; Piwek, J.; Frackowiak, E., Sustainable Materials for Electrochemical Capacitors. *Mater. Today* **2018,** *21* (4), 437-454.

(190) Lin, Z.; Goikolea, E.; Balducci, A.; Naoi, K.; Taberna, P. L.; Salanne, M.; Yushin, G.; Simon, P., Materials for Supercapacitors: When Li-Ion Battery Power is not Enough. *Mater. Today* **2018,** *21* (4), 419-436.

(191) Conway, B. E., Transition from Supercapacitor to Battery Behavior in Electrochemcial Energy-Storage. *J. Electrochem. Soc.* **1991,** *138* (6), 1539-1548.

(192) de Levie, R., On Porous Electrodes in Electrolyte Solutions—IV. *Electrochim. Acta* **1964,** *9* (9), 1231-1245.

(193) Liu, Q.; Zhou, J. W.; Song, C. H.; Li, X. L.; Wang, Z. P.; Yang, J.; Cheng, J. L.; Li, H.; Wang, B., 2.2V High Performance Symmetrical Fiber-Shaped Aqueous Supercapacitors Enabled by "Water-in-Salt" Gel Electrolyte and N-Doped Graphene Fiber. *Energy Storage Mater.* **2020,** *24*, 495-503.

(194) Yan, J.; Wang, Q.; Wei, T.; Fan, Z. J., Recent Advances in Design and Fabrication of Electrochemical Supercapacitors with High Energy Densities. *Adv. Energy Mater.* **2014,** *4* (4), 43.

(195) Harmas, R.; Palm, R.; Harmas, M.; Pohl, M.; Kurig, H.; Tallo, I.; Tee, E.; Vaas, I.; Vali, R.; Romann, T.; Oll, O.; Kanarbik, R.; Liivand, K.; Eskusson, J.; Kruusma, J.; Thomberg, T.; Janes, A.; Miidla, P.; Lust, E., Influence of Porosity Parameters and Electrolyte Chemical Composition on the Power Densities of Non-Aqueous and Ionic Liquid Based Supercapacitors. *Electrochim. Acta* **2018,** *283*, 931-948.

(196) Zhu, Z. Q.; Zhang, R. Z.; Lin, J. H.; Zhang, K. F.; Li, N.; Zhao, C. H.; Chen, G. R.; Zhao, C. J., Ni,Zn-Codoped $MgCo_2O_4$ Electrodes for Aqueous Asymmetric Supercapacitor and Rechargeable Zn Battery. *J. Power Sources* **2019,** *437*, 8.

(197) Shen, H. D.; Li, H. J.; Li, M. J.; Li, C. P.; Qian, L. R.; Su, L.; Yang, B. H., High-Performance Aqueous Symmetric Supercapacitor Based on Polyaniline/Vertical Graphene/Ti Multilayer Electrodes. *Electrochim. Acta* **2018,** *283*, 410-418.

(198) Sun, F.; Gao, J. H.; Pi, X. X.; Wang, L. J.; Yang, Y. Q.; Qu, Z. B.; Wu, S. H., High Performance Aqueous Supercapacitor Based on Highly Nitrogen Doped Carbon Nanospheres with Unimodal Mesoporosity. *J. Power Sources* **2017,** *337*, 189-196.

(199) Zhang, M.; Li, Y. T.; Shen, Z. R., "Water-in-Salt" Electrolyte Enhanced High Voltage Aqueous Supercapacitor with All-Pseudocapacitive Metal-Oxide Electrodes. *J. Power Sources* **2019,** *414*, 479-485.

(200) Lee, W. S. V.; Xiong, T.; Loh, G. C.; Tan, T. L.; Xue, J. M., Optimizing Electrolyte Physiochemical Properties toward 2.8 V Aqueous Supercapacitor. *ACS Appl. Energ. Mater.* **2018,** *1* (7), 3070-3076.

(201) Avireddy, H.; Byles, B. W.; Pinto, D.; Galindo, J. M. D.; Biendicho, J. J.; Wan, X. H.; Flox, C.; Crosnier, O.; Brousse, T.; Pomerantseva, E.; Morante, J. R.; Gogotsi, Y., Stable High-Voltage Aqueous Pseudocapacitive Energy Storage Device with Slow Self-Discharge. *Nano Energy* **2019,** *64*, 10.

(202) Bu, X. D.; Su, L. J.; Dou, Q. Y.; Lei, S. L.; Yan, X. B., A Low-Cost "Water-in-Salt" Electrolyte for a 2.3 V High-Rate Carbon-Based Supercapacitor. *J. Mater. Chem. A* **2019,** *7* (13), 7541-7547.

(203) Droguet, L.; Grimaud, A.; Fontaine, O.; Tarascon, J.-M., Water-in-Salt Electrolyte (WiSE) for Aqueous Batteries: A Long Way to Practicality. *Adv. Energy Mater. n/a* (n/a), 2002440.

(204) Hasegawa, G.; Kanamori, K.; Kiyomura, T.; Kurata, H.; Abe, T.; Nakanishi, K., Hierarchically Porous Carbon Monoliths Comprising Ordered Mesoporous Nanorod Assemblies for High-Voltage Aqueous Supercapacitors. *Chem. Mat.* **2016,** *28* (11), 3944-3950.

(205) Bichat, M. P.; Raymundo-Pinero, E.; Beguin, F., High Voltage Supercapacitor Built with Seaweed Carbons in Neutral Aqueous Electrolyte. *Carbon* **2010,** *48* (15), 4351-4361.

(206) Suo, L. M.; Borodin, O.; Wang, Y. S.; Rong, X. H.; Sun, W.; Fan, X. L.; Xu, S. Y.; Schroeder, M. A.; Cresce, A. V.; Wang, F.; Yang, C. Y.; Hu, Y. S.; Xu, K.; Wang, C. S., "Water-in-Salt" Electrolyte Makes Aqueous Sodium-Ion Battery Safe, Green, and Long-Lasting. *Adv. Energy Mater.* **2017,** *7* (21), 10.

(207) Suo, L. M.; Oh, D.; Lin, Y. X.; Zhuo, Z. Q.; Borodin, O.; Gao, T.; Wang, F.; Kushima, A.; Wang, Z. Q.; Kim, H. C.; Qi, Y.; Yang, W. L.; Pan, F.; Li, J.; Xu, K.; Wang, C. S., How Solid-Electrolyte Interphase Forms in Aqueous Electrolytes. *J. Am. Chem. Soc.* **2017,** *139* (51), 18670-18680.

(208) Peled, E.; Menkin, S., Review-SEI: Past, Present and Future. *J. Electrochem. Soc.* **2017,** *164* (7), A1703-A1719.

(209) Fong, R.; Vonsacken, U.; Dahn, J. R., Studies of Lithium Intercalation into Carbons Using Nonaqueous Electrochemical-Cells. *J. Electrochem. Soc.* **1990,** *137* (7), 2009-2013.

(210) Choi, M. G.; Kang, S. B.; Yoon, J. R.; Lee, B. G.; Jeong, D. Y., The Surface Modification of Electrode with Solid Electrolyte Interphase for Hybrid Supercapacitor. *J. Electr. Eng. Technol.* **2015,** *10* (3), 1102-1106.

(211) Li, W. Y.; Xu, K. B.; An, L.; Jiang, F. R.; Zhou, X. Y.; Yang, J. M.; Chen, Z. G.; Zou, R. J.; Hu, J. Q., Effect of Temperature on the Performance of Ultrafine MnO_2 Nanobelt Supercapacitors. *J. Mater. Chem. A* **2014,** *2* (5), 1443-1447.

(212) Zhou, H. Q.; Yu, F.; Zhu, Q.; Sun, J. Y.; Qin, F.; Yu, L.; Bao, J. M.; Yu, Y.; Chen, S.; Ren, Z. F., Water Splitting by Electrolysis at High Current Densities under 1.6 Volts. *Energy Environ. Sci.* **2018,** *11* (10), 2858-2864.

(213) Gambou-Bosca, A.; Belanger, D., Electrochemical Characterization of MnO_2-Based Composite in the Presence of Salt-in-Water and Water-in-Salt Electrolytes as Electrode for Electrochemical Capacitors. *J. Power Sources* **2016,** *326*, 595-603.

(214) Faisal, S. N.; Haque, E.; Noorbehesht, N.; Zhang, W. M.; Harris, A. T.; Church, T. L.; Minett, A. I., Pyridinic and Graphitic Nitrogen-Rich Graphene for High-Performance Supercapacitors and Metal-Free Bifunctional Electrocatalysts for ORR and OER. *Rsc Adv.* **2017,** *7* (29), 17950-17958.

(215) Lasia, A., *Electrochemical Impedance Spectroscopy and its Applications*. Springer-Verlag New York: 2014; p XIII, 367.

(216) Kang, J.; Wen, J. Z.; Jayaram, S. H.; Yu, A. P.; Wang, X. H., Development of an Equivalent Circuit Model for Electrochemical Double Layer Capacitors (EDLCs) with Distinct Electrolytes. *Electrochim. Acta* **2014,** *115*, 587-598.

(217) Laheaar, A.; Janes, A.; Lust, E., Electrochemical Properties of Carbide-Derived Carbon Electrodes in Non-Aqueous Electrolytes Based on Different Li-Salts. *Electrochim. Acta* **2011,** *56* (25), 9048-9055.

(218) Kurig, H.; Vestli, M.; Janes, A.; Lust, E., Electrical Double Layer Capacitors Based on Two 1-Ethyl-3-Methylimidazolium Ionic Liquids with Different Anions. *Electrochem. Solid State Lett.* **2011,** *14* (8), A120-A122.

(219) Kurig, H.; Vestli, M.; Tonurist, K.; Janes, A.; Lust, E., Influence of Room Temperature Ionic Liquid Anion Chemical Composition and Electrical Charge Delocalization on the Supercapacitor Properties. *J. Electrochem. Soc.* **2012,** *159* (7), A944-A951.

(220) McEldrew, M.; Goodwin, Z. A. H.; Kornyshev, A. A.; Bazant, M. Z., Theory of the Double Layer in Water-in-Salt Electrolytes. *J. Phys. Chem. Lett.* **2018,** *9* (19), 5840-5846.

(221) McOwen, D. W.; Seo, D. M.; Borodin, O.; Vatamanu, J.; Boyle, P. D.; Henderson, W. A., Concentrated Electrolytes: Decrypting Electrolyte Properties and Reassessing Al Corrosion Mechanisms. *Energy Environ. Sci.* **2014,** *7* (1), 416-426.

(222) Masarapu, C.; Zeng, H. F.; Hung, K. H.; Wei, B. Q., Effect of Temperature on the Capacitance of Carbon Nanotube Supercapacitors. *ACS Nano* **2009,** *3* (8), 2199-2206.

(223) Yan, J. A.; Khoo, E.; Sumboja, A.; Lee, P. S., Facile Coating of Manganese Oxide on Tin Oxide Nanowires with High-Performance Capacitive Behavior. *ACS Nano* **2010,** *4* (7), 4247-4255.

(224) Yuan, C. Z.; Zhang, X. G.; Wu, Q. F.; Gao, B., Effect of Temperature on the Hybrid Supercapacitor Based on NiO and Activated Carbon with Alkaline Polymer Gel Electrolyte. *Solid State Ion.* **2006,** *177* (13-14), 1237-1242.

(225) Liu, X. R.; Pickup, P. G., Performance and Low Temperature Behaviour of Hydrous Ruthenium Oxide Supercapacitors with Improved Power Densities. *Energy Environ. Sci.* **2008,** *1* (4), 494-500.

(226) Smart, M. C.; Ratnakumar, B. V.; Surampudi, S., Electrolytes for Low-Temperature Lithium Batteries Based on Ternary Mixtures of Aliphatic Carbonates. *J. Electrochem. Soc.* **1999,** *146* (2), 486-492.

(227) Huang, C. K.; Sakamoto, J. S.; Wolfenstine, J.; Surampudi, S., The Limits of Low-Temperature Performance of Li-Ion Cells. *J. Electrochem. Soc.* **2000,** *147* (8), 2893-2896.

(228) Steinhauer, M.; Risse, S.; Wagner, N.; Friedrich, K. A., Investigation of the Solid Electrolyte Interphase Formation at Graphite Anodes in Lithium-Ion Batteries with Electrochemical Impedance Spectroscopy. *Electrochim. Acta* **2017,** *228*, 652-658.

(229) Barua, A.; Paul, A., Unravelling the Role of Temperature in a Redox Supercapacitor Composed of Multifarious Nanoporous Carbon@Hydroquinone. *Rsc Adv.* **2020,** *10* (3), 1799-1810.

(230) Grahame, D. C., The Electrical Double Layer and the Theory of Electrocapillarity. *Chem. Rev.* **1947,** *41* (3), 441-501.

(231) Goodenough, J. B.; Park, K. S., The Li-Ion Rechargeable Battery: A Perspective. *J. Am. Chem. Soc.* **2013,** *135* (4), 1167-1176.

(232) Whittingham, M. S., Lithium Batteries and Cathode Materials. *Chem. Rev.* **2004,** *104* (10), 4271-4301.

(233) Parker, J. F.; Chervin, C. N.; Pala, I. R.; Machler, M.; Burz, M. F.; Long, J. W.; Rolison, D. R., Rechargeable Nickel-3D Zinc Batteries: An Energy-Dense, Safer Alternative to Lithium-Ion. *Science* **2017,** *356* (6336), 414-417.

(234) Xue, L.; Zhang, Q. H.; Zhu, X. H.; Gu, L.; Yue, J. L.; Xia, Q. Y.; Xing, T.; Chen, T. T.; Yao, Y.; Xia, H., 3D $LiCoO_2$ Nanosheets Assembled Nanorod Arrays via Confined Dissolution-Recrystallization for Advanced Aqueous Lithium-Ion Batteries. *Nano Energy* **2019,** *56*, 463-472.

(235) Glatz, H.; Tervoort, E.; Kundu, D., Unveiling Critical Insight into the Zn Metal Anode Cyclability in Mildly Acidic Aqueous Electrolytes: Implications for Aqueous Zinc Batteries. *ACS Appl. Mater. Interfaces* **2020,** *12* (3), 3522-3530.

(236) Kim, H.; Hong, J.; Park, K. Y.; Kim, H.; Kim, S. W.; Kang, K., Aqueous Rechargeable Li and Na Ion Batteries. *Chem. Rev.* **2014,** *114* (23), 11788-11827.

(237) Li, W.; Dahn, J. R.; Wainwright, D. S., Rechargeable Lithium Batteries with Aqueous-Electrolytes. *Science* **1994,** *264* (5162), 1115-1118.

(238) Suo, L. M.; Han, F. D.; Fan, X. L.; Liu, H. L.; Xu, K.; Wang, C. S., "Water-in-Salt" Electrolytes Enable Green and Safe Li-Ion Batteries for Large Scale Electric Energy Storage Applications. *J. Mater. Chem. A* **2016,** *4* (17), 6639-6644.

(239) Qu, L. N.; Hou, X. H.; Huang, X. Y.; Liang, Q.; Ru, Q.; Wu, B.; Lam, K. H., Self-Assembled Porous $NiFe_2O_4$ Floral Microspheres Inlaid on Ultrathin Flake Graphite as Anode Materials for Lithium Ion Batteries. *ChemElectroChem* **2017,** *4* (12), 3148-3155.

(240) Demirocak, D. E.; Srinivasan, S. S.; Stefanakos, E. K., A Review on Nanocomposite Materials for Rechargeable Li-Ion Batteries. *Appl. Sci.-Basel* **2017,** *7* (7), 26.

(241) Wang, Y.; Wu, J. J.; Tang, Y. F.; Lii, X. J.; Yang, C. Y.; Qin, M. S.; Huang, F. Q.; Li, X.; Zhang, X., Phase-Controlled Synthesis of Cobalt Sulfides for Lithium Ion Batteries. *ACS Appl. Mater. Interfaces* **2012,** *4* (8), 4246-4250.

(242) Xu, C.; Zeng, Y.; Rui, X. H.; Xiao, N.; Zhu, J. X.; Zhang, W. Y.; Chen, J.; Liu, W. L.; Tan, H. T.; Hng, H. H.; Yan, Q. Y., Controlled Soft-Template Synthesis of Ultrathin C@FeS Nanosheets with High-Li-Storage Performance. *ACS Nano* **2012,** *6* (6), 4713-4721.

(243) Wang, J. G.; Liu, H. Y.; Zhou, R.; Liu, X. R.; Wei, B. Q., Onion-like Nanospheres Organized by Carbon Encapsulated Few-Layer MoS_2 Nanosheets with Enhanced Lithium Storage Performance. *J. Power Sources* **2019,** *413*, 327-333.

(244) Shi, Y. M.; Zhou, W.; Lu, A. Y.; Fang, W. J.; Lee, Y. H.; Hsu, A. L.; Kim, S. M.; Kim, K. K.; Yang, H. Y.; Li, L. J.; Idrobo, J. C.; Kong, J., van der Waals Epitaxy of MoS_2 Layers Using Graphene as Growth Templates. *Nano Lett.* **2012,** *12* (6), 2784-2791.

(245) Teng, Y. Q.; Zhao, H. L.; Zhang, Z. J.; Li, Z. L.; Xia, Q.; Zhang, Y.; Zhao, L. N.; Du, X. F.; Du, Z. H.; Lv, P. P.; Swierczek, K., MoS_2 Nanosheets Vertically Grown on Graphene Sheets for Lithium-Ion Battery Anodes. *ACS Nano* **2016,** *10* (9), 8526-8535.

(246) Jacobson, A. J.; Chianelli, R. R.; Rich, S. M.; Whittingham, M. S., Amorphous Molybdenum Trisulfide-New Lithium Battery Cathode. *Mater. Res. Bull.* **1979,** *14* (11), 1437-1448.

(247) Wildervanck, J. C.; Jellinek, F., Preparation and Crystallinity of Molybdenum and Tungsten Sulfides. *Z. Anorg. Allg. Chem.* **1964,** *328* (5-6), 309-318.

(248) Bhattacharya, R. N.; Lee, C. Y.; Pollak, F. H.; Schleich, D. M., Optical Study of Amorphous MoS_3 - Determination of the Fundamental Energy-Gap. *J. Non-Cryst. Solids* **1987,** *91* (2), 235-242.

(249) Wei, H.; Cheng, S. X.; Zhang, X. Z.; Zhuo, R. X., Thermo-Sensitive Polymeric Micelles Based on Poly(N-Isopropylacrylamide) as Drug Carriers. *Prog. Polym. Sci.* **2009,** *34* (9), 893-910.

(250) Mei, Y.; Lu, Y.; Polzer, F.; Ballauff, M.; Drechsler, M., Catalytic Activity of Palladium Nanoparticles Encapsulated in Spherical Polyelectrolyte Brushes and Core-Shell Microgels. *Chem. Mat.* **2007,** *19* (5), 1062-1069.

(251) Gu, S.; Lu, Y.; Kaiser, J.; Albrecht, M.; Ballauff, M., Kinetic Analysis of the Reduction of 4-Nitrophenol Catalyzed by Au/Pd Nanoalloys Immobilized in Spherical Polyelectrolyte Brushes. *Phys. Chem. Chem. Phys.* **2015,** *17* (42), 28137-28143.

(252) Sourisseau, C.; Gorochov, O.; Schleich, D. M., Comparative IR and Raman Studies of Various Amorphous MoS_3 and Li_xMoS_3 Phases. *Mater. Sci. Eng. B-Solid State Mater. Adv. Technol.* **1989,** *3* (1-2), 113-117.

(253) Vrubel, H.; Merki, D.; Hu, X. L., Hydrogen Evolution Catalyzed by MoS_3 and MoS_2 Particles. *Energy Environ. Sci.* **2012,** *5* (3), 6136-6144.

(254) Ye, H. L.; Ma, L.; Zhou, Y.; Wang, L.; Han, N.; Zhao, F. P.; Deng, J.; Wu, T. P.; Li, Y. G.; Lu, J., Amorphous MoS_3 as the Sulfur-Equivalent Cathode Material for Room-Temperature Li-S and Na-S Batteries. *Proc. Natl. Acad. Sci. U. S. A.* **2017,** *114* (50), 13091-13096.

(255) Gao, T.; Ji, X.; Hou, S.; Fan, X. L.; Li, X. G.; Yang, C. Y.; Han, F. D.; Wang, F.; Jiang, J. J.; Xu, K.; Wang, C. S., Thermodynamics and Kinetics of Sulfur Cathode during Discharge in $MgTFSI_2$-DME Electrolyte. *Adv. Mater.* **2018,** *30* (3), 8.

(256) Burns, J. C.; Jain, G.; Smith, A. J.; Eberman, K. W.; Scott, E.; Gardner, J. P.; Dahn, J. R., Evaluation of Effects of Additives in Wound Li-Ion Cells Through High Precision Coulometry. *J. Electrochem. Soc.* **2011,** *158* (3), A255-A261.

(257) Perreault, L. L.; Colo, F.; Meligrana, G.; Kim, K.; Fiorilli, S.; Bella, F.; Nair, J. R.; Vitale-Brovarone, C.; Florek, J.; Kleitz, F.; Gerbaldi, C., Spray-Dried Mesoporous Mixed Cu-Ni Oxide@Graphene Nanocomposite Microspheres for High Power and Durable Li-Ion Battery Anodes. *Adv. Energy Mater.* **2018,** *8* (35), 12.

(258) Marinaro, M.; Mancini, M.; Nobili, F.; Tossici, R.; Damen, L.; Marassi, R., A Newly Designed Cu/Super-P Composite for the Improvement of Low-Temperature Performances of Graphite Anodes for Lithium-Ion Batteries. *J. Power Sources* **2013,** *222*, 66-71.

(259) Shi, P. C.; Zheng, H.; Liang, X.; Sun, Y.; Cheng, S.; Chen, C. H.; Xiang, H. F., A Highly Concentrated Phosphate-Based Electrolyte for High-Safety Rechargeable Lithium Batteries. *Chem. Commun.* **2018,** *54* (35), 4453-4456.

(260) Gaikwad, A. M.; Khau, B. V.; Davies, G.; Hertzberg, B.; Steingart, D. A.; Arias, A. C., A High Areal Capacity Flexible Lithium-Ion Battery with a Strain-Compliant Design. *Adv. Energy Mater.* **2015,** *5* (3), 11.

(261) Cannarella, J.; Arnold, C. B., Stress Evolution and Capacity Fade in Constrained Lithium-Ion Pouch Cells. *J. Power Sources* **2014,** *245*, 745-751.

(262) Liu, X. D.; Lyu, Y. C.; Zhang, Z. H.; Li, H.; Hu, Y. S.; Wang, Z. X.; Zhao, Y. M.; Kuang, Q.; Dong, Y. Z.; Liang, Z. Y.; Fan, Q. H.; Chen, L. Q., Nanotube Li_2MoO_4: A Novel and High-Capacity Material as a Lithium-Ion Battery Anode. *Nanoscale* **2014,** *6* (22), 13660-13667.

(263) Matsuyama, T.; Hayashi, A.; Ozaki, T.; Mori, S.; Tatsumisago, M., Electrochemical Properties of All-Solid-State Lithium Batteries with Amorphous MoS_3 Electrodes Prepared by Mechanical Milling. *J. Mater. Chem. A* **2015,** *3* (27), 14142-14147.

(264) Tang, W.; Liu, L. L.; Zhu, Y. S.; Sun, H.; Wu, Y. P.; Zhu, K., An Aqueous Rechargeable Lithium Battery of Excellent Rate Capability Based on a Nanocomposite of MoO_3 Coated with PPy and $LiMn_2O_4$. *Energy Environ. Sci.* **2012,** *5* (5), 6909-6913.

(265) Bourgeteau, T.; Tondelier, D.; Geffroy, B.; Brisse, R.; Laberty-Robert, C.; Campidelli, S.; de Bettignies, R.; Artero, V.; Palacin, S.; Jousselme, B., A H_2-Evolving Photocathode Based on Direct Sensitization of MoS_3 with an Organic Photovoltaic Cell. *Energy Environ. Sci.* **2013,** *6* (9), 2706-2713.

(266) Cao, J.; Mei, S. L.; Jia, H.; Ott, A.; Ballauff, M.; Lu, Y., In Situ Synthesis of Catalytic Active Au Nanoparticles onto Gibbsite-Polydopamine Core-Shell Nanoplates. *Langmuir* **2015,** *31* (34), 9483-9491.

(267) Sevilla, M.; Yu, L. H.; Ania, C. O.; Titirici, M. M., Supercapacitive Behavior of Two Glucose-Derived Microporous Carbons: Direct Pyrolysis versus Hydrothermal Carbonization. *ChemElectroChem* **2014,** *1* (12), 2138-2145.

(268) Samantara, A. K.; Sahu, S. C.; Ghosh, A.; Jena, B. K., Sandwiched Graphene with Nitrogen, Sulphur Co-Doped CQDs: An Efficient Metal-Free Material for Energy Storage and Conversion Applications. *J. Mater. Chem. A* **2015,** *3* (33), 16961-16970.

(269) David B. Williams, C. B. C., *Transmission Electron Microscopy*. Springer, Boston, MA: 2009.

(270) https://myscope.training/legacy/tem/background/concepts/imagegeneration/detail.php.

(271) Huang, J.; Cavanaugh, T.; Nur, B.; Camp, W. K.; Diaz, E.; Wawak, B., An Introduction to SEM Operational Principles and Geologic Applications for Shale Hydrocarbon Reservoirs. In *Electron Microscopy of Shale Hydrocarbon Reservoirs*, American Association of Petroleum Geologists: 2013; Vol. 102, p 0.

(272) NanoAnalysis, O. I., An Introduction to Energy-Dispersive and Wavelength-Dispersive X-Ray Microanalysis. *MICROSCOPY AND ANALYSIS* **2006**.

(273) Sun, S. F., *Physical Chemistry of Macromolecules: Basic Principles and Issues*. Wiley: 2004.

(274) Jayasooriya, U. A.; Jenkins, R. D., Introduction to Raman Spectroscopy. In *An Introduction to Laser Spectroscopy: Second Edition*, Andrews, D. L.; Demidov, A. A., Eds. Springer US: Boston, MA, 2002; pp 77-104.

(275) John F. Watts, J. W., *An Introduction to Surface Analysis by XPS and AES*. Wiley: 2003.

List of Figures

List of Tables

List of Abbreviations

LIBs	Li-ion batteries
PDA	polydopamine
HCPs	hollow carbon nanoplates
Li_2SO_4	lithium sulfate
LiTFSI	lithium bis(trifluoromethanesulfonyl)imide
WISE	“water-in-salt” electrolyte
EIS	electrochemical impedance spectroscopy
WIS-LIBs	“water-in-salt” Li-ion batteries
SPB	spherical polyelectrolyte brushes
XRD	X-ray diffraction
EDL	electric double layer
EDLCs	electric double layer capacitors
ESR	equivalent series resistance
ALIBs	aqueous Li-ion batteries
HER	H_2 evolution reaction
OER	O_2 evolution reaction
SEI	solid-electrolyte interphase
LiOTf	lithium trifluoromethane sulfonate
TMSs	transition metal sulfides
GO	graphene oxide
TEM	transmission electron microscopy
TGA	thermogravimetric analysis
CV	cyclic voltammetry
SPB	spherical polyelectrolyte brushes
AEMH	2-Amino-ethylmethacrylate hydrochloride
THF	tetrahydrofuran

STEM	scanning transmission electron microscopy
HAADF	high angle annular dark field
HR-TEM	high resolution transmission electron microscopy
WDS	wavelength dispersed spectroscopy
SEM	scanning electron microscopy
XPS	X-ray photoelectron spectroscopy
SHE	standard hydrogen electrode
SSIPs	solvent-separated ion pairs
CIPs	contact ion pairs
AGGs	cation-anion aggregates
HOMO	highest occupied molecular orbital
LUMO	lowest unoccupied molecular orbital
TMDs	transition metal dichalcogenides
SIBs	sodium ion batteries
AAO	anodic aluminium oxide
BJH	Barrett-Joyner-Halenda
BET	Brunauer–Emmett–Teller
PS	polystyrene
HMEM	2-[p-(2-Hydroxy-2-methylpropiophenone)]-ethyleneglycol methacrylate
LED	light-emitting diode
AIP	aluminum isopropoxide
ASB	aluminum sec-butoxide
TEOS	tetraethyl orthosilicate
PVP	polyvinylpyrrolidone
PVDF	polyvinylidene fluoride
V50	2,2’-azobis(2-amidinopropane)dihydrochloride
CTAB	cetyltrimethylammonium bromide

PTFE	poly(tetrafluoroethylene)
NMP	1-methyl-2-pyrrolidinone
$(NH_4)_2MoS_4$	ammonium tetrathiomolybdate
NH_4HF_2	ammonium hydrogen difluoride
Tris	tris(hydroxymethyl) aminomethane
Na_2MoO_4	sodium molybdate
$(NH_4)_2MoS_4$	ammonium tetrathiomolybdate
$LiMn_2O_4$	lithium manganese oxide
E	specific energy
P	specific power
C	capacitance
C_{sp}	specific (gravimetric) capacitance
ε_r	the dielectric constant of the electrolyte
ε_0	the dielectric constant of vacuum
ψ_s	the potential at the electrode surface
C_S^{St}	Stern areal capacitance
C_S^D	diffuse layer areal capacitance
$C_{sp\text{-}cv}$	the specific capacitance calculated from CV curves
ν	the scan rate
ΔV	the potential window
m	the mass loading of the active material on one electrode
Δt	the discharging time
F	Faraday constant
Z_{Re}	real parts of the impedance
Z_{Im}	imaginary parts of the impedance
ϕ	the phase angle
R_s	the internal resistance

R_{ct}	the charge-transfer resistance
W	Warburg impedance
C_{ef}	interfacial capacitance
C_{ads}	adsorption capacitance
C_{dl}	double-layer capacitance
R_{ads}	the adsorption resistance

Publication list

(1) **Quan, T.;** Xu, Y. L.; Tovar, M.; Goubard-Bretesché, N.; Li,Z. L.; Kochovski, Z.; Kirmse, H.; Skrodczky, K.; Mei, S. L.; Yu, H. T.; Abou-Ras, D.; Wagemaker, M.; Lu, Y.; Hollow MoS_3 Nanospheres as Efficient Electrode Material for "Water-in-Salt" Li-Ion Batteries. *Batteries & Supercaps* 2020, 3(8): 747-756.

(2) **Quan, T.;** Härk, E.; Xu, Y. L.; Ahmet, I., Höhn, C., Lu, Y. Unveiling the Formation of Solid Electrolyte Interphase and its Temperature Dependence in "Water-in-Salt" Supercapacitors. *ACS Appl. Mater. Interfaces* 2021, 13, 3, 3979-3990.

(3) **Quan, T.;** Goubard-Bretesche, N.; Härk, E.; Kochovski, Z.; Mei, S. L.; Pinna, N.; Ballauff, M.; Lu, Y., Highly Dispersible Hexagonal Carbon-MoS_2-Carbon Nanoplates with Hollow Sandwich Structures for Supercapacitors. *Chem.-Eur. J.* 2019, 25 (18), 4757-4766.

(4) Jia, H.; **Quan, T.;** Liu, X. L.; Bai, L.; Wang, J. D.; Boujioui, F.; Ye, R.; Vald, A.; Lu, Y.; Gohy, J. F., Core-Shell Nanostructured Organic Redox Polymer Cathodes with Superior Performance. *Nano Energy* **2019,** *64*,

(5) Yu, H. T.; **Quan, T.;** Mei, S. L.; Kochovski, Z.; Huang, W.; Meng, H.; Lu, Y., Prompt Electrodeposition of Ni Nanodots on Ni Foam to Construct a High-Performance Water-Splitting Electrode: Efficient, Scalable, and Recyclable. *Nano-Micro Lett.* **2019,** *11* (1), 13.

(6) Xu, Y.L.; **Quan, T.;** Ahmet, I.; Li, Z. L.; Meng, X.Q.; Yu, H. T.; Kochovski, Z.; Höhn, C.; Krol, R.; Wagemaker, M.; Lu, Y., Ultra-Stable High-Rate Aqueous MoS_3/Zn Batteries with Dominating Zn-Ion Insertion and Suppressed Proton Uptake, submitted.

(7) Jia, H.; Friebe, C.; Schubert, U. S.; Zhang, X. Z.; **Quan, T.;** Lu, Y.; Gohy, J. F., Core-Shell Nanoparticles with a Redox Polymer Core and a Silica Porous Shell as High-Performance Cathode Material for Lithium-Ion Batteries. *Energy Technol.*, **2019**, 8.

Acknowledgement

At this point I want to take the opportunity to express my gratitude to all the people I have met, worked with and learnt from, and from whom I have received considerable inspiration, encouragement and support during my Ph.D. journey.

First, I would like to thank Prof. Matthias Ballauff and Prof. Yan Lu, not only for the opportunity on this interesting and challenging topic under their supervision in the whole process of my Ph.D. research but for their help in my career development. The constant guidance and support they provided throughout these years have helped me to be on track of Ph.D. process and to move forward in doing independent and professional research.

Further, I am particularly grateful to those who helped me to start and complete the work for this thesis. Special thanks to Dr. Yaolin Xu for the kind introduction to the fundamental knowledge of electrochemistry and the discussions about all electrochemical problems in experiments, to Dr. Eneli Härk for our fruitful discussions and her support with the supercapacitor analysis, to Dr. Nicolas Goubard-Bretesché for the teaching about how to prepare electrodes and to discuss the measured data of supercapacitors. I would say without their academic attitude and patient perseverance, I will not be shaped into a chemist that I am today.

My sincere thanks also go to the collaborators who make important contributions to this thesis. I want to thank Prof. Nicola Pinna (HU Berlin) who provided the opportunity to do hydrothermal experiments in his lab and helped review the manuscript of MoS_2 work, Dr. Michael Tovar (EM-ASD, HZB) who taught me all basic information about XRD and helped me much with the XRD data fitting, Dr. Zdravko Kochovski who leaded me into TEM measurements and passed countless TEM images, Kai Skrodczky (HU Berlin) for his help with the synthesis of MoS_2 and Raman spectra measurements and other collaborators like Dr. Daniel Abou-Ras (EM-ASD, HZB) for SEM measurements, Dr. Hongtao Yu for three-electrode measurements, Dr. Shilin Mei for SPB synthesis, Dr. Holm Kirmse (HU Berlin) for STEM images and Prof. Marnix Wagemaker (TU Delft) for pouch cell assembly. Without their contributions, this thesis will not be possible.

Next, I would like to thank all the fantastic former and current colleagues in EM-AEES (HZB), who are great persons to work with and also nice friends in life. There are many names I would

like to mention with great pleasure, Dr. Sebastian Risse, Dr. Duong Tung Pham, Xiangqi Meng, Xuefeng Pan, Dongjiu Xie, Yuhang Zhao, Daniel Besold, Oumeima Jouini, Linda Schmalz, Dr. Sasa Gu, Dr. Jie Cao, Dr. He Jia, Dr. Qidi Ran. I am very grateful for all the scientific discussions as well as all the interesting discussions at leisure time.

Great thanks go to China Scholarship Council (CSC) for the financial support during the past three and a half years.

Last but not least, I must express my deepest gratitude to my parents for their constant and unconditional love, encouragement and support on me. You are my most important people in the world and I will love you forever.

Selbstständigkeitserklärung

Hiermit erkläre ich die vorliegende Arbeit selbst verfasst und nur unter Zuhilfenahme der angegebenen Hilfsmittel angefertigt zu haben.

Ferner erkläre ich, dass ich nicht anderweitig mit oder ohne Erfolg versucht habe, eine Dissertation einzureichen oder mich einer Doktorprüfung zu unterziehen.

Berlin, den 04.11.2020

Ting QUAN